National Library of Canada
Acquisitions and Bibliographic Services Branch
395 Wellington Street
Ottawa, Ontario
K1A 0N4

Bibliothèque nationale du Canada
Direction des acquisitions et des services bibliographiques
395, rue Wellington
Ottawa (Ontario)
K1A 0N4

NOTICE

The quality of this microform is heavily dependent upon the quality of the original thesis submitted for microfilming. Every effort has been made to ensure the highest quality of reproduction possible.

If pages are missing, contact the university which granted the degree.

Some pages may have indistinct print especially if the original pages were typed with a poor typewriter ribbon or if the university sent us an inferior photocopy.

AVIS

La qualité de cette microforme dépend grandement de la qualité de la thèse soumise au microfilmage. Nous avons tout fait pour assurer une qualité supérieure de reproduction.

S'il manque des pages, veuillez communiquer avec l'université qui a conféré le grade.

La qualité d'impression de certaines pages peut laisser à désirer, surtout si les pages originales ont été dactylographiées à l'aide d'un ruban usé ou si l'université nous a fait parvenir une photocopie de qualité inférieure.

Canada

EMI Potential of Multiple Sources Within a Shielded Enclosure

by
Robert J.H. Crawhall

A thesis submitted to the
School of Graduate Studies and Research
in partial fulfillment of the requirements for the degree of

Doctor of Philosophy

Ottawa-Carleton Institute for Electrical Engineering

Department of Electrical Engineering
Faculty of Engineering
University of Ottawa

ISBN 0-315-89617-5

Canada

UNIVERSITÉ D'OTTAWA
UNIVERSITY OF OTTAWA

Abstract

An analytic model is developed for the prediction of electromagnetic emissions potential due to multiple integrated circuits (ICs) within a shielded enclosure. Detailed analysis of the radiated emissions from an IC leads to dipole representations of the sources. These dipole sources are then applied in the determination of the fields and currents induced on the inside of the enclosure. The magnitude of these disturbances is taken as a metric of electromagnetic emissions potential.

The power spectral density and the radiation efficiency of the ICs are investigated. ICs are represented by magnetic and electric dipoles, the magnitude and polarization of which are determined through measurement or calculation.

Green's functions are derived that relate the dipole sources to the electromagnetic disturbances induced on the walls of the enclosure. Mapping matrices are proposed that relate multiple sources to multiple points on the wall. The role of source diversity in the summing problem is discussed. A stochastic analysis of the multiple source problem determines the distribution of disturbances due to known probability distributions of significant source factors.

The shielding effectiveness of enclosures is determined using perturbation models of the leakage paths driven by the disturbances calculated through the application of the mapping matrices.

Acknowledgments

I would like to thank my thesis supervisor Dr. George Costache of the University of Ottawa and Mr. Stan Xavier of Bell Northern Research for their guidance and support during my studies and for their tireless drive to build a centre of excellence in electromagnetic compatibility engineering.

I am deeply indebted to my colleagues at Bell Northern Research, University of Ottawa, Bell Canada, University of Toronto and Northern Telecom with whom I have spent innumerable hours trying to demystify this fascinating area of research and along with whom I have spent many days in the labs and test sites when practical reality got ahead of theoretical comprehension. Several deserve explicit recognition for the contributions they have made to this thesis: Mr. Dick Goulette, Dr. Liliana Diaz-Olavarrieta, Dr. Larry Wong, Dr. Boris Livshits, Mr. Denis Lalonde, Mr. Rod Wallace, Mr. Marcel Cohen, Dr. Keith Balmain and Mr. Tom Montor for their input to the technical content.

I would like to thank Bell Northern Research and Northern Telecom for the facilities and assistance that made this thesis possible, in particular, my two directors Mr. Geoff Goodinson and Mr. John Pittman.

I look back with gratitude to my Master's supervisor, Dr. Tom Pavlasek of McGill University who believed that a Mechanical Engineer could understand electromagnetic theory as well as anyone and thereby started me on this path.

And finally the greatest thanks to my wife, Ms. Theresa Duk, who personally sacrificed a lot of good times to my pursuit of this goal.

Contents

List of Figures

List of Tables

Chapter 1

Introduction

"That old black magic..." *Mercer-Arlen*

1.1 Objective

The objective of this thesis is to provide an **analytic** approach to the prediction of **electromagnetic disturbances** induced on the inner surface of a **shielded enclosure** which houses **multiple integrated circuits** (ICs) at **non-resonant** frequencies. This analysis will lead to the modelling of the **electromagnetic interference** (EMI) potential of ICs and the **shielding effectiveness** (SE) of the enclosure that houses them.

Three basic issues are addressed:

- The radiated electromagnetic emissions from an IC source;
- The electric current and field disturbances that each of these sources induce on the enclosure wall; and
- The total disturbance resulting from multiple sources.

The complex multiple source EMI problem will be decomposed into its basic elements to permit modelling in terms of simplified radiation structures, in this case **magnetic and electric dipoles**. This will facilitate the prediction of the interference potential of the sources, the shielding effectiveness of the enclosure, the interpretation of EMI measurement data and the implementation of source level mitigation techniques.

These simplified source models will be used in conjunction with **dyadic Green's functions** to predict the likely electric current and field induced on the walls of the enclosure by a set of devices. They will also provide a quantifiable understanding of the factors which can mitigate or exacerbate the EMI problem in an enclosed multiple source environment.

These models are intended to be applied in the early stages of electronic equipment design. Prediction of the currents and fields on the enclosure wall establishes a basis for determining both the required and the expected levels of shielding effectiveness based on **perturbation models** of leakage paths through the enclosure.

1.2 Motivation

The EMI problem is of rapidly growing interest in the field of **electromagnetic compatibility** (EMC) in electronic system design. For manufacturers of information technology equipment, the majority of the EMI engineering effort is directed towards meeting **regulatory electromagnetic emissions limits**.

Three trends in industry are necessitating a thorough understanding of the fundamentals of the electromagnetic interference problem:

- The increasing speed and density of digital logic circuits are resulting in greater interference potential;

- The competitive nature of the global market requires expeditious implementation of cost effective solutions; and
- The international standards and national regulatory requirements for electromagnetic emissions control are tightening, making compliance mandatory in almost all major markets.

There is a small but growing body of academic reference texts that address the EMI problems as a separate engineering discipline with its own theory and solution methodologies (e.g. [Ott 88], [Paul 92]). The principle sources of new technical papers in the area of information technology equipment are the **IEEE Transactions on Electromagnetic Compatibility**, and two international symposia, the **IEEE International EMC Symposium** in the United States and the **International EMC Symposium** in Europe.

There remains a pressing need to develop a rigorous understanding of the electromagnetic interference potential of complex printed circuit packs within metallic enclosures. This will allow the effective inclusion of emissions reduction strategies during the early design stages of electronic systems.

1.3 Approach

This thesis provides a methodology to solve the specific EMI problem of relating the direct radiated emissions from multiple integrated circuits to the currents and fields that are produced on the conducting walls of the enclosure that houses them at non-resonant frequencies. An analytic approach is used to determine the magnitude and polarization of the primary emissions sources. This information is then used as the input to a Green's function model of the enclosure to determine the induced fields and currents. Stochastic modelling of the multiple source problem is used to establish the likely magnitude of the disturbances based on probability distributions of various source factors.

The problem is structured in a manner that is compatible with the design environment in which it must be solved. It reflects the practical separation between the disciplines of circuit, silicon, component packaging, printed circuit board (pcb) and mechanical enclosure design. All of which are critical in solving the system level EMI problem.

A four step approach is presented:

- **The modelling of ICs as primary radiators**: Localized sources of radiated energy, in particular large integrated circuits, are modelled as orthogonal dipoles of electric and magnetic current. Their continuous emissions energy spectra are reduced to discrete spectral magnitudes that are readily incorporated in analytic models;
- **The linkage between the primary radiators and the induced disturbances on the enclosure wall**: Mapping matrices based on three-dimensional electromagnetic modeling relate sources to induced currents and fields; and
- **The likely effect of multiple sources on the amplitude of the induced disturbance**: Monte Carlo analysis used to relate the probability distributions of key source characteristics to the induced disturbances on the wall.
- **Electromagnetic emissions from the enclosure are quantified**: Perturbation models, driven by the field and current magnitudes derived in the preceding analysis, are used to establish the shielding effectiveness of the enclosure.

An extensive analysis is performed of the energy spectrum typical of the ICs which are to be modelled. In particular the interference potential of non-periodic signals is investigated.

The identification and quantification of sources of electromagnetic energy in the context of EMI problems is found to be different from the analysis required for functional signal simulation.

In order to determine the cumulative disturbance created by many different source signal spectra in the context of a regulatory compliance prediction, the magnitude of the sources is determined with respect to a defined set of measurement instrumentation, specifically a **quasi-peak detector** with a 120 kHz bandpass input. It is shown that these complex IC sources may then be correlated to electric or magnetic dipole moments through modelling or measurement[1].

Once the IC sources are characterized in terms of electric and magnetic dipole moments they are used in a dyadic Green's function model of an ideal cavity. This model permits the evaluation of currents and electric fields on the walls of a shielded enclosure due to sources at specific points within. The contributions of these individual sources are summed through **superposition.**

The Green's function provides a one to one mapping between a source point and a disturbance point within the enclosure. This mapping is a property of the enclosure at a given frequency. A **mapping matrix,** that relates a predefined set of source and disturbance points, is proposed for computational efficiency and a numerical characterization of the enclosure.

The analysis is then extended to include probabilistic distributions of sources. Sensitivity to changes in frequency, phase, polarization and placement are investigated. The probability distribution of currents on the enclosure wall due to the distribution of source characteristics is determined stochastically through the use of Monte Carlo techniques.

Particular attention is paid throughout the thesis to subjects that have largely been overlooked in the literature such as the response characteristics of the measurement instrumentation to broadband source signals.

1. The measurement methods, developed by the author and his colleagues at BNR and presented in this thesis, are currently being considered for adoption by the Society of Automotive Engineers [SAE 93]

The use of Green's functions within conducting enclosures follows the approach of [Rahmat-Samii 75] and [Tai 76]. This methodology was first applied to the EMI problem by Mendez [Mendez 78]. The modelling of integrated circuits as electric and magnetic dipoles is based on work presently underway at Bell Northern Research [Goulette 92-1,2]

1.4 Thesis Outline

In Chapter 2 a general description of the electromagnetic interference problem is provided as it applies to information technology equipment in the telecommunications and data processing sectors.

The power spectral densities of various time harmonic and non-periodic source signals are investigated in Chapter 3. Non-periodic digital signals are shown to consist of both **broadband** and **narrowband** components. These narrowband components are **inherent** in **cyclostationary** stochastic processes such as synchronized data signals.

Spectral energy that contributes to interference potential is shown to be due to **intentional** and **unintentional** characteristics of the information coding scheme and hardware implementation of the circuit design [Crawhall 91]. The unintentional signals are composed of **parasitic** and **unconstrained** parts. The influence of the response characteristics of the **quasi-peak detector** in the determination of interference potential from broadband signals is examined and quantified.

In Chapter 4 the electromagnetic fields radiated directly from large integrated circuits are modelled as **electric and magnetic dipoles**. The magnitude and orientation of the dipoles may be determined through detailed calculation, measurement or design specifications. This work, presently under development by the author and several of his colleagues at Bell

Northern Research and Northern Telecom[2], represents a significant advance in analytic modelling of EMI problems [Goulette 92-1,92-2].

In Chapter 5 equations are developed relating the IC dipole model to current and field values present on the enclosure walls. These are derived from **dyadic Green's functions** for the field distributions within a perfectly conducting rectangular cavity. The analysis is valid for non-resonant frequencies only. Results are compared with measured data. Some examples of current and field disturbances due to single source components are provided. The equations derived in this chapter are then applied to the solution of deterministic multiple source problems in Chapter 6 and stochastic multiple source problems in Chapter 7.

In Chapter 6 **mapping matrices** are introduced to relate the IC sources to the currents and fields on the walls of a shielded enclosure. These mapping matrices, based on the Green's function, yield considerable insight into position and polarization dependence of the enclosure-source interaction The sum of disturbances on the wall of the enclosure is shown to depend on the **diversities** of the sources. These are defined as **spectral** diversity, **spatial** diversity, **angular** diversity and **phase** diversity.

Chapter 7 addresses the problem of determining the likely current and field levels that a shielded enclosure would be required to contain prior to the availability of detailed knowledge about the printed circuit board and its ICs. The **mean magnitude, standard deviation** and **9th decile magnitude** of the induced current on the wall are calculated based on **probability distributions** of basic source parameters.

Differences in induced current at various frequencies and under various constraints are calculated through the use of **Monte Carlo** simulations. The existence of a source at a particular

2. Mr. R. Goulette, Dr. L. Diaz-Olavarrieta, Dr. L.Wong, Mr. T.Montor, Mr. M.Radojicic, Ms. A.Lau, Mr. T.Sterzyck

point is given in terms of a **Bernoulli distribution**. This leads to a **binomial distribution** of the number of sources. These statistical trends are compared with the observations made in Chapter 6. The source distributions are mapped into current distributions on the wall using the mapping matrices. Sensitivities to frequency, phase and placement constraints are examined.

In Chapter 8 a simple emissions model is described that would account for **small apertures** in the enclosure boundary. This is typical of models that could be used to relate the currents and field induced on the interior of the shielded enclosure to the emissions levels measured outside.

1.5 Restrictions in the Scope of the Thesis

This thesis is structured to provide a continuous theoretical development through the various levels of the EMI problem, from the measurement method and power spectrum of the signal source through to the emissions from shielded enclosures. There has been no attempt to provide a comprehensive treatment of all the sources of noise or the mechanisms for their radiation from the enclosure. Rather, the focus has been placed on aspects of the problem that are important but have not yet received extensive exposure in the literature.

The detailed development of an overall emissions model is expected to require several more years of refinement. Specifically absent from this treatment are:

- Equipment for which the cavity model of the shielding structure does not apply;
- Resonant effects within the enclosure;
- Emissions from distributed sources within the enclosure;
- Cable emissions; and

- Software dependency.

The enclosure models presented are valid for non-resonant conditions. Cavity behavior at resonance has been extensively investigated, particularly in the context of microwave communications. Resonant cavity theory is presented in most standard texts [e.g. Ramo 84]. The accuracy of the resonant cavity model is dependent in part on the characterization of loss within the cavity. This subject is not dealt with in this thesis although it would provide an interesting area for further investigation.

The Green's function models presented in Chapter 5 may be extended to the analysis of large distributed sources such as tracks on a printed circuit board through integration over the source current distribution. Alternatively a large contributing source could be modelled in terms of discrete elements using the techniques presented in Chapter 6. The computational issues raised by either of these approaches have not been treated in this thesis.

The prediction of emissions from cables using thin wire Method of Moments has been performed in industry for many years with limited success. The difficulty that has been found in predicting actual radiated field strength is due in part to the variability in measurement due to cable position. This is predominantly a flaw in test methodology which must be addressed by the appropriate regulatory and standards bodies. Additional difficulties arise due to the computational time and space requirements and the interaction of large numbers of nearly parallel wires in loose bundles. Recent improvements in the Method of Moments algorithm have resolved some of the inherent computational limitations in this area. [Tilston 90].

A significant variation in emissions levels is often observed when the operating software of the equipment under test is changed. The analysis of Chapter 3 provides a number of insights into the reasons for this in terms of the spectral density of the transmitted signal. No attempt has been made to relate this to specific approaches to software coding.

1.6 Contributions

This thesis provides the first comprehensive analysis of direct radiated emissions from multiple integrated circuits within a shielded enclosure. As such it is a significant addition to the existing literature in the field of EMC with immediate relevancy to current engineering challenges. It is also the first published application of stochastic techniques in the evaluation of emissions potential within a shielded enclosure. The specific contributions are as follows:

1. A comprehensive framework is presented for the analytic evaluation of direct radiated emissions from multiple integrated circuits within a shielded enclosure. This approach is structured to permit design for compliance rather than evaluation of existing equipment. It includes treatment of the measurement instrumentation, the spectral density of the source signals, the modelling of the ICs, the effects of placement, phase, frequency, amplitude and orientation as well as the nature of the imperfections in the shielded enclosure.

2. A detailed investigation is made into the composition of the energy spectrum associated with the EMI problem. Signals are classified as narrowband and broadband, intentional and unintentional, parasitic, unconstrained and inherent. Examples are given of each signal type.

3. Equations are derived from dyadic Green's functions which permit the creation of mapping matrices. These matrices define the relationship between dipole models of multiple IC sources within a shielded enclosure and the electric currents and fields induced on the enclosure wall. The use of mapping matrices greatly simplifies the numerical algorithms for multiple source problems.

4. The emissions potential of multiple sources within shielded enclosures are traced back to fundamental electromagnetic characteristics of the IC sources which may be influenced in the design process.

5. Statistical techniques are applied in order to assess the likely effect of different factors within the enclosure on the emissions potential of the enclosed system. Effects of phase variation and component placement are shown to vary significantly and predictably with frequency when normalized to the major dimensions of the enclosure.

1.7 Conclusion

It is shown in this thesis that it is both possible and feasible to predict the electromagnetic emissions of specific enclosed multi-source systems through the application of analytic techniques. It is also possible to design an enclosure with a known shielding effectiveness with a predefined level of confidence prior to the availability of detailed source information through the application of stochastic techniques in the characterization of the enclosure space.

The amplitude of the EMI source signal is dependent on many factors. Some of these are due to the desired functionality of the system such as the lower harmonic content of the clock and data signals. Many sources of radiated energy that are a potential source of EMI exist due to the physical implementation of the circuit such as the higher harmonics of intentional signals, groundbounce and the skew of balanced signals.

Data signals are becoming an important source of EMI. Accurate modelling of data signals requires a detailed knowledge of the coding schemes, the EMI measurement instrumenta-

tion and their interaction. Proper modelling of the quasi-peak detector used in regulatory compliance measurements may result in a 50% reduction in perceived EMI risk.

If a time harmonic signal component is present in the circuit it has at least 20 dB more EMI potential than most data signals of equivalent amplitude and rate for the same location and polarization. However, the placement and polarization factors within the enclosure may result in a 60 dB variation in EMI potential when measured in terms of induced disturbance on the enclosure wall for source frequencies below the first resonant frequency of the enclosure.

Chapter 2

Background

2.1 Introduction

The radiated emissions of electromagnetic energy becomes **interference** when it has a detrimental effect on the operation of some other piece of equipment. The level of emissions required to cause interference is dependent on the **immunity** or **susceptibility** of the victim equipment. The circuits which are the most sensitive to interference tend to be those which are specifically designed as receivers of radiated energy such as radio, television or wireless communications system.

It is not uncommon for high speed, high density digital equipment to convert hundreds of watts of d.c. power into an energy spectrum that extends to 10^{10} Hz. Without careful engineering, the resultant disturbances of the ambient electromagnetic field in the vicinity of this equipment will be quite significant.

In order to avoid widespread disruption of broadcast and communications services most countries have regulations that limit the allowable electromagnetic emissions from electronic equipment to a generally acceptable level [FCC 89].

In order to meet these requirements, manufacturers of electronic equipment expend considerable resources during the design and manufacturing process to ensure that the equipment is EMI compliant. The technical base for EMI engineering has expanded rapidly in the last decade since the introduction of the FCC regulations. Considerable effort has gone into applying basic electromagnetic theory to develop an understanding of the behavior of the component parts of the system. This analysis has been published in books such as **Noise Reduction Techniques in Electronic Systems** [Ott 88] and **Introduction to Electromagnetic Compatibility** [Paul 92] as well as others listed in the Reference section of this thesis.

One of the major problems faced by engineers is the transfer of theoretical concepts into the practical results required by regulations. One of the key areas of difficulty relates to the concept of **shielding effectiveness.** This is generally defined in terms of the ability of a piece of material to prevent a plane-wave from passing from one infinite half-space to another as shown in Figure 2.1.

Figure 2.1: Shielding Effectiveness

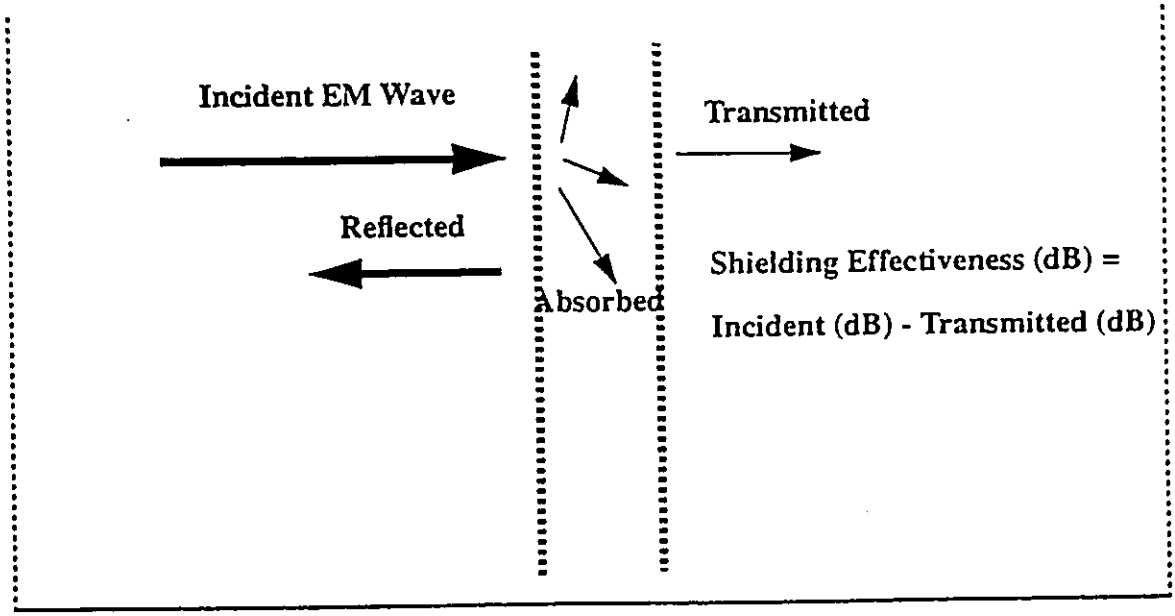

Unfortunately this ideal plane wave characterization is often confused with the ability of an enclosure to isolate a source of electromagnetic energy from its environment or *vice versa*. It will be shown in Chapter 5 that the currents and fields induced on the inner surface of an enclosure are very sensitive to the position of the primary radiator. These induced disturbances are different in magnitude and polarization from those due to an incident plane wave. For this reason the shielding effectiveness properties of bulk materials does not give an adequate indication of the likely emissions from a shielded system.

In 1978, Mendez showed that the Green's function for a cavity could be used to determine the field distribution within a rectangular enclosure for a specific source current distribution. This could then be used in conjunction with perturbation models to obtain a realistic estimation of the shielding effectiveness of the source-enclosure system.

In 1991, this model was used by Cooray, Crawhall and Costache [Cooray 91-1] to investigate the interaction of multiple sources within an enclosure. This thesis builds on that investigation by taking a detailed look at the source characteristics, the multiple source-enclosure interaction and the probabilities associated with distributions of sources within the enclosure.

This understanding of the multiple source systems is a fundamental step in linking the existing device and printed circuit board radiation models that are used in EMI design into behavioral models of systems that may be used to assess performance relative to regulatory compliance requirements.

2.2 Regulatory Compliance

To date the vast majority of EMI engineering effort in the commercial sector has been expended in the area of regulatory compliance. Due to the commercial and legal implica-

tions, the requirements for regulatory compliance have been clearly and somewhat arbitrarily defined. Interference is a subjective relationship between an emitter of energy and another piece of electronic equipment. The many possible modes of interference between the piece of equipment being designed and possible interference victims cannot practically be taken into account. Driven by the need to protect the AM radio and TV broadcast bands, the quasi-peak detector was selected as the reference standard for interference measurements of commercial equipment between 9 kHz and 1000 MHz [CISPR 87]. Understanding the response characteristics of this detector to both narrowband and broadband interference signals is becoming important when identifying the principle energy sources in high speed data systems.

It is a characteristic of the regulatory requirements for radiated EMI control that the pass fail criterion is based on the single highest emission level measured through a 120 kHz filter over a frequency range from 30 MHz to 1000 MHz[1]. The level of the rest of the spectrum is effectively disregarded. Based on the ratio of the bandwidth to the range under consideration, this represents the top 0.01% of the energy spectrum.

Typically this peak value will be due to the complex sum of higher harmonics of a number of digital pulse sources within the equipment. Rearrangement of cabling or a change of software may cause a shift, not only of amplitude but also of the frequency and position in space at which the peak electromagnetic field value is found. The task of determining the exact compliance margin for a complex system can be assumed to be impossible. Any models used for EMI design will be either implicitly or explicitly probabilistic.

1. In the United States this has recently been extended to 40 GHz.

2.3 An Analytic Approach to EMI

Regulatory compliance criteria are enforced at the system level. To be able to design for compliance a thorough understanding of the electromagnetic interactions of the components within the system is required. An analytic approach to the EMI problem leads to the identification of the specific source parameters which are important in determining the level of system emissions

Due to the complexity of this problem computer aided design (CAD) tools must be used. One objective of this thesis is to develop the underlying theory that can ensure the efficacy of such a CAD tool in the evaluation of shielding effectiveness of enclosures that contain multiple sources of emissions energy.

There are two fundamental requirements of an effective engineering design tool for EMI avoidance:

- The problem definition must be aligned to the design requirements and the design process; and
- The tool must be structured around variables that can be practically influenced and provide results that lead to an implementable solution.

In this case the problem definition may be regarded as "how do changes in the design, selection and placement of the IC's affect the emissions levels registered on a quasi-peak detector?"

Logically an EMI system design should commence with the elimination of all unnecessary interference energy at the source level. Decisions relating to the shielding effectiveness of the enclosure would follow once the extent of the residual problem is known. Unfortunately, the practical constraints of a commercial environment frequently require that decisions regarding the enclosure design be made before many of the relevant details regarding its

content are known. In addition, the electronic components that make up the source of electromagnetic energy may be updated several times in the life of the enclosure. A significant portion of EMI engineering is therefore aimed at risk management, design constraints and trade-off analysis.

The design of electronic equipment traditionally follows a hierarchical progression: logic design; implementation in software; capture in hardware elements such as integrated circuits; interconnection through a variety of structures; and finally mounting within an enclosure. At each of these steps decisions are made that influence the electromagnetic performance of the final structure. A CAD tool should be structured around variables that can be influenced at each of these steps. These include factors such as system clock speed, synchronous vs. asynchronous architectures, coding schemes, IC current drive capabilities, IC packages, structure of the board level interconnect and the design of the shielded enclosure and cabling.

2.3.1 A Four Part Electromagnetic Model

In this thesis the EMI problem has been divided into four parts as shown in Figure 2.2. These are:

1. The generation of electromagnetic energy within the enclosure from IC sources;
2. The induced field and current distribution on the inner surface of the enclosure boundary;
3. The transfer of energy from the inner surface of the boundary to the outer surface; and
4. Radiation from the outer surface of the enclosure boundary to the measurement detector.

The evaluation of enclosure shielding effectiveness requires consideration of all four parts of the problem.

In terms of EMI engineering solutions the first part of the model relates to source suppression, the second to mitigation of the cumulative effects of multiple sources, the third to enclosure integrity and the fourth to re-radiation and test methodology. The focus of this thesis will be on parts (1) and (2) of the model. Parts (3) and (4) will be dealt with briefly in Chapter 8.

Figure 2.2: A Four Part Electromagnetic Model

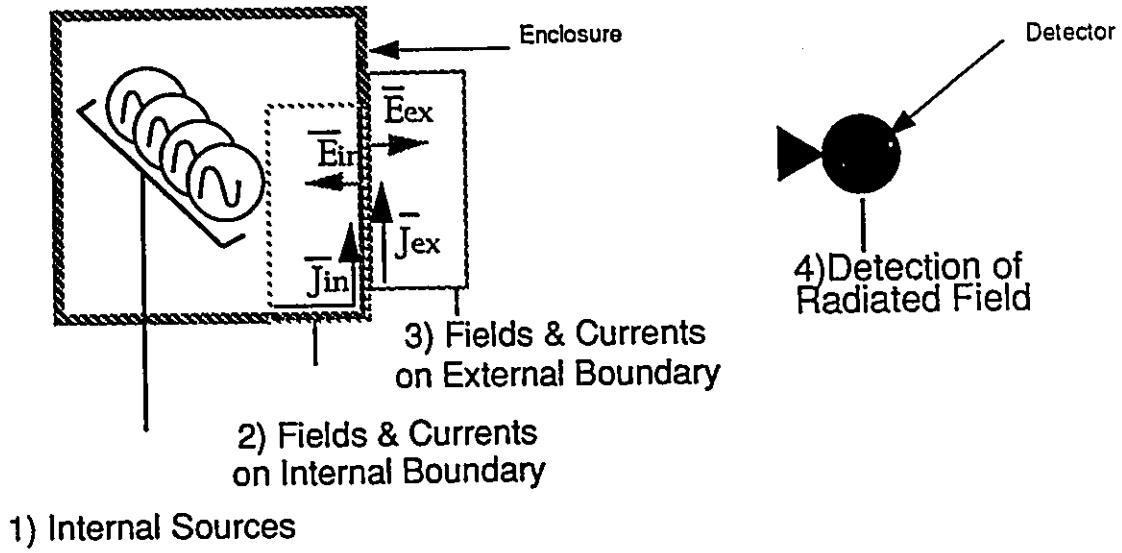

2.3.2 Internal Sources

There are four generators of electromagnetic energy within electronic systems; clock oscillators, digital logic, I/O drivers and switch mode power converters[2]. These generators drive

2. Power converters tend to have a very broadband spectral output that concentrates at frequencies below 30 MHz

time varying currents along conduction paths which results in a complex interaction between the fields, the conductors and the enclosure. Figure 2.3 illustrates some of the many potential radiating structures on a printed circuit pack.

The emissions potential of a source is determined by its energy spectrum and the coupling efficiency of its physical structure to leakage paths in the enclosure. In practice the EMI levels at any particular frequency tend to be determined by a small subset of the possible sources within the system. The dominant radiators must be identified for each problem.

Figure 2.3: Radiating Sources on a Printed Circuit Board

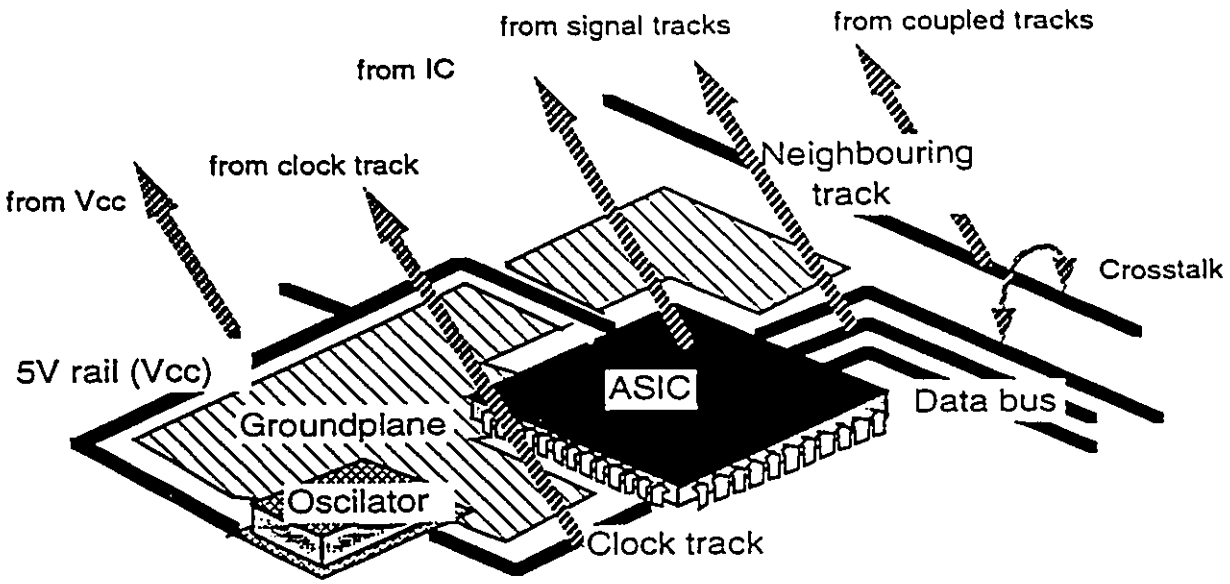

Unlike many traditional electromagnetic field problems, the energy spectra of digital circuits cover a broad frequency range. Time harmonic sources such as clock oscillators have a 'comb' spectrum while data carrying signals are characterized by a continuous distribution of energy. The dominant sources may vary with frequency, even for related harmonics of the same signal.

On many high speed pcbs the signal and clock tracks are buried between two layers of copper in a stripline structure and do not contribute significantly to the radiated energy. In these cases the large application specific integrated circuits (ASICs) and inter-board connectors are one of the major sources.

Radiation from ASICs is the principle emissions source modelled in this thesis. The relationship between these devices and the dipole source model used in the multiple source model is dealt with in Chapters 3 and 4. Radiation from connectors can be modelled in a similar manner as that from ICs so long as the dipole model is still accurate. This may not be the case if the connector is in very close proximity to the wall of the enclosure.

2.3.3 Fields and Currents on Internal Boundary

The sources of electromagnetic energy within the enclosure impress a current density and an orthogonal electric field on the internal conducting surface of the enclosure. In Chapters 5 through 7 this problem is modelled as multiple dipole sources within an ideal cavity. The analysis is performed through the use of dyadic Green's functions. For each enclosure size and frequency, a set of mapping matrices may be formed that relates a dipole representation of the source to the current and electric field on the wall of the enclosure. The matrices are applied to the multiple complex source problem through the principle of superposition.

Numerical methods such as the **transmission line method** (TLM) [Hoefer 86], **finite element method** (FEM) [Silvester 83],**time domain-finite volume method** (TD-FV) [Shankar 89], **finite difference** [Mitchell 80] and **finite difference time domain** (FD-TD) [Yee 66], [Taflove 89] could all be used to determine the coefficients of the mapping matrix.

Numerical methods are more flexible than Green's functions in terms of the shape of the enclosure that can be analyzed, inhomogeneity of the media within the enclosure and discontinuities in the conducting boundary that cannot be addressed using perturbation tech-

niques. All of the numerical techniques require a full field solution for each variation in the source configuration.

The dyadic Green's function describes a direct relationship between the source distribution and the disturbance point of interest. In this thesis it is simplified to give a functional relationship between the source at a single point and the disturbance at a single point. This is computationally efficient and preserves a large amount of analytic information about the behavior of fields within the cavity.

Within the electromagnetic interference and compatibility (EMI/EMC) engineering community expert systems are gaining popularity [Lovetri 90], [Wood 91]. The work presented in this thesis would fit well into such a computational framework by providing a linkage between the detailed interaction of the components and the behavior of the overall system.

2.3.4 Energy Transfer From Inner to Outer Boundary Surface

The shielding effectiveness of an enclosure is largely limited by the energy which is transferred across it due to apertures, seams with finite conductance and penetrating cables as shown in Figure 2.4. An appropriate transconductance model may be developed to determine the shielding effectiveness once the current and field distributions are determined on the inside of the enclosure. If the imperfections in the enclosure do not significantly alter the current and field distributions on the inner boundary, perturbation techniques may be used to model these leakage paths.The example of small apertures are discussed briefly in Chapter 8.

Figure 2.4: **Features of an Imperfect Enclosure**

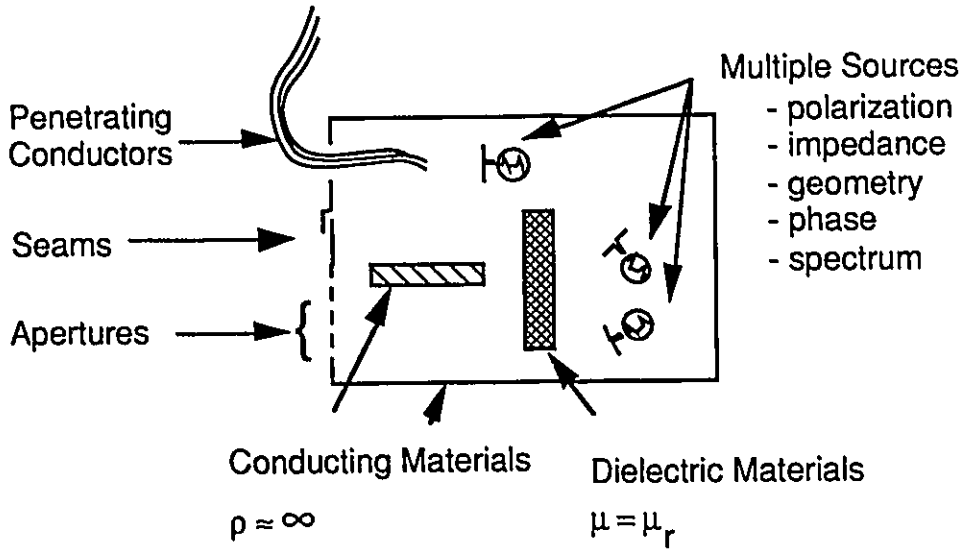

2.3.5 The Radiation Problem

The unbounded radiated field problem as relevant to modelling of EMI compliance is shown schematically in Figure 2.5. The combination of frequency range and test configuration results in both "near field" an "far field" situations [Stutzman 81]. Neither electrostatic nor ray optic approximations are appropriate over the full frequency range due to the size of physical features of the system relative to wavelength.

The radiation problem consists of modelling the electronic system, including its enclosure and cabling, as a secondary radiator of the energy generated inside and determining the peak signal amplitude that will be registered by the measurement system.The radiation problem is not addressed in this thesis except with respect to the quasi-peak detector characteristics.

Figure 2.5: The Radiation Problem in Regulatory Compliance

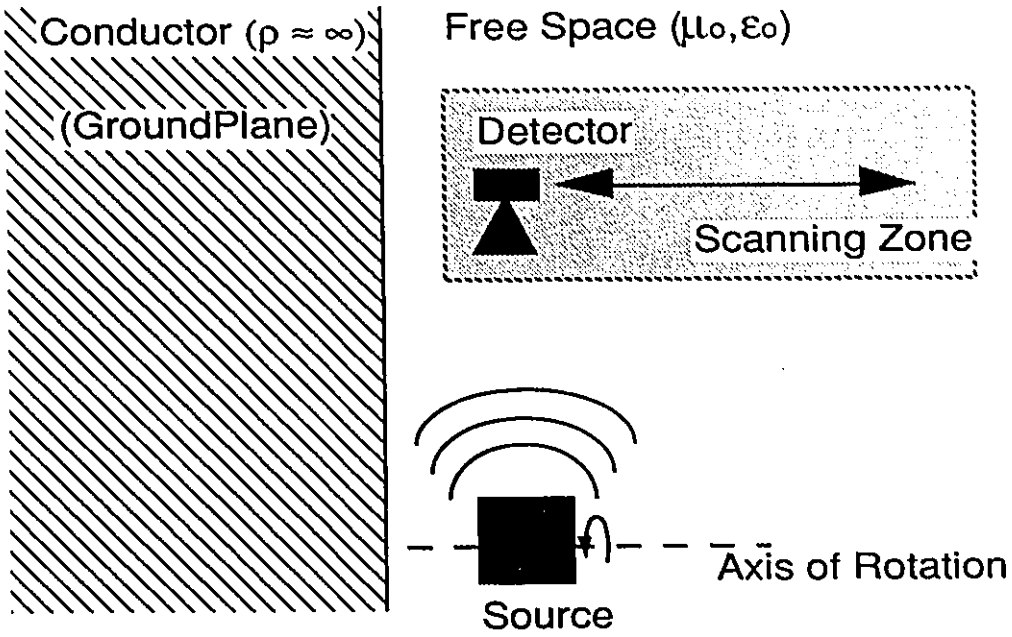

2.4 Applicability of the Cavity Model

Large electronic systems such as a telecommunications network comprise a number of interconnected pieces of equipment of different shapes, sizes and functions. Increasing standardization and tightening regulations are driving electronic systems designs in some specific directions, particularly with respect to the suppression of EMI.

The two pieces of equipment shown in Figure 2.6 are typical of current technology both in their physical construction and functionality. The geometry is essentially that of a rectangular conducting enclosure with a series of apertures, seams and connectors. The enclosure provides physical support and radio frequency (r.f.) shielding for the equipment. If the enclosure is well designed for EMI containment, these discontinuities in the conducting

boundary should not cause a significant perturbation in the electromagnetic boundary conditions.

Figure 2.6: Typical Electronic Equipment Enclosures

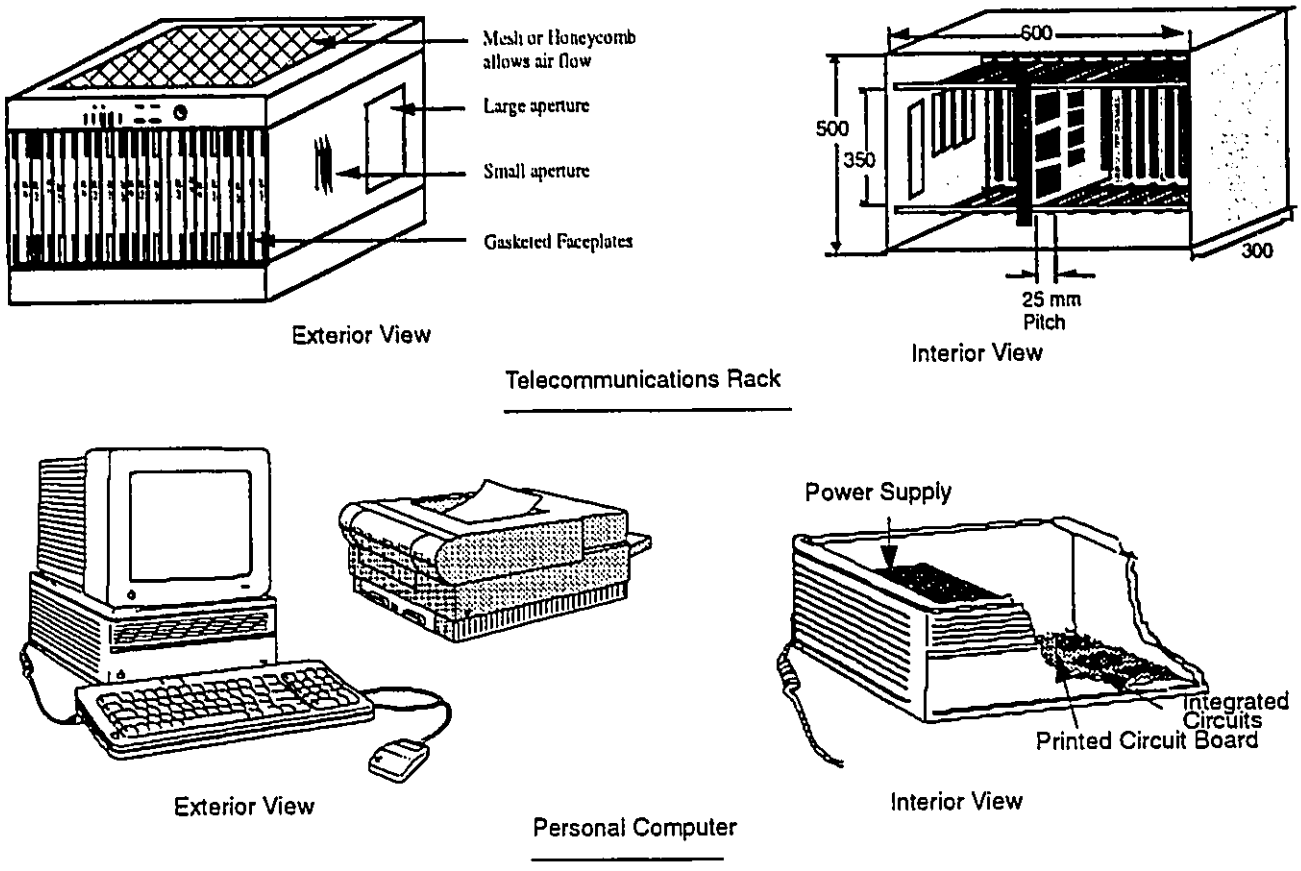

The shielding effectiveness of the enclosure is always compromised due to the need for cable penetration, maintenance access and cooling air flow. To mitigate this degradation, large apertures may be covered with perforated metal or honeycomb to permit air flow while providing r.f. attenuation.

Points at which conducting surfaces mate generally present an impedance to the current flow on the inside surface of the enclosure and a leakage path to the outside (even with RF

gasketting in place). This is due to a combination of resistive and capacitive effects. Small openings may be regarded as inductive impedances. Models may easily be created for these leakage paths based on their size and structure. The difficulty is generally found in determining the impedance and strength of the excitation source for the model.

The outer containment of the equipment consists of sheet metal or conductive paint on plastic which serves as a r.f. shield. In the Green's cavity model there is an implicit assumption of good ground connectivity between all six surfaces of the cavity.

At the shielded enclosure level the EMI design intent is to provide a "Faraday cage" for the equipment within the functional and cost constraints of the design. The outer boundary should therefore be quite close to an ideal boundary condition and leakages through gaskets, screens and cables can be treated using perturbation techniques.

The validity of this assumption will vary from equipment to equipment and will generally deteriorate with increasing frequency and in the vicinity of resonances. In those instances where the assumption is not valid alternative numerical approaches, such as those listed in Section 2.3.3 may be used.

Chapter 3

Interference Energy

3.1 Introduction

The first step in the analysis of EMI is to provide a methodology to determine the amplitude of the radiated signal. In this thesis the analysis will be restricted to the emissions from integrated circuits. Integrated circuits are complex radiators. Many have tens or even hundreds of major signals contributing to the EMI problem. Each of these signals has a characteristic energy spectrum and each has a different current flow path.

The direct radiation from the IC is determined by the vector sum of all of these sources. The magnitude and phase of each contributing signal will be determined by the spectral energy density of the signal and its delay relative to some reference signal. The radiation efficiency of the IC and the polarization of the radiated signal is determined by the geometry of the current path as discussed in the following chapter (Figure 4.3).

There are three practical problems involved in the determination of the net EMI potential of an IC:

- The net signal strength is the result of the vector sum of a set of signals with different distributed power spectral densities;
- Applying this source signal to a spectral domain model requires a single frequency input if an integration over frequency is to be avoided in the propagation calculation; and
- The predicted emissions level from the model should correlate to the answer that would be obtained during a regulatory EMI test.

All three issues are resolved by determining the amplitude of each signal in terms of the response of the measurement instrumentation used in regulatory compliance testing. The first and third issues are resolved because the model quantifies the multiple signals in a manner that is consistent with the output of the measurement instrumentation.

The second issue is resolved because a 120kHz bandpass filter is used in the measurement. Thus the source energy of interest is distributed over a very narrow frequency range relative to any of the frequencies being modelled (30 MHz - 1000 MHz). This permits all of the propagation calculations associated with each measurement to be made at the centre frequency of the band thereby avoiding group delay effects.

If the signal strength inputs to the problem come from measured data taken with a quasi-peak detector and the polarization information is preserved, then this information may be used directly in the analytic formulas to determine disturbance levels. If the signal strength is determined by calculation then the effects of the quasi-peak detector must be taken into account in the calculation. For narrowband components of the signal this is a trivial exercise since all detectors are calibrated to give the same amplitude response to a narrowband signal. For broadband components of the signals the effects of the quasi-peak detector must be taken into account. The influence of the detector on this class of signals will depend on the data rate of the signal and the density of the energy spectrum.

There are many different sources of electromagnetic energy within a piece of electronic equipment, each with a characteristic energy spectrum. The key contributors to the radiated EMI spectrum may be quite different from the important elements associated with conducted data or clock signals such as fundamental frequency or rise and fall time.

Digital systems are characterized by broad, unconstrained emissions spectra that are readily measurable from a few kilohertz to many gigahertz. This spectrum is a composite of many millions of contributions from individual gates switching within the integrated circuits. Detailed analysis of the IC generally shows that the majority of the radiated emissions energy is due to a small subset of the possible sources.

These source signals may be decomposed into **intentional** components, such as those due to clock and data signals which perform a defined timing or information function and as **unintentional** components, which are not theoretically required but exist as a consequence of the physical implementation of the circuit.

The time domain behavior of these signals range from the highly periodic to the highly random depending on whether their primary function is linked to timing and synchronization or to information transfer [Cover 91]. When viewed in the frequency domain these signals are seen to be composed primarily of **narrowband** and **broadband** energy respectively. These terms are defined based on their behavior relative to the bandwidth of the measurement equipment.

In practical EMI engineering it is often found to be the unintentional spectral components which determine the compliance margin of the equipment. Examples of these unintentional signals are the very high harmonics of clock signals, unexpected parasitic energy on a control line or data bus, unbalance in a high speed transmission signal and groundbounce on a large ASIC.

In order that these complex source spectra can be captured in the system models presented in following chapters, it is necessary to convert them into single frequency point sources. The particular source model that will be used is a set of orthogonal **magnetic** and **electric dipoles**. The amplitude of the dipole moments will be determined by the radiation efficiency of the device being modelled and the spectral density of the signals that are driving it.

To convert the various source spectral energy densities into a single signal magnitude at a specific frequency, the output signal level that each of the sources would induce in the measurement receiver is determined (Figure 2.5). This requires a basic understanding of the filter and response characteristics of the **quasi-peak detector**. The use of other detectors, such as peak, average or r.m.s. as measurement criteria will not correctly predict the relative importance of the different spectrum types.

The ability to calculate the various components of the source signal spectra is important for two reasons. Firstly it permits modelling of the source to take place long before samples are available for measurement. This is crucial if the objective of the modelling is EMI mitigation since it permits remedial action to be taken during the initial component design.

Secondly it facilitates the decomposition of the spectral signature of a data signal into its basic contributing elements. For example, a measured radiated signal such as shown in Figure 3.1 is made up of both broadband and narrowband components. The narrowband signal may have many sources. It may be composed of the narrowband components of the data stream, the clock signal, groundbounce due to large amounts of simultaneous switching, another component nearby or a repetitive piece of preliminary software. Simple calculations can confirm whether the magnitudes of the measured signal can be accounted for by one source or another. Similar analysis may be performed on the broadband portion of the spectrum.

Figure 3.1: Narrowband and Broadband Signals

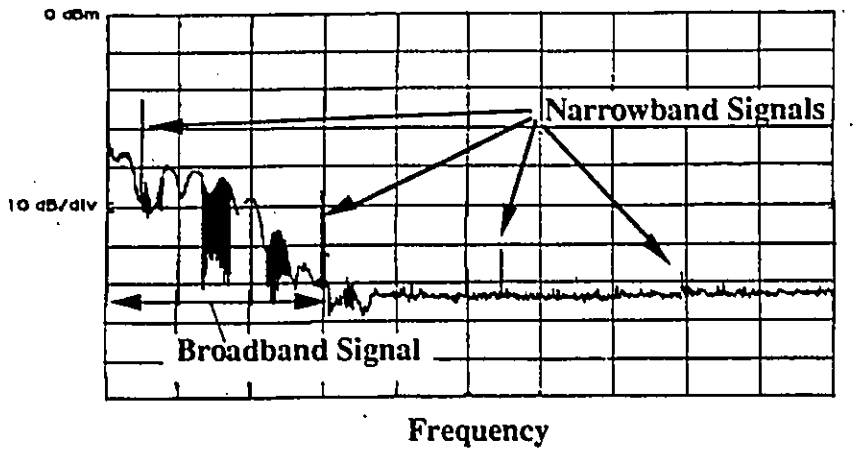

This chapter contains two derivations that have already been presented elsewhere; one for the narrowband energy content of data signals [Bylanski 80] and the other for the response characteristics of the quasi-peak detector [Cook 79]. They are provided to show the origins of terms that may be used in detailed calculations. It is the first time that cyclo-stationary signal processes have been presented in terms of EMI problems.

3.2 Source Spectra

EMI analysis is fundamentally different from circuit analysis in that all sources of electromagnetic energy must be considered. These sources may be broadband or narrowband in nature. It is not uncommon for the compliance limit of equipment to be determined by a spectral component that is the 20th or 30th harmonic of a clock or data signal. In identifying and modelling a signal source it is necessary to understand how its time domain characteristics will convert to a spectral amplitude on the specific measurement equipment being used.

The portion of the signal that causes the regulatory compliance problem may be fundamental to the information processing or transporting function of the equipment, excess energy which is generated as an inevitable result of the present state of electronic component design or as an avoidable result of poor EMI engineering.

3.2.1 Narrowband Spectra

A narrowband spectral component is pragmatically defined as one whose amplitude does not vary more than ± 0.5 dB when the resolution bandwidth of the receiver/detector is varied ± 6 dB. It is seen as a clear, distinct spectral line (Figure 3.1). The amplitude of a pure narrowband signal will not vary with the type of detector used in the measurement. [Nano 73].

Narrowband signals are readily modelled in the frequency domain since their energy density is represented as a Dirac distribution with a specific amplitude which may be used directly in the calculation.

3.2.2 Broadband Spectra

The term *broadband* is generally applied to signals which carry information such as data busses, address busses and transmission signals or to noise sources such as switch mode power supplies. The broadband signal appears as a continuous distribution on the spectrum analyzer screen (Figure 3.1). Changing the bandwidth of the measurement receiver will change the measured amplitude of the broadband signal. The amount of change depends both on the impulse response characteristics of the detector and the probability density function (pdf) of the non-periodic signal.

This continuous energy distribution is difficult to work with in computational electromagnetics in the frequency domain since the relationship between the source and any disturbance point varies with wavelength. Two solutions are generally employed, either the

calculations are done in time domain and then transformed back into frequency domain or the energy distribution is represented as energy levels at discrete frequencies.

Time domain modelling is not very effective for random data streams because a large number of pulses are necessary in order to generate the appropriate spectrum.

The second approach is much more efficient for the solution of EMI problems since it is the spectral content of the signal that is of interest. This is different from the signal propagation problem in which it is the time domain waveform that is important in determining the integrity of the data flow. The difficulty is to ensure that, in a mixed broadband/narrowband system, the various components are given proper weighting when their contributions to the total interference level are summed.

3.2.3 Impulse Response

Impulsive signals are a special case of broadband signals. They occur infrequently relative to the bandwidth of the receiver. The amplitude is determined by the impulse response of receiver and detector circuit. Impulsive signals are not generally found to be a concern in regulatory EMI compliance of information technology equipment, however, analysis of the **impulse response** of the detector is helpful in the understanding of its characteristics.

3.3 Major EMI Sources within Electronic Equipment

The EMI spectrum is composed of two types of spectral energy, intentional and unintentional. The intentional part of the spectrum is included in the system for its timing or information carrying properties. Although this may not represent the optimum way of implementing the function, removing this energy content without redesign of the functionality would prevent the functional design from working in even a theoretical manner. Unin-

tentional spectral content refers to energy that is not required in the location that it is found in the system. In theory this energy could be completely eliminated without jeopardizing the design. In fact metrics such as bit error rate may improve if this excess energy is removed.

3.3.1 Intentional Signals

3.3.1.a Clock Signals

The dominant part of the EMI spectrum is often due to the clock. The term "clock" refers to those signals which carry only timing information for the electronic system. These signals are typically regarded as time harmonic trapezoids and have a narrowband comb spectrum that fits within a spectral envelope as shown in Figure 3.2. Although there are relatively few clock signals within a piece of electronic equipment, they have been found to presented the majority of the EMI problems due to their strong spectral signature when measured with narrow bandwidth receiver or spectrum analyzer and their distribution throughout the equipment. Analysis of clock signals has been presented in a number of publications (e.g. [Paul 92], [Violette 87]).

Figure 3.2: Time and Frequency Characteristics of a Time Harmonic Signal

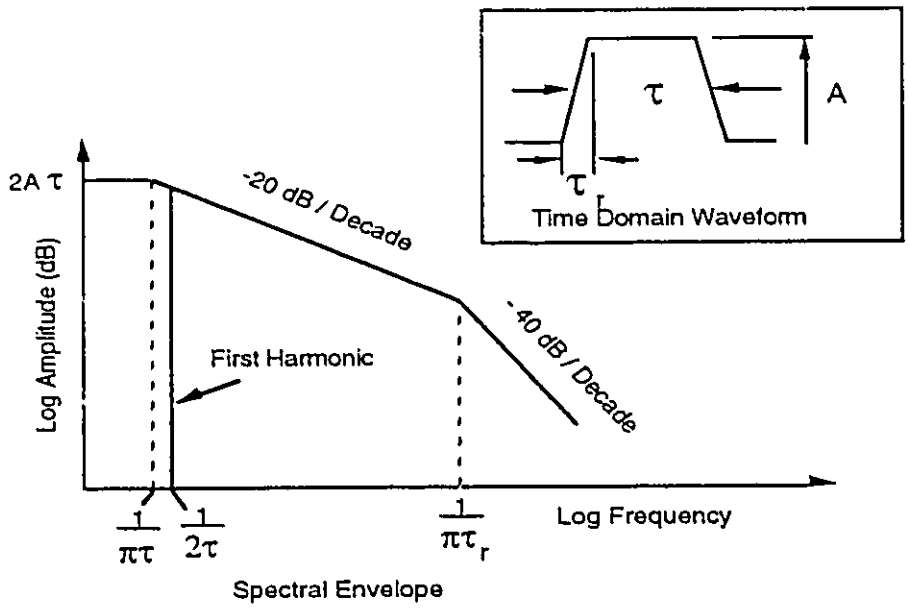

3.3.1.b Data Signals

The class of intentional signals includes a variety of non-periodic waveforms. Non-periodic signals have received less attention than clock signals in EMI analysis as their intrinsic randomness reduces the interference potential and the consequent threat to compliance. However, increasing data rates and processing speeds, accompanied by the success of design strategies to reduce the emissions potential of clock signals, have required that this source of emissions be more carefully examined [Crawhall 91].

The spectral content of a data signal is more difficult to establish than that of a simple clock signal because of its random state at any given point in time. For this reason it is generally necessary to view the non-periodic signal as a discrete-time random process [Leon-Garcia

89][1]. A detailed investigation of the spectral composition of non-periodic signals will be given in the next chapter.

3.3.2 Unintentional Signals

There are two categories of unintentional signals, **parasitic** and **unconstrained**. Parasitic signals are those which are not designed into the primary function of the circuit being observed. Examples are switching noise due to power converters, clock feedthrough on idle control lines and groundbounce due to simultaneous switching and cross talk.

Parasitic signals are often a problem in EMI engineering because they are unexpected and therefore no provision is made for their mitigation. Recognition of their existence and determination of their amplitudes leads to appropriate design methodologies.

The term *unconstrained* refers to signals which are spread over a larger bandwidth than is required for their functionality. Generally all of the necessary time domain information required for the functioning of digital circuitry can be captured in the first 10 harmonics of the waveform. In practice it is not unusual to have significant spectral content at the 100th harmonic. This is problematic as radiation efficiency of systems often increases with frequency. Elimination of this "waste" energy through techniques such as slew rate control on switching transistors is one of the principal techniques for source level EMI mitigation.

In practice data signals are hybrid in character, containing both broadband and narrowband components (Figure 3.1). This is an important observation because many EMI difficulties may be due to the narrowband components of the data signals rather than the clock, particularly those corresponding to the higher harmonics of the data rate.

1. Because the use of random variables and stochastic processes has not generally been considered part of an EMI analysis, a brief review of basic terms is given in Appendix II.

3.4 Spectral Analysis of Data Signals

Increasing speeds of LANs and microprocessors require that non-periodic signals such as data line signals, address busses and control lines be analyzed when assessing the EMI potential of an equipment. Calculating the power spectral density of a data signal for EMI engineering purposes requires that a number of intentional and unintentional factors be taken into account

The power spectrum of these signals may be divided into two parts; a broadband component consisting of data and noise and a narrowband component, which may be related to **intrinsic** or parasitic timing information.

3.4.1 Broadband Spectral Content

The broadband com ponent of a data signal is described by the probability density function (pdf) of its power spectrum. Unlike the clock signal, this is a continuous function of frequency. If the data signal can be modelled as a **stationary random process**[2] then the power spectral density may be related to its autocorrelation function $R(\tau)$ [Papoulis 84].

(3-1)

$$S(\omega) = \int_{-\infty}^{\infty} R(\tau)\, e^{-j\omega\tau} d\tau$$

where $S(\omega)$ is the power spectrum of a random process or data stream f(t), and R(t) is the autocorrelation of f(t) defined by:

2. See Appendix II

(3-2)

$$R(\tau) = \lim_{T\to\infty} \frac{1}{T}\int_{-T/2}^{T/2} f(t)f(t+\tau)\,dt$$

f(t) is described in terms of the probability of it assuming a given value at a particular point in time. For example a rectangular pulse train **f(t)** may only be either a '1' or a '0' at any time t.

The broadband portion of the power spectrum (S_{bb}) is real and non-periodic so that equation (3-1) can be re-written as [Bylanski 80]:

(3-3)

$$S_{bb}(\omega) = \int_{-\infty}^{\infty} R(\tau)\cos(\omega\tau)d\tau$$

For a random rectangular pulse of amplitude A, duration t_o and period T ($t_o < T$), the continuous, broadband portion of the energy spectrum is given by the well known equation:

(3-4)

$$S_{bb}(\omega) = A^2\left(\frac{t_o}{2T}\right)^2 T\left(\frac{\sin^2\chi}{\chi^2}\right)$$

where:

$$\chi = \frac{\omega t_o}{2}$$

This equation gives the broadband energy content for an ideal rectangular data signal as shown in Figure 3.3 through Figure 3.5 .. This is the formula which is generally applied to determine the spectral energy content of a data signal. The relative importance of this part of

Figure 3.3: Continuous and Discrete Components of a FULL Period Waveform [Bylanski 80]

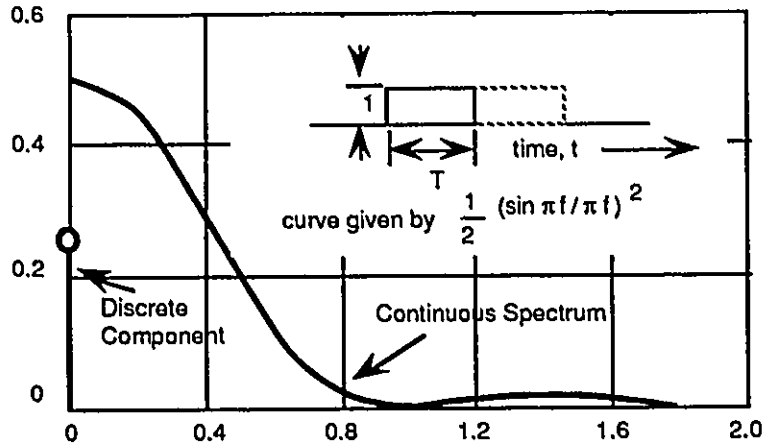

Note: p = probability that any pulse is present. Vertical axis assumes p = 0.5. For other values of p do: a) multiply by 4p(1-p) for continuous spectrum, b) multiply by 4p2 for discrete terms, Horizontal axis is frequency normalized to data rate.

Figure 3.4: Continuous and Discrete Spectral Components of a HALF Period Waveform [Bylanski 80]

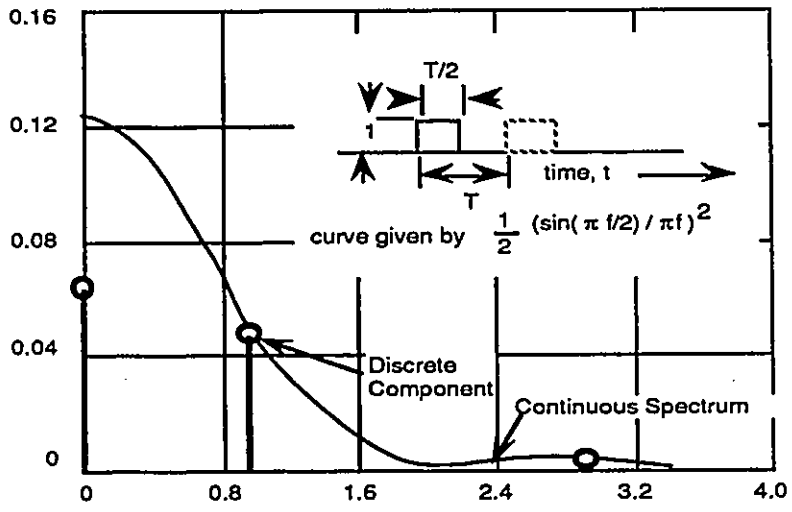

Note: p = probability that any pulse is present. Vertical axis assumes p = 0.5. For other values of p do: a) multiply by 4p(1-p) for continuous spectrum, b) multiply by 4p2 for discrete terms. Horizontal axis is frequency normalized to data rate.

Figure 3.5: Continuous and Discrete Components of a 1/4 Period Waveform [Bylanski 80]

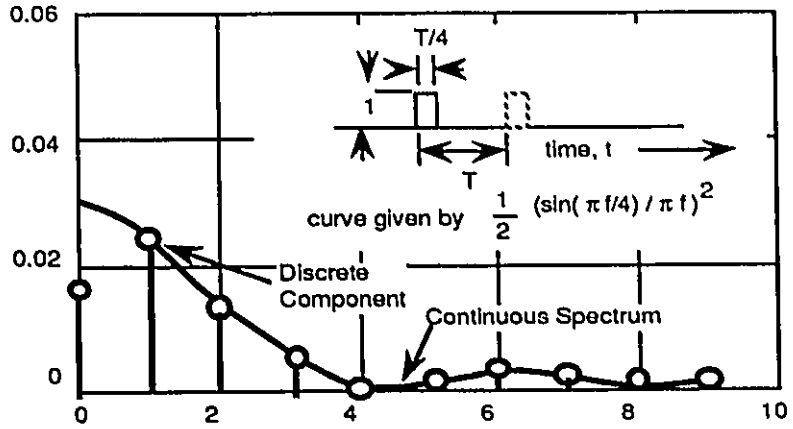

Note: p = probability that any pulse is present. Vertical axis assumes p = 0.5. For other values of p do: a) multiply by 4p(1-p) for continuous spectrum, b) multiply by 4p2 for discrete terms. Horizontal axis is frequency normalized to data rate.

the spectral energy content compared to the narrowband contributions will be illustrated in the following sections.

3.4.2 Narrowband Spectral Content

There are 3 major sources of narrowband energy within a non-periodic signal:

- Those that are intrinsic in the ideal waveform;
- Those which arise from the specific data activity as determined by the software; and
- Those which are due to the physical implementation.

3.4.2.a Intrinsic Narrowband Energy

Although data streams are often considered random they contain considerable narrowband energy which is related to the duty cycle and the bit rate. [Bennett 58]. This intrinsic narrowband energy is often used as the basis for clock recovery in data transmission. Although this imbedded timing information is a practical necessity in many instances, it contributes to the

interference potential of the signal. The following derivation shows how the narrowband components can be calculated for a random bit stream. This applies to either ideal trapezoids or arbitrary waveforms such as those found in typical data streams.

For the example of the simple rectangular waveform for which the power spectrum of the broadband signal was given in equations (3-3) and (3-4), the periodic part of the spectrum has an autocorrelation function:

(3-5)

$$R(\tau) = \sum_{n=-\infty}^{\infty} a_n^2 \cos(n\omega\tau)$$

where a_n = 1 or 0: the value of the waveform at t = nT.

This results in the energy spectrum being a series of discrete lines or narrowband signals given by:

(3-6)

$$S_{nb}(\omega_0) = A^2 \left(\frac{t_0}{2T}\right)^2 \frac{\sin^2 \xi}{\xi^2}$$

where:

$$\xi = \frac{n\omega_0 t_0}{2} = \frac{n\pi t_0}{T}$$

The preceding formulas indicate that, for a pulse that fills the entire clock period (i.e. $t_0 = T$, duty cycle = 50%), no narrowband components should be present above d.c. (Figure 3.3). This is equivalent to the ideal non-return-to-zero (NRZ) signal. For signals in which the duty cycle is less than 50%, such as a return-to-zero (RZ) signal or a non-ideal NRZ signal, narrowband components appear at the harmonics of the data rate (Figure 3.6).

Figure 3.6: Unipolar Return-to-Zero (RZ) and Non-Return-to-Zero (NRZ) Waveforms

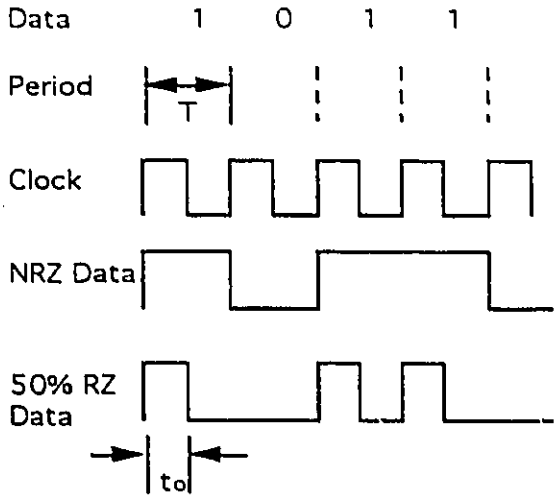

This appearance of narrowband energy is not restricted to ideal square wave forms. It is a fundamental property of data streams that are related to a clocking structure. To accurately predict the amplitude of these components, a representation of the waveform is required.

Bennett introduced the concept of "cyclo-stationary" processes in 1954. He showed that the common zero crossing frequency of a synchronous data signal results in a periodic variation of the mean of the power spectrum. This prevents the simple correlation between power spectral density and autocorrelation that holds for a stationary or wide sense stationary process[3] from being applicable. On the other hand, a similar relationship can be established in terms of the time averages of the processes providing that the process is ergodic[4]. [Bennett 58].

3. For a definition of "stationary", "wide-sense stationary" and "cyclo-stationary" processes, see Appendix II

4. see Appendix II

Bennett started with the assumption that the transmitted waves are based on a finite width pulse g(t) such that:

$$x(t) = \sum_{n=-\infty}^{\infty} a_n g(t - nT)$$

where the values a_n represent the message values (e.g. 1 1 0 1 0....).

The power spectrum of this message x(t) at any time t can be represented as the sum of its average (av[x(t)]) and a deviation from the average (y(t)):

$$x(t) = av[x(t)] + y(t) \tag{3-7}$$

If the digital message is modelled as a random noise source then the mean m_1 is given by the ensemble average[5] $m_1 = av\,[a_n]$ and the autocovariance C(n) is given by
$C(n) = av\,[(a_k\, a_k + n)]$ for fixed k.

It can therefore be shown that:

(3-8)

$$av\,[x(t)] = av\left[\sum_{n=-\infty}^{\infty} a_n g(t - nT)\right]$$

$$= m_1 \sum_{n=-\infty}^{\infty} g(t - nT)$$

5. See Appendix II

indicating that the ensemble average of the power spectrum varies with period T. From this observation a Fourier series expansion is possible. Using the term c_m to represent the Fourier coefficients leads to the following derivation:

(3-9)

$$\text{av}\,[x(t)] = \sum_{m=-\infty}^{\infty} c_m e^{(2m\pi j f_r t)}$$

$$c_m = f_r \int_0^T \text{av}\,[x(t)] e^{-(2m\pi j f_r t)} dt$$

$$= m_1 f_r \sum_{n=-\infty}^{\infty} \int_0^T g(t - nT) e^{-(2m\pi j f_r t)} dt$$

$$c_m = m_1 f_r \int_0^T g(u) e^{-(2m\pi j f_r u)} du$$

However, the Fourier transform of the basic pulse is given by:

(3-10)

$$G(f) = \int_{-\infty}^{\infty} g(t) e^{-j2\pi ft} dt$$

which allows c_m to be given by:

(3-11)

$$c_m = m_1 f_r G(m f_r)$$

Hence the harmonically varying ensemble average of the digital message that is responsible for the "cyclo-stationary" behavior is given by:

(3-12)

$$av\{x(t)\} = m_1 f_r \sum_{m=-\infty}^{\infty} G(mf_r) e^{j2m\pi f_r t}$$

This formula may be used to calculate the magnitude of the narrowband components of a data signal of known waveform.

3.4.2.b Software Induced Components:

Most EMC engineers have experienced the frustration of receiving hardware with "preliminary software" only to find that the emissions spectrum changes significantly once the fully operational system is tested. This is frequently due to short looping sequences or bit toggling in the prototype software which give rise to narrowband components at the frequency of loop repetition. Such software induced components of the spectral signature are generally recognizable because they introduce periodic patterns that are several orders of magnitude lower in frequency than the data rate. If the number of instructions in the software loop is known then this pattern may be easily correlated to the spectrum. This effect becomes more pronounced with higher bit rates as is demonstrated in the examples of Section 3.6.

On the other hand there are occasions when a software sequence or particular operational mode results in a highly repetitive waveform. In the worst case a data signal may become completely "clock-like" for significant periods of time. Such inappropriate choices of data formats may result in as much as a 20 dB increase in emissions potential from a track or signal port.

3.4.2.c Narrowband Spectral Components due to Physical Construction of PCBs and Devices

One of the most difficult contributions to predict in the emissions potential of a data signal is the influence of **parasitic clock components**. This narrowband spectral energy may be due to relatively low levels of direct coupling between the clock signal and the data signal (or reset and control line etc.). Even signals which are barely perceptible on an oscilloscope can be quite evident on a spectrum analyzer due to high level of synchronization and repetitiveness. The magnitude of a clock harmonic required to dominate an NRZ data spectrum is given in Figure 3.7[6].

Figure 3.7: NB Signal to Dominate a NRZ Signal Using a 120kHz Filter.

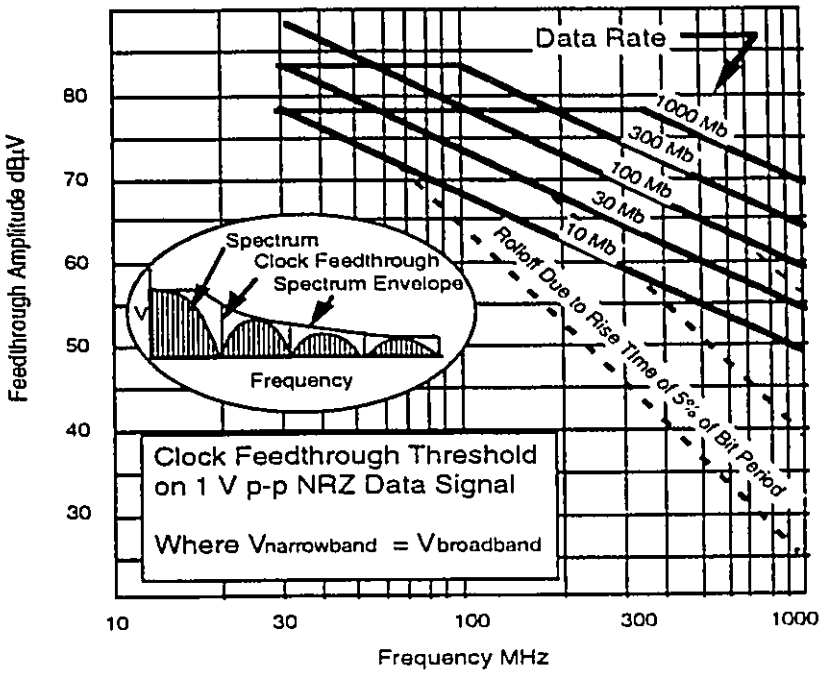

Some sources of this parasitic noise are well documented such as near and far end cross-talk and the pick-up and re-radiation of clock signals by tracks and cables. Other mechanisms

6. Curtesy of R.Goulette

are less well recognized such as the transparency of I/O cells of ASICs and microprocessors to clock activity within the chip. These parasitic clock signals are often characterized by sub-nanosecond rise-times and frequencies many times the bit rate of the data stream. The need to control this element of the emissions problem points to the advantages of having a generally accepted IC emissions specification in the electronics industry [Goulette 92-1].

If these contributions to the signal spectra are to be determined through calculation, detailed knowledge of the physical construction of the IC is required. If the data is obtained through measurements of individual signals, then it is advisable to measure all signals to ensure that the unintentional spectral content is correctly modelled. If the magnetic and electric dipole moments are measured using the techniques presented in Section 4.2 then the data can be used directly in the models of Chapter 5.

3.4.3 Transmission Signals

Signals used for data transmission over extended distances are a special instance of non-periodic data signals. For transmission signals considerable effort is made to constrain the bandwidth of the power spectrum to attain good transmission properties [Duc 75,77].

The average spectral power distribution is controlled through the use of data translation codes (line coding). In this case the pdf and the power spectrum can be assumed to conform to its intended spectral distribution (Figure 3.8). There are certain specific exceptions due to the signalling state of the equipment such as the INFO 2 signal for Basic Rate ISDN [ANSI 87-1,2]. This has an alternating mark-space pattern that results in a narrowband spectrum similar to a clock signal. Mathematical models for a number of these data protocols can be found in [ANSI 89] and further data is available in Appendix III.

Figure 3.8: Power Spectra of Common Coding Schemes

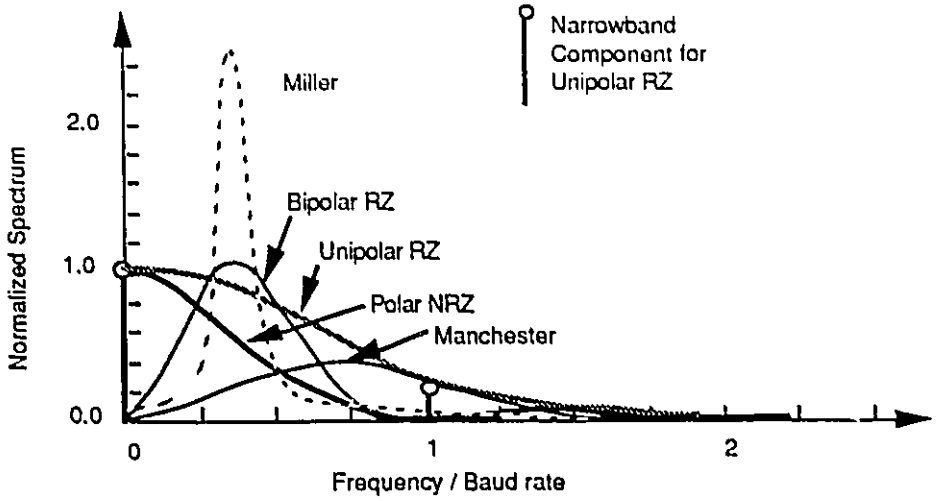

There are a large number of transmission protocols used in telecommunications systems. Some of the major ones are listed inTable 3.1. Fuller descriptions of the waveforms are given in Appendix III

Digital transmission signals are designed to optimize certain spectral characteristics for improved reliability of communication. Specifically:

- They must carry timing information which can be recovered at the end of a transmission link. This clock information may be extracted from the received line signal itself, or it may be an added timing component which has been inserted into the transmitted line signal;
- If the transmitted signal is a.c. coupled to the transmission medium, it must have no d.c. component and may contain only a small amount of low-frequency energy.

Table 3.1 Common Protocols

Protocol	Data Rate	Cable Length	Cable Type
P-ISDN	1.544/2.048 Mb/s		
DS-1	1.544 Mb/s	199.6 m (655 ft.)	22 ga. Twisted Pair
DS-3	44.736 Mb/s	137.2 m (450 ft.)	75 Ω Coaxial
STS-1	51.84 Mb/s	37.2 m (450 ft.)	5 Ω Coaxial
FDDI	125 Mb/s	not yet known	not yet known
STS-3	55.52 Mb/s	67.5 m (225 ft.)	75 Ω Coaxial

3.4.4 Poorly Balanced Signals

Emissions potential is often reduced substantially by running signals in a balanced configuration. Ideally the sources on both sides of the balanced system create equal and opposite fields. Within a practical circuit this is hard to ensure. Figure 3.9 shows the basic ways in which the signal balance can be corrupted.

Figure 3.9: Deterioration in Balanced Systems

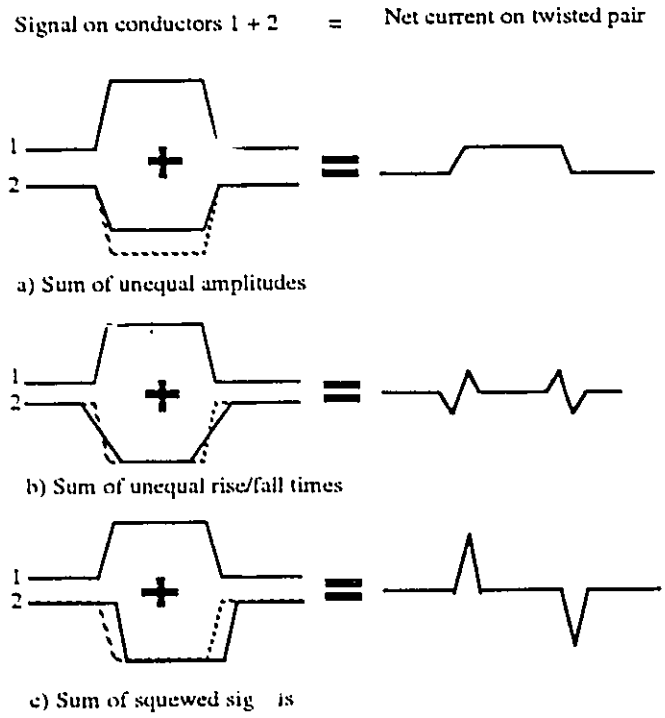

A poorly balanced signal may have significantly reduced spectral energy in the lower frequency ranges but a higher level associated with the higher harmonics. This may significantly alter the distribution of spectral energy attributed to the point sources in a system emissions model.

3.4.5 Ringing and Overshoot

Many signals display deviations from the ideal waveform due to inductive and capacitive effects in the circuit (Figure 3.10). In many instances the higher harmonics of a signal spectrum will be completely determined by the second order effects such as ringing and overshoot.

Figure 3.10: Effect of Overshoot on Spectral Content

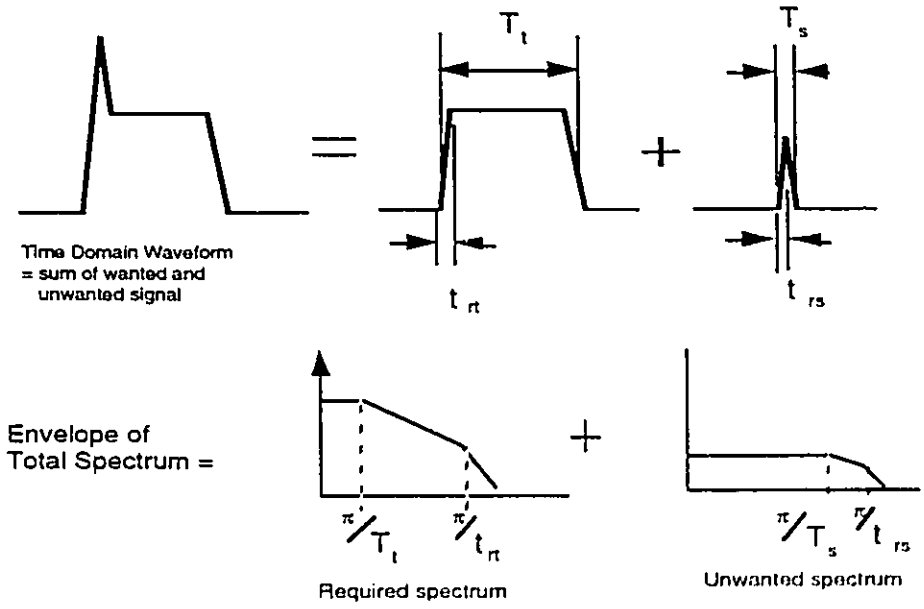

These effects are readily accounted for by taking the Fourier transform of a time domain model of the IC driver and the signal path. This may be done using a simulation package such as H-Spice. The increase in narrowband energy due to the ringing and overshoot can be calculated using equation (3-9)

3.4.6 Groundbounce

Groundbounce is often responsible for radiated emissions directly from the chip and for the unexpectedly high conducted emissions on some pins.

Figure 3.11: Groundbounce

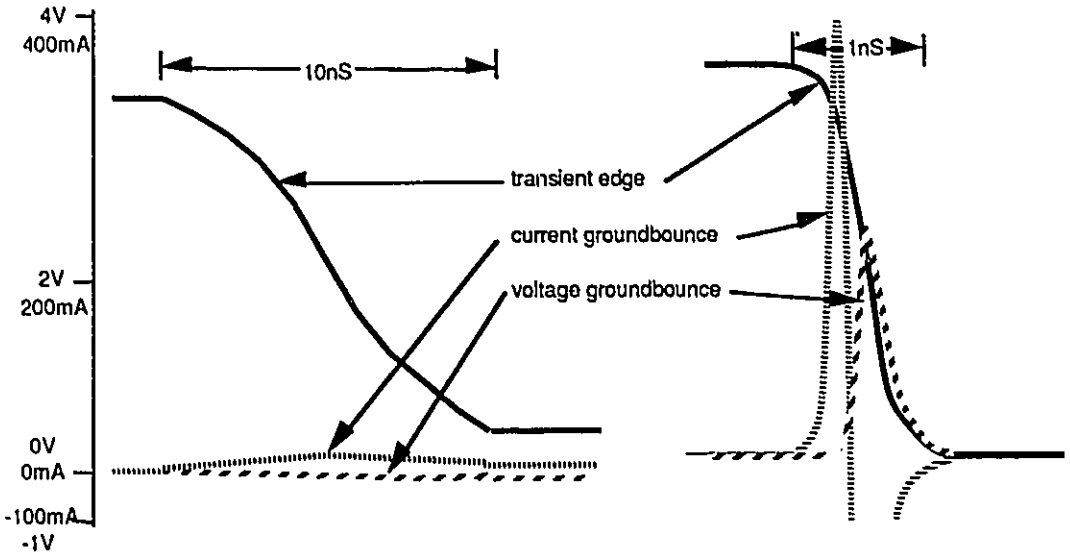

The groundbounce is a rise in the potential of the ground reference on the chip relative to the ground reference on the pcb. This is due to rapid changes in current on and off the chip and the inductive impedance of the pins, the leadframe and the tracking. The level of ground potential rise on the die is dependent on the rise time of the driver circuits (dI/dt) and the effectiveness of the on-board decoupling.

Figure 3.11 shows the difference in groundbounce voltage and current for a 0.5V/ns voltage swing from a 5V/ns swing as found on a typical ASIC. This potential difference will not be same all over the IC which will also result in some unintentional current flow within the die [Diaz-Olavarrieta 91].

Although groundbounce may result in unwanted current flow on the die, it is the voltage difference generated between the die and the pcb groundplane below, more generally associated with the electric dipole moment, that causes the predominant emissions mode of the device.

3.5 Implications of the Measurement System

By using the output of the regulatory compliance measurement system as the common basis for comparison of magnitudes of broadband and narrowband signal the EMI model is coupled tightly to the engineering problem that it is intended to help solve. Unfortunately the response characteristics of the particular detector selected for these measurements are more complicated with respect to broadband than narrowband signals. This introduces the need for probabilistic techniques in the solution process that are not generally employed in EMC engineering.

The regulatory compliance measurement system consists of a 120 kHz filter followed by a quasi-peak detector (Figure 3.13). EMI measurements of broadband signals may be significantly higher (6-12 dBmV/m) than those taken with an average detector and significantly lower (up to 6 dB) than the same measurements taken with a peak detector.

Most published power spectrum information is provided without reference to a particular measurement device. Broadband energy is described in terms of dBm/MHz referenced to 1 Ω. Narrowband energy is represented in terms of a Dirac delta distribution with an amplitude corresponding to the Fourier coefficient of the specific harmonic. The power spectra of data signals such as those given in Figure 3.8 assume an infinitely long series of data values.

Figure 3.12 shows the amplitude response of a peak, QPD and average detector to a DS-3 transmission signal. The QPD signal voltage is 4-5 dB lower than that registered by the peak detector and 4-5 dB higher than that given by the average detector.

Since these three detectors are calibrated to give the same response to a time harmonic clock signal it is evident that the interaction between the detector and the broadband data signal is playing a significant role in determining the total emissions level.

Figure 3.12: DS-3 Amplitude Using Different Detectors

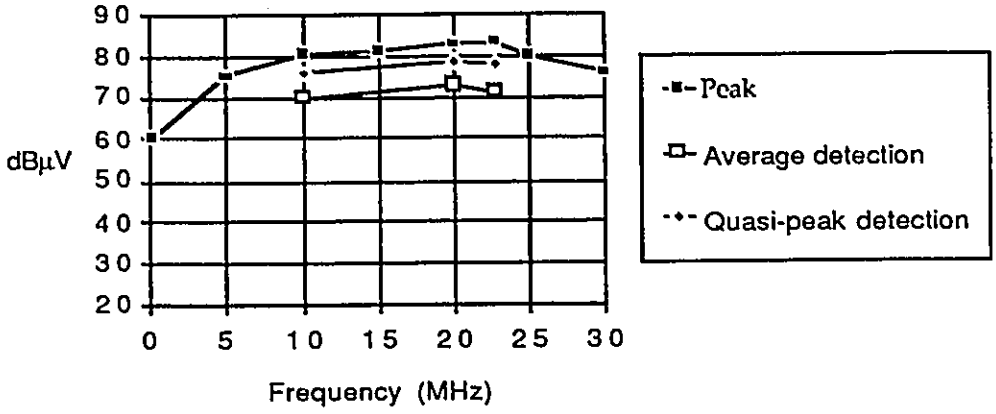

3.5.1 Components of the Measurement System

The radiated emissions are measured with a tuned half-wave dipole antenna via a 50 Ω cable [CISPR 84]. The half-wave dipole is oriented so as to receive either horizontal or vertical polarized waves. This is followed by a bandpass filter with a 6 dB bandwidth (B_6) of 120 kHz and a quasi-peak detector. (Figure 3.13).

Figure 3.13: Compliance Measurement System

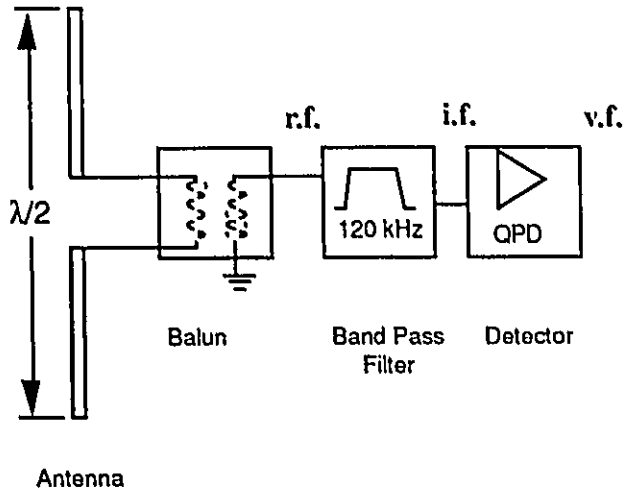

3.5.1.a The Pre-Detector Stage

The pre-detector stage consists of a radio receiver or spectrum analyzer with the 120 kHz bandpass filter. This filter is modelled as two double-tuned, critically-coupled resonant circuits. The amplitude of the envelope of the i.f. output (A) is given by: [Nano 73]:

(3-13)

$$A(t) = 8\, a_p^2\, F(\omega)\, \omega_o\, G\, e^{-\omega_o t} \left(\sin(\omega_o t) - \omega_o t \cos(\omega_o t)\right)$$

where:
a_p = pulse area
G = overall gain of the r.f. and i.f. stages
$\omega_o = \pi B_6/\sqrt{2}$
f = tuning frequency
$F(\omega)$ = Fourier transform of the measured pulse

The characteristics of the filter for the frequency band of 30 MHz to 1000 MHz are given in Figure 3.14. The corresponding response of the filter described by equation (3-13) is given in Figure 3.15.

Figure 3.14: Selectivity 0f 120 kHz Filter

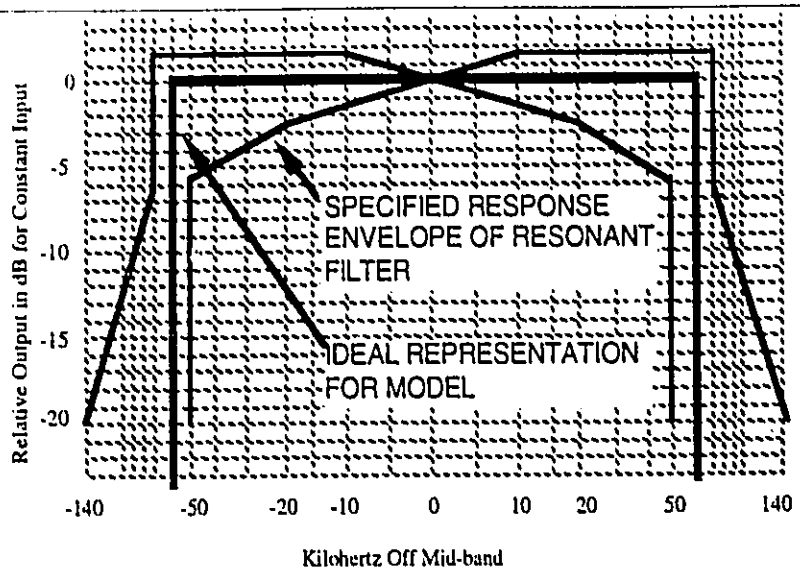

Figure 3.15: Response of 120 kHz Filter to a Single Pulse

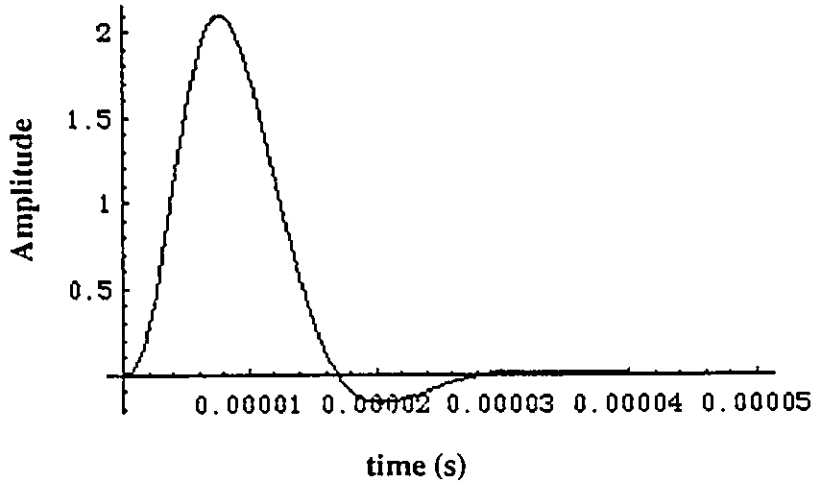

3.5.1.b Quasi-Peak Detector

The baseband or envelope signal coming out of the i.f. stage of the receiver is fed into the quasi-peak detector. The detector is characterized by a fast response to the signal from the pre-detector stage followed by a slow decay. These response times are governed by the

charging and discharging resistors R_c and R_d and the capacitor C as shown in Figure 3.16. This is contrasted to the slightly simpler circuit of the peak detector shown in Figure 3.17.

Figure 3.16: The Quasi-Peak Detector

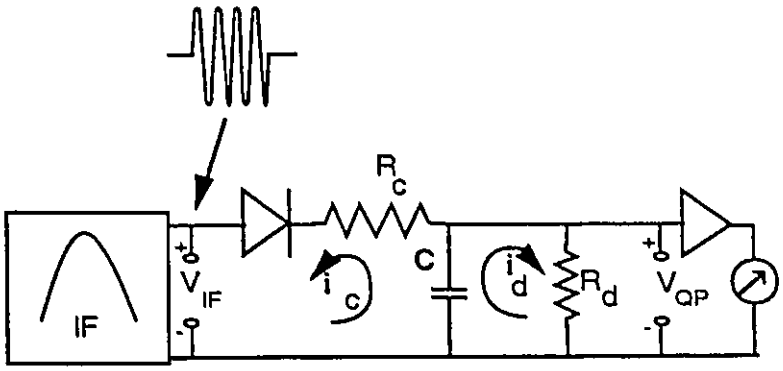

Figure 3.17: The Peak Detector

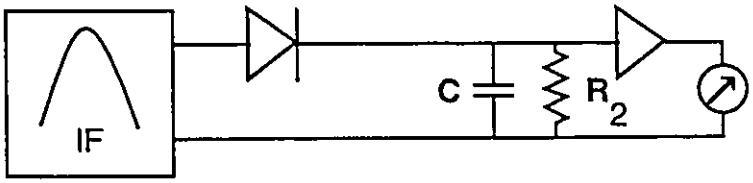

The characteristics of the QPD are defined in [CISPR 87]. The principle characteristics are given in Table 3.2

The differential rise and fall response of the detector was intended to account for the perceived interference to an AM radio receiver as detected by the human ear.

When measuring data signals with the quasi-peak detector, an equilibrium is established between the average arrival rate of the pulses and the response and decay characteristics of the detector.

Table 3.2 **Fundamental Characteristics of Quasi-Peak Detector**

Fundamental Characteristics of Quasi-Peak Detector		
Frequency Band (MHz)	-	30 - 1000
Bandwidth @ 6 dB (kHz)	-	120
Charge-Time Constant (ms)	t_c	1
Discharge-Time Constant (ms)	t_d	550
Meter Time Constant ‡ (ms)	t_m	100

‡ Mechanical time constant of critically damped indicating instrument. Assumes that the indicating instrument is linear where: $t_c = R_c C$; $t_d = R_d C$

3.5.2 Response of the QPD to Data Signals

A practical approach to the problem of modelling the QPD response to data signals recognizes the slow response of the QPD output relative to the typical rate of variation of the input from the i.f. stages (Figure 3.18). This permits an analysis on the basis of the average quasi-peak voltage output. Errors introduced by this approximation can be assessed for different situations but are generally found not to be significant [Cook 79].

Figure 3.18: Response of a QPD to Repetitive Pulses [Nano 73]

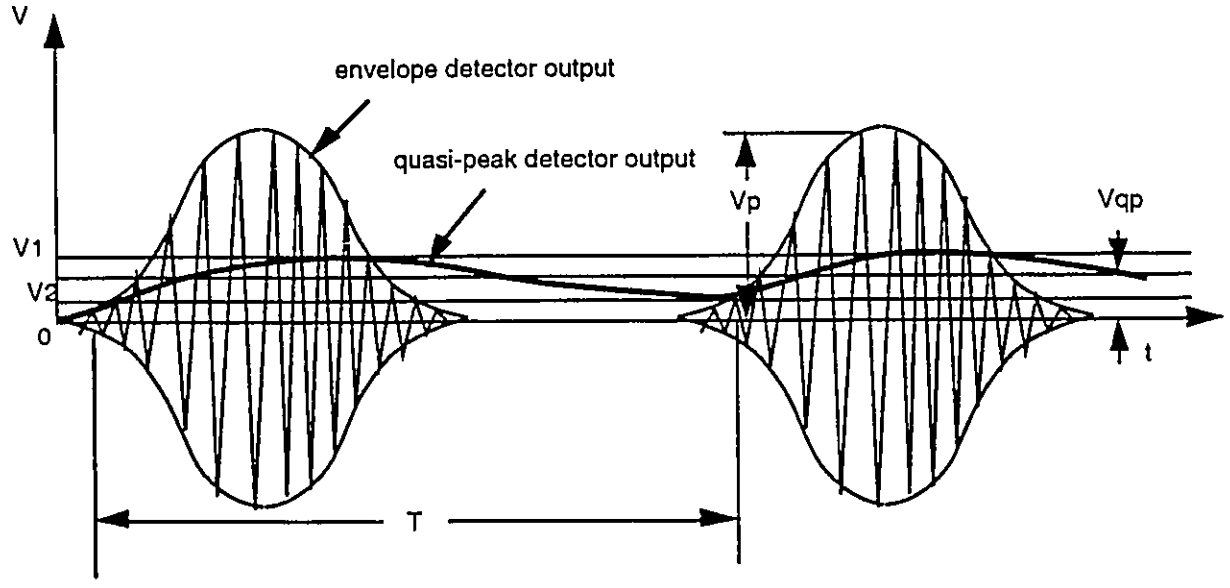

Table 3.3 Amplitude Response of Quasi-Peak Detector

Quasi-Peak Amplitude of CISPR Pulse

(dBmV)

Pulse Repetition Frequency (Hz)	Amplitude
1000	68.0 +/- 2.5
100	60.0 +/- 1.5
60	-
25	-
20	51.0 +/- 2.5
10	46.0 +/- 3.0
5	-
2	34.0 +/- 3.5
1	31.5 +/- 3.5
Isolated Pulses	28.5 +/- 3.5

Since it is the equilibrium state of the detector which is of interest, it is appropriate to model the circuit of Figure 3.16 in terms of average current and voltage values. The average discharge current $\langle i_d \rangle$ is related to the average QPD voltage output $\langle V_{QP} \rangle$ by the equation:

(3-14)

$$\langle i_d \rangle = \frac{\langle V_{QP} \rangle}{R_d}$$

The average current in the charging capacitor is determined by the arrival rate of the data. This is given in terms of the probability density function ($p_e(e)$) associated with the i.f. voltage amplitude (V_{IF}). Hence the average current in the charging capacitor is given by:

(3-15)

$$\langle i_c \rangle = \int_{\langle V_{QP} \rangle}^{\infty} \frac{e - \langle V_{QP} \rangle}{R_c} p_e(e) de$$

where **e** is a random variable representing the instantaneous voltage V_{IF} from the pre-detector stage. Since the average charging and discharging currents must be equal over time the following equilibrium equation results:

(3-16)

$$\langle V_{QP} \rangle = \frac{R_d}{R_c} \int_{\langle V_{QP} \rangle}^{\infty} (e - \langle V_{QP} \rangle)\, p_e(e) de$$

The quasi-peak voltage is found in terms of the amplitude probability distribution (APD) by showing that:

(3-17)

$$p_e(e) = \frac{1}{\pi} \int_{e}^{\infty} \frac{-\frac{d}{dA} P(A)}{\sqrt{A^2 - e^2}} dA$$

where:

A = a random variable representing the envelope amplitude of **e**.
P(A) = APD or cumulative distribution function (CDF) of **e**

The cumulative probability distribution of the amplitude (P(A)) is related to its probability density function (p(A)) by the equation:

(3-18)

$$p(A) = -\frac{d(P(A))}{dA}$$

Equation (3-16) can therefore be solved numerically for the quasi-peak output voltage so long as the APD for the signal coming from the i.f. stage is known.

3.6 Measurement of Data Signals

The significance of a number of the factors described in this chapter including the use of the quasi-peak detector, can be demonstrated through the following examples. Near ideal data signals were generated in a controlled environment with a high speed signal generator. Conducted measurements were made of these signals by sending them directly into a spectrum analyzer using a matched 50 Ω coaxial cable.

3.6.1 Example # 1

A 2.5 Volt, 100 Mb/s data stream is coded as both a return-to-zero (RZ) and a non-return-to-zero (NRZ) sequence (Figure 3.6). Figure 3.19 and Figure 3.20 show the spectrum of these two scenarios as measured with a peak detector using a 120 kHz bandwidth in a log magnitude mode from 30 MHz to 300 MHz.

The RZ coding (Figure 3.19) has a much stronger narrowband component at the clock fundamental and its harmonics. This is because the pulse width t_0 is only 50% of the period T. This is in agreement with equation (3-6) above. In the ideal case for the NRZ coding there would be no narrowband signal. However, the finite rise and fall times of the waveform cause the actual period measured at mid height of the waveform to be marginally less than the total period T. This accounts for the residual narrowband signal in Figure 3.20.

Figure 3.19: 100Mb/s, 2.5V, RZ Spectrum

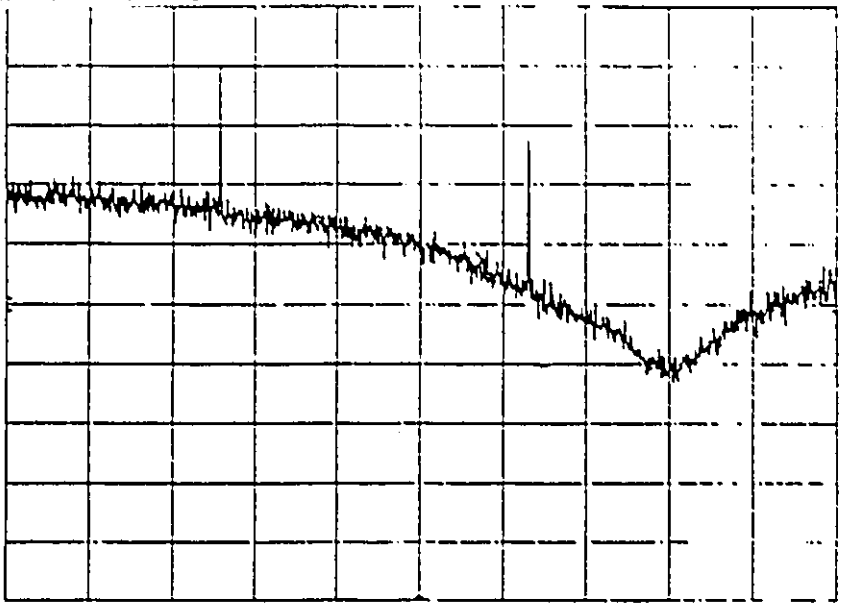

Freq. Span:30MHz -300MHz Mag. 10dB/div Res BW: 120kHz Pos.Peak SWP 150mS

Figure 3.20: 100Mb/s, 2.5V, NRZ Spectrum

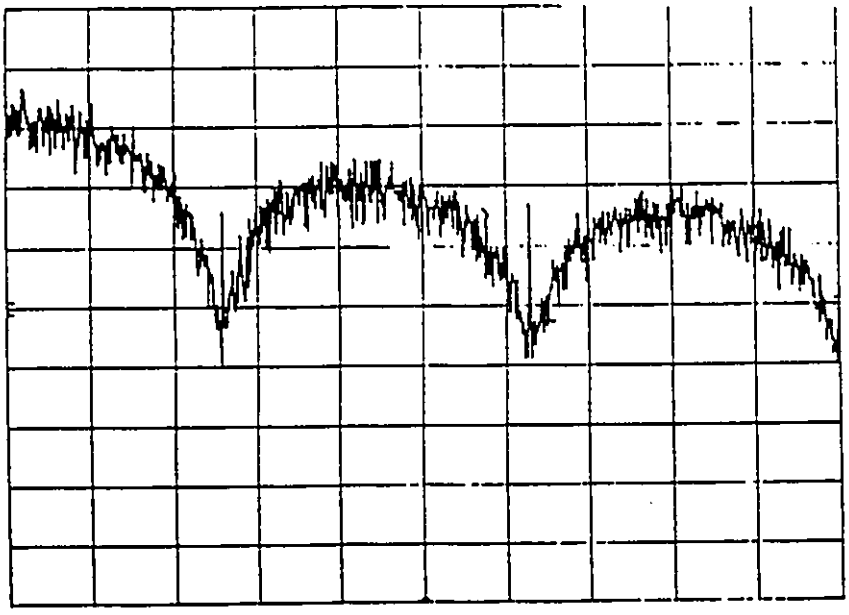

Freq. Span:30MHz -300MHz Mag. 10dB/div Res BW: 120kHz Pos.Peak SWP 1500mS

When measured with a quasi-peak detector the RZ and NRZ values at the first fundamental of the data rate (100 MHz) are 220 mV and 5 mV respectively. This can be compared to the magnitude of the corresponding harmonic of a trapezoidal clock signal of the same rate and pulse amplitude. The RZ signal is found to have a narrowband amplitude at 100 MHz which is 20dB lower than the magnitude of the fundamental of a 100 MHz trapezoidal clock.

From Figure 3.20 it appears that the broadband energy in the NRZ signal will have more emissions potential below 100 MHz than the 5 mV narrowband component at 100 MHz. Figure 3.21 shows the quasi-peak levels which are about 30 mV at from 30 to 50 MHz.

Figure 3.21: Quasi-peak Measurement of Broadband Segment of Long NRZ Signal

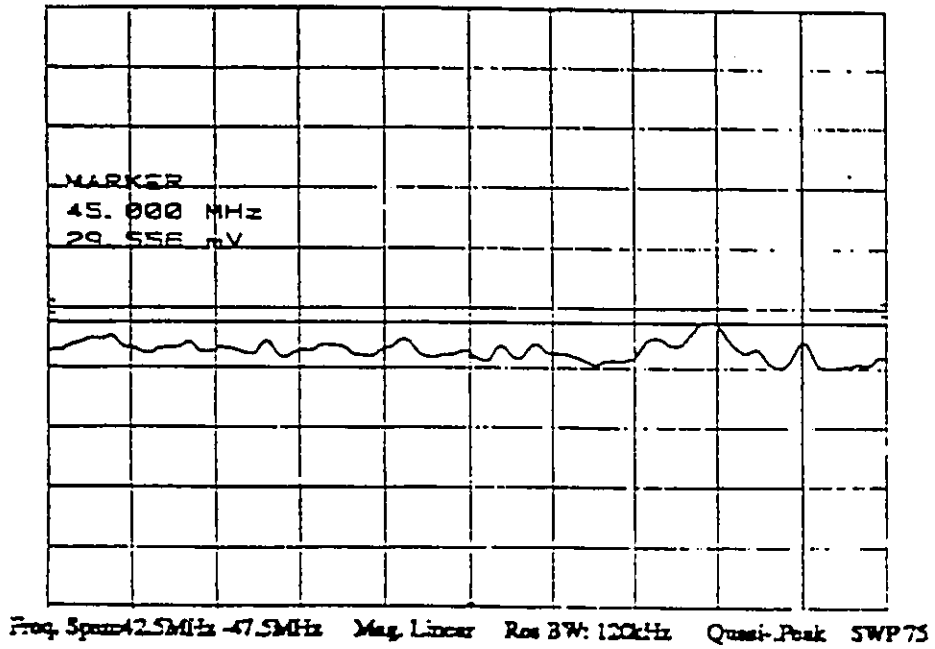

The data so far has been for effectively infinite random signals (random bit stream of length 2^{23} - 1). Figure 3.22 shows the effect of short, repetitious random sequences in high bit rate

systems. This is a typical characteristic of short looping software or repetitive coding schemes.

The measurement is repeated for a random bit stream length of 127 (2^7 - 1) bits corresponding to a data cycle rate of 787 kHz. This results in the discretization of the emissions spectrum and a 4.4 dB rise of the peak amplitude from 30 mV to almost 50 mV. Similar effects can be seen for the RZ signal but the 100 MHz narrow band signal still dominates the spectrum. The change in bit stream length had no effect on the amplitude of the 100 MHz narrowband harmonic for either the RZ or the NRZ case.

Figure 3.22: Quasi-Peak Measurement of Broadband Segment of Short NRZ Signal

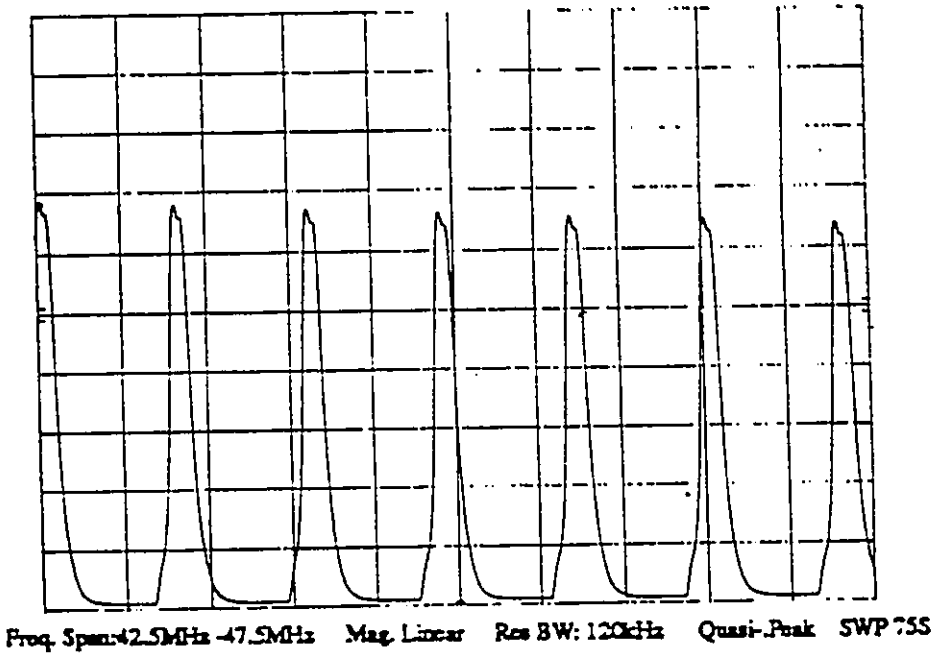

3.6.2 Example # 2

The exercise above is repeated for a 1 MBit/sec data stream. The spectrum of the RZ signal from 30 MHz to 300 MHz is shown in Figure 3.23. The spectrum of the NRZ signal is similar. The narrowband spectral content is not as evident as at the higher bit rates.

The quasi-peak response from 38.5 MHz to 43.5 MHz is shown in Figure 3.24 and Figure 3.25 for the RZ and the NRZ signals respectively.

As before the RZ signal is dominated by the narrowband components resulting in an absolute amplitude of 8.7 mV as compared to 3.7 mV for the NRZ case. The NRZ spectrum has nulls at the harmonics and the cyclo-stationary effect is not evident as it was in the 100 MBit/sec case.

Figure 3.23: 1 Mb/s, 2.5V, RZ Spectrum

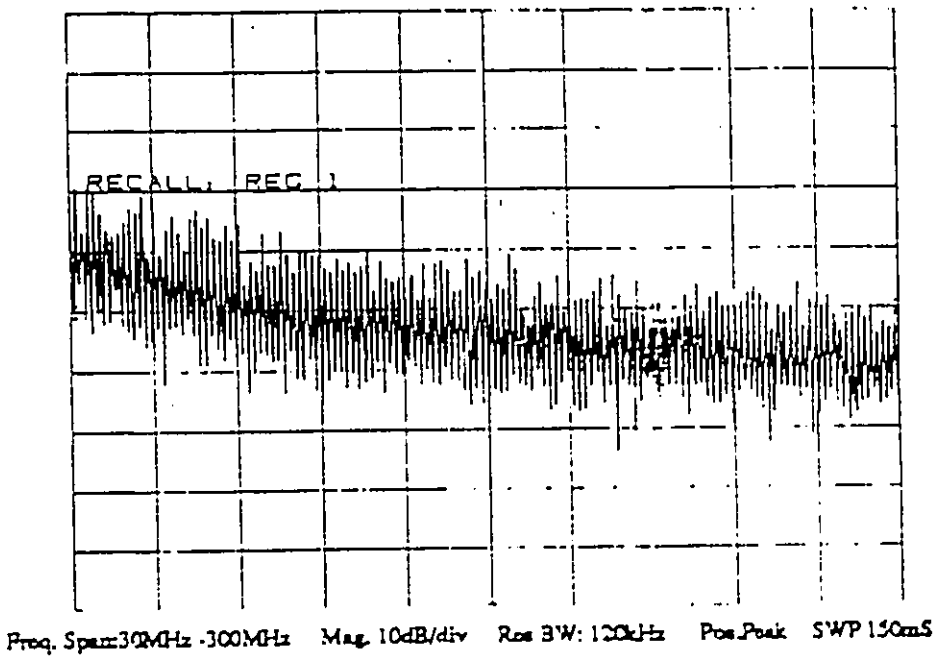

Figure 3.24: Quasi-Peak Measurement of Broadband Segment of a RZ Signal.

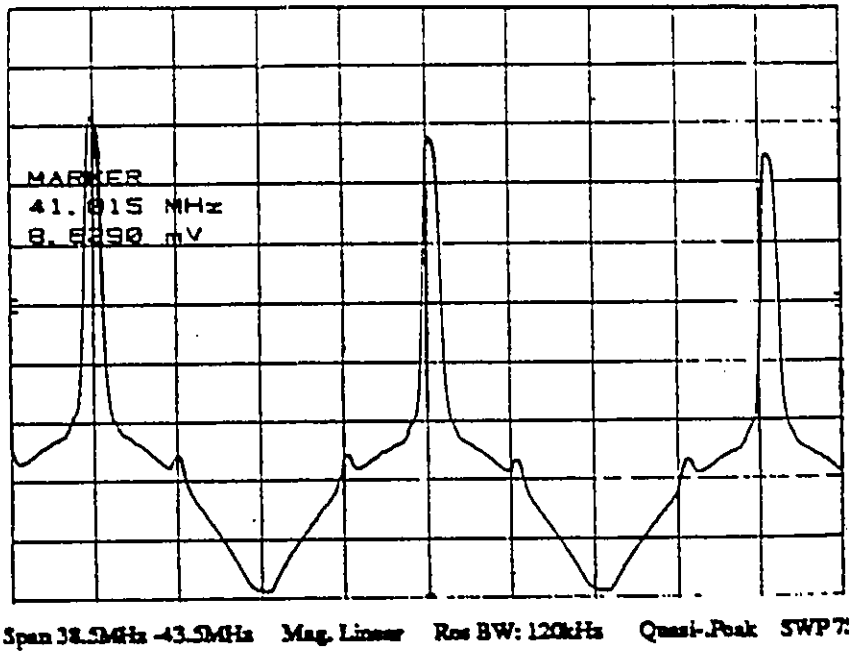

Figure 3.25: Quasi-Peak Measurement of Broadband Segment of a NRZ Signal.

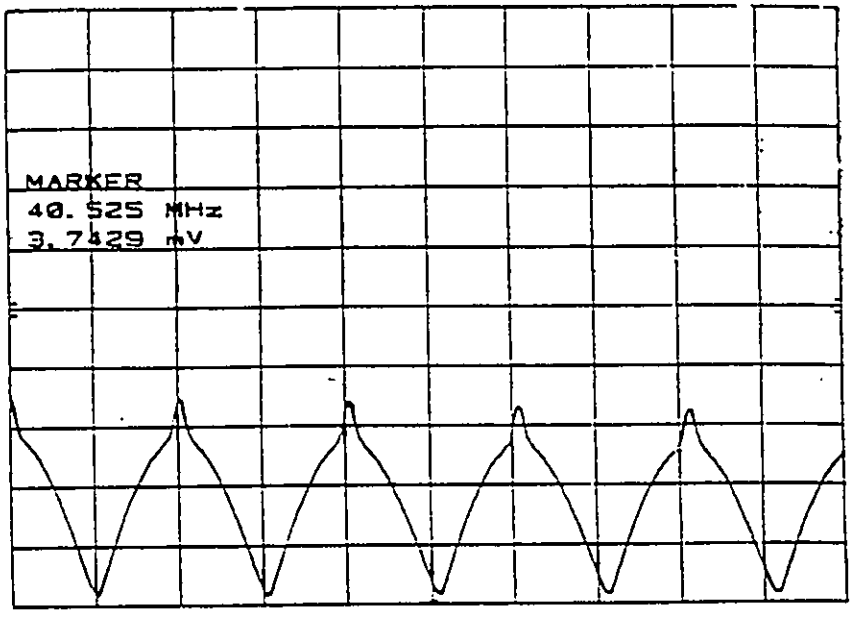

Because of the slower bit rate relative to the 120 kHz bandwidth of the QPD the case of repetitive random sequences does not influence the spectrum. Even with a short random sequence of 127 bits the repetition rate is 7 kHz, appearing almost infinite to the detector.

3.7 Conclusion

The relative amplitudes of each of the components of the power spectra discussed above will vary widely and must be taken into account if an accurate representation of the system performance is to be achieved. Determination of the relative contributions can be made for specific examples for which a lot of detailed information exists.

Some general comments can be made based on the formulas and graphs presented above. For example, using Figure 3.7, the spectral envelope of a 5 volt, 100 MBit/s data stream, when viewed through a 120 kHz bandpass filter at 200 MHz, is smaller in amplitude than the fundamental harmonic of a 30 mV, 200 MHz clock signal[7]. A clock signal of such low voltage is readily induced on a data track or cable through parasitic coupling.

A narrowband clock signal is at least 20dB higher in EMI potential than the broadband components of a data signal of equivalent amplitude and frequency when measured with a quasi-peak detector.

This indicates that, even in a data-rich, high speed system extreme care must be taken with the management of the timing signals. The levels to which their parasitic effects must be suppressed are far lower than those required by the noise margins of the digital logic.

7. This is determined from Figure 3.7 by tracing the line upwards from 200 MHz on the frequency axis to the line representing 100 Mb/s and then across to the vertical axis where the amplitude of the equivalent clock harmonic can be read. This value corresponds to a 1 Volt data signal and must then be scaled for the actual amplitude of the data signal.

On the other hand it must not be assumed that all narrowband energy content is derived from the clocking network. Significant levels of narrowband energy are generated directly or indirectly by the information carrying signals. These contributions can only be mitigated through careful design of the integrated circuits and the waveforms they generate.

It is possible to calculate the quasi-peak detector response to any signals for which the power spectral density is known. It will be shown in Chapters 5 and 6 that components located near the wall of a shielded enclosure have a dominant effect on the emissions performance of the system at low frequencies. The disturbances produced by these components may be more than 60 dB greater than those due to similar sources placed elsewhere within the enclosure. If such a component had a strong broadband spectrum then the difference in predicted emissions through using a quasi-peak rather than a peak detector model for the signal strength could exceed 50%.

Because there is considerable computational overhead involved in a detailed spectral analysis of a complex electronic system, engineering judgement must be employed to determine when the effort is worthwhile.

Chapter 4

Modelling Integrated Circuits

4.1 Introduction

Integrated circuits, along with pcb traces and connectors, are primary radiators in the enclosed, multiple source problem. Accurate measurement and modelling of these devices is required to produce a representative dipole model that can be applied in the calculation of disturbances within the enclosure.

The measurements and models discussed in this chapter are a summary of the work done by the author and his colleagues at Bell Northern Research. It is presented here as it performs a critical role in the development of the multiple source problem. This work has been published in journals such as the Transactions in Communications of the IEICE, Japan [Goulette 92-1] and presented at the International EMC Symposium of the IEEE [Goulette 92-2]. The measurement methods are being considered for adoption by the ANSI accredited SAE task force on IC EMC involving representatives of many of the major producers of ICs.

Large components such as microprocessors and application specific integrated circuits (ASICS) have become an increasingly important source of electromagnetic interference

energy in the last few years. This is due to their higher clock speeds, greater current consumption and ever increasing size.

Figure 4.1 illustrates the coupling of both conducted and radiated energy from the IC into printed circuit board structures as well as radiated coupling into cavities and onto cables and connectors. The total energy from all of these sources makes up the EMI potential of the equipment.

In this chapter it is proposed to characterize integrated circuits such as microprocessors and ASICs in terms of their equivalent magnetic or electric dipole moments. The dipole moment is a value that can be measured and calculated. It is found to be very useful for evaluation and comparison of different IC designs.

Figure 4.1: Coupling Paths From Component Emissions

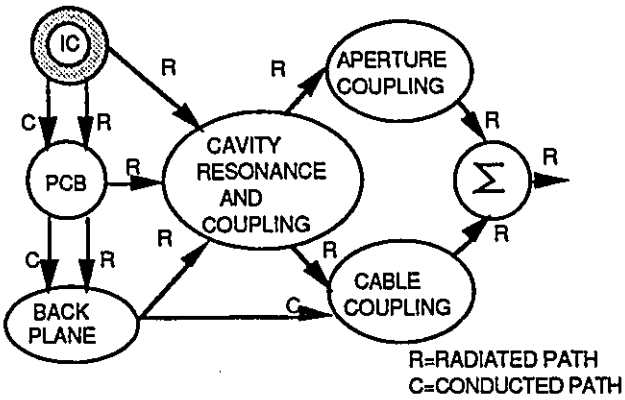

The magnetic dipole moment is the product of loop area and loop current. The electric dipole moment is the product of length and current (Figure 4.2). These dipole moments may be obtained from measurements at or near the device, or calculated from device currents, voltages and geometries. The spectral densities of the current and voltage used in calculations are determined using the methods outlined in the previous chapter.

Figure 4.2: Electric and Magnetic Dipoles

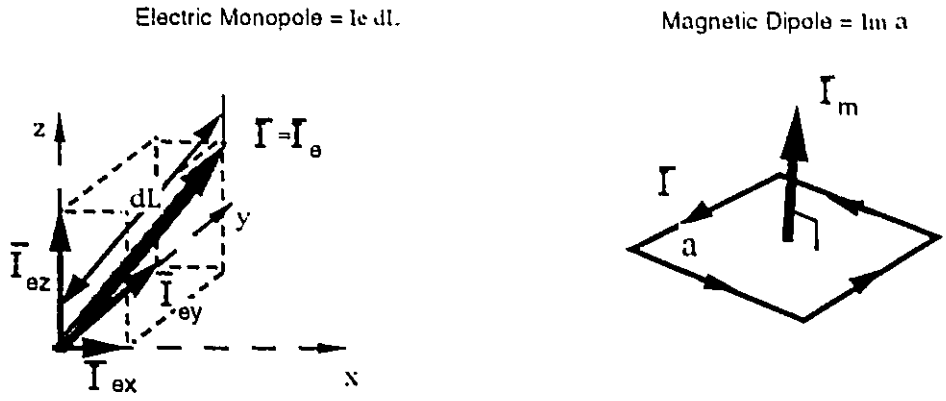

Large ICs are found to act as both magnetic loops and electric dipoles as illustrated in Figure 4.3. Currents flow in loops formed principally by the active power, ground and signal leads of the device as well as the corresponding printed circuit board tracks and nearby power decoupling capacitors.

Figure 4.3: Electric and Magnetic Moments of ICs

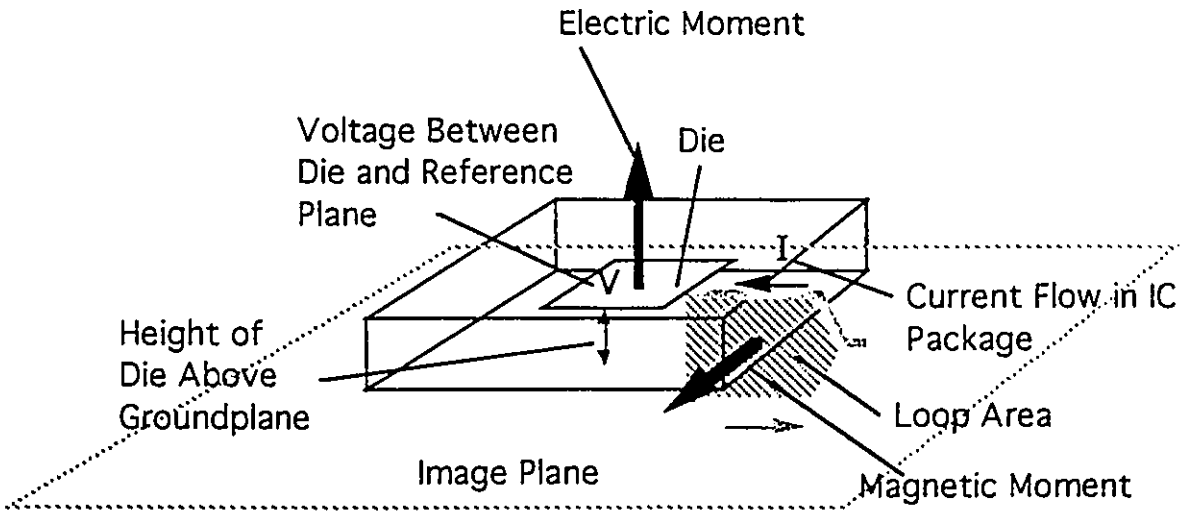

Bulk currents within the device may reach hundreds of milli-amperes due to extensive internal clock distribution networks as well as repetitive simultaneous switching of many parallel outputs. Extreme examples of latest generation microprocessors draw peak currents of nearly 50 amps.

Dimensions of these packages may be as great as 50mm on a side and more than 3mm high. This represents one of the largest radiating structures on the printed circuit board.

The potential difference between the ground reference on the IC die and the groundplane on the pcb may exceed 1/10th of a volt. The time harmonic fluctuation of this voltage will result in both conducted and radiated disturbances.

When the magnetic or electric dipole moment of an IC is measured using one of the methods presented in the next section, it comprises contributions from many individual current generators and current paths within the IC. This is a vector quantity with a time harmonic amplitude variation and a polarization. Both the magnitude and polarization will be functions of frequency as various components of the IC activity dominate the total signal strength over different frequency ranges.

When measuring the dipole moment with a hand-held probe or a transverse electromagnetic (TEM) cell it is necessary to post-process the data to obtain the value of dipole moment.

To calculate the dipole moment, it is necessary to identify the major contributing sources, calculate their magnitude and polarization and then sum them together while preserving their phase relationship. This task involves large amounts of detailed information and must be done using computer simulation.

4.2 Measurement of Magnetic and Electric Dipole Moment

Measurement of IC emissions is important both for the characterization of existing ICs and to calibrate design models.

In order to obtain a realistic emissions profile the IC must be exercised in one or more typical operating modes. This must include operation of the data ports into representative loads. This may be achieved by in-situ testing on an operating board or in conjunction with a test simulator.

If the measurements are made at a distance from the board the component can be represented by a point source. The magnetic and electric dipole moments are then calculated using standard dipole formulas [Stutzman 81]. This is generally impractical as emissions from other components on the pcb will strongly influence the total electromagnetic field. To avoid this problem measurements are made in close proximity to the IC or in an isolated test chamber.

4.2.1 Measurement of Magnetic Dipole Moment

The *in-situ* measurements of magnetic dipole moment are performed using a 2 cm X 2 cm square loop. The loop is rotated about a vertical axis to achieve the maximum magnetic field reading (Figure 4.4).

To relate this field to a magnetic dipole moment it is necessary to make an assumption about the effective radiating loop area.This can be achieved by performing two measurements at different heights (h_1 and h_2 in Figure 4.4) and comparing the measured levels with theoretical values or simple method of moment models.

Figure 4.4: Measurement of Magnetic Dipole Moment With Magnetic Field Probe

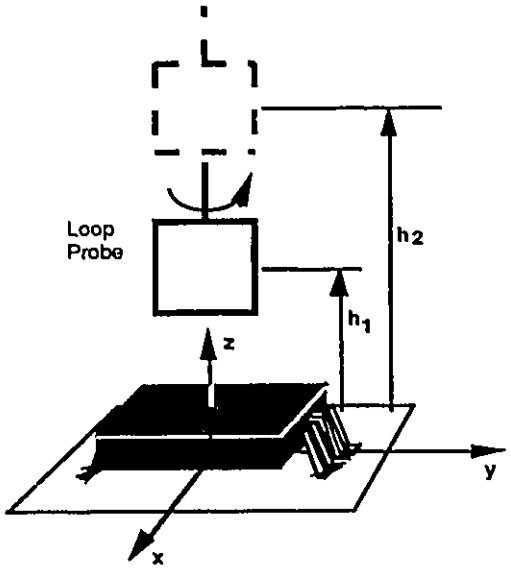

4.2.2 Measurement of Electric Dipole Moment

The electric dipole moment is generated by a potential difference between the IC die and the pcb groundplane. One approach to determining the dipole moment is to measure the voltage of the die and apply it to an annular slot antenna model as shown in Figure 4.5. This is a more accurate model than the simple electric dipole shown in Figure 5.2 as it better represents the the aspect ratio of the IC package.

The voltage measurement is somewhat complicated because it is being made between two points, both of which are supposed to be ground reference but which have a distributed inductance between them. It has been done using a high impedance probe and a metal plate on top of the IC package (Figure 4.6). This plate is capacitively coupled to the die and leadframe beneath due to its physical proximity. The voltage determined from this measurement can be converted into the electric dipole moments using equation (4-5).

Figure 4.5: Annular Slot Model of IC For E-Field Emissions

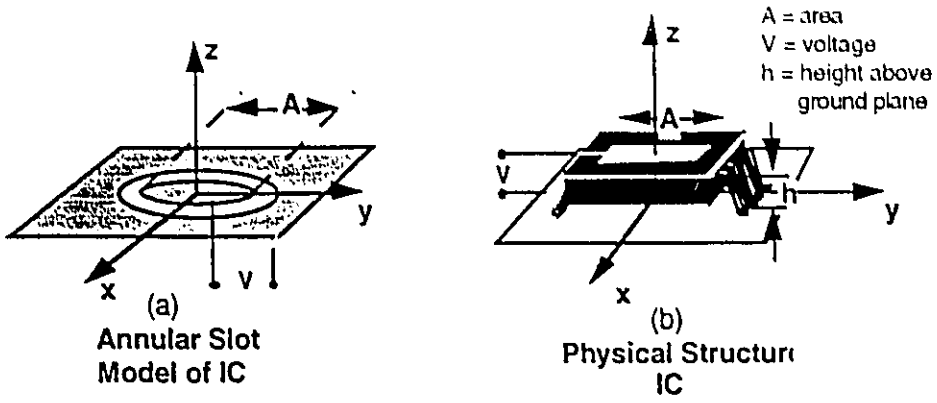

Figure 4.6: Measurement of Electric Dipole Moment With Voltage Probe

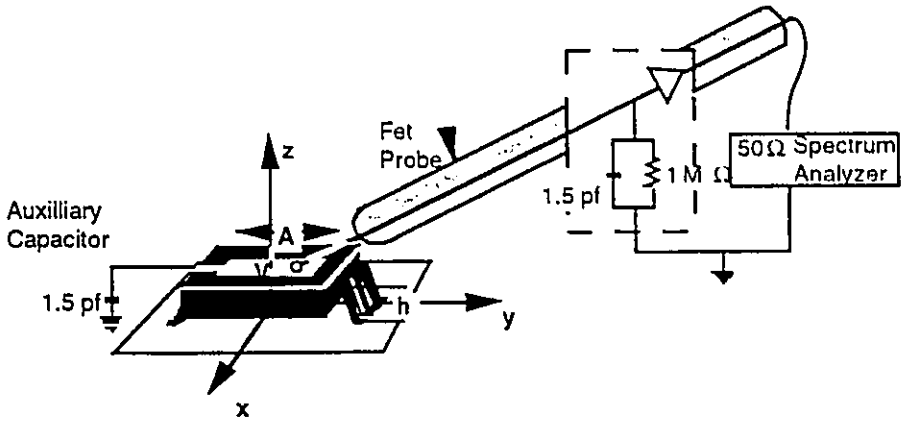

4.2.3 Measurement of Dipole Moment in TEM Cell

The measurement of the IC may also be made in a wide band TEM cell [Bronaugh 91]. A test coupon is laid out with the IC under test on one side and the supporting components and simulators connected to the other side. This is mounted in the TEM cell such that the IC under test is isolated from all other noise (Figure 4.7).

Figure 4.7: Measurement in Wide-band TEM Cell

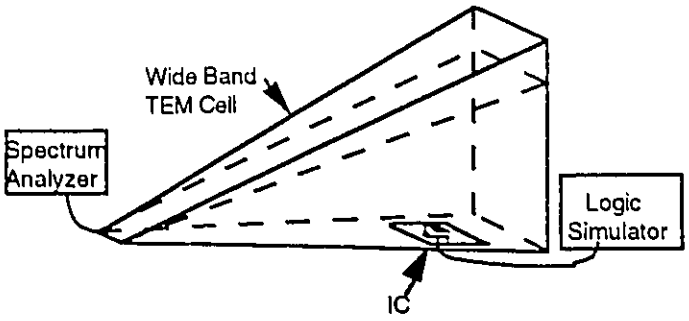

Measurement within the wide-band TEM cell or within a small conventional TEM cell with a 1 GHz bandwidth has numerous advantages in terms of controllability and repeatability. Correlation of the voltage generated at the spectrum analyzer to the dipole moment of the device under test may be done through calculation or calibration through the substitution of simplified source structures.

4.3 Measured Data From ICs

4.3.1 Measured Data Using Hand-Held Probes

Twenty large ICs, including microprocessors and ASICs have been measured using hand-held probes. The measured magnetic dipole moment values fell within the shaded regions shown in Figure 4.8 andFigure 4.9.

The sloped lines on the plots represent the dipole moment values that would yield a constant free-space far field amplitude. These fall off at 40 dB per decade for the magnetic dipole moment, 20 dB per decade for the electric dipole moment. [Stutzman 81].

The four levels represent recommendations for emissions standards for ICs. These are being discussed in several industry forums.

Figure 4.8: Measurements of IC Magnetic Dipole Moment

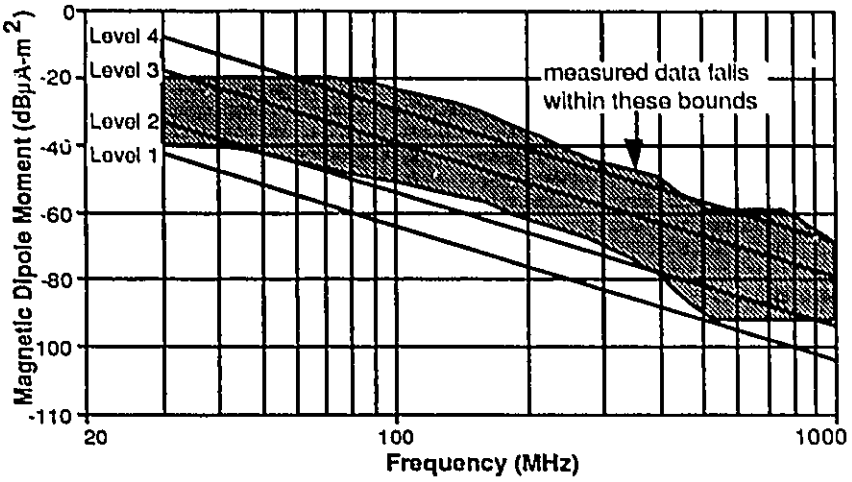

Figure 4.9: Measurement of IC Electric Dipole Moment

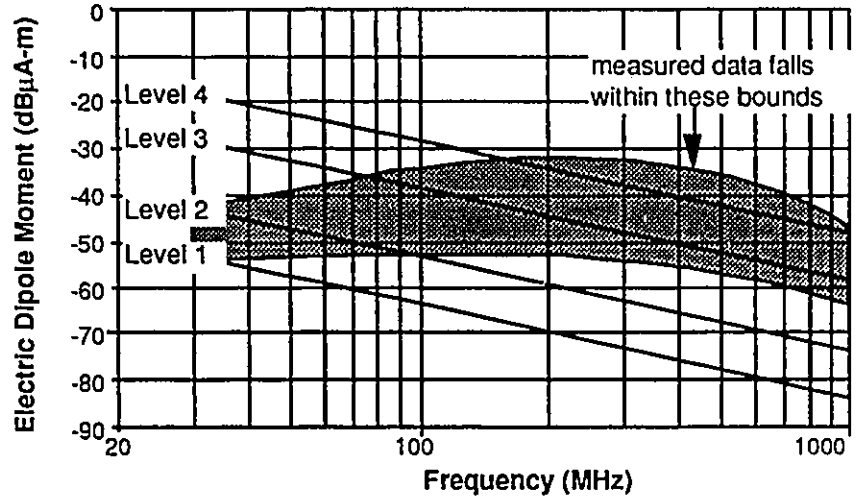

4.3.2 Measured Data Using TEM Cell

Comparative measurements have been performed in a wideband TEM cell for a test die mounted using two different packaging strategies; a through-hole Pin Grid Array (PGA), which has a large ceramic body and a bare die wireboneded to a pcb which is called Chip-

On-Board (COB) technology and represents one of the smallest profile packaging strategies. Figure 4.10 shows the spectrum analyzer output of this die mounted in a PGA package. Figure 4.11 shows the spectrum for the same die mounted directly on the pcb using a COB.

Figure 4.10: Test Die In PGA Package Measured in TEM Cell

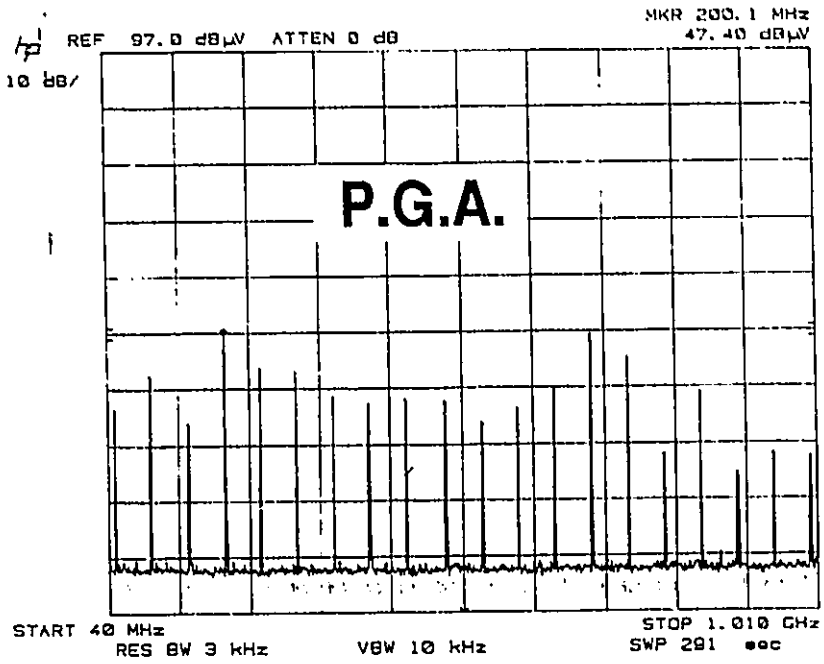

The COB strategy reduces the horizontal cross sectional area of the package by more than 60 % and reduces the die height above ground by a factor of ten. The activity on the die remained constant. A 16 dB drop in peak emissions was achieved through this shift in packaging strategy. This is a good example of achieving source level suppression by changing the radiation efficiency of the source without effecting the basic functionality.

Figure 4.11: Chip-On-Board Technology Measured in a TEM Cell

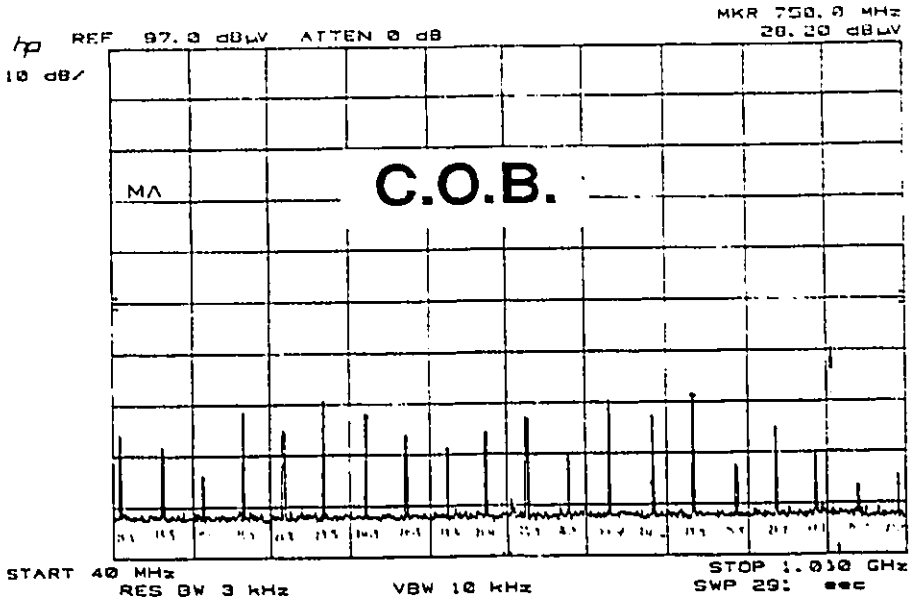

4.4 Calculation of Magnetic and Electric Dipole Moment

The true value of the analytic approach to the EMI problem is seen when the model can be used to influence the basic design of the IC to reduce emissions potential. To achieve this the dominant sources within the IC must be identified, modelled in terms of their dipole moments and summed to give the total dipole model of the IC.

A source is found to be dominant by virtue of the energy spectrum of its driving signal and the radiation efficiency of its current path or the geometry of the structure over which it creates a time harmonic potential difference.

The power spectrum of the driving signal is determined using the techniques of the previous chapter. This section deals with the radiation efficiency of the current path.

The physical structure of the IC constitutes a complex radiating structure. Current flow paths are different for positively (logic zero to logic 1) and negatively (logic 1 to logic 0) going edges of signals. This is because the current flows to the signal port from the V_{cc} power distribution system in the first case (Figure 4.13)and from the signal port to the ground reference system of the circuit in the second case (Figure 4.14).

The power and ground currents generally flow through multiple pins to be distributed to the set of simultaneously switching drivers (Figure 4.13 and Figure 4.14) The distribution of the bulk current flowing through the power and ground pins is dependent on the relative impedances of the paths and the mutual inductance with respect to the switching signal.

4.4.1 Magnetic Dipole Moment

For the evaluation of the magnetic moment, the complexity of the radiating structure is dealt with by a process of decomposition. Simple loops are identified and the portion of current flowing through these loops is calculated. The magnetic moment contributed by each current loop is summed to give the total magnetic dipole moment of the device.

Current loops may be due to a signal path that enters the IC from the outside, comes to the die at the centre and then leaves the die by some other route. This type of model is shown in Table 4.1. Alternatively each bonding wire and branch of the leadframe may be modelled as a surface dipole with a mirror image in the groundplane as shown in Figure 4.12.

The individual magnetic dipole moments are summed together using the principle of superposition. Certain simplifications can be made to the modelling by taking advantage of symmetries that cause cancellation of signals. This is done by creating simple canonical structures composed of pairs or symmetric triplets of pins (see Table 4.1). The disturbances from each of these simple structures are then added to give the total dipole moment.

Table 4.1: **Current Vector Representation, Calculated and Measured**

Current Vector Orientation	Based Upon Summation of Dipole Moments	Based Upon G-TEM Cell Measurements (100MHz)	Based Upon Method of Moments Check
a) 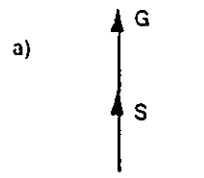	0.00 dB	0.00 dB	0.00 dB
b) 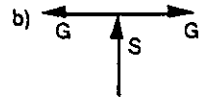	-6.00 dB	-5.60 dB	-5.90 dB
c) 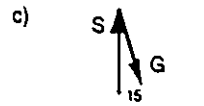	-17.76 dB	-19.00 dB	-18.00 dB
d) 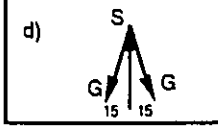	-29.35 dB	-28.00 dB	-29.60 dB

In this simplified model the current flows from the pins at the perimeter of the IC package to the silicon die at the centre and then back out to the perimeter along a different path. Table 4.1(a) represents a current which enters a chip on one side and exits on the opposite side. The value of this magnetic moment is normalized to 0 dB. Configurations 4.1(b) through 4.1(d) show some other current flow patterns and the corresponding reduction of the magnetic moment due to the physical flow pattern of the current in the IC. These values serve as weighting factors for the current amplitudes associated with each of the flow paths.

The current vectors of magnitude (I_s) and length (L) are assumed to lie parallel to the printed circuit board ground at a height (h) above the groundplane. This is equivalent to half the package width and the die height (Figure 4.12).

The electric moment (**p**) is given by the formula:

$$p = I_s \times L \qquad (4\text{-}1)$$

The resultant moment (p_r) of two vectors at an angle (θ) (Table 4.1 (a) and (c)) is:

$$p_r = 2 I_s L \sin(\theta/2) \tag{4-2}$$

Figure 4.12: Current Vector Representation

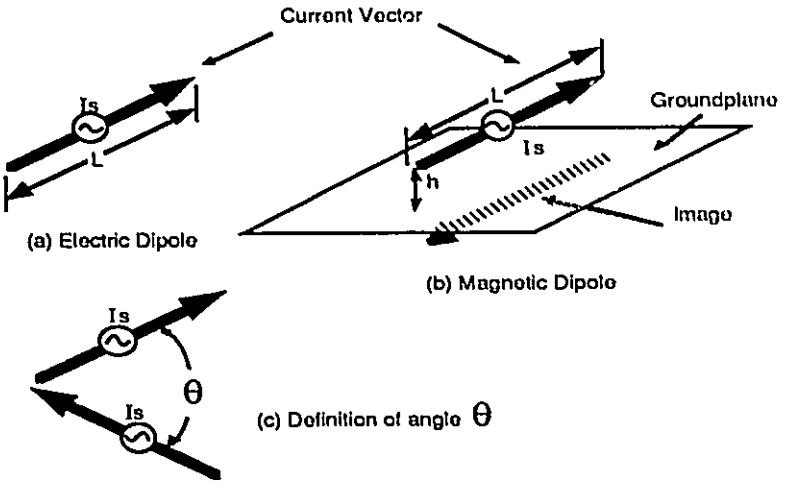

for a symmetric vector triplet (Table 4.1(b) and (d)) the resultant moment (p_r) is:

$$p_r = I_s L (1 - \cos(\theta)) \tag{4-3}$$

By themselves these current vectors provide a horizontal electric moment. However, this has a corresponding image in the groundplane of the printed circuit board. These two current elements result in a magnetic moment (m_r) parallel to the plane of the printed circuit board given by the formula:

$$m_r = | p_r \times 2h | \tag{4-4}$$

If the power and ground structures of the IC are closely coupled and similarly distributed around the chip then the switching action of the drivers appears as a 180° phase shift in the magnetic dipole. If the physical layout of the power and ground structures, such as number and location of pins, are significantly different, then signal switching will result in a change in the magnitude and orientation of the dipole moment.

The total radiation loop area is dependent on the position of the power and ground structures relative to the signal pin. It has been shown that for large ICs the ground and power pins in close proximity to the switching transistors will carry the majority of the current flow [Diaz-Olavarrieta 91]. This is due to the inductive coupling between the pins and the resistance across the die surface.

The two horizontal components of the magnetic dipole relate to the current that is circulating in a vertical plane, from the printed circuit board and up into the silicon chip via the pins and leadframe The third, orthogonal component is related to current circulating in the plane of the pcb, either through the leadframe or on the silicon die itself. All three components will be used in the Green's function model of the next chapter.

4.4.1.a Positive Logic Transition

Figure 4.13 shows the current flow path for a positive logic transition. The initial current source can be assumed to be the decoupling capacitor for the IC.

To start the current flow, transistor T_1 turns on and transistor T_2 turns off. This switching action turns the initial d.c. potential of the power and ground supply rails into a signal with a broad energy spectrum. The rate of the switching of T_1 and T_2 is the principle determinant of the shape of this spectrum; the faster the switching the broader the spectrum.

There is a period of time at the beginning of the switching action, when most of the high end spectral content is being produced, during which T_1 has turned on but T_2 has not fully turned off. This results in a short circuit current flow from the power supply rail (V_{cc}) to the ground potential rail (V_{ss}). This current flow path starts and ends with the decoupling capacitor for the chip.

In high speed circuits this short circuit current may represent up to 50% of the peak current flow. The polarization of this contribution to the magnetic dipole moment may be quite different than that of the signal path (V_{dd} to I_{sp}) due to the different path of current flow.

Figure 4.13: Current Flow for Positive Logic Transition

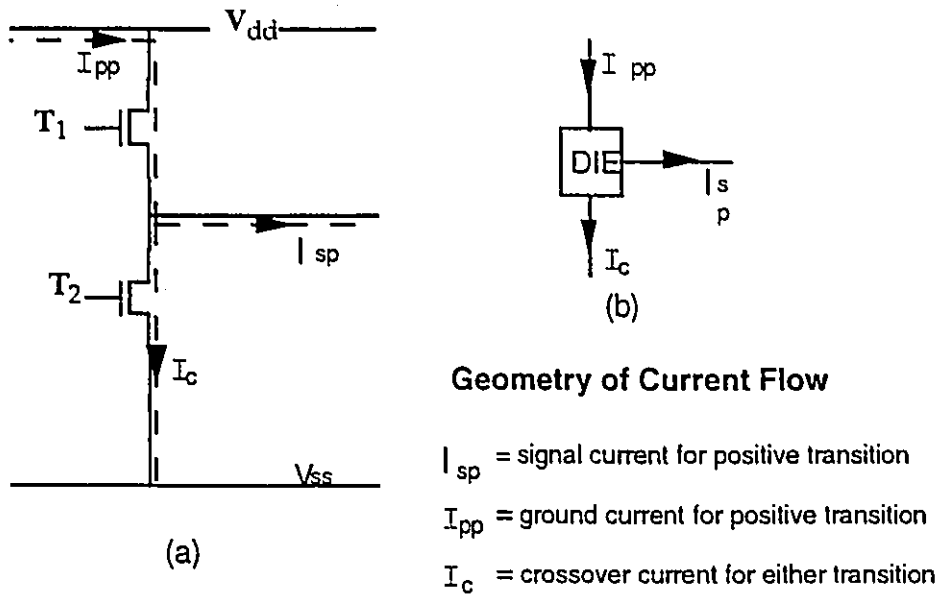

4.4.1.b Negative Logic Transition

Figure 4.14 shows the equivalent current flow path for a negative going transition. In this case the effect of a symmetric ground current path has been shown in terms of both the schematic and its vector representation. The crossover current will also occur in this instance but has not been illustrated.

Figure 4.14: Current Flow for Negative Logic Transition

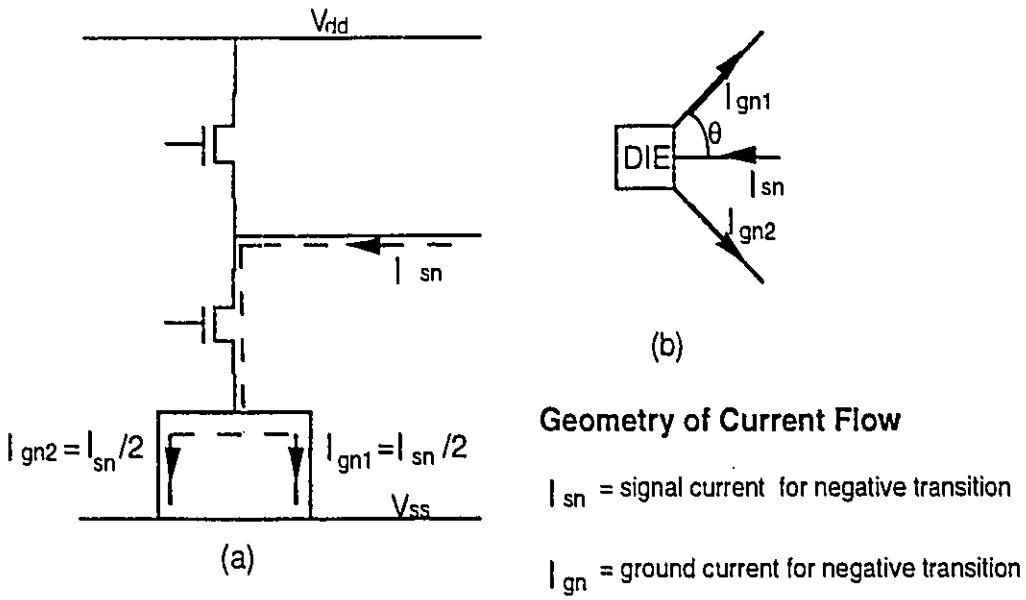

4.4.1.c Comparison of Calculated and Measured Magnetic Dipole Moments

Accurate modelling of IC emissions is a complex task that must merge the spectral content of all the signals with the geometric structure of the IC package. This information is seldom available in a readily usable form. Figure 4.15 shows preliminary results of modelling based on the principles discussed above. This work is presently being done at BNR.

4.4.2 Electric Dipole Moment

The current flow determined in the previous sections takes place across the inductive impedance of the IC package. This results in a voltage differential between the pcb ground reference and the IC die ground structure. When looked at from the perspective of the whole chip this voltage differential is seen as groundbounce[1].

1. The calculation of groundbounce voltage is beyond the scope of this thesis.

The annular slot has been proposed for the electric field radiation model (Figure 4.5). This may be used to relate either calculated groundbounce values to the strength of an electric dipole [Goulette 92-1].

Figure 4.15: Comparison of Calculated and Measured Magnetic Dipole Moment

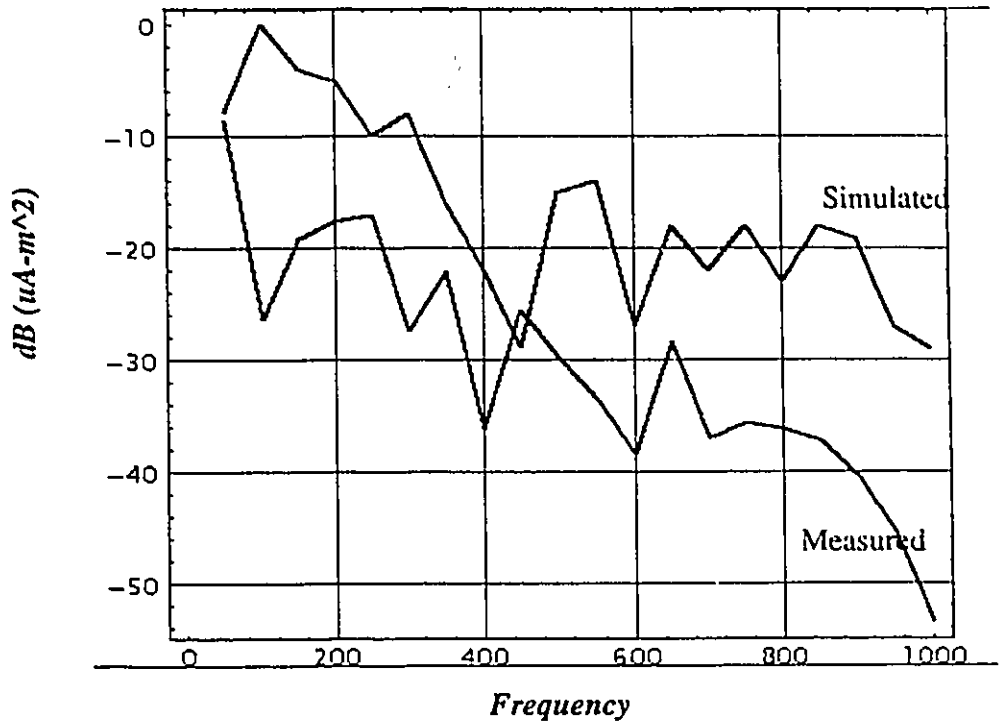

The electric dipole moment (p) is determined from the groundbounce voltage (V) and the surface area (A) of the IC using the formula:

$$p = V A / 60 \lambda \qquad (4\text{-}5)$$

where λ is the wavelength of the frequency in question [Wolff 88].

Due to the physical mounting and operation of an IC on a printed circuit board, the only electric dipole source considered in this model is the one oriented normal to the ground-

plane. This is consistent with the radiation patterns of the annular slot model presented in the previous chapter.

A horizontal dipole would imply a high impedance structure with no return current flow lying in the plane of the IC die. No such behavior has yet been observed during experimentation and the physical structure of the IC does not lead to an intuitive rationale for such a source contributing to a significant emissions level.

4.5 Conclusion

The radiated electromagnetic emissions of an integrated circuit can be characterized in terms of magnetic and electric dipole moments. The magnitude and polarization of the dipole representation is achieved through measurement or calculation.

Measurements may be performed using hand-held probes or transverse electromagnetic cells. This measurement data is generally collected in terms of voltages and field strengths. Post-processing of the data is required in order to determine the magnetic and electric dipole moment.

Calculation of the dipole moments requires detailed knowledge of the construction and functionality of the integrated circuit. Magnetic and electric dipole moments are calculated for the most significant individual current loops. These are then summed through superposition.

Initial efforts have shown reasonably good correlation between the measured and the calculated estimations. Discussions are presently underway to introduce the test methodologies into the integrated circuit industry.

The analytic modelling of the IC demonstrates the increase in emissions potential that is due to the current flow paths. This information can be applied to the determination of source level mitgation techniques such as selection of low profile packages or placement of power and ground pins.

Chapter 5

The Cavity Model

5.1 Introduction

The EMI potential of an enclosed system is measured in terms of the currents and fields induced on the walls of the enclosure. Unlike the free-space radiation problem, the magnitude and polarization of the current and field distribution are as much a function of the enclosure dimensions as they are characteristics of the primary radiators.

The interaction between the source signals and the enclosure are described in terms of dyadic Green's functions. The Green's function for a rectangular cavity is an appropriate description for the shielded enclosure under study. These functions may be used with any electric or magnetic source current distribution, however, simple, closed form solutions may be obtained if the sources are modelled as magnetic and electric dipole moments.

The Green's function approach was selected for this problem as it can provide a direct relationship between a source point and a point on the cavity wall. This is computationally efficient and permits general statements to be made about characteristics of the source-boundary interaction. In the next two chapters the behavior of sources will be shown

to depend on the relationship between the frequency, the dimensions of the enclosure and the position of the source.

The dipole source inside a perfectly conducting cavity is an idealized model of integrated circuits (ICs) on a printed circuit board (pcb) inside a rectangular shielded enclosure. Use of this physical model permits the signal strength, polarization and geometry of the IC sources to be directly related to the surface current density and the normal electric field on the wall of the enclosure.

The wall current densities and electric field strength calculated from this model may then be applied to a number of perturbation models for imperfections in the enclosure such as seams with a finite conductance or small apertures. This permits a determination of the shielding effectiveness of the enclosure. The magnitude of the disturbance on the walls of the enclosure provides a metric for the radiated emissions potential of the unit.

The use of the Green's function in the modelling of enclosures for EMC was first proposed by Mendez [Mendez 78]. The equations presented by that author were for small dipoles with sinusoidal current distribution. In this model the dipole sources defined in Chapter 4 will be used. These were first published by Cooray, Crawhall and Costache [Cooray 91-1,2]

Figure 5.1: Ideal Cavity Model

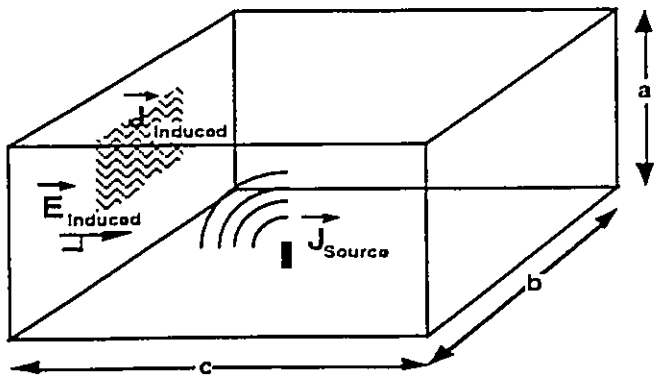

The approach followed in this thesis is aimed at producing the simplest form of the equations that can be used to relate measured or modelled source data to the current and field distribution at the location of interest, in this case the wall of the enclosure.

5.2 Dyadic Green's Functions

Dyadic Green's functions are a powerful tool for solving three dimensional electromagnetic field problems when they exist in a closed form for the case under investigation. In the following derivation they will be used to calculate both the electric and the magnetic fields within the cavity from either an electric or magnetic dipole. By treating these dipoles as point sources the convolution integral reduces to an infinite summation.

5.2.1 Green's Function for an Electric Dipole Source

The sources of electromagnetic energy may be modeled in terms of a known electric current distribution (J_e). In general the electric or magnetic fields (F) can be determined through the use of a Green's function of the form:

(5-1)

$$\bar{F}(\bar{r}) = \iiint_v \bar{\bar{G}}(\bar{r} \mid \bar{r}') \, \bar{J}_e(\bar{r}') \, dV'$$

In this formulation the position vector (r) refers to the field point of interest, the position vector (r') refers to the source location and the volume (V') refers to the volume containing the source current.

For a small electric dipole the electric current density is assumed to be evenly distributed over a cylindrical volume of length L_e and cross-section A_e (Figure 5.2). In this case the current is given by:

$$\bar{I}_e = \bar{J}_e \cdot A_e \tag{5-2}$$

The electric dipole moment is then given by:

$$\bar{p} = \bar{I}_e \cdot L_e \tag{5-3}$$

Figure 5.2: Electric Dipole

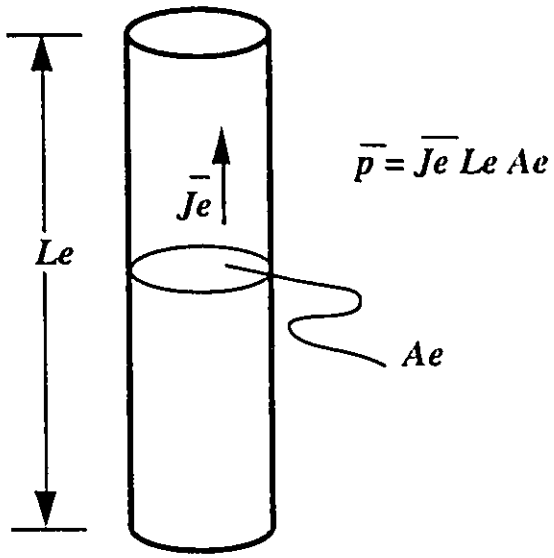

In practice the electric current may be oriented arbitrarily and the cartesian components are given by:

$$\bar{p} = \bar{J}_e \, dL = I_0 \cdot (L_x \hat{x} + L_y \hat{y} + L_z \hat{z}) \, \delta(\bar{r} - \bar{r}') \tag{5-4}$$

Assuming that L_e is small relative to $|r|$, the distance to the field point, equation (5-1) can be simplified to the form:

$$\bar{F}(\bar{r}) = \bar{\bar{G}}(\bar{r} \mid \bar{r}') \cdot \bar{p}(\bar{r}') \tag{5-5}$$

5.2.2 Green's Function for a Magnetic Dipole Source

In order to make the same point source assumptions as for the electric dipole case, the Green's function for a magnetic dipole is expressed in terms of a known magnetic current distribution (J_m):

(5-6)

$$\bar{f}(\bar{r}) = \iiint_v \bar{\bar{g}}(\bar{r} \mid \bar{r}') \, \bar{J}_m(\bar{r}') \, dV'$$

The magnetic dipole moment ($\bar{m}$) can be defined in two ways, either in terms of the magnetic current ($\bar{I}$) and the magnetic dipole length (L_m) or in terms of the electric current ($\bar{I}_e$) and the loop area (A_l). This is shown in Figure 5.3

Figure 5.3: Magnetic Dipole

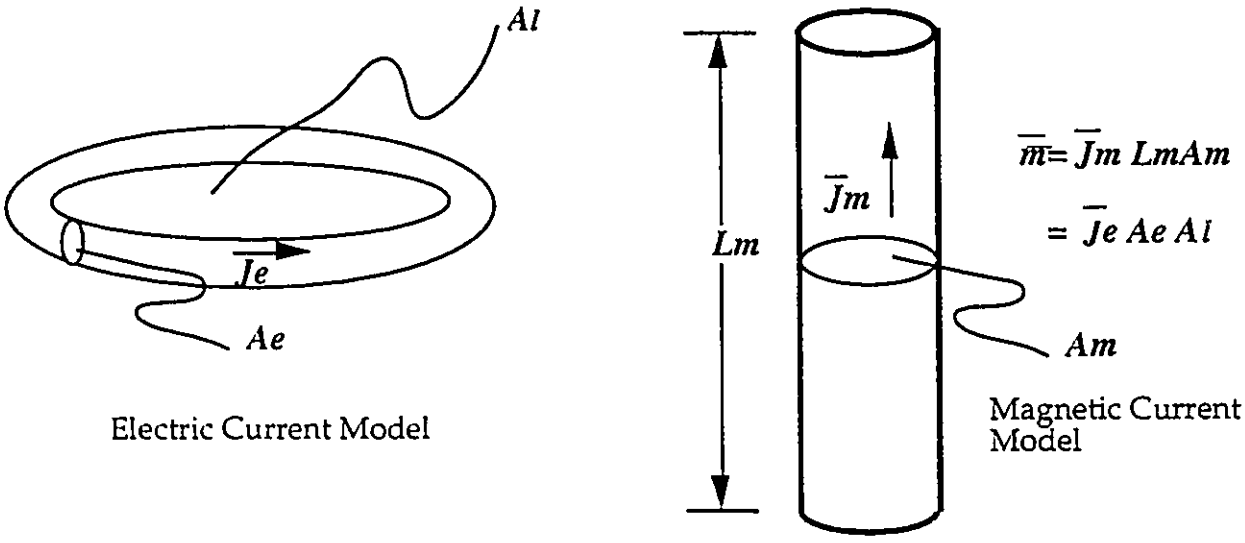

Following the steps taken for the electric dipole, equation (5-6) becomes:

(5-7)

$$\bar{f} = \bar{\bar{g}}(\bar{r} \mid \bar{r}') \cdot \bar{m}(\bar{r}')$$

where the magnetic moment ($\overline{m}$) is given by:

(5-8)

$$\overline{m} = \bar{J}_m A_m L_m = \bar{I}_m L_m = \bar{J}_e A_e A_l = \bar{I}_e A_l$$

5.2.3 Using Green's Function to Calculate Electric and Magnetic Field Values

The Green's functions can be used to calculate the electric and magnetic field distribution within the rectangular cavity for any distribution of source current. In convolution integral expressions (5-9) and (5-10) the electric current density ($\bar{J}$) is distributed over the source volume V' where V' is a subset of the total cavity volume.

The electric and magnetic fields due to an electric current distribution are given by:

(5-9)

$$\overline{E}^e(\overline{r}) = \int_{V'} \overline{\overline{G}}_e(\overline{r} \mid \overline{r}\,') \, \overline{J}(\overline{r}\,') \, dV'$$

(5-10)

$$\overline{H}^e(\overline{r}) = \int_{V'} \frac{1}{j\omega\mu_o} \overline{\overline{G}}_h(\overline{r} \mid \overline{r}') \, \overline{J}(\overline{r}') \, dV'$$

Similarly the fields due to a magnetic current distribution are:

(5-11)

$$\overline{E}^h(\overline{r}) = \int_{V'} \frac{1}{j\omega\mu_0} \overline{\overline{g}}_e(\overline{r} \mid \overline{r}\,') \cdot \overline{J}(\overline{r}\,') \, dV'$$

(5-12)

$$\overline{H}^h(\overline{r}) = \int_{V'} \overline{\overline{g}}_h(\overline{r} \mid \overline{r}\,') \cdot \overline{J}(\overline{r}\,') \, dV'$$

5.3 Dyadic Green's Functions In a Rectangular Cavity

Green's functions have been derived for both electric and magnetic fields due to electric and magnetic currents by Tai [Tai 76] and Rahmat-Samii [Rahmat-Samii 75] respectively. In the following section the Green's functions of equations (5-1) and (5-6) are derived and reduced to a form that is appropriate for the analysis of disturbances induced on the walls of the cavity.

5.3.1 Green's Functions for Electric Current Sources

The starting point for the derivation is the Green's function for the magnetic vector potential [Tai 76]. For a rectangular cavity of dimensions a,b,c source points (x', y', z') and field points (x,y,z) this is:

(5-13)

$$\overline{\overline{G_A}} = \frac{1}{abc}\sum_{m,n,l=0}^{\infty} \frac{e_m e_n e_l}{K^2 + k^2}[(cc)_x(ss)_y(ss)_z\hat{x}\hat{x}' + (ss)_x(cc)_y(ss)_z\hat{y}\hat{y}' + (ss)_x(ss)_y(cc)_z\hat{z}\hat{z}']$$

where:

(5-14)

$$(cc)_x = \cos k_x x \cos k_x x' \qquad (ss)_x = \sin k_x x \sin k_x x'$$
$$(cc)_y = \cos k_y y \cos k_y y' \qquad (ss)_y = \sin k_y y \sin k_y y'$$
$$(cc)_z = \cos k_z z \cos k_z z' \qquad (ss)_z = \sin k_z z \sin k_z z'$$

and in which the wave number and propagation constants are given by:

$$k = \omega\sqrt{\mu_0\varepsilon_0} = \frac{2\pi}{\lambda}$$

$$k_x = \frac{m\pi}{a},\ k_y = \frac{n\pi}{b},\ k_z = \frac{l\pi}{c}$$

$$K^2 = k_x^2 + k_y^2 + k_z^2$$

$$e_i = \begin{cases} 1, & i = 0 \\ 2, & i \neq 0 \end{cases}$$

The electric and magnetic fields due to an electric current source can then be found from their respective Green's functions. These are derived from the magnetic vector potential using the relationships:

$$\overline{\overline{G}}_e = \left(\overline{\overline{I}} + \frac{1}{k^2}\nabla\nabla\right) \cdot \overline{\overline{G}}_A \tag{5-15}$$

$$\overline{\overline{G}}_h = \nabla \times \overline{\overline{G}}_A \tag{5-16}$$

5.3.2 Green's Functions for Magnetic Current Sources

Equation (5-17) is the Green's function for the electric vector potential [Rahmat–Samii 75]:

$$\overline{\overline{g}}_F = \frac{1}{abc}\sum_{m,n,l=0}^{\infty} \frac{e_m e_n e_l}{K^2 + k^2}[(ss)_x(cc)_y(cc)_z\hat{x}\hat{x} + (cc)_x(ss)_y(cc)_z\hat{y}\hat{y} + (cc)_x(cc)_y(ss)_z\hat{z}\hat{z}] \tag{5-17}$$

The dyadic Green's functions for the E and H field due to a magnetic current source are found from the electric vector potential using:

$$\overline{\overline{g}}_e = -\nabla \times \overline{\overline{g}}_f \tag{5-18}$$

$$\overline{\overline{g}}_h = \left(\overline{\overline{I}} + \frac{1}{k^2}\nabla\nabla\right) \cdot \overline{\overline{g}}_f \tag{5-19}$$

5.4 Four Fundamental Green's Functions

The equations to be derived in the rest of this chapter will be special cases of the Green's functions that have been defined in (5-15), (5-16), (5-18) and (5-19). These simplifications will

be based on restrictions on source and field points and on the application of boundary conditions at the walls of the enclosure.

5.4.1 Terminated Waveguide

The solution of the four basic equations is done in terms of modal expansions around a source plane (z = z') as in Figure 5.4 [Pathak 83]. This results in two sets of equations one on either side of the plane.

Figure 5.4: Source Plane

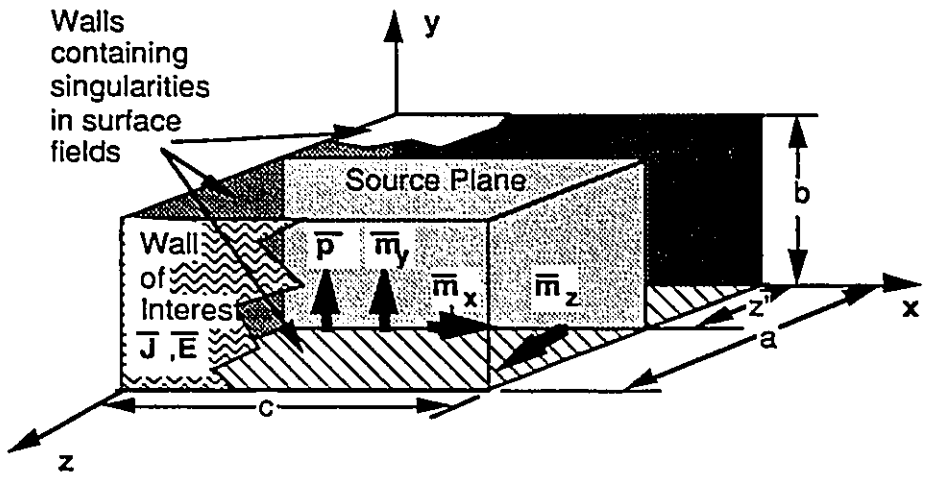

The triple summation in (5-13) and (5-17) is reduced to a double summation through the application of the trigonometric identities given in (5-20). The effect of this substitution is to reformulate the cavity problem in terms of propagation within a terminated waveguide.

To apply these identities let $k_g^2 = (k^2 - k_c^2)$ where $k_c^2 = (k_x^2 + k_y^2)$. Replace k_g with $(-i)(i)k_g$ and let $a = ik_g$.

(5-20)

$$\sum_{l=1}^{\infty} \frac{1}{k_z^2 + \alpha^2} \sin k_z z \sin k_z z' = \frac{c}{2\alpha \sinh(\alpha c)} \sinh(\alpha z_<) \sinh(\alpha(c - z_>))$$

$$\sum_{l=0}^{\infty} \frac{e_l}{k_z^2 + \alpha^2} \cos k_z z \cos k_z z' = \frac{c}{\alpha \sinh(\alpha c)} \cosh(\alpha z_<) \cosh(\alpha(c - z_>))$$

$$\sum_{l=1}^{\infty} \frac{k_z}{k_z^2 + \alpha^2} \cos k_z z_< \sin k_z z_> = \frac{c}{2\sinh(\alpha c)} \cosh(\alpha z_<) \sinh(\alpha(c - z_>))$$

$$\sum_{l=1}^{\infty} \frac{k_z}{k_z^2 + \alpha^2} \sin k_z z_< \cos k_z z_> = \frac{-c}{2\sinh(\alpha c)} \sinh(\alpha z_<) \cosh(\alpha(c - z_>))$$

5.4.2 Full Dyadic Form

Substituting (5-13) and (5-14) into (5-15) yields the dyadic Green's function for electric field generated by an electric current distribution:

(5-21)

$$\begin{aligned}
\overline{\overline{G_e}} = {} & \frac{1}{k^2}\delta(\bar{r} - \bar{r}\,') - \frac{1}{abcK^2} \sum_{m,n,l=0}^{\infty} e_m e_n e_l \times \\
& \left[\left(\frac{\bar{m}_e \bar{m}\,'_e}{k_c^2} + \frac{k_g^2 \bar{n}_o \bar{n}\,'_o}{k^2 k_c^2} \right) \left(\sin(k_z z) \sin(k_z z')\right) \right. \\
& + \frac{k_c^2}{k^2} \left(\bar{l}_o \bar{l}\,'_o\right) \left(\cos(k_z z) \cos(k_z z')\right) \\
& - \frac{k_z}{k^2} \left(\bar{l}_{o<} \bar{n}\,'_{o>}\right) \left(\cos(k_z z_<) \sin(k_z z'_>)\right) \\
& \left. - \frac{k_z}{k^2} \left(\bar{n}_{o<} \bar{l}\,'_{o>}\right) \left(\sin(k_z z_<) \cos(k_z z'_>)\right) \right]
\end{aligned}$$

where the <,> notation is defined as:

(5-22)

$$\left.\begin{aligned} z_< &= \min(z,z') \\ z_> &= \max(z,z') \end{aligned}\right\} 0 \le z,\, z' \le c$$

$$\bar{l}_{o<} = \begin{cases} \bar{l}_o \,;\, z < z' \\ \bar{l}\,'_o \,;\, z > z' \end{cases}$$

$$\bar{l}\,'_{o>} = \begin{cases} \bar{l}\,'_o \,;\, z < z' \\ \bar{l}_o \,;\, z > z' \end{cases}$$

$$\bar{n}_{o<} = \begin{cases} \bar{n}_o \,;\, z < z' \\ \bar{n}\,'_o \,;\, z > z' \end{cases}$$

$$\bar{n}\,'_{o>} = \begin{cases} \bar{n}\,'_o \,;\, z < z' \\ \bar{n}_o \,;\, z > z' \end{cases}$$

where:

$$\bar{l}_o = \phi_o \hat{z}$$
$$\bar{m}_e = \nabla_t \phi_e \times \hat{z}$$
$$\bar{n}_o = \nabla_t \phi_o$$

in which:

$$\nabla_t = \frac{\partial}{\partial x}\hat{x} + \frac{\partial}{\partial y}\hat{y}$$
$$\phi_o = \sin k_x x \, \sin k_y y$$
$$\phi_e = \cos k_x x \, \cos k_y y$$

Through substitution and algebraic manipulation it can be shown that expression (5-23) is equivalent to expression (5-21). Hence the Green's function for the electric field due to an electric dipole source is given by:

(5-23)

$$\overline{\overline{G}}_e = \frac{1}{ab}\sum_m \sum_n e_m e_n \times$$

$$\begin{bmatrix} \frac{\alpha}{k_c^2}\left(m_{ey}m'_{ey} + \frac{k_g^2}{k^2}n_{ox}n'_{ox}\right) & \frac{\alpha}{k_c^2}\left(-m_{ey}m'_{ex} + \frac{k_g^2}{k^2}n_{ox}n'_{oy}\right) & \frac{\psi}{k^2}n_{ox}l'_o \\ \frac{\alpha}{k_c^2}\left(-m_{ex}m'_{ey} + \frac{k_g^2}{k^2}n_{oy}n'_{ox}\right) & \frac{\alpha}{k_c^2}\left(m_{ex}m'_{ex} + \frac{k_g^2}{k^2}n_{oy}n'_{oy}\right) & \frac{\psi}{k^2}n_{oy}l'_o \\ \frac{\gamma}{k^2}l_o n'_{ox} & \frac{\gamma}{k^2}l_o n'_{oy} & \frac{ab}{k^2}\delta(\bar{r} - \bar{r}')\,\delta(m)\delta(n) - \frac{\beta}{k^2}k_c^2 l_o l'_o \end{bmatrix}$$

where:

(5-24)

$$\alpha = \frac{\sin k_g z_< \sin k_g(c - z_>)}{k_g \sin k_g c}$$

$$\beta = \frac{\cos k_g z_< \cos k_g(c - z_>)}{k_g \sin k_g c}$$

$$\gamma = \frac{-\cos k_g z \sin k_g(c - z')}{\sin k_g c}, \quad z < z'$$

$$= \frac{\sin k_g z' \cos k_g(c - z)}{\sin k_g c}, \quad z > z'$$

$$\psi = \frac{\sin k_g z \cos k_g(c - z')}{\sin k_g c}, \quad z < z'$$

$$= \frac{-\cos k_g z' \cos k_g(c - z)}{\sin k_g c}, \quad z > z'$$

Applying these identities to expressions (5-16), (5-18) and (5-19) provides the three remaining dyadic Green's functions.

The function for a magnetic field due to an electric current distribution is given by:

(5-25)

$$\overline{\overline{G}}_h = \frac{1}{ab}\sum_m \sum_n e_m e_n \times$$
$$\begin{bmatrix} 0 & \gamma(ss)_x(cc)_y & -k_y\beta(ss)_x(cs)_y \\ -\gamma(cc)_x(ss)_y & 0 & k_x\beta(cs)_x(ss)_y \\ -k_y\alpha(cc)_x(cs)_y & k_x\alpha(cs)_x(cc)_y & 0 \end{bmatrix}$$

The function for an electric field due to a magnetic current distribution is given by:

(5-26)

$$\overline{\overline{g}}_e = \frac{-1}{ab}\sum_m \sum_n e_m e_n \times$$
$$\begin{bmatrix} 0 & -\psi(ss)_x(cc)_y & -k_y\alpha(cc)_x(sc)_y \\ \psi(ss)_x(cc)_y & 0 & k_x\alpha(sc)_x(cc)_y \\ -k_y\beta(ss)_x(sc)_y & k_x\beta(sc)_x(ss)_y & 0 \end{bmatrix}$$

And finally the function for the magnetic field due to a magnetic current is given by.

(5-27)

$$\overline{\overline{g}}_h = \frac{1}{ab}\sum_m \sum_n e_m e_n \times$$
$$\begin{bmatrix} \frac{-\beta}{k_c^2}\left(m_{oy}m'_{oy} + \frac{k_g^2}{k^2}n_{ex}n'_{ex}\right) & \frac{\beta}{k_c^2}\left(m_{oy}m'_{ox} - \frac{k_g^2}{k^2}n_{ex}n'_{ey}\right) & \frac{\gamma}{k^2}n_{ex}l'_e \\ \frac{\beta}{k_c^2}\left(m_{ox}m'_{oy} - \frac{k_g^2}{k^2}n_{ey}n'_{ex}\right) & \frac{-\beta}{k_c^2}\left(m_{ex}m'_{ex} + \frac{k_g^2}{k^2}n_{ey}n'_{ey}\right) & \frac{\gamma}{k^2}n_{ey}l'_e \\ \frac{-\psi}{k^2}l_e n'_{ex} & \frac{-\psi}{k^2}l_e n'_{ey} & \frac{ab}{k^2}\delta(\bar{r}-\bar{r}')\delta(m)\delta(n) + \frac{\alpha}{k^2}k_c^2 l_e l'_e \end{bmatrix}$$

5.5 Green's Functions for Disturbances on the Enclosure Boundary

5.5.1 Point Sources

Sources will be represented by their three cartesian components. The electric dipole will only be applied in the orthogonal mode (i.e. perpendicular to the floor of the cavity), reflecting the boundary condition imposed by the proximity to the pcb ground plane. The fields and currents due to the three components of the magnetic dipole will be calculated separately and then summed using the principle of superposition.

It will be seen in the following derivations that each of the cartesian components reacts with the enclosure wall in a unique but predictable manner. The decomposition of the dipole moments into orthogonal components aligned with the axes of the enclosure is a key step in determining behavioral trends in the multiple source system investigated in the next two chapters.

The fields generated by these sources are given by equations (5-9),(5-10), (5-11) and (5-12) with the dipole moment given by:

(5-28)

$$\overline{p} = \begin{bmatrix} 0 \\ p \\ 0 \end{bmatrix}, \overline{m}_x = \begin{bmatrix} m_x \\ 0 \\ 0 \end{bmatrix}, \overline{m}_y = \begin{bmatrix} 0 \\ m_y \\ 0 \end{bmatrix}, \overline{m}_z = \begin{bmatrix} 0 \\ 0 \\ m_z \end{bmatrix}$$

5.5.2 Wall Points

The points of interest with respect to the field inside the cavity will be restricted to the boundaries. From the boundary conditions the magnetic and electric fields can be related to

the current density on the inner surface of the enclosure and the perpendicular electric field at the boundary respectively.

5.5.3 Normalization to Wavelength

The Green's functions are formulated in terms of the cavity dimensions and the wavelength or frequency of the source. Normalization of the cavity dimensions to the wavelength of the source increases computational efficiency and permits a broader interpretation and application of the results.

Dimensional analysis of the Green's function shows that the normalized version of equation (5-1) yields a result in terms of field-wavelength product. This must be taken into account if results are compared for the same enclosure at different frequencies.

The relationships in (5-29) allow the equations for magnetic and electric field to be normalized to wavelength.

(5-29)

$$a = \alpha \cdot \lambda$$
$$b = \beta \cdot \lambda$$
$$\kappa_x = \frac{m\,\pi}{\alpha}$$
$$\kappa_y = \frac{n\,\pi}{\beta}$$
$$\kappa = 2\,\pi$$
$$\kappa_g = \sqrt{\kappa_x^2 + \kappa_y^2 - 4\,\pi^2}$$

5.5.4 Structural Form of the Equation

The equations for disturbances due to dipole sources will be shown to have the following structural form:

(5-30)

$$\left[\begin{array}{c}\text{Ratio of}\\ \text{Constant}\\ \text{Components}\end{array}\right] \times \left[\begin{array}{c}\text{Linear}\\ \text{Function}\\ \text{of m, n}\end{array}\right] \times \left[\begin{array}{c}\text{Linear}\\ \text{Function}\\ \text{of } k_g\end{array}\right] \times \left[\begin{array}{c}\text{Ratio of}\\ \text{Trigonometric/}\\ \text{Hyperbolic}\\ \text{Functions of } k_g\end{array}\right] \times \left[\begin{array}{c}\text{Sinusoidal}\\ \text{Terms Based}\\ \text{on Geometric}\\ \text{Factors}\end{array}\right]$$

The waveguide propagation coefficient, k_g, is defined as $k_g^2 = (k^2 - k_c^2)$ where $k_c^2 = (k_x^2 + k_y^2)$. Once the indices of summation 'm' and 'n' in equations (5-23), (5-25), (5-27) and (5-28) get sufficiently large, k_c becomes greater than k and k_g becomes imaginary.

When this happens, the trigonometric ratio of sinusoids becomes a ratio of hyperbolic sines or cosines. This term shrinks exponentially. This effect will be examined in greater detail in Section 5.9. For source frequencies below the first resonant frequency of the cavity all of the terms will be hyperbolic. For higher frequencies a finite number of standing wave modes will exist.

This structure is shared by all of the source-boundary equations that follow and will allow the identification of some basic properties of these equations that will be of use in developing engineering guidelines.

5.6 Effect of Dipole Sources on Adjacent Wall

The equations explicitly developed in this section are for electric field and current disturbances on the wall of the cavity due to each of the electric and magnetic dipole sources positioned on the floor. This is shown in Figure 5.1 and Figure 5.4. Typically this is the surface of greatest interest in the EMI problem since it often contains the connectors and apertures that make up the primary leakage paths.

5.6.1 Case 1: E-Field on Wall Due to Orthogonal Electric Dipole Source

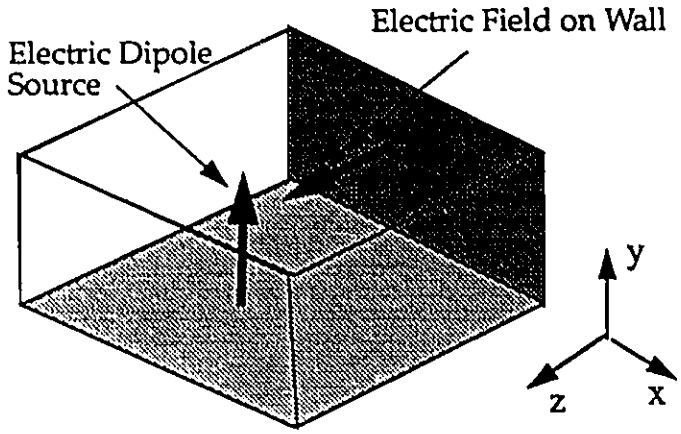

Equations (5-9), (5-21) and (5-23) combine to provide the equation for the normal electric field on the wall:

(5-31)

$$\overline{E}^{p} = \frac{p}{ab}\sum_{m}\sum_{n} e_m e_n \left\{ \frac{\alpha}{k_c^2}\left(-m_{cy}m'_{cx} + \frac{k_g^2}{k^2}n_{ox}n'_{oy}\right) + \frac{\alpha}{k_c^2}\left(m_{ex}m'_{cx} + \frac{k_g^2}{k^2}n_{oy}n'_{oy}\right) + \frac{\gamma}{k^2}l_o n'_{oy} \right\} \hat{z}$$

By observation it is evident that only the 'z' component of the electric field will exist. When the boundary conditions of the source are taken into account (5-31) simplifies to:

(5-32)

$$\overline{E}^{p} = \frac{p}{ab} \sum_{m} \sum_{n} e_m e_n \frac{\gamma}{k^2} I_0 n' \hat{z}$$

Applying the identities of (5-23) yields:

(5-33)

$$\overline{E}^{p} = \frac{p}{ab} \sum_{m} \sum_{n} e_m e_n \frac{k_y}{k^2} \left(\frac{\sin(k_g z') \cos(c-z)}{\sin(k_g c)} \right) \sin(k_x x) \sin(k_y y) \sin(k_x x') \cos(k_y y') \hat{z}$$

Restricting the solution to the cavity wall (i.e. z = c):

(5-34)

$$\overline{E}^{p} = \frac{p}{ab} \sum_{m} \sum_{n} e_m e_n \frac{k_y}{k^2} \left(\frac{\sin(k_g z')}{\sin(k_g c)} \right) \sin(k_x x) \sin(k_y y) \sin(k_x x') \hat{z}$$

Note that if y' in equation (5-33) were not equal to zero, (i.e. the dipole were elevated from the lower wall of the cavity), the term $\cos(k_y y')$ would be less than 1, resulting in a reduction in the magnitude of the electric field. For small displacements the change would not be significant.

Normalizing the cavity dimensions to wavelength as per Section 5.5.3 yields:

(5-35)

$$\overline{E}^{p} \cdot \lambda = \frac{p}{\alpha\beta} \sum_{m} \sum_{n} e_m e_n \frac{\kappa_y}{\kappa^2} \left(\frac{\sin(k_g z')}{\sin(k_g c)} \right) \sin(k_x x) \sin(k_y y) \sin(k_x x') \hat{z}$$

5.6.2 Case 2: Current on Wall Due to Orthogonal Electric Dipole Source

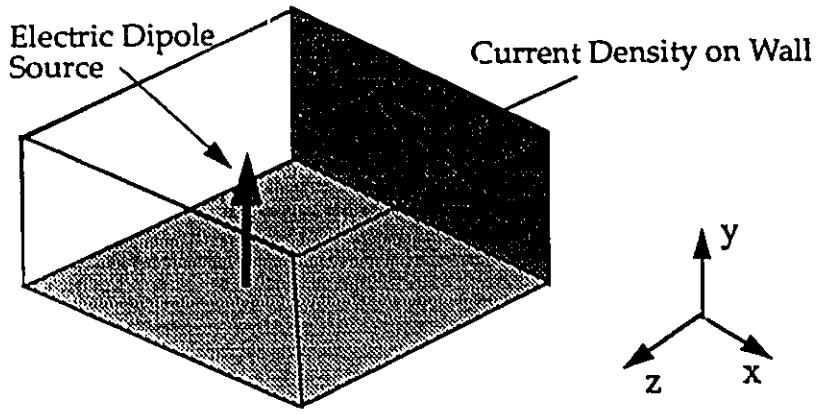

Due to the assumption of perfectly conducting boundaries, the surface current J_s on the wall is given by the relationship:

(5-36)

$$\bar{J} = \hat{n} \times \bar{H}$$

where H represents the magnetic field at the boundary. For the surface being examined:

(5-37)

$$\hat{n} = -\hat{z}$$

Therefore H_y yields J_x and H_x yields $-J_y$ where H_y is the component of the magnetic field in the 'y' direction. Hence, equations (5-10), (5-25) and (5-22) combine to provide the equation for the current on the wall (J):

(5-38)

$$\bar{J} = \frac{-p}{j\omega\mu_0 ab} \sum_m \sum_n e_m e_n (\gamma (ss)_x (cc)_y) \hat{y}$$

Applying (5-24) yields:

(5-39)

$$\bar{J} = \frac{-p}{j\omega\mu_0 ab}\sum_m \sum_n e_m e_n \left(\left(\frac{\sin(k_g z') \cos(k_g(c-z))}{\sin(k_g c)} \right) \sin(k_x x) \sin(k_x x') \cos(k_y y) \cos(k_y y') \right) \hat{y}$$

Restricting the solution domain to the wall finally yields:

(5-40)

$$\bar{J} = \frac{-p}{j\omega\mu_0 ab}\sum_m \sum_n e_m e_n \left(\left(\frac{\sin(k_g z')}{\sin(k_g c)} \right) \sin(k_x x) \sin(k_x x') \cos(k_y y) \right) \hat{y}$$

Normalizing the right hand side of (5-40) with respect to wavelength yields:

(5-41)

$$\bar{J} \cdot \lambda = \frac{-p}{j2\pi c\mu_0 \alpha\beta}\sum_m \sum_n e_m e_n \left(\left(\frac{\sin(k_g z')}{\sin(k_g c)} \right) \sin(k_x x) \sin(k_x x') \cos(k_y y) \right) \hat{y}$$

where 'c' in the constant ratio before the double summation is the speed of light and should not be confused with the dimension 'c' in the trigonometric term $\sin(k_g c)$.

This shows that the current on the wall is only induced in a direction parallel to the electric dipole source polarization, regardless of position on the wall or the elevation of the source. Time harmonic fluctuations of the current are 90° out of phase with the source. It is also clear from this equation that the phase of the wall current is unrelated to the physical position of the source in the cavity. This is of major significance in the application of the mapping matrix in the next chapter.

If the source were not on the floor of the cavity but slightly above it, then the last cosine term in (5-39) would remain. The magnitude of $\bar{J}$ will decline slowly in response to raising the source a small distance from the floor.

5.6.3 Case 3: E-Field on Wall Due to Magnetic Dipole Source

There are three possible orientations of the magnetic dipole source. In practice the horizontal component of the magnetic dipole moment of an IC due to current through the pins and down to the pcb, will be arbitrarily oriented relative to the 'x' and 'z' axes. The ' y' oriented dipole moment is due to currents circulating in the plane of the IC die and demonstrates significantly different behavior which is described in 5.6.3.c.

As discussed in Chapter 4, there will be some cases in which a source will have a predominant moment orientation in others it may change with system functionality. In a freespace regime, rotation of the moment around a vertical axis would result in a symmetric rotation of the field structure. This is not the case for the cavity problem due to the interaction with the walls. The differences and similarities in behavior between the two coplanar components will be evident in the following derivations of sub-sections 5.6.3.a and 5.6.3.b.The Green's dyadic that is applicable for this section is given in equation (5-26).

5.6.3.a E-Field on Wall Due to Magnetic Dipole Parallel to Wall

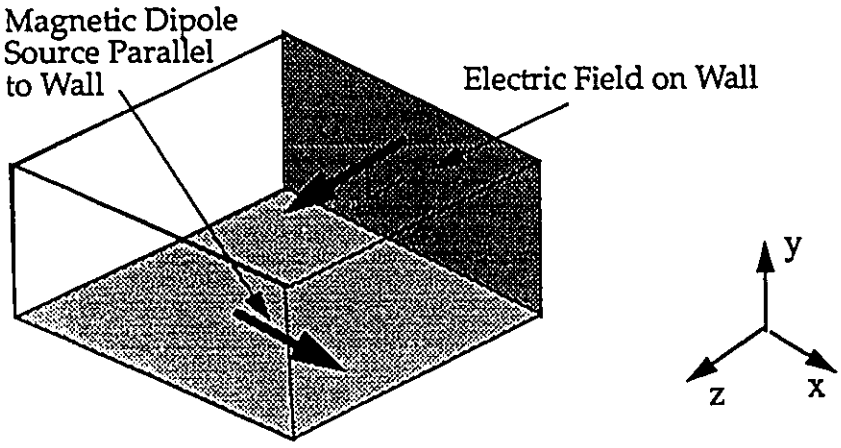

For this configuration the source current density due to the magnetic dipole has only an 'x' component as shown in Figure 5.4. Applying (5-26) and (5-14) to equation (5-11) yields:

(5-42)

$$\overline{\mathbf{E}}^{m_x} = \frac{-m_x}{j\omega\mu_o ab}\sum_m\sum_n e_m e_n\left[(-\psi(ss)_x(cc)_y)\,\hat{y} + (k_y\beta(ss)_x(sc)_y)\,\hat{z}\right]$$

Applying the source boundary conditions leads to:

(5-43)

$$\overline{\mathbf{E}}^{m_x} = \frac{-m_x}{j\omega\mu_o ab}\sum_m\sum_n e_m e_n\left(k_y\beta(ss)_x(sc)_y\right)\hat{z}$$

which expands to:

(5-44)

$$\overline{\mathbf{E}}^{m_x} = \frac{-m_x}{j\omega\mu_o ab}\sum_m\sum_n e_m e_n\left[\frac{k_y\cos(k_g z_<)\cos(k_g(c - z_>))}{k_g \quad \sin(k_g d)}\right] \cdot\sin(k_x x)\sin(k_x x')\sin(k_y y)\cos(k_y y')\,\hat{z}$$

Applying the geometric conditions z = c and y' = 0 derived from the ideal model gives the final equation:

(5-45)

$$\overline{\mathbf{E}}^{m_x} = \frac{-m_x}{j\omega\mu_o ab}\sum_m\sum_n e_m e_n\left[\frac{k_y\cos(k_g z')}{k_g\sin(k_g c)}\right]\sin(k_x x)\sin(k_x x')\sin(k_y y)\,\hat{z}$$

Normalizing the right hand side yields:

(5-46)

$$\overline{\mathbf{E}}^{m_x}\lambda = \frac{-m_x}{j\,2\pi c\mu_o\alpha\beta}\sum_m\sum_n e_m e_n\left[\frac{\kappa_y\cos(k_g z')}{\kappa_g\sin(k_g c)}\right]\sin(k_x x)\sin(k_x x')\sin(k_y y)\,\hat{z}$$

5.6.3.b E-Field on Wall Due to Magnetic Dipole Perpendicular to Wall,

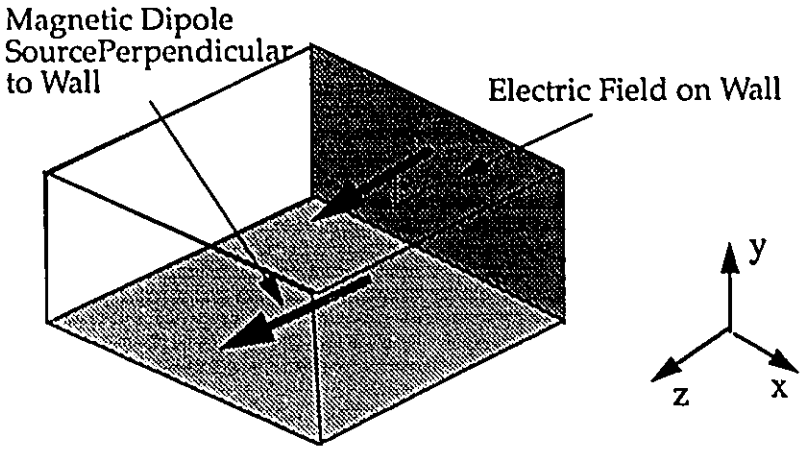

For this orientation the magnetic dipole has only a 'z' component. From the boundary conditions on the perfectly conducting wall and the Green's dyadic given in equation (5-26) , it is evident that no electric field is induced on the wall by the component of the magnetic dipole that is perpendicular to that wall regardless of where the source is located in the x-z plane. If the wall were not a perfect conductor then the source would tend to induce a electric field component in the plane of the wall.

5.6.3.c E-Field on Wall Due to Magnetic Dipole Orthogonal to Cavity Floor

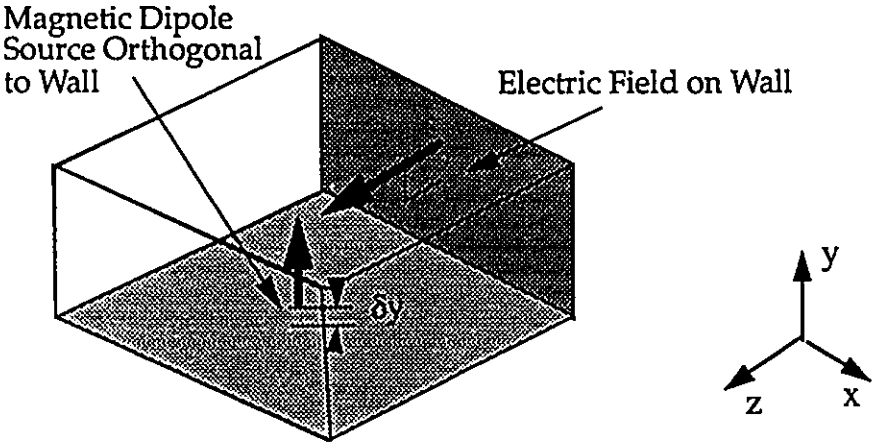

This component of the magnetic dipole source corresponds to the net circulation of current within the silicon die of the IC or in the leadframe of the IC package. As such it is typically located a small distance (y' = δy) from the ground reference at the bottom of the cavity.

In this orientation only a 'y' component of the current density exists. Reapplication of equations (5-14), (5-26) and (5-11) leads to the normalized equation:

(5-47)

$$\overline{E}^{m_y}\lambda = \frac{-m_y}{j\,2\pi c\mu_o\alpha\beta}\sum_m\sum_n e_m e_n\left[\frac{\kappa_x\cos(k_g z')}{\kappa_g\,\sin(k_g c)}\right]\sin(k_x x)\cos(k_x x')\sin(k_y y)\sin(k_y \delta y)\,\hat{z}$$

The magnitude of the electric field given by equation (5-47) is quite sensitive to small displacements of the source in the 'y' direction due to the final sinusoidal term. For small values of $k_y\delta y$ this is a linear relationship.

5.6.4 Case 4: Currents on Wall Due to Magnetic Dipole Source

There are three orientations of the magnetic dipole. Each of these induces in-phase current on the wall in both the 'x' and 'y' directions. The tangential magnetic field induced at the wall is calculated using the Green's function given in (5-9). Applying the relationships between surface current and magnetic field given in equations (5-36) and (5-37) yields the relationships for induced surface current detailed in the following sub-sections.

5.6.4.a Current on Wall Due to Magnetic Dipole Parallel to Wall

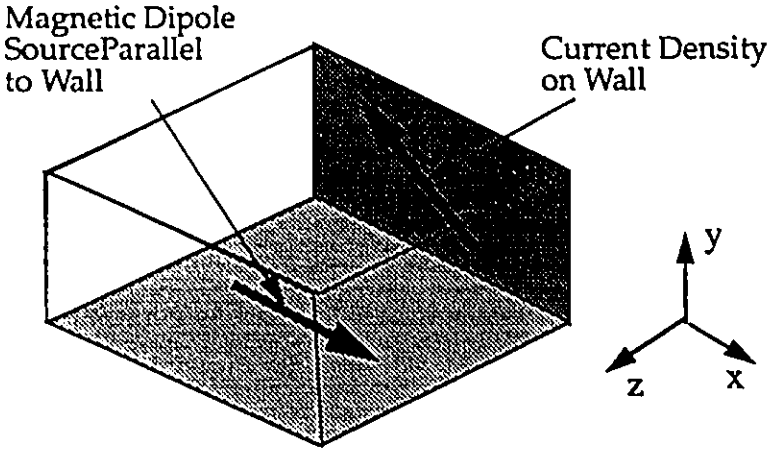

The current induced on the cavity wall by a magnetic dipole parallel to that wall is given by:

(5-48)

$$\bar{J}^{m_x} = \frac{-m_x}{ab}\sum_m \sum_n e_m e_n \left[\left(\frac{k_g}{k_c^2\, k^2}\right)\frac{\cos(k_g z')}{\sin(k_g c)}\right] \times$$
$$\{[k_x k_y \cos(k_x x)\sin(k_y y)\sin(k_x x')]\,\hat{x}$$
$$-[k_x^2 \sin(k_x x)\cos(k_y y)\sin(k_x x')]\,\hat{y}\}$$

From this equation it is clear that there is no current flow at the corners of the wall and the current flow at the edges is perpendicular to those edges. The relative sensitivity of the 'x' and 'y' components of the current to the 'x' position of the source is inversely proportional to the 'x-y' aspect ratio due to the k_x and k_y terms in the vector portion of (5-48)

The normalized version of (5-48) is:

(5-49)

$$\bar{J}^{m_x}\lambda = \frac{-m_x}{\alpha\beta}\sum_m \sum_n e_m e_n \left[\left(\frac{\kappa_g}{\kappa_c^2\kappa^2}\right)\frac{\cos(k_g z')}{\sin(k_g c)}\right] \times$$
$$\{[\kappa_x \kappa_y \cos(k_x x)\sin(k_y y)\sin(k_x x')]\,\hat{x}$$
$$-[\kappa_x^2 \sin(k_x x)\cos(k_y y)\sin(k_x x')]\,\hat{y}\}$$

5.6.4.b Current on Wall Due to Magnetic Dipole Perpendicular to Wall

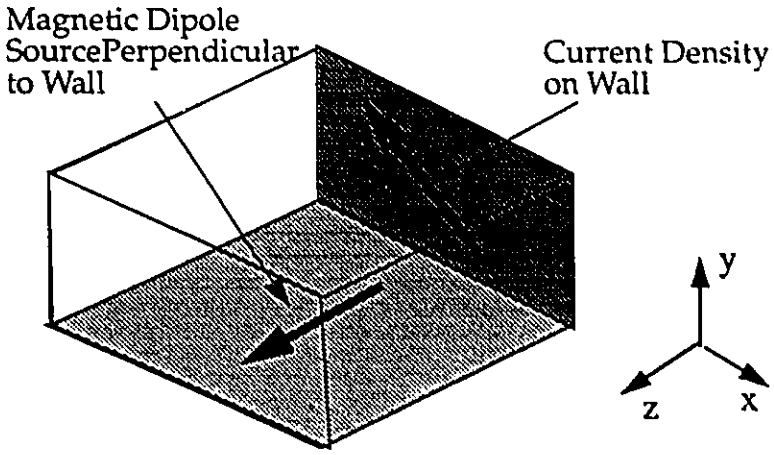

The current induced on the cavity wall by a magnetic dipole perpendicular to that wall is given by:

(5-50)

$$\bar{J}^{m_z} = \frac{-m_z}{ab}\sum_m\sum_n e_m e_n \left[\left(\frac{1}{k^2}\right)\frac{\sin(k_g z')}{\sin(k_g c)}\right]\times$$
$$\{[-k_y \cos(k_x x)\sin(k_y y)\cos(k_x x')]\,\hat{x}$$
$$+[k_x \sin(k_x x)\cos(k_y y)\cos(k_x x')]\,\hat{y}\}$$

Equation (5-50) is similar in structure to (5-48) but has some significant differences relative to the z' and x' coordinates since the roles of sine and cosine are reversed.

The normalized version of equation(5-50) is:

(5-51)

$$\bar{J}^{m_z}\cdot\lambda = \frac{-m_z}{\alpha\beta}\sum_m\sum_n e_m e_n \left[\left(\frac{1}{4\pi^2}\right)\frac{\sin(k_g z')}{\sin(k_g c)}\right]\times$$
$$\{[-\kappa_y \cos(k_x x)\sin(k_y y)\cos(k_x x')]\,\hat{x}$$
$$+[\kappa_x \sin(k_x x)\cos(k_y y)\cos(k_x x')]\,\hat{y}\}$$

5.6.4.c Current on Wall Due to Magnetic Dipole Orthogonal to Cavity Floor

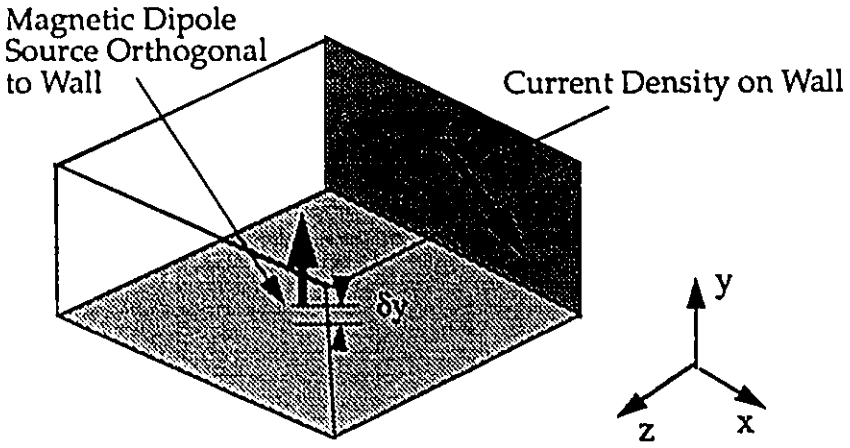

Following the derivation of the previous sections, equations (5-9) and (5-36) lead to the following expression:

(5-52)

$$\bar{J}^{m_y} = \frac{-m_y}{ab}\sum_m \sum_n e_m e_n \left[\frac{1}{k_c^2 k_g}\frac{\cos(k_g z')}{\sin(k_g c)}\right]\times$$
$$\left\{k_y^2\left[\cos(k_x x)\sin(k_y y)\cos(k_x x')\sin(k_y \delta y) + \frac{k_g^2}{k^2}\cos(k_x x)\sin(k_y y)\cos(k_x x')\sin(k_y \delta y)\right]\hat{x}\right.$$
$$\left. + k_x k_y\left[\cos(k_x x)\sin(k_y y)\sin(k_x x')\cos(k_y \delta y) + \frac{k_g^2}{k^2}\sin(k_x x)\cos(k_y y)\cos(k_x x')\sin(k_y \delta y)\right]\hat{y}\right.$$

Note that, if $\delta y = 0$ (i.e. the source is on the floor of the cavity), only the first term of the 'y' component is non-zero. On the other hand, the second term of both the 'x' and the 'y' component start to have an influence proportional to $k_y \delta y$ and the ratio k_g^2/k^2 as the source is raised from the floor of the cavity.This is particularly important since k_g^2/k^2 can become quite large. This effect will be mitigated by the convergence of the hyperbolic terms, the rate of convergence of which will be determined by the relative magnitude of the distance between the source and the wall given by the dimensions z' and c.

The normalized form of (5-52) is:

(5-53)

$$\bar{J}^{m_y} \cdot \lambda = \frac{-m_y}{\alpha\beta} \sum_m \sum_n e_m e_n \left[\frac{1}{\kappa_c^2 \kappa_g} \frac{\cos(k_g z')}{\sin(k_g c)} \right] \times$$
$$\left\{ \kappa_y^2 \left[\cos(k_x x) \sin(k_y y) \cos(k_x x') \sin(k_y \delta y) + \frac{\kappa_g^2}{\kappa^2} \cos(k_x x) \sin(k_y y) \cos(k_x x') \sin(k_y \delta y) \right] \hat{x} \right.$$
$$\left. + \kappa_x \kappa_y \left[\cos(k_x x) \sin(k_y y) \sin(k_x x') \cos(k_y \delta y) + \frac{\kappa_g^2}{\kappa^2} \sin(k_x x) \cos(k_y y) \cos(k_x x') \sin(k_y \delta y) \right] \hat{y} \right\}$$

5.7 Effect of Sources on Upper Cavity Surface

The derivation of equations for the upper cavity surface proceeds in the same manner as those for the wall in Section 5.6. The only significant difference is that the orientation of the terminated waveguide formulation changes. The relevant coordinate system is provided in Figure 5.5.

Figure 5.5: Enclosure Model for Upper Cavity Surface.

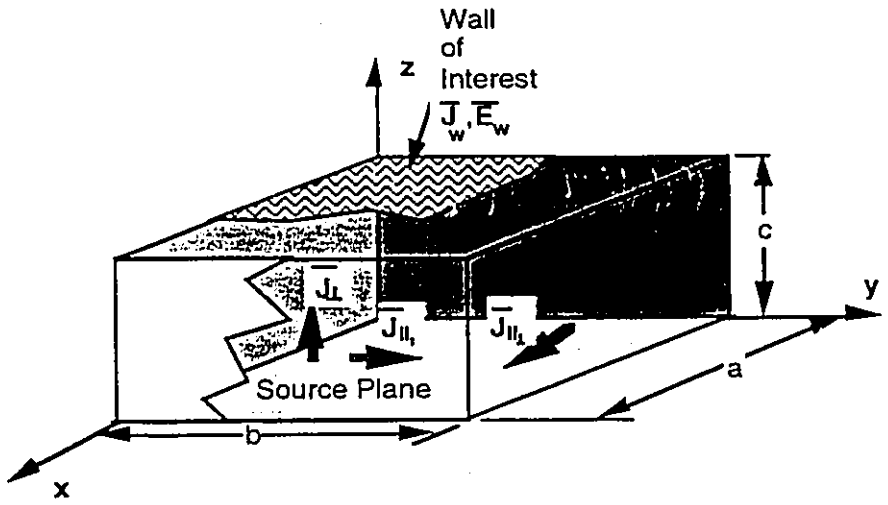

5.8 Plots of Equations

Each of the equations in Section 5.6 can be plotted to show the distribution of electric field or current density on the wall of the enclosure. The following plots are of the 'x' component of equation (5-50), the current density on the wall due to a magnetic dipole perpendicular to the wall. The case under study is the cavity shown in Figure 5.6. The current density profile on the enclosure wall due to a single source point is calculated for three source points and four frequencies. The three source points are chosen to accentuate differences in behavior due to location. The first two frequencies, 100 MHz and 800 MHz, are below the resonant frequency of the cavity. The third frequency, 1400 MHz, is above the resonant frequency in the longitudinal dimension of the cavity but below that due to the height. The fourth frequency, 2500 MHz, is above the first resonant frequency in each dimension.

Figure 5.6: Enclosure Dimensions and Source Location

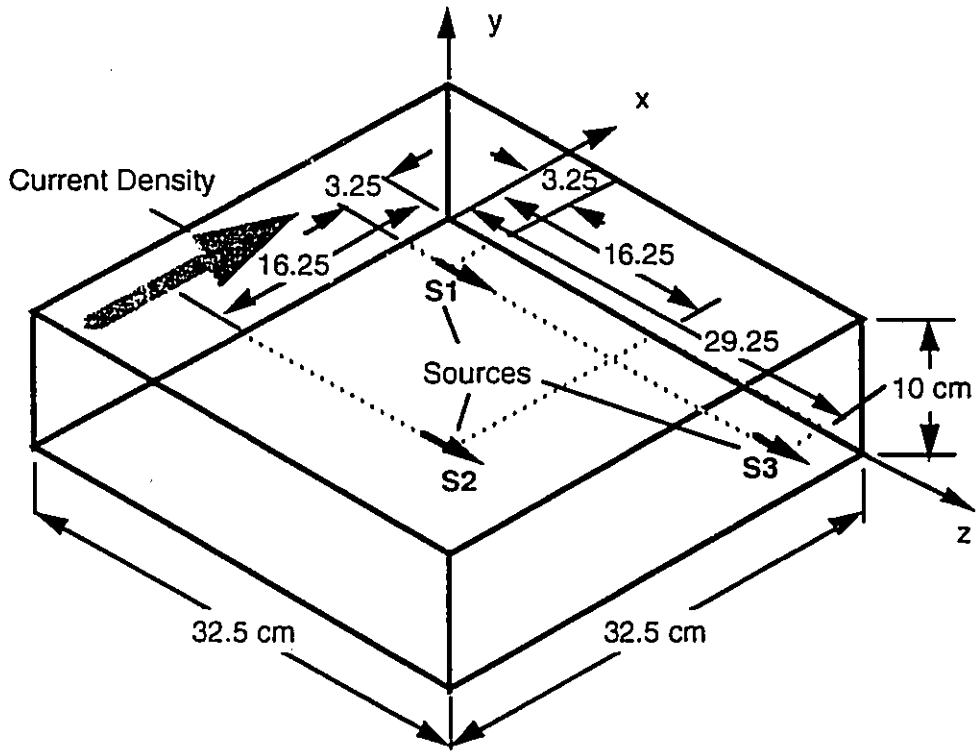

Figure 5.7: Current on Wall, Source Point #2, 100 MHz

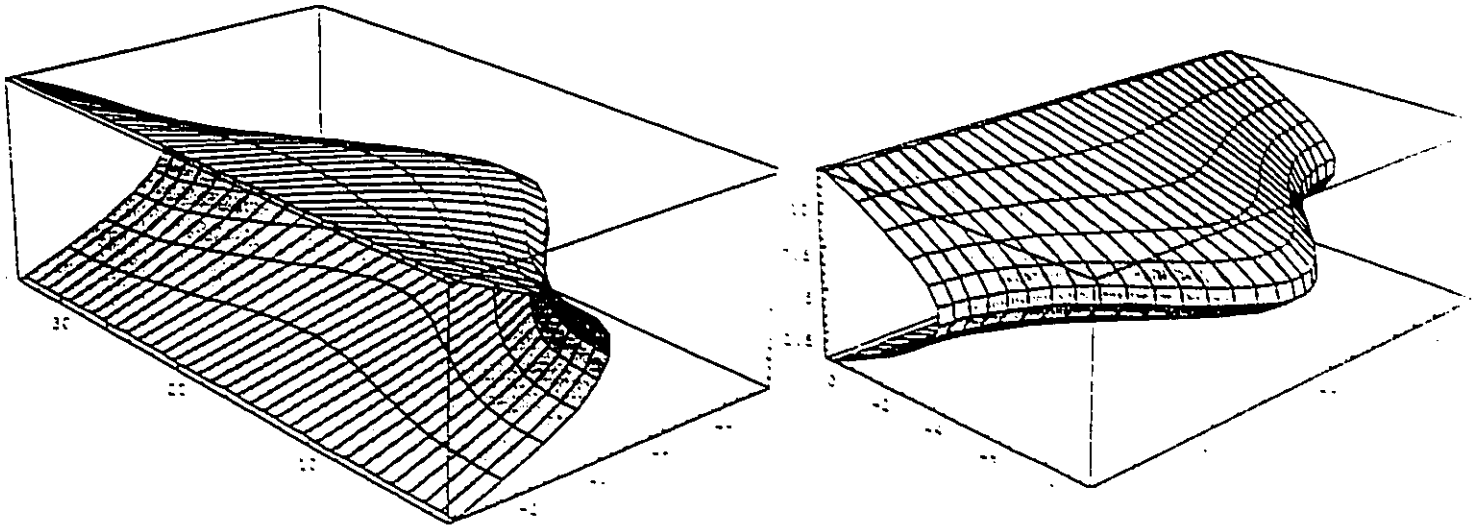

Figure 5.8: Current on Wall, Source Point #3, 100 MHz

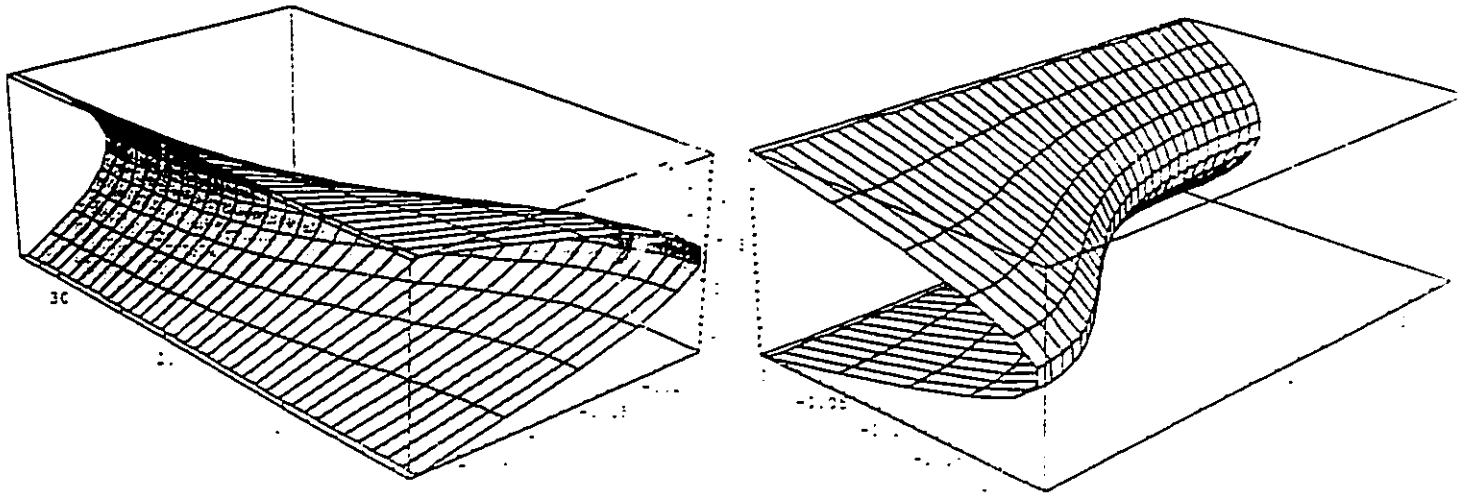

Figure 5.9: Current on Wall, Source # 2, 800 MHz

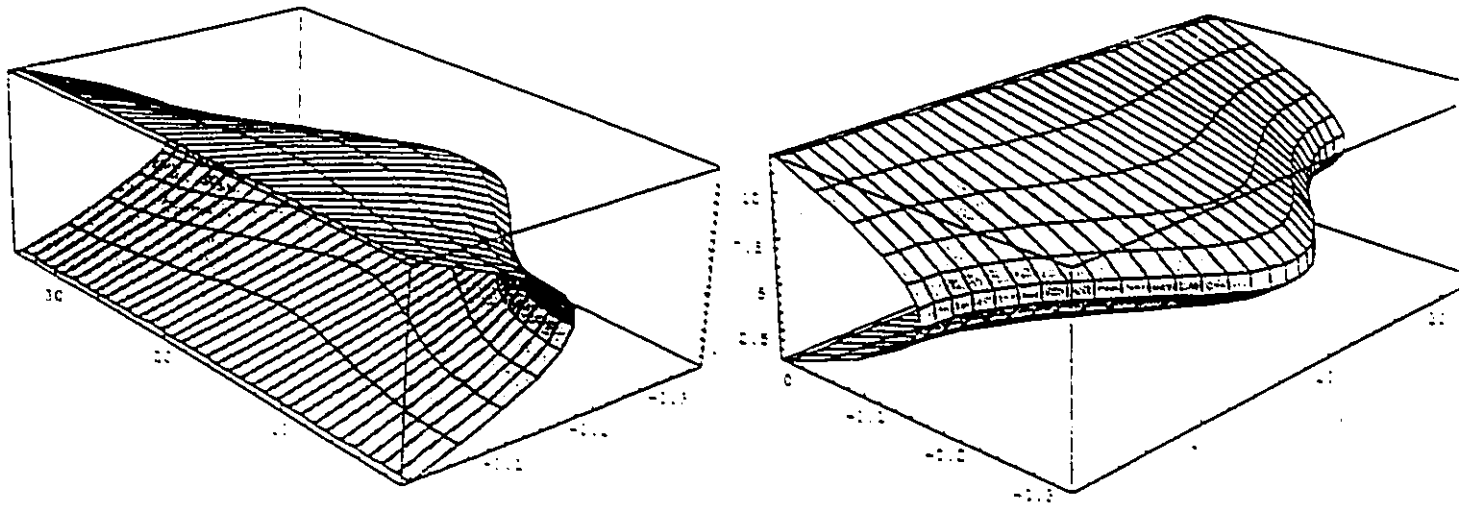

Figure 5.10: Current on Wall, Source # 1, 800 MHz

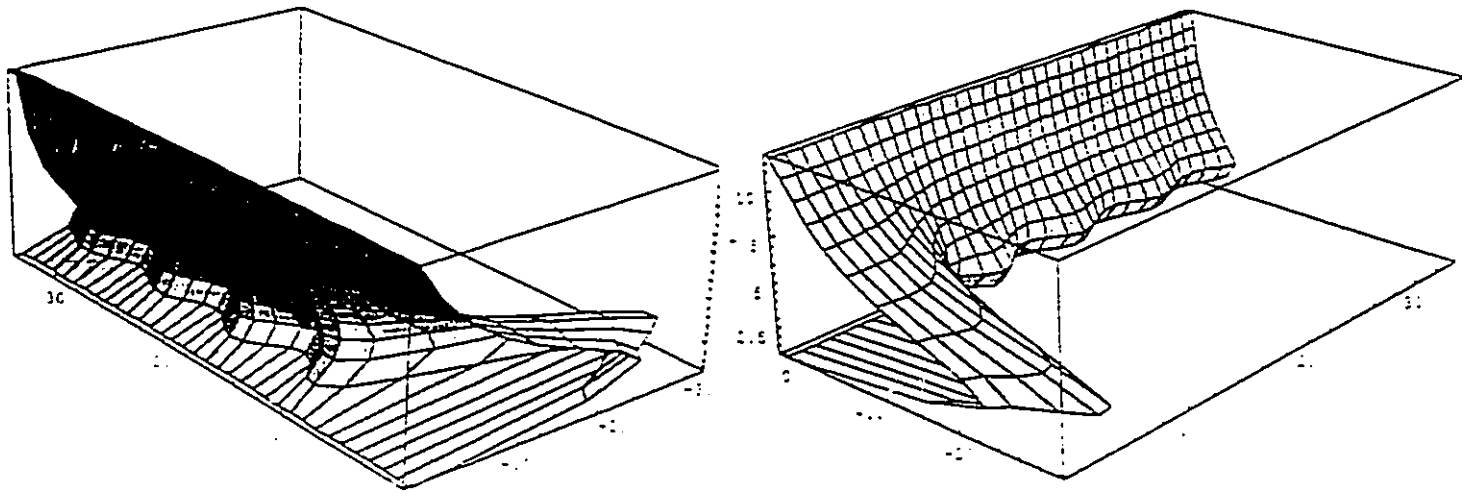

Figure 5.11: Current on Wall, Source # 2, 1400 MHz

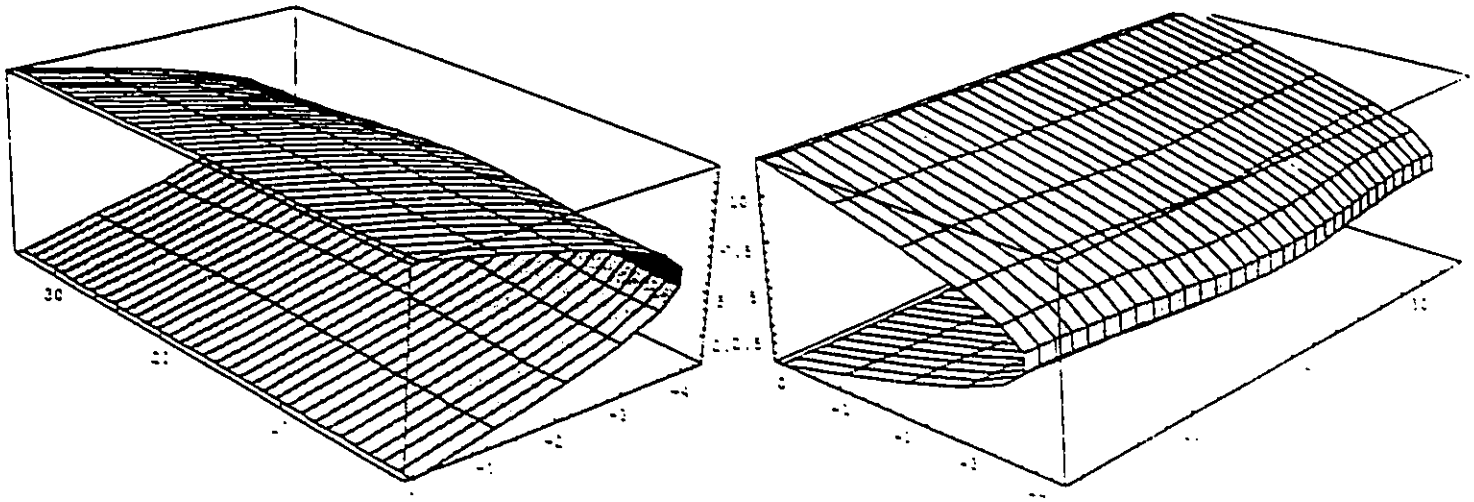

Figure 5.12: Current on Wall, Source # 3, 1400 MHz

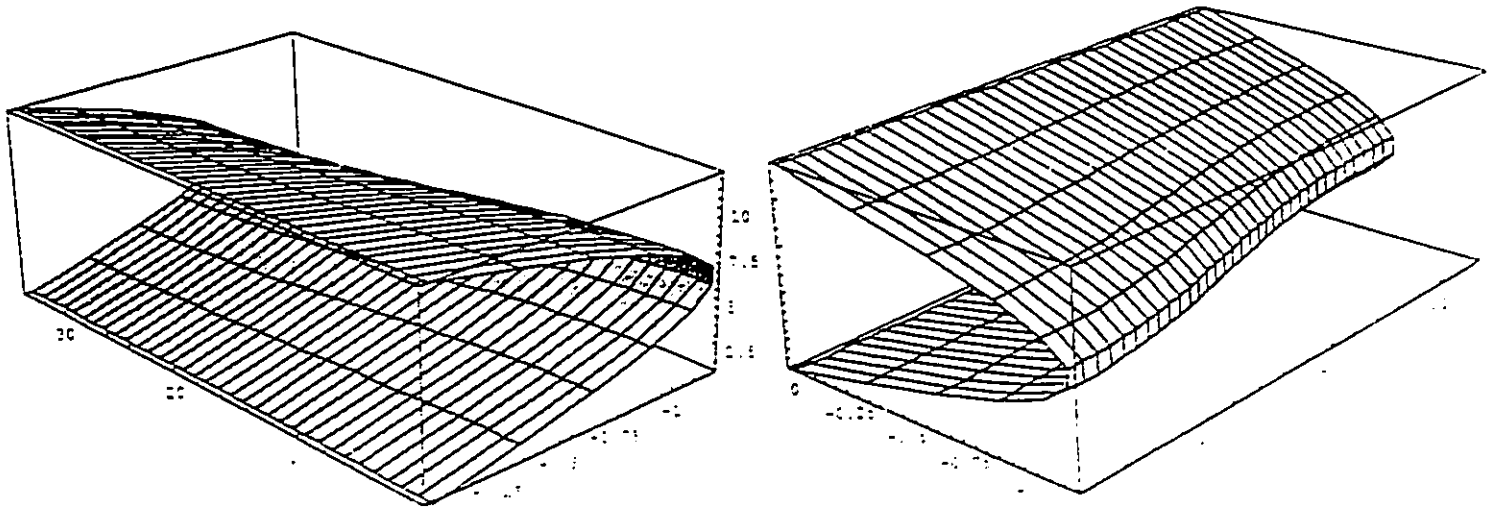

Figure 5.13: Current on Wall, Source # 2, 2500 MHz

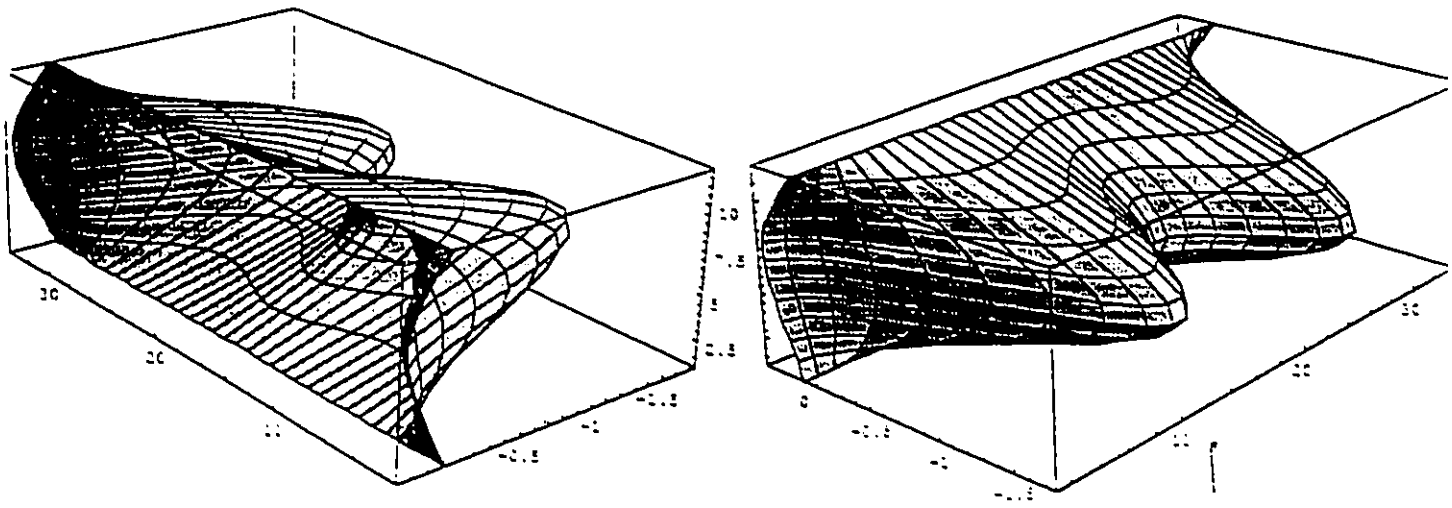

Figure 5.14: Current on Wall, Source # 1, 2500 MHz

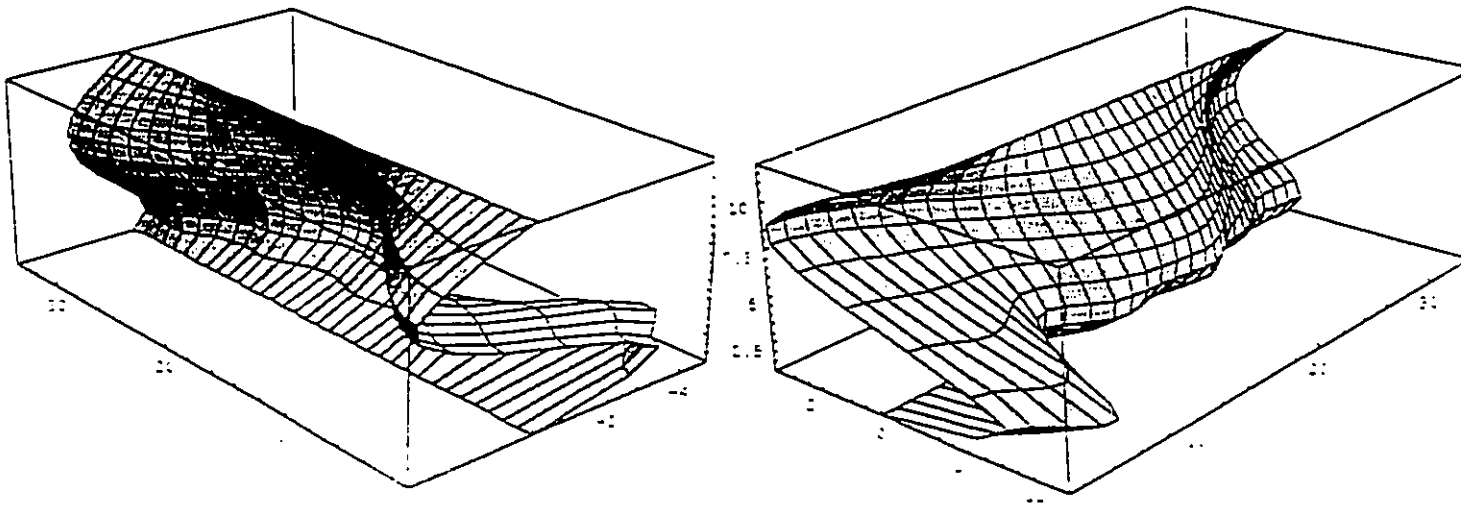

Figure 5.15: Current on Wall, Source #3, 2500 MHz

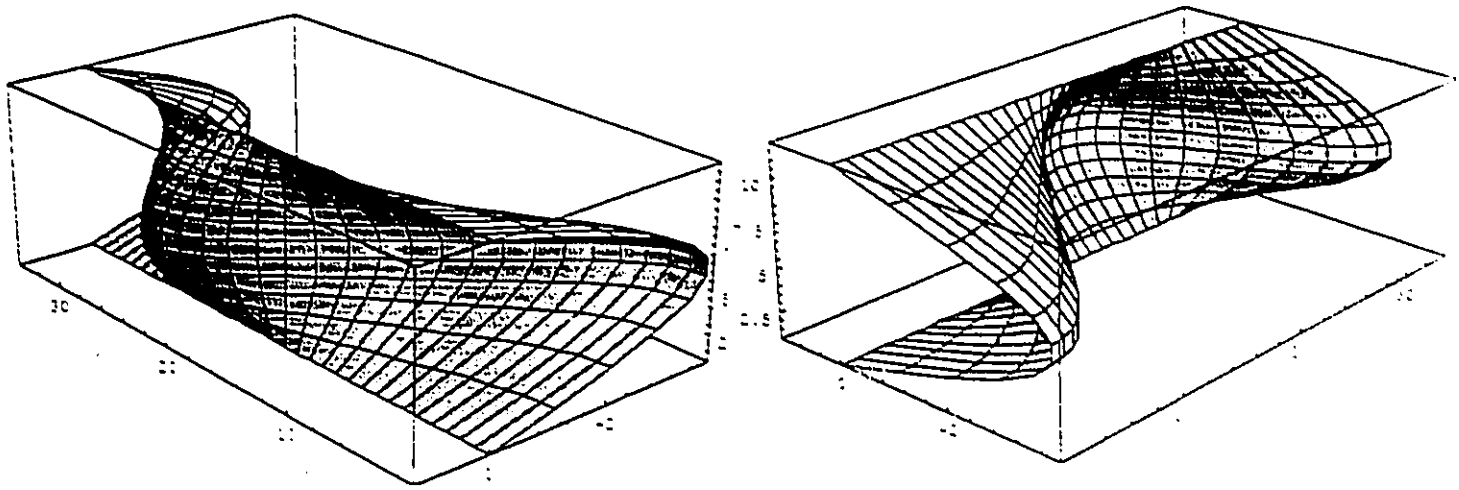

The plots above clearly show trends in current distribution and magnitude with changes in frequency and location. This is a significant advantage of addressing the mapping problem on a vector component basis. The symmetry or asymmetry of the distribution is determined mostly by the trigonometric terms in 'x' and 'y' as can be seen from equation (5-50). The relative amplitudes are harder to see by inspection and are primarily due to the rate of conversion of the hyperbolic functions of 'z'. This topic will be treated in greater detail in the next chapter.

5.9 Convergence of the Equations

The convergence of the equations in Section 5.6 is dependent on three principle factors:

- the choice of axes;
- the ratio of source wavelength to cavity dimension; and

- the proximity of the source to the cavity wall.

5.9.1 Selection of Axes to Avoid Convergence Difficulties

It has already been noted that equation (5-21) introduces a source plane that contains the source vector and is perpendicular to the 'z' axis as was shown in Figure 5.4.

This source plane introduces a singularity plane into the Green's function formulation. Dealing with singularities in the source region of a Green's function is a topic that has been investigated by numerous authors [Yaghjian 80], [Lee 80], [Tai 81], [Wang 82].

In the case of the rectangular waveguide, Rahmat-Samii shows that computation of the dyadic Green's function in the source plane requires the addition of a Dirac delta distribution to offset the singularity [Rahmat-Samii 75]. Although this singularity strictly holds in the source plane only, it is also reflected in a slow convergence in the neighbourhood of the source plane. This effect is clearly demonstrated in Figure 5.16 where, after 100 iterations,

Figure 5.16: Effect of Source Plane Intersecting Wall of Interest.

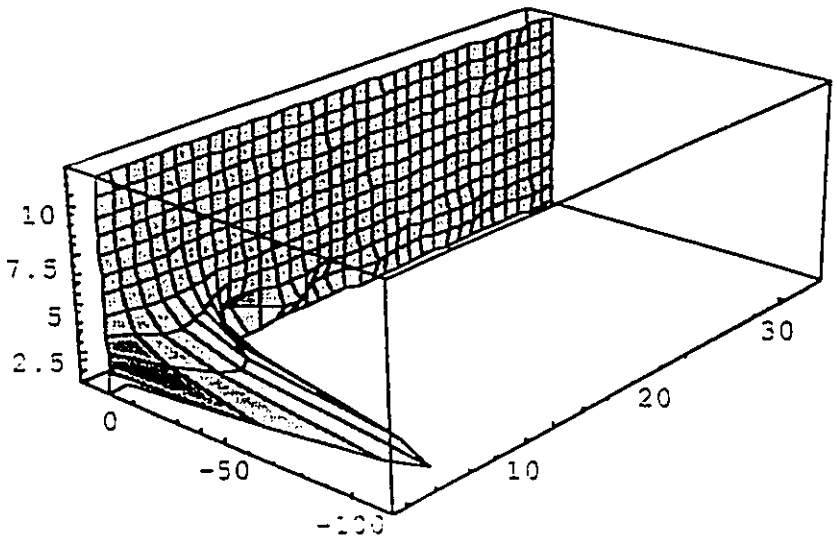

the singularity induced by the source plane is still the dominant factor across 10% of the surface area.

In Section 5.9.2 it is shown that, for most circumstances, the convergence is complete relative to the factors of wavelength and wall proximity at substantially less than 100 iterations. For this reason the axes were chosen so as not to include the source plane in the wall of interest. This is accomplished through the selection of the appropriate terms of equations (5-23) and (5-27).

5.9.2 Wavelength and Proximity

The equations in Section 5.6 contain double infinite summations. These equations can be seen to converge from the ratio of hyperbolic functions shown in equation (5-30). The rate of convergence will depend on the hyperbolic and the linear terms in k_g.

Each of the equations contains a ratio of sinusoidal terms which are a function of the propagation constant k_g. This propagation term becomes imaginary for sufficiently large modal values m and n resulting in a ratio of hyperbolic sines and cosines. The argument in the numerator is ($k_g z'$) and the argument in the denominator is ($k_g c$) where c is the dimension of the cavity in the 'z' direction. Since c is greater than z' by definition, this part of the equation will converge exponentially as shown in the following:

(5-54)

$$\frac{\cosh k_g z'}{\sinh k_g c} = \frac{e^{jk_g z'} + e^{-jk_g z'}}{e^{jk_g c} - e^{-k_g c}}$$
$$\approx \frac{e^{k_g z'}}{e^{jk_g c}} = e^{-k_g (c - z')}$$

the rate of convergence is governed by the modal propagation constant k_g and the separation distance between the source and the wall (c - z'). The term k_g is given by:

(5-55)

$$k_g = \sqrt{\left(\frac{n\pi}{a}\right)^2 + \left(\frac{m\pi}{b}\right)^2 - \left(\frac{2\pi}{\lambda}\right)^2}$$

If 'a' is significantly larger than 'b' (Figure 5.4) then k_g can be approximated for convergence analysis as:

(5-56)

$$k'_g = \sqrt{\left(\frac{p\pi}{\alpha}\right)^2 - \left(\frac{2\pi}{\lambda}\right)^2}$$

where α is the approximate representation of the linear dimension 'a'.

If 'a' is approximately the same as 'b' then the summation will be over a combination of the two indices m and n. This would be a useful analysis if it were necessary to optimize the running time of the algorithm. For the purposes of this analysis the form of equation (5-56) will be used.

The package dimension α is normalized to the source wavelength λ using the relationship $\alpha = \phi\lambda$. This provides an approximate, normalized propagation constant:

(5-57)

$$k_\phi = \frac{1}{\phi\lambda}\sqrt{(p\pi)^2 - (2\pi\phi)^2}$$

The second factor that influences the rate of convergence is the separation distance between the source and the enclosure wall. Assuming that the dimension 'c' is roughly the same as 'a' then:

(5-58)

$$(c - z') = c\left(1 - \frac{z'}{c}\right) = \phi\lambda(1 - \gamma)$$

If 'c' and 'a' are significantly different then a scaling factor would be required. The impact of an additional linear scaling factor in (5-54) may be inferred from the curves in Figure 5.17 through Figure 5.22.

Substituting (5-57) and (5-58) into (5-54) yields the amplitude convergence factor:

(5-59)

$$A = e^{-\pi\sqrt{p^2 - 4\phi^2}(1 - \gamma)}$$

in terms of the wavelength and wall proximity.

This factor is plotted below in order to show the sensitivity of the number of steps to convergence (p) to the normalized dimensional parameter (ϕ) and the spacing ratio (γ). Note that for ϕ sufficiently large relative to p the system does not converge but rather oscillates. This is indicative of a mode that is above the resonant frequency, the k_g terms are real and the ratio is trigonometric rather than hyperbolic. Eventually the value of p will become sufficiently large that the trigonometric ratio will become hyperbolic and the sum will start to converge

The following three figures show the number of modes p required to converge for $\phi = 0.1$, 1.0 and 10.0. The three lines on each figure are for the source separation ratios $z'/c = \gamma$ of 0.95, 0.75 and 0.5.

Figure 5.17: Rate of Convergence For $\phi = 0.1$

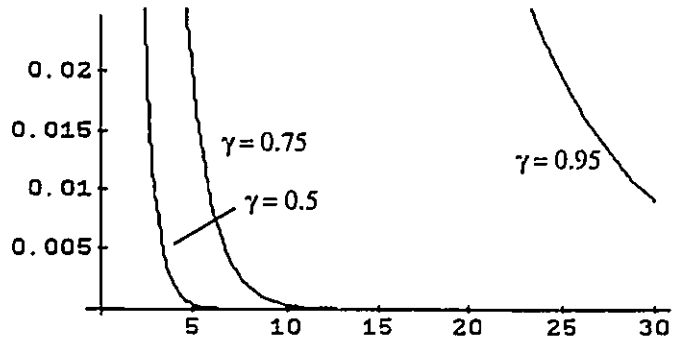

Figure 5.17 shows that, for source frequencies significantly below the resonant frequency of the enclosure, a good approximation may be obtained with 5 terms or less over three quarters of the board area. To obtain 95% board coverage requires considerably more terms.

Figure 5.18: Rate of Convergence For ϕ =1.0

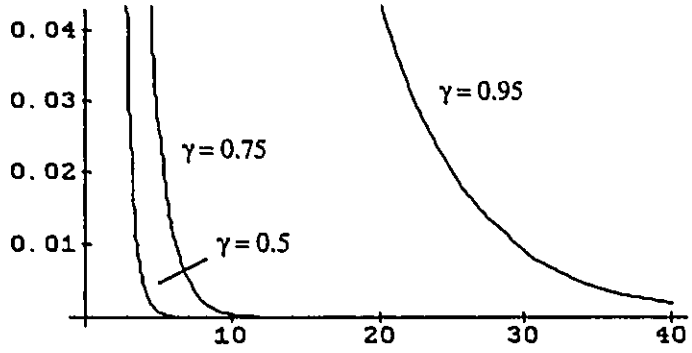

Figure 5.18 shows that the rate of convergence for an a dimension equal to wavelength is close to that for sources well below resonance. As stated previously, this model is not applicable at resonance since there are no loss terms present to contain the amplitude.

Figure 5.19: Rate of Convergence For ϕ = 10.0

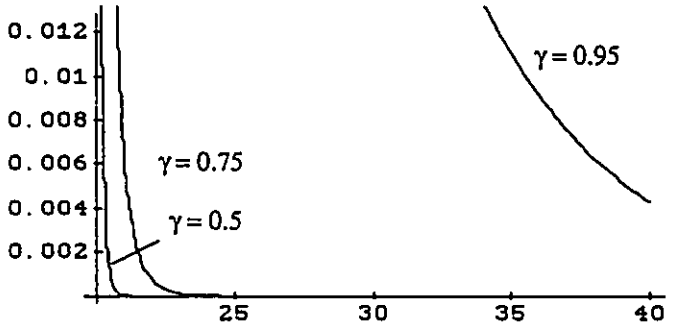

Figure 5.19 shows the same trends as the previous two cases. From this comparison it is clear that, for the dimensional assumptions made in terms of relative lengths and the range of frequencies of interest, there is not a great deal of sensitivity of the number of terms nec-

essary for convergence to the frequency under consideration. This would change if $\phi = 100$ because of the large number of trigonometric terms that would be required before convergence started, however, the number of hyperbolic terms would remain quite small for most cases.

5.9.3 Sensitivity to Linear Terms in k_g

The equations in Section 5.6 vary due to the 'linear function of k_g' identified in equation (5-30). The variance lies in the different ratios of k_c, k_y k_x and k. Although dimensionally consistent, these terms have different sensitivities relative to the 'm' and 'n' indices.

Some of these terms, such as equation (5-47), maintain a neutral balance between the numerator and the denominator of the linear term with the ratio (k_x/k_g) which will remain less than 1 for all values of k_x. Others such as equation (5-50) have an extra k_x or k_y term in the numerator. This can be accounted for in the convergence by multiplying equation (5-59) by 'p' to give

(5-60)

$$A = pe^{-\pi\sqrt{p^2 - 4\phi^2}(1 - \gamma)}$$

Figure 5.20 through Figure 5.22 show that the impact of the additional linear term is not very high on the rapidly converging summations related to $\gamma = 0.5$ and 0.75 however a significant increase in convergence time is evident in the slow convergence associated with $\gamma = 0.95$.

Figure 5.20: **Rate of convergence for $\phi = 0.1$ and Linear Multiplier p**

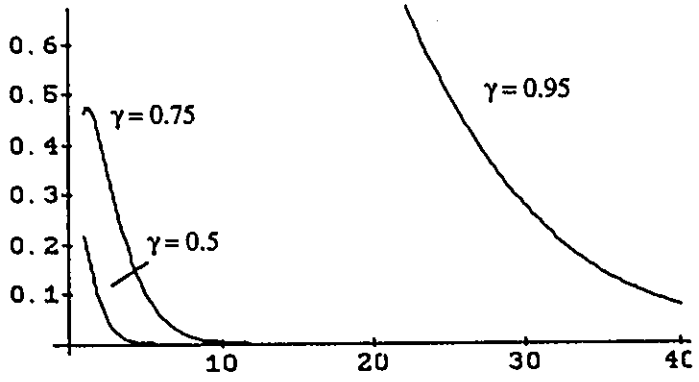

Figure 5.21: **Rate of convergence for $\phi = 10.0$ and Linear Multiplier p**

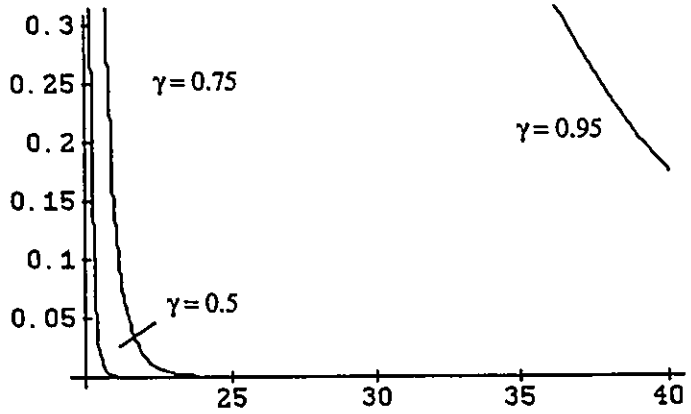

Figure 5.22: **Rate of Convergence For $\phi = 0.1$, $\gamma = 0.95$ and Linear Multiplier p**

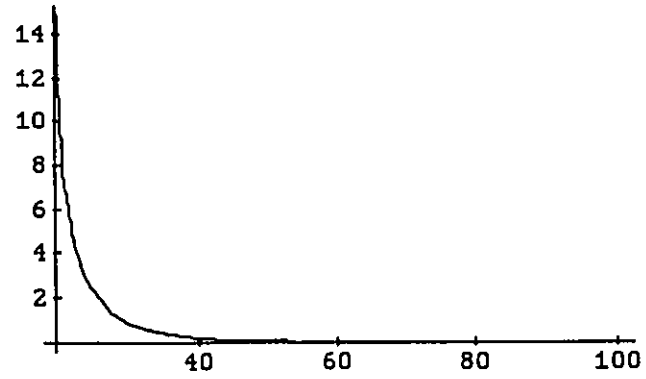

Figure 5.23 shows that increasing the linear term in equation (5-60) to p^2 does not significantly alter the convergence time but it does result in a much higher weighting on the initial terms of the convergence, in this instance twenty times greater than in Figure 5.22

Figure 5.23: Rate of Convergence For $\phi = 0.1$, $\gamma = 0.95$ and Linear Multiplier p^2

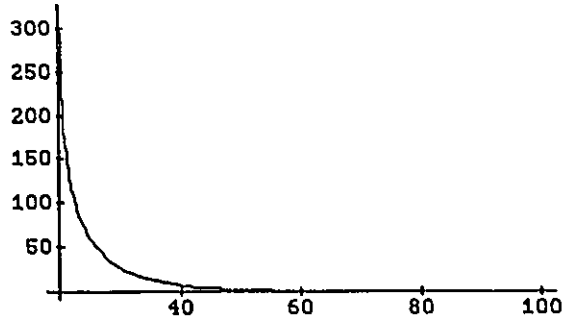

5.10 Conclusion

The dyadic Green's function for electric scalar potential and magnetic vector potential can be used as a basis for modelling sources within an enclosure. The magnetic and electric dipole models of IC sources simplify the solution of the Green's function. Decomposition of these sources into their cartesian components reveals behavioral trends in the EMI problem related to position and polarization. A separate equation is generated for each variation of the disturbance-dipole source coupling.

For sources in the central area of the cavity floor, at frequencies below the resonant frequency of the cavity, the summation of terms converges after only five terms. As the source point approaches the cavity wall as many as 100 terms may be needed.

Chapter 6

Multiple Sources

6.1 Introduction

The existence of multiple sources plays a fundamental part in the structure of EMI problems. Digital systems generally consist of a number of different sources that radiate at the harmonics of a common frequency. The contributions from each of these sources will sum as vectors in amplitude, direction and phase on the wall of the enclosure.

In all practical instances the EMI problems of the type being investigated in this thesis occur in a linear medium. Extensive use is made of the principle of superposition. Efficient analysis of multi-source systems requires that the most significant contributing factors to the total field or current magnitude be identified. It is found that the relative importance of factors such as phase or position vary with frequency.

In the commercial design environment, information regarding the coupling between a source location and a point on the wall is most useful before commitments have been made to pcb layout. This is achieved in the following methodology by dividing the bottom of the cavity (representing the pcb) into a regular grid. The coupling between each source point

and a point on the wall is then determined using the equations of the previous chapter. The resultant array of coupling coefficients is referred to in this thesis as a **mapping matrix**. This matrix forms the basis of the statistical modelling in the next chapter.

6.2 Mapping Matrix For Enclosure Characterization

An alternative to evaluating the EMI problem based on a set of design specific source positions is to assume a standard distribution of sources and evaluate the coupling from these points to the enclosure wall. The information gathered from this exercise would be applied during the layout process.

The enclosure is divided into a rectangular **n** X **m** grid as shown in Figure 6.1. These grid nodes may be thought of as representing individual components or as a discrete representation of the average source current distribution over a sector of the board. If the nodes are regarded as individual components then there should be a correlation between the number of nodes and the number of components likely to be found on the board. In this case it would be possible to generate numerical values that have absolute significance in terms of magnitude.

At lower frequencies the spacing of the grid is determined by the sensitivity of the Green's function equations to the proximity of the source to the wall. For these cases, the first one or two rows of the grid may be adequate to characterize the problem. At frequencies above resonance the grid must be small enough to accurately reflect the sensitivity to position. A practical example of this is given in Section 6.4.

Figure 6.1: Source Grid Within Cavity

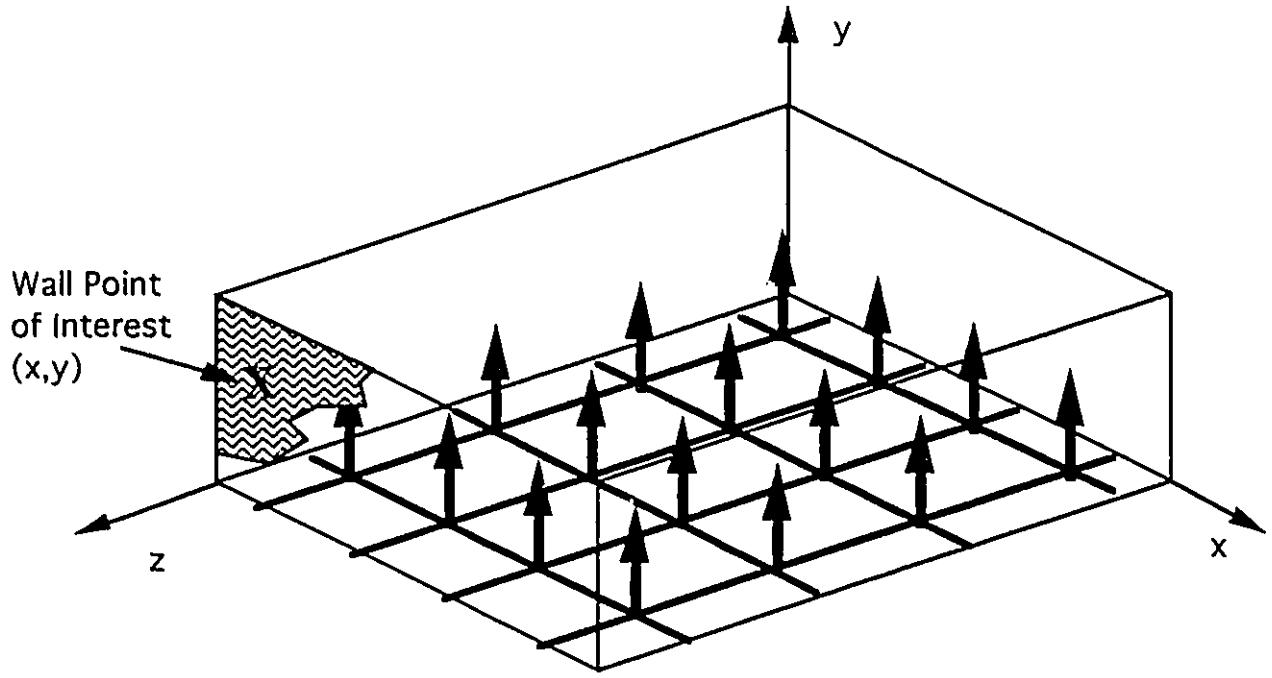

The equations in the previous chapter were derived in both absolute and normalized units. Normalization relative to wavelength provided solutions in terms of a current-wavelength product or a field-wavelength product. It is important to recognize that the electromagnetic system of dipoles within a cavity is not simply scalable in frequency. This must be taken into account when comparing coupling coefficients at different frequencies.

The EMI problem can be viewed as a mapping from four elements distributed in the 'source-space', one electric dipole and three magnetic dipoles, to three elements distributed in the 'disturbance-space', one orthogonal electric field and two coplanar currents as shown in Figure 6.2.

Figure 6.2: EMI Problem as a Mapping From Source-Space To Disturbance-Space

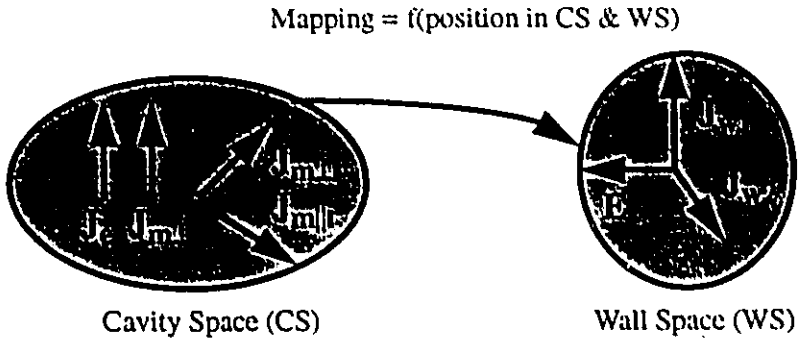

The amplitude mapping of each of these possible source points to a specific point on the wall will be given by a matrix of values (ρ_{nm}) calculated from each of the equations of Section 5.6 and depicted in Figure 6.3.

Figure 6.3: Mapping Matrix

$$\begin{bmatrix} \rho_{11} & \rho_{21} & \cdots & \rho_{(m-1)1} & \rho_{m1} \\ \rho_{12} & \rho_{22} & & \rho_{(m-1)2} & \rho_{m2} \\ \vdots & & \ddots & & \\ \rho_{1(n-1)} & \rho_{2(n-1)} & & \rho_{(m-1)(n-1)} & \rho_{m(n-1)} \\ \rho_{1n} & \rho_{2n} & \cdots & \rho_{(m-1)n} & \rho_{mn} \end{bmatrix}$$

6.3 Sum of Sources

Simple scalar models such as voltage or power addition are often used to estimate the total disturbance from a multiple source emitter. This approach is not supported by practical experimental evidence. Empirical data gathered during regulatory compliance measure-

ments have shown a number of interesting trends regarding peak values when sources are added and taken away. One observation is that large swings in disturbance values may be observed when working with less than 10 sources whereas the addition of more sources does not appear to result in a corresponding increase in emissions. Another is that the summing algorithm is dependent on the clocking strategy used within the circuit.[1]

6.3.1 Superposition

Maxwell's equations in a linear medium (i.e. μ,ε are not functions of signal amplitude) obey the principle of superposition. For this reason a multi-source problem may be solved as a set of single source problems and the solutions summed to give the total disturbance at the point of interest.

It was noted in the previous chapter that the phase of the current or field on the wall is the same as that of the source within a multiple of $\pm 90°$. The phase relationship between the individual sources should be maintained when applying the superposition principle.

The total electric field or current density on the wall is quite sensitive to source variables such as magnitude, phase and polarization. This means that accurate values can only be obtained once the sources within the cavity are fully defined. This approach is principally of use for diagnosing problems that have already occurred or for verifying designs before they are committed to manufacture. This is a reactive process that is not well suited for designing generic enclosures that can contain numerous different pcbs or for concurrent design of systems.

Three practical approaches to the design problem will be considered:

1. Dr. Boris Livshits, private correspondence

- Perform a worst case analysis for the deterministic problem and design conservatively (see next section);
- Ensure that the diversity of the sources is fully accounted for in the deterministic problem (see Section 6.3.3); and
- Perform a statistical analysis of the system (see next chapter).

6.3.2 Worst Case Estimation

The normalized current and field equations of the previous chapter were shown in equation (5-30) to have the form:

$$\begin{bmatrix}\text{Ratio of}\\ \text{Constant}\\ \text{Components}\end{bmatrix}\times\begin{bmatrix}\text{Linear}\\ \text{Function}\\ \text{of m, n}\end{bmatrix}\times\begin{bmatrix}\text{Linear}\\ \text{Function}\\ \text{of } k_g\end{bmatrix}\times\begin{bmatrix}\text{Ratio of}\\ \text{Trigonometric/}\\ \text{Hyperbolic}\\ \text{Functions of } k_g\end{bmatrix}\times\begin{bmatrix}\text{Sinusoidal}\\ \text{Terms Based}\\ \text{on Geometric}\\ \text{Factors}\end{bmatrix} \tag{6-1}$$

The maximum magnitude of the "Sinusoidal Terms Based on Geometric Factors" is unity since all of the terms are of sine and cosine form. The "Linear Function of m,n" has the value of 4 except for the case 'm and/or n = 0' in which case it is 1 or 2.

The amplitude of the equation is governed by the "Ratio of Trigonometric/Hyperbolic Functions of k_g" and is mitigated or accelerated by the "Linear Function of k_g". Based on the convergence study in the previous chapter it is possible to make worst case estimations of amplitude for each source.

This maximization approach to the worst case analysis could lead to a gross over design of the system shielding that would negate the benefits of the multiple source analysis. A hybrid approach in which derating factors based on the statistical evaluation of the following chapter could be applied when repetitive calculations are performed on a known structure.

6.3.3 Diversity of Sources

The manner in which the emissions from each of the sources should be added depends on the following factors:

- Source signal amplitude (Chapter 3);
- Source polarization and radiation efficiency (Chapter 4);
- Amplitude mapping from source to point on boundary of interest (Chapter 5); and
- Synchronization scheme of the signals (Random, delayed, synchronous).

6.3.3.a Spectral Diversity

The use of the quasi-peak detector results in a measurement bandwidth of 120kHz within the frequency range 30MHz to 1GHz. Components of the emissions spectrum that do not fall within this bandwidth do not sum together in terms of the regulatory measurement. This spectral selectivity has a significant effect on the problem structure. For the purpose of summing multiple sources only those with emissions that fit within a common 120kHz bandwidth are of interest.

In general this means that only a subset of the components on the pcb will contribute to any specific measurement. At harmonics of the clock frequency this may be a large percentage of the total chip count however there tends to be only a few dominant IC sources. At harmonics of the data rate there are often fewer IC sources but many more signals per source due to the width of the data and address busses.

There is evidently a correlation between the harmonics of a signal. Given the differences in amplitude mapping functions and the frequency dependence of the emissions structure, it is proposed that even the harmonics of the same clock signal can be treated as independent

entities when modelling a specific source. Henceforth the multi-source modelling will be done in terms of discrete frequencies by which it is inferred that there is a ±60 kHz bandwidth around that frequency.

6.3.3.b Spatial Diversity

The various emissions sources are located at different locations within the enclosure. The effects of this separation on the emissions profile is referred to as the spatial diversity.

Spatial diversity due to position has a direct and an indirect effect on the summing problem. The direct effect is to introduce a different mapping factor between each source and each wall point for a given frequency. This ratio between any two of these factors may be as high as several orders of magnitude. As will be seen in Section 6.4, a 180° phase shift may be introduced through a small change in position around the central axis of the enclosure resulting in subtraction rather than addition of the signals. Position of the sources is the single most important factor in the multisource modelling problem.

The indirect effect has to do with phase delay introduced by clock distribution. The physical separation of components is closely related to the pcb routing distance between them necessary for clock distribution. This in turn has an influence on the phase relationships between the sources that increases with frequency. This is dealt with in more detail in Section 6.3.3.d.

6.3.3.c Angular Diversity

The source dipoles have different polarizations which result in different induced currents and fields on the aperture wall, even if the position and amplitude are the same.

Electric field components are always normal to the wall and therefore will sum directly regardless of the source polarization. The angular diversity only exists in the relative amplitude of the component induced by a given source polarization.

For wall current components induced by magnetic dipole distributions cross polarization takes place, resulting in two orthogonal components from a single source polarization. The relative magnitude of each of the components is dependent on both source and wall position.

In this model angular diversity will be dealt with by solving the problem for one source polarization and one wall polarization at a time. This means that all of the equations will have to be solved before a full picture of the wall currents and fields materializes.

6.3.3.d Effects of Phase Diversity

The phase of each induced current and field on the wall is directly related to the phase of the generating source within $\pm 90°$ or $\pm 180°$ depending on the Green's function that governs the mapping. The actual phase of each of the sources is dependent on the specific implementation on the printed circuit pack.

In many instances the phase relationship between different parts of the board are tightly controlled for functional reasons. In others there is a pseudo-random relationship. For practical reasons of implementation it is very difficult to have all of the sources in synchronization over a significant board area due to the finite propagation time of the clock signal.

Phase relationship on a printed circuit pack is determined by the delay of the clock signal. Part of this delay is due to the finite speed of propagation of the clock signal around the board. Part is due to delays within the IC. This delay will have a less significant effect at lower frequencies as it represents a smaller percentage of the clock period.

6.3.3.e Effects of Symmetry and Anti-Symmetry

A particular characteristic of the dipole source in cavity formulation of this problem is the existence of symmetric and anti-symmetric modes. The problem as described in Figure 6.4

has an axis of symmetry down the centre. The mapping function from any source location to any wall location has a mirror image. For example the mapping coefficient of source point #3 to wall point #11 should be the same magnitude as that from source point # 15 is from wall point # 5.

It will be shown in Section 6.4 that certain components of the dipole sources result in symmetric mapping coefficients to current distributions on the wall. Others result in anti-symmetric ones (i.e. 180° phase shift). Hence in some circumstances there will be constructive interference and in others it is will be destructive. This is distinct from other forms of diversity such as angular and phase because it is a fundamental characteristic of the problem and not a variable parameter.

6.4 Examples of Mapping Matrices

To illustrate many of the issues raised above, some of the mapping matrices are calculated for a sample problem.

Three frequencies have been selected, low, medium and high. At low frequency the length of the longest side of the enclosure is one tenth of a wavelength. At the medium frequency the length of the longest side is 1.4 times the wavelength of the source but the height is still sub resonant. At high frequency the longest side is 4.2 times wavelength and the height is 1.26 times wavelength.

The first set of calculations provide the low frequency mapping matrices for each of the wall current elements due to the two horizontal magnetic dipole moments. The second set of calculations looks at examples of medium and high frequency response for one of the elements. The third set of calculations shows the change in mapping values that may be achieved through the restriction of regions in which sources may be found.

The cavity used in this example has a square base and a height that is 30% of the base dimension. Due to the use of normalized equations the mapping matrix was originally found in terms of the product of current density and wavelength. To permit the comparison of relative disturbance magnitudes the wavelength term has been factored out.

Figure 6.4: Source and Current Locations for Example

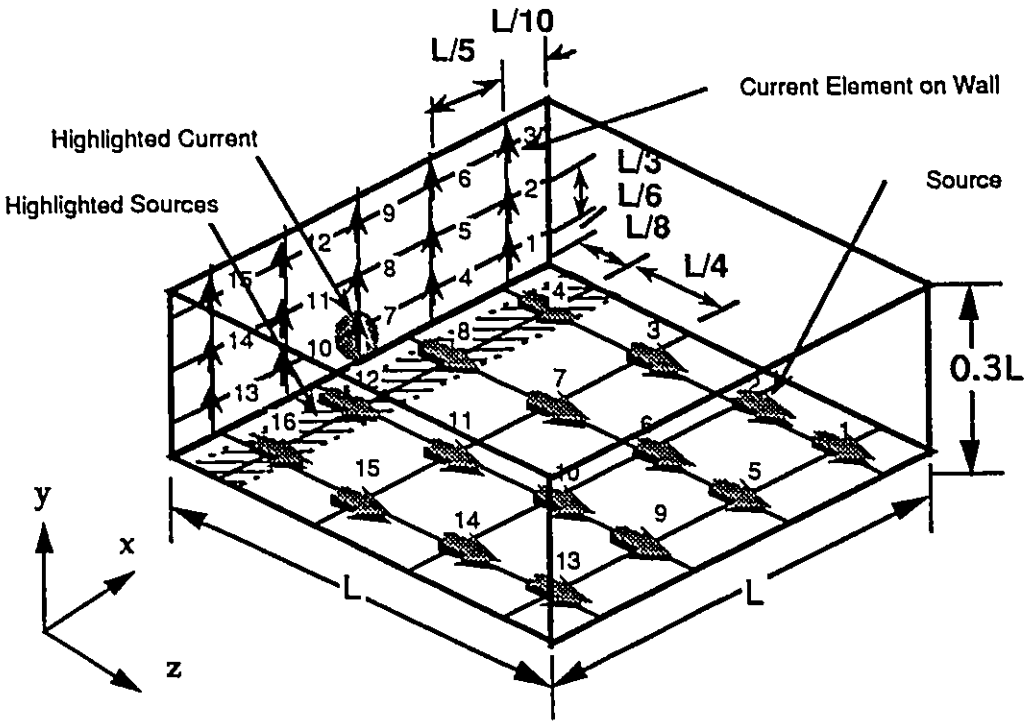

The mapping matrix is developed for 16 source points and 15 current points. This number of source points was chosen for two reasons; it was found to give a reasonable resolution to the problems and it reflected a typical density of integrated circuits on a pcb.

6.4.1 Example 1: Low Frequency Behavior

The low frequency behavior of the source-enclosure system is compared for magnetic dipole sources that are perpendicular and parallel to the enclosure wall. This demonstrates some of the significant differences in disturbance distribution due to polarization of the source.

6.4.1.a Perpendicular Magnetic Dipole

The perpendicular magnetic dipole (Figure 6.5) induces two current components (x and y) on the wall of the enclosure. The mapping coefficients are calculated from equation (5-51).

Figure 6.5: Perpendicular Magnetic Dipole

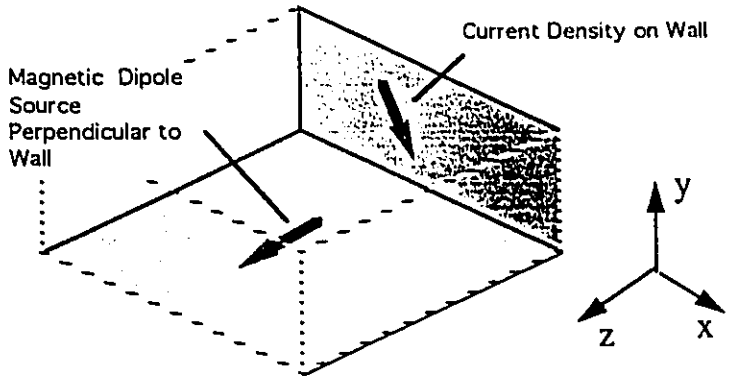

Matrix 1 and Matrix 2 below are the mapping factors for the low frequency case. The first is for the x-component and the second is for the y-component. Each row corresponds to a source point on the floor of the cavity. Each column corresponds to a point on the wall at which the disturbance is observed. Source points in the closest proximity to the wall are shown in bold. Mapping values relating to the lower middle wall point (highlighted in Figure 6.4) are shown in outline font. The maximum amplitude value is underlined.

Matrix 1: a = 0.1λ, x-Component Current, Perpendicular Magnetic Source

1) {0,0,0,0,0,0,0,0,0,0,0,0,0,0,0}
2) {-4,-7,-4,-2,-4,-2,-1,-1,-1,0,0,0,0,0,0}
3) {-61,-112,-52,-27,-52,-24,-5,-10,-5,-1,-1,-1,0,0,0}
4) {-3106,-1627,-350,-142,-318,-110,77,-6,-9,73,11,0,70,12,0}
5) {0,0,0,0,0,0,0,0,0,0,0,0,0,0,0}
6) {-1,-3,-1,-2,-4,-2,-2,-4,-2,-1,-2,-1,0,0,0}
7) {-13,-26,-13,-40,-73,-33,-32,-60,-28,-8,-15,-7,-1,-2,-1}
8) {-208,-110,-37,-1979,-1116,-241,-762,-647,-170,-49,-46,-18,-30,-9,-2}
9) {0,0,0,0,0,0,0,0,0,0,0,0,0,0,0}
10) {0,0,0,-1,-2,-1,2,-4,-2,-2,-4,2,-1,-3,-1}
11) {-1,-2,-1,-8,-15,-7,-32,-60,-28,-40,-73,-33,-13,-26,-13}
12) {-30,-9,-2,-49,-46,-18,-762,-647,-170,-1979,-1116,-241,-208,-110,-37}
13) {0,0,0,0,0,0,0,0,0,0,0,0,0,0,0}
14) {0,0,0,0,0,0,-1,-1,-1,-2,-4,-2,-4,-7,-4}
15) {0,0,0,-1,-1,-1,-5,-10,-5,-27,-52,-24,-61,-112,-52}
16) {70,12,0,73,11,0,77,-6,-9,-142,-318,-110,-3106,-1627,-350}

Matrix 2: a = 0.1λ, y-Component Current, Perpendicular Magnetic Source

1) {14, 14, 14, 34, 34, 34, 35, 35, 35, 24 24, 24, 8, 8, 8},
2) {61, 60, 59, 136, 134, 133, 126, 125, 125, 77, 77, 77, 25, 25, 25}
3) {209, 196, 183, 428, 399, 372, 271, 263, 255, 124, 123, 122, 35, 35, 35},
4) {-1012, -157, -108, 1545, 1090, 821, 152, 212, 196, 11, 55, 57, -2, 12, 13}
5) {1, 1, 1, 7, 7, 7, 16, 15, 15, 17, 16, 16, 7, 7, 7}
6) {-8, -7, -7, 12, 12, 12, 63, 62, 61, 70, 69, 68, 28, 28, 27}
7) {-112, -99, -87, -96, -78, -63, 249, 225, 204, 211, 200, 190, 65, 63, 62}
8) {-464, -336, -260, -3593, -1623, -1196, 3092, 1580, 1163, 475, 333, 284, 92, 65, 60}
9) {-7, -7, -7, -17, -16, -16, -16, -15, -15, -7, -7, -7, -1, -1, -1}
10) {-28, -28, -27, -70, -69, -68, -63, -62, -61, -12, -12, -12, 8, 7, 7}
11) {-65, -63, -62, -211, -200, -190, -249, -225, -204, 96, 78, 63, 112, 99, 87}
12) {-92, -65, -60, -475, -333, -284, -3092, -1580, -1163, 3593, 1623, 1196, 464, 336, 260}
13) {-8, -8, -8, -24, -24, -24, -35, -35, -35, -34, -34, -34, -14, -14, -14}
14) {-25, -25, -25, -77, -77, -77, -126, -126, -125, -136, -134, -133, -61, -60, -59}
15) {-35, -35, -35, -124, -123, -122, -271, -263, -255, -428, -399, -372, -209, -196, -183}
16) {2, -12, -13, -11, -55, -57, -152, -212, -196, -1545, -1090, -821, 1012, 157, 108}

Three observations may be made:

- The highest currents are found at the bottom of the wall. They are particularly high in the central region. These values are more than three orders of magnitude (60 dB) higher than many of the coupling coefficients. This gain is more than enough to dominate the relative influences of broadband and narrowband energy described in Chapter 3. It

is clear that, at low frequencies, proximity to the cavity wall is the dominant variable in the problem. If a component is in an area of high coupling, then many of the other components on the board may be ignored. In these circumstances the multiple source problem is reduced to a quasi-single source problem;

- The first matrix is symmetric, the second is anti-symmetric. Equivalent dipole sources distributed symmetrically around the centre point of the axis will induce current components that sum in the x-direction and cancel in the y-direction. This illustrates the importance of reducing the multiple source systems to cartesian components before looking for behavioral trends; and
- The phase shift (± sign shift) in the low frequency matrix comes infrequently. This implies that similar components clustered in a fairly broad area will add constructively to the current total and the current variations on the wall will be quite slow. This is an expected behavior of low frequency systems.

6.4.1.b Parallel Magnetic Dipole

As in the previous case the parallel magnetic dipole (Figure 6.6) induces two current components (x and y) on the wall of the enclosure. The mapping coefficients are calculated from equation (5-49).

Figure 6.6: Parallel Magnetic Dipole

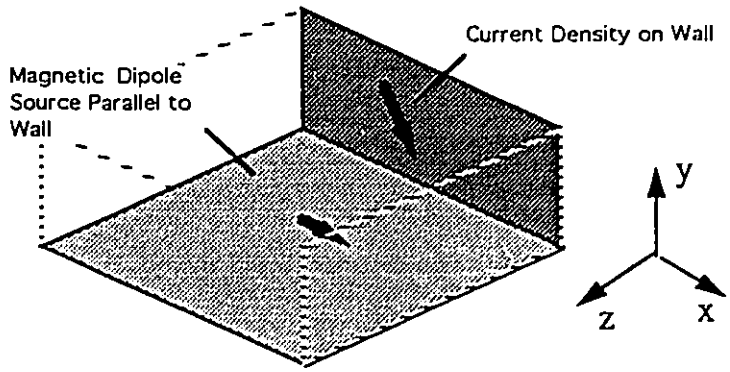

Matrix 3: a = 0.1λ, x-Component Current, Parallel Magnetic Source

1) {0,0,0,0,0,0,0,0,0,0,0,0,0,0,0}
2) {-1,-1,-1,0,0,0,0,1,0,0,0,0,0,0,0}
3) {-13,-25,-12,8,15,7,4,8,4,1,2,1,0,0,0}
4) {-567,-539,-164,419,444,132,58,68,27,41,17,4,39,11,1}
5) {0,0,0,0,0,0,0,0,0,0,0,0,0,0,0}
6) {-1,-1,-1,0,-1,0,0,1,0,0,1,0,0,0,0}
7) {-11,-21,-10,-8,-15,-7,11,20,9,7,13,6,2,3,2}
8) {-117,-191,-82,-980,-634,-144,367,666,170,149,126,47,82,32,7}
9) {0,0,0,0,0,0,0,0,0,0,0,0,0,0,0}
10) {0,0,0,0,-1,0,0,-1,0,0,1,0,1,1,1}
11) {-2,-3,-2,-7,-13,-6,-11,-20,-9,8,15,7,11,21,10}
12) {-82,-32,-7,-149,-126,-47,-367,-666,-170,980,634,144,117,191,82}
13) {0,0,0,0,0,0,0,0,0,0,0,0,0,0,0}
14) {0,0,0,0,0,0,0,-1,0,0,0,0,1,1,1}
15) {0,0,0,-1,-2,-1,-4,-8,-4,-8,-15,-7,13,25,12}
16) {-39,-11,-1,-41,-17,-4,-68,-68,-27,-419,-444,-132,567,539,164}

Matrix 4: a = 0.1λ, y-Component Current, Parallel Magnetic Source

1) {17,17,17,39,39,39,39,39,39,25,25,25,8,8,8}
2) {47,46,46,82,82,81,56,56,56,26,26,26,7,7,7}
3) {270,247,227,232,229,225,51,55,59,4,6,7,-1,-1,0}
4) {4743,2894,2161,-879,-162,29,-356,-202,-142,-138,-84,-72,-39,-23,-21}
5) {34,34,34,84,84,84,96,96,96,70,70,70,25,25,25}
6){61,61,61,154,154,153,158,158,157,94,94,95,29,29,29}
7) {111,114,117,415,402,389,344,338,332,83,89,95,10,11,13}
8) {-248,-140,-37,1885,1501,1256,-413,240,330,-421,-266,-179,-98,-73,-62}
9) {25,25,25,70,70,70,96,96,96,84,84,84,34,34,34}
10){29,29,29,94,94,95,158,158,157,154,154,153,61,61,61}
11) {10,11,13,83,89,95,344,338,332,415,402,389,111,114,117}
12) {-98,-73,-62,-421,-266,-179,-413,240,330,1885,1501,1256,-248,-140,-37}
13) {8,8,8,25,25,25,39,39,39,39,39,39,17,17,17}
14) {7,7,7,26,26,26,56,56,56,82,82,81,47,46,46}
15) {-1,-1,0,4,6,7,51,55,59,232,229,225,270,247,227}
16){-39,-23,-21,-138,-84,-72,-356,-202,-142,-879,-162,29,4743,2894,2161}

The following observations are made for the case of the parallel magnetic source.

- For the parallel dipole the x-component is anti-symmetric and the y-component is symmetric. If a general source is composed of both parallel and perpendicular dipole sources, the interaction of the components of the induced currents on the wall will be quite different for each com-

ponent. Significant changes in the total amount of current on the wall could be achieved through a simple rotation of one of the parts; and

- The peak magnitudes of current in the vertical (y) orientation are five times those in the horizontal. This compares to a 14% difference in the perpendicular source case. For this particular set of dimensions and wavelengths there is a significant sensitivity to polarization in terms of peak current value and orientation that does not exist for the parallel case.

Table 6.1 provides a summary of the four permutations including symmetry, peak coupling value and the location of the maximum current.

Table 6.1: Low Frequency Coupling Summary

	Horizontal Current	**Vertical Current**
Parallel Dipole	Anti-symmetric peak mag = 980 Bottom Off-Centre	Symmetric peak mag = 4743 Bottom Corner
Perpendicular Dipole	Symmetric peak mag = 3106 Bottom Corner	Anti-symmetric peak mag = 3593 Bottom Off-Centre

Mapping matrix analysis of the enclosure provides a basis for design recommendations. Keeping components with high levels of low frequency energy away from the wall is clearly a guideline that could be applied without detailed knowledge of the component structure. Similarly, discontinuities in the enclosure that are susceptible to low frequency leakage should be kept in the upper regions of the box.

The contrary trends of the symmetric and the anti-symmetric coupling make it impossible to provide a generalized comment with respect to the summing or cancelling effects of multiple components without cartesian decomposition of the magnetic dipoles. If the emissions from the IC show a distinct polarization, this may be taken into account along with the phase information at a more detailed stage of the design effort.

6.4.2 Example 2: Medium and High Frequency Behavior

In this example the mapping matrix for the case of the perpendicular magnetic dipole source and the vertical current is recalculated for the medium and high frequency cases. These are given in Matrix 5 and Matrix 6 respectively.

6.4.2.a Medium Frequency

Recalculating the mapping matrix for the medium frequency case results in the following matrix:

Matrix 5: a = 1.4λ, y-Component Current, Perpendicular Magnetic Source

1) {-23, -23, -23, -36, -36, -36, [illegible], 4, 44, 44, 44, 26, 26, 26}
2) {-26, -26, -26, -42, -42, -42, [illegible], 0, 0, 43, 43, 43, 27, 27, 27}
3) {23, 23, 22, 35, 34, 33, [illegible], -7, -7, -41, -41, -41, -23, -23, -23}
4) **{20, 25, 25, 53, 49, 46, [illegible], 0, -1, -40, -40, -40, -24, -24, -24}**
5) {25, 25, 25, 41, 41, 41, [illegible], 2, 2, -39, -39, -39, -25, -25, -25}
6) {25, 25, 25, 42, 42, 42, [illegible], 2, 2, -43, -43, -43, -28, -28, -28}
7) {-27, -27, -27, -41, -40, -40, [illegible], 2, 2, 35, 34, 34, 19, 19, 19}
8) **{-31, -30, -29, -66, -53, -50, [illegible], 15, 11, 42, 41, 40, 23, 23, 23}**
9) {25, 25, 25, 39, 39, 39, [illegible], -2, -2, -41, -41, -41, -25, -25, -25}
10) {28, 28, 28, 43, 43, 43, [illegible], -2, -2, -42, -42, -42, -25, -25, -25}
11) {-19, -19, -19, -35, -34, -34, [illegible], -2, -2, 41, 40, 40, 27, 27, 27}
12) **{-23, -23, -23, -42, -41, -40, [illegible], -15, -11, 66, 53, 50, 31, 30, 29}**
13) {-26, -26, -26, -44, -44, -44, [illegible], -4, -4, 36, 36, 36, 23, 23, 23}
14) {-27, -27, -27, -43, -43, -43, [illegible], 0, 0, 42, 42, 42, 26, 26, 26}
15) {23, 23, 23, 41, 41, 41, [illegible], 7, 7, -35, -34, -33, -23, -23, -22}
16) **{24, 24, 24, 40, 40, 40, [illegible], 0, 1, -53, -49, -46, -20, -25, -25}**

There are five significant observations:

- The anti-symmetric behavior of the mapping matrix is preserved as the frequency goes above the first resonant point;
- There is a significant reduction in the amplitude of the mapping coefficient. This is equivalent to about 40dB/decade relative to the low frequency case;
- The bottom central wall point is now one of the lowest emissions potential areas;
- Distance from the wall is no longer a clear indication of coupling strength; and
- The mapping matrix is based on a unit magnitude dipole. If this frequency were a higher harmonic of the low frequency case it would be expected that the equivalent source magnitude would be less than unity.

6.4.2.b High Frequency

The mapping matrix for the high frequency example is given by:

Matrix 6: a = 4.2λ, y-Component Current, Perpendicular Magnetic Source

1) {-1, -2, -3, -12, 5, -16, -6, 17, -1, -4, 21, 2, 2, -6, -17},
2) {7, -2, 7, -8, 2, 3, 8, -18, -4, 4, 7, 6, -4, -10, 5},
3) {-5, -15, 2, 8, 7, 7, 4, -10, 6, -5, -7, -10, 2, -8, 8},
4) {-14, -1, -5, -11, 9, -11, -9, 11, -2, -6, 14, -9, 6, 8, -2},
5) {-10, 5, -15, 0, -3, -7, -9, 12, 7, 7, -3, -9, -3, 19, 8},
6) {-8, 12, 0, 14, -20, 2, -13, 18, 0, 6, -23, 1, 5, 21, 3},
7) {12, 28, -5, 3, -16, 10, -2, 9, -2, -1, -19, 8, -5, 10, -23},
8) {7, 3, -8, -8, -2, 1, -12, 10, -8, 7, 4, 4, 0, 1, -6},
9) {3, -19, -8, -7, 3, 9, 9, -12, -7, 0, 3, 7, 10, -5, 15},
10) {-5, -21, -3, -6, 23, -1, 13, -18, 0, -14, 20, -2, 8, -12, 0},
11) {5, -10, 23, 1, 19, -8, 2, -9, 2, -3, 16, -10, -12, -28, 5},
12) {0, -1, 6, -7, -4, -4, 12, -10, 8, 8, 2, -1, -7, -3, 8},
13) {-2, 6, 17, 4, -21, -2, 6, -17, 1, 12, -5, 16, 1, 2, 3},
14) {4, 10, -5, -4, -7, -6, -3, 18, 4, 8, -2, -3, -7, 2, -7}
15) {-2, 8, -8, 5, 7, 10, -4, 10, -6, -8, -7, -7, 5, 15, -2},
16) {-6, -8, 2, 6, -14, 9, 9, -11, 2, 11, -9, 11, 14, 1, 5}

Three observations may be made with respect to the high frequency matrix:

- The amplitude of the coefficients is generally lower than that of the medium frequency case. However, the change is proportionately smaller than that found between the low and medium frequencies. This is due to the relatively greater distance of the dipole from the wall when measured in wavelengths;
- The anti-symmetric behavior of the mapping matrix still holds; and
- The amplitude and phase (+/-) of the coefficients is much more random than was found in the previous examples. This variation will have a clear effect on the statistical analysis in the next chapter. As a rough metric of this variability it is observed that the average number of times that the polarity of the mapping coefficient changes in each row of the matrix for the high frequency case is 6.75. This compares to 0.625 and 1.0 for the low and medium frequencies respectively.

It is much more difficult to make clear recommendations on design strategies for frequencies above the first resonance of the cavity. The lack of a single dominant source location significantly reduces the advantages of the restricted layout. This will be demonstrated in the next example.

6.4.3 Example 3: Restricted Layout

One of the easiest design rules to implement is a restriction in the area of the pcb that a device with high radiation potential can be placed. For the purposes of analysis a symmetric restriction is imposed as shown in Figure 6.7. The mapping matrix is calculated for the perpendicular source and vertical current as given by equation (5-49)

Figure 6.7: Source Placement for Restricted Layout

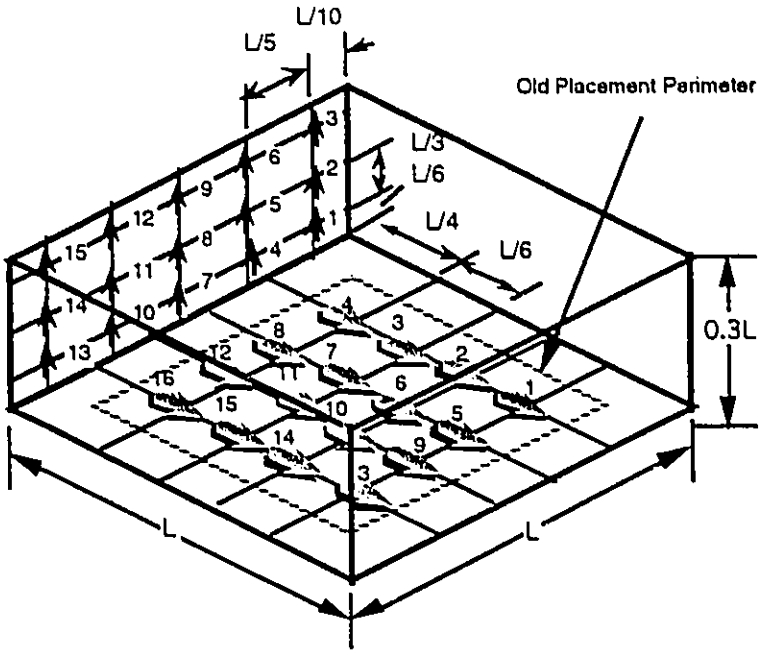

6.4.3.a Low Frequency

The mapping matrix for low frequencies for the restricted layout is given in Matrix 7.

Predictably the highest coupling coefficients have dropped. For this particular example a doubling of the minimum separation distance has resulted in an order of magnitude drop in the peak value.

A little less expected was the two fold increase in the influence of the other two source points close to the wall on the centre point of the wall. (This is the outlined value in rows 4 and 16 of the matrix. Assuming that the regions of highest coupling would be avoided when placing apertures or seams in the enclosure, care must be taken to ensure that mitigation practices that are applicable for the peak values provide the same advantages at the locations of interest.

Matrix 7: a = 0.1λ, Restricted Layout

1) {8, 8, 8, 24, 24, 23, 31, 30, 30, 23, 23, 23, 8, 8, 8}
2) {12, 13, 13, 47, 46, 45, 64, 62, 60, 45, 45, 44, 15, 15, 15}
3) {-7, 0, 7, 92, 84, 77, 132, 121, 110, 74, 71, 68, 22, 21, 21}
4) **{-259, -129, -44, 314, 195, 123, 301, 231, 173, 95, 87, 80, 23, 22, 21}**
5) {-2, -2, -2, 1, 1, 1, 12, 12, 12, 16, 16, 16, 7, 7, 7}
6) {-11, -10, -9, -9, -8, -7, 27, 26, 25, 40, 38, 37, 17, 16, 16}
7) {-44, -38, -32, -61, -48, -37, 74, 63, 54, 97, 87, 78, 33, 31, 30}
8) **{-130, -98, -70, -399, -229, -118, 379, 218, 119, 227, 176, 133, 49, 44, 39}**
9) {-7, -7, -7, -16, -16, -16, -12, -12, -12, -1, -1, -1, 2, 2, 2}
10) {-17, -16, -16, -40, -38, -37, -27, -26, -25, 9, 8, 7, 11, 10, 9}
11) {-33, -31, -30, -97, -87, -78, -74, -63, -54, 61, 48, 37, 44, 38, 32}
12) **{-49, -44, -39, -227, -176, -133, -379, -218, -119, 399, 229, 118, 130, 98, 70}**
13) {-8, -8, -8, -23, -23, -23, -31, -30, -30, -24, -24, -23, -8, -8, -8}
14) {-15, -15, -15, -45, -45, -44, -64, -62, -60, -47, -46, -45, -12, -13, -13},
15) {-22, -21, -21, -74, -71, -68, -132, -121, -110, -92, -84, -77, 7, 0, -7}
16) **{-23, -22, -21, -95, -87, -80, -301, -231, -173, -314, -195, -123, 259, 129, 44}}**

6.4.3.b Medium Frequency

The mapping matrix for the medium frequency case is:

Matrix 8: a = 1.4λ, Restricted Layout

1) {0, 0, 0, 1, 1, 1, 2, 2, 2, 1, 1, 1, 0, 0, 0}
2) {-1, -1, -1, -1, -1, -1 0, 0, 0, -1, -1, -1, -1, -1, -1}
3) {-2, -2, -2, -2, -2, -2, 0, -1, -1, -2, -2, -2, -2, -2, -2}
4) **{-4, -3, -2, 1, 0, -1, 3, 2, 1, -1, -1, -1, -1, -1, -1}**
5) {22, 22, 22, 36, 36, 36, 1, 1, 1, -35, -35, -35, -22, -22, -22}
6) {11, 11, 11, 19, 19, 19, 1, 1, 1, -20, -20, -20, -13, -13, -13}
7) {-11, -11, -10, -17, -16, -16, 1, 1, 0, 15, 14, 14, 8, 8, 8}
8) **{-23, -23, -22, -38, -37, -35, 4, 3, 2, 35, 34, 33, 20, 20, 19}**
9) {22, 22, 22, 35, 35, 35, -1, -1, -1, -36, -36, -36, -22, -22, -22}
10) {13, 13, 13, 20, 20, 20, -1, -1, -1, -19, -19, -19, -11, -11, -11}
11) {-8, -8, -8, -15, -14, -14, -1, -1, 0, 17, 16, 16, 11, 11, 10}
12) **{-20, -20, -19, -35, -34, -33, -4, -3, -2, 38, 37, 35, 23, 23, 22}**
13) {0, 0, 0, -1, -1, -1, -2, -2, -2, -1, -1, -1, 0, 0, 0}
14) {1, 1, 1, 1, 1, 1, 0, 0, 0, 1, 1, 1, 1, 1, 1}
15) {2, 2, 2, 2, 2, 2, 0, 1, 1, 2, 2, 2, 2, 2, 2}
16) **{1, 1, 1, 1, 1, 1, -3, -2, -1, -1, 0, 1, 4, 3, 2}}**

This matrix is characterized by very low coupling down the two outer rows of source points, reflecting an area of poor coupling within the cavity. This was not expected from the values generated in the equivalent non-restricted case above. This indicates that there are

channels of low coupling potential determined by the trigonometric portion of the Green's function equation.

6.4.3.c High Frequency

The mapping matrix for the high frequency restricted layout is:

Matrix 9: a = 4.2λ, Restricted Layout

1) {2, -13, 15, 1, 5, -3, 11, -15, 11, 0, -3, -9, -6, -9, 14}
2) {8, -12, -4, -8, 11, -4, 4, -6, 3, -12, 17, -3, 16, -18, -2}
3) {4, -4, 6, -4, 11, -14, -4, -14, 11, 1, 19, -10, 4, -7, 11}
4) {4, -18, 5, -7, 2, 3, 21, -12, -2, -7, -3, 7, 3, -6, 5}
5) {-2, 10, -13, 3, -16, 15, -2, 7, -13, 4, -10, 16, 2, 10, -14}
6) {-14, 14, 4, 11, -15, 3, -10, 21, -6, 12, -20, 0, -19, 16, 2}
7) {-4, 17, -16, 2, -11, 13, 0, 14, -13, 0, -16, 14, -4, 18, -16}
8) {-8, 11, 2, 14, -15, 3, -14, 6, 2, 15, -9, -1, -7, 8, 1},
9) {-2, -10, 14, -4, 10, -16, 2, -7, 13, -3, 16, -15, 2, -10, 13}
10) {19, -16, -2, -12, 20, 0, 10, -21, 6, -11, 15, -3, 14, -14, -4}
11) {4, -18, 16, 0, 16, -14, 0, -14, 13, -2, 11, -13, 4, -17, 16}
12) {7, -8, -1, -15, 9, 1, 14, -6, -2, -14, 15, -3, 8, -11, -2}
13) {6, 9, -14, 0, 3, 9, -11, 15, -11, -1, -5, 3, -2, 13, -15}
14) {-16, 18, 2, 12, -17, 3, -4, 6, -3, 8, -11, 4, -8, 12, 4}
15) {-4, 7, -11, -1, -19, 10, 4, 14, -11, 4, -11, 14, -4, 4, -6}
16) {-3, 6, -5, 7, 3, -7, -21, 12, 2, 7, -2, -3, -4, 18, -5}}

Comparing the coupling coefficients of Matrix 9 with those of Matrix 6 shows that there is effectively no gain in terms of reduced EMI potential through the imposition of a layout restriction.

6.5 Conclusion

The mapping matrix is introduced as a method for characterizing the enclosure behavior and facilitating multiple source calculation. This matrix approach clearly illustrates the different characteristics of low, medium and high frequency performance as well as the role of source polarity in the multiple source problem.

Based on the analysis s it is recommended that the cartesian components of the source dipole moments and the components of the currents and fields on the enclosure wall be calculated independently.

The disturbances contributed by multiple sources are summed using the principle of superposition. Accurate summing requires that the effects of source diversity be taken into account. Four aspects of diversity have been identified as well as the symmetric/anti-symmetric characteristics of the mapping matrix which are preserved over the entire frequency range.

Chapter 7

Stochastic Determination of Currents & Fields

7.1 Introduction

In this chapter Monte Carlo techniques are used to relate probability distributions of the source parameters to likely distributions of the disturbances. Since the behavior of the source-enclosure model is significantly different for each of the source polarizations, the analysis is performed on one source polarity at a time. The mapping matrices introduced in the previous chapter are applied in this methodology.

The determination of induced disturbances on the walls of a conducting enclosure in a multiple source system is governed to a large extent by small variations in the placement and radiation characteristics of the ICs. In practical engineering applications, source variability persists until quite late in the design process. By that time changes in the enclosure design required to mitigate the emissions are usually difficult to implement.

A probabilistic analysis of the EMI potential of an enclosed electronic system is advantageous since it permits risk-limiting decisions to be made early in the design process. In addition it provides a quantification of major trends in multiple source systems.

For any given set of sources, the disturbances created on the wall of an ideal cavity are completely deterministic. It is the source characteristics which will be defined in terms of probability distributions. The statistical problem therefore becomes one of mapping the source characteristic distributions onto the wall of the enclosure in terms of probability distributions of an induced current or field.

In theory the statistical description of the induced disturbance can be derived directly in terms of the underlying functions that characterize the source distributions. For example, if the probability of a given amplitude of a source was described in terms of a Gaussian distribution, then the current induced on the wall would be given by that distribution multiplied by the appropriate mapping matrix coefficient. The total current at the location would consist of the sum of all the distributions multiplied by their mapping coefficients. Unfortunately, once the existence of each source, its location, amplitude, phase and polarization are all taken into account through the use of probability distributions and mapping matrices, the final sum on the wall becomes so complex as to defy analysis.

For this reason an indirect, stochastic approach is taken. Monte Carlo analysis is used to generate a set of disturbance data through repetitive calculation based on a random series of source configurations. The ensemble of source configurations conforms to the underlying probability distributions of the source parameters.

The outline of this stochastic approach is as follows:

- Randomly define sets of source according to known distributions;

- Map each set of multiple sources onto a representative set of wall points using mapping matrices; and
- Generate a probabilistic description of the disturbance at that point based on the accumulated data.

These results are then analyzed with respect to their major sensitivities and compared with previous observations based on the deterministic calculations of the earlier chapters.

7.2 Details of the Stochastic Approach

There are a number of source variables which have been shown to be significant in the overall sum of currents and fields on the walls of the enclosure. The major ones are:

- Number of components;
- Their position relative to the wall of interest;
- Their amplitude;
- Source type (electric or magnetic dipole);
- Polarization; and
- Phase relationship relative to other sources;

7.2.1 Probability Distributions

Assumptions must be made with respect to probability distributions of each of these variables. In practice these assumptions should be based on historical data and future design projections. For the purposes of this thesis the data is either based on experience in the design area, such as the number of significant sources that are likely to be present, or sensitivity analysis, such as that performed for the phase relationships.

The number of significant sources of emissions is seldom more than about 10 and is often lower. The distribution of components over the board is usually fairly even because of the

pressures to minimize board area and increase device density although the concentration of components running at a particular speed may be functionally localized.

The magnetic dipole sources have been observed to dominate the emissions picture below 300 MHz while electric field dipole sources dominate above [Goulette 92-1].

7.2.2 Implementing the Monte Carlo Approach

The source variables are applied through the use of a Monte Carlo algorithm. For the purposes of this thesis one thousand iterations were performed for each distribution. The computer programs that were used for this analysis are included in Appendix V. This program was written in Mathematica on an Mac IIci computer. Since the Mathematica software is platform independent, the programs could be run on other, more powerful computers. There would be some small gains in accuracy with the use of more iterations, however, sensitivity analysis with respect to the one thousand iterations showed the practical increase in relevant information to be negligible since only major trends are of interest.

7.3 Application of Mapping Matrices

7.3.1 Mapping Strategy for Source Distribution

In reality the placement of IC's on a pcb follows a continuous distribution. However, the use of a discretized model (Figure 7.1) equivalent to that employed for the mapping matrices in the previous chapter results in significant computational simplifications. Effectively there will be a discrete number of IC's placed randomly at grid points over the pcb surface.

The grid-based model will serve to generate statistics regarding the areas of highest risk on the enclosure surface and to permit an assessment of specific design rules such as distance restrictions from the boundary or the impact of intrinsic variables such as phase variations

as a function of frequency. From this analysis it will be possible to determine the more significant variables in the problem.

Figure 7.1: Grids Within Cavity

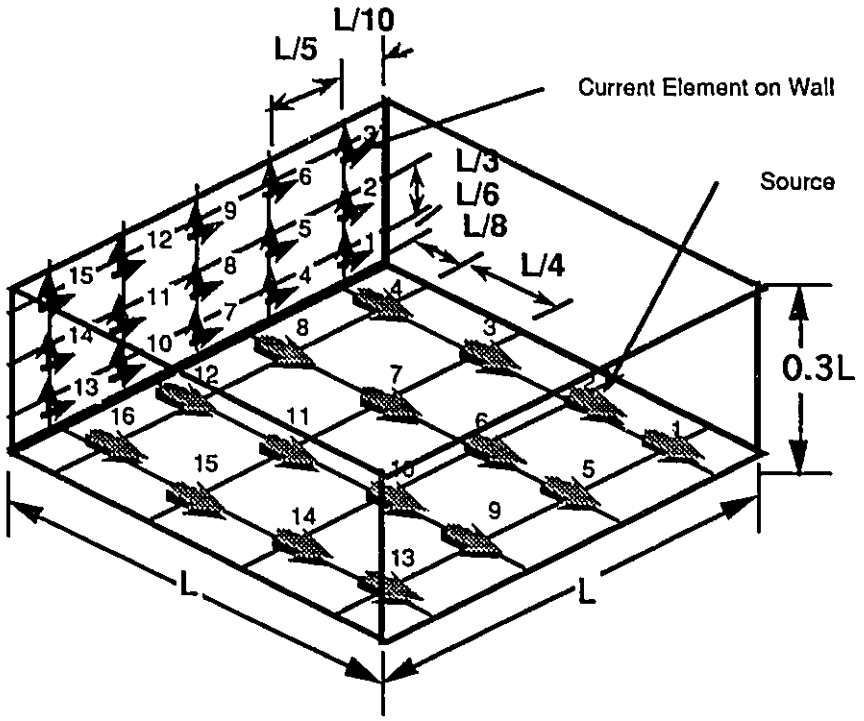

7.3.2 Random Distributions

To achieve the random distribution of sources necessary for the stochastic analysis, each coupling coefficient ρ_{ij} in the mapping matrix defined in Chapter 6 (equation Figure 6.3:) will be multiplied by the random variable ζ that can take on some value representative of the problem structure with a given probability distribution as shown in (7-1). The following sub-sections are characterized by different forms of ζ. The individual elements ζ_{ii} may or may not be independent depending on the nature of the problem.

(7-1)

$$\begin{bmatrix} \zeta_{11}\rho_{11}\ \zeta_{21}\rho_{21} & \cdots\cdots & \zeta_{(m-1)1}\rho_{(m-1)1}\ \ \zeta_{m1}\rho_{m1} \\ \zeta_{12}\rho_{12}\ \zeta_{22}\rho_{22} & & \zeta_{(m-1)2}\rho_{(m-1)2}\ \ \zeta_{m2}\rho_{m2} \\ \vdots & \ddots & \vdots \\ \zeta_{1(n-1)}\rho_{1(n-1)}\ \zeta_{2(n-1)}\rho_{2(n-1)} & & \zeta_{(m-1)(n-1)}\rho_{(m-1)(n-1)}\ \ \zeta_{m(n-1)}\rho_{m(n-1)} \\ \zeta_{1n}\rho_{1n}\ \ \ \zeta_{2n}\rho_{2n} & \cdots\cdots & \zeta_{(m-1)n}\rho_{(m-1)n}\ \ \ \zeta_{mn}\rho_{mn} \end{bmatrix}$$

7.3.2.a Mapping Existence Only

In the most basic probabilistic case only the existence of a unit amplitude source at a given position is modelled. The probability of existence is a constant **p** (where $0 \leq p \leq 1$) at each of the grid nodes. The coefficient ζ in the mapping matrix is seen to be a a Bernoulli random variable from the set [0,1]. If **p** = 0.5 the number of sources found on the board follows a binomial distribution. The implicit assumptions in this model are simultaneous phase and unitary amplitude.

A more refined model would apply different probability weightings to each of the node points. For instance the probability of a chip existing in the centre of the board may be **p** = 0.8 while the probability of it being placed at the perimeter may be **p** = 0.2.

Knowing the underlying structure of the statistical distribution it is possible to calculate the number of iterations of the Monte Carlo simulation necessary for the number of data points. In theory the minimum number of iterations required to generate the full distribution is the sum of the coefficients of the binomial expansion of order **n** X **m**. This can result in a rapid increase in the number of iterations required based on the number of source points used in the analysis. A 4 X 4 grid would require a minimum of sixty-five thousand iterations as shown in Figure 7.2. A 5 X 5 grid would require thirty three million.

Figure 7.2: Binomial Coefficients for a 4X4 Grid (N = 16)

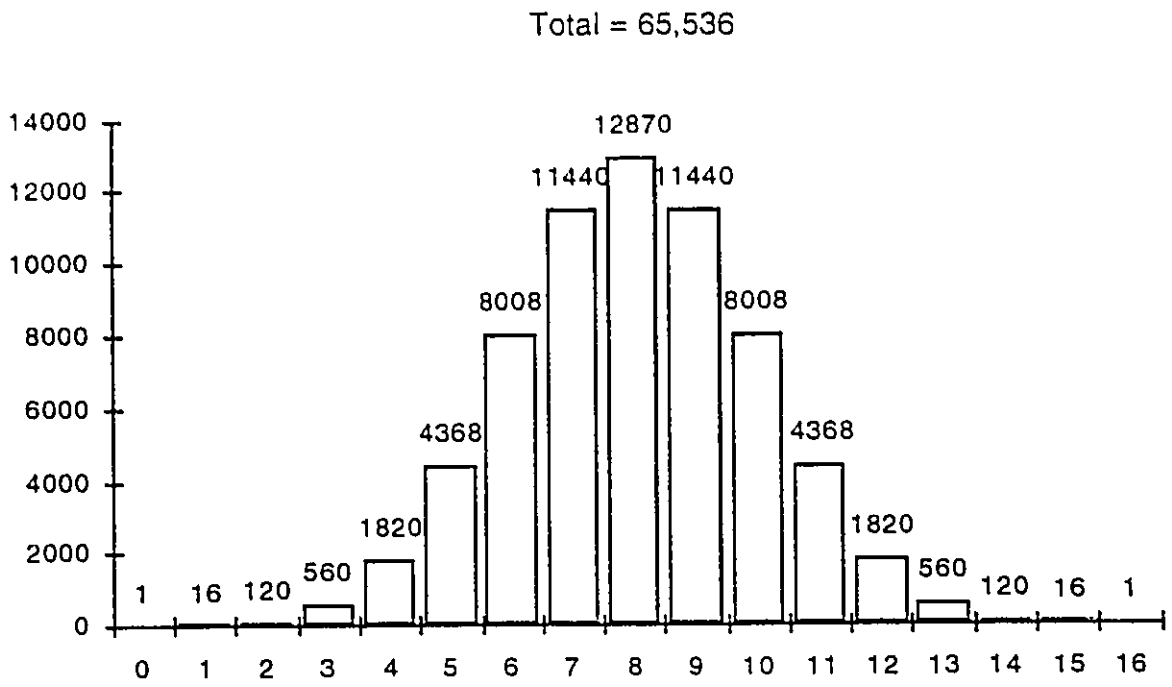

A reasonable approximation of the distribution may be obtained with a smaller sample number. In the examples that follow one thousand randomly selected sets of source points are generated. The expected distribution of numbers of source points for one thousand cases is given in Figure 7.3. This ideal distribution may be compared with the actual numbers of source points generated from the Monte Carlo simulation to give a preliminary evaluation of the statistical relevance of the sample.

Figure 7.3: Expected Numbers of Source Points for 1000 Cases

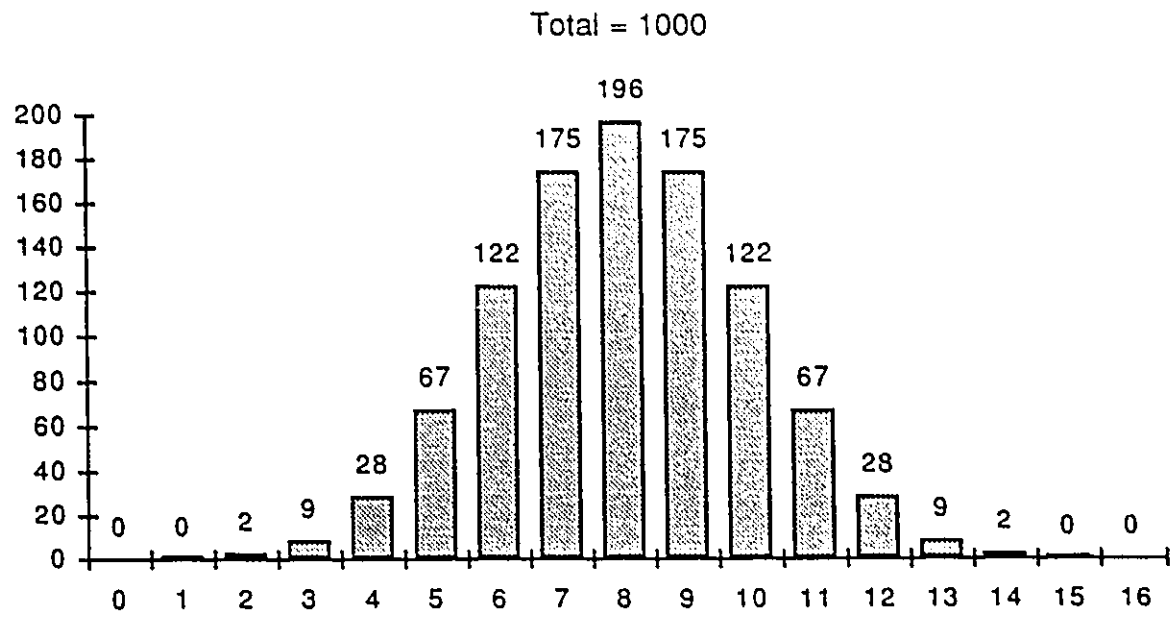

7.3.2.b Mapping Position and Amplitude

Each source will have a different magnitude. At this time there is very little information available regarding the range and distribution of source amplitudes since measurements have only been completed on a small set of devices (Figure 4.8 and Figure 4.9) and calculations are only just starting to be made (Figure 4.15).

One approach that may be used is to assume that the devices can be designed or procured to a pre-set specification. A four level specification has been proposed [Goulette 92-1] which makes a good basis for design assessment and for component selection. The amplitudes of the dipole sources for this specification are given in Figure 4.8 and Figure 4.9. Since these are log amplitude values which vary linearly with log frequency they have to be calculated for each frequency of interest. In this case the discrete random variable ζ will be drawn from the

set of values $[0, a_1, a_2, a_3, a_4]$ with probabilities of existence $[p_0, p_1, p_2, p_3, p_4]$ where the sum of the probabilities equals 1.0 and the probability distributions are appropriate to the functionality typical for the design. For example p_0 may be 0.5 indicating a binomial distribution of numbers of sources. The probabilities p_1 through p_4 may each be taken as 0.125 unless additional information is available.

In the examples that follow, the source component amplitudes are not variable.

7.3.2.c Mapping Position and Phase

A more realistic view of the summation of sources within the enclosure occurs when variations in phase are taken into account. Since the phase relation between sources is preserved during the summation of the disturbance on the wall, the distribution of the relative phases of the disturbances may be applied through the source variable ζ and the mapping factor phase shift of ±90° and ±180°. Variation in source phase is not generally an independent quantity since sources with a common set of spectral emissions harmonics are often driven from the same clock circuit. It is determined by the timing skew between various components and is a known parameter in any specific design implementation. For this reason constraints are applied to the range of phase variability.

For the purposes of determining behavioral trends, it is appropriate to deal with phase in terms of a sensitivity analysis. This is found to be particularly important in enclosed, multiple source systems since the expected effects of phase are generally found to be masked by the positional factors of positive and negative amplitude which are captured in the deterministic mapping matrices. In the examples that follow, ζ is taken to vary between ±15°, ±30°, ±45° and ±180°.

7.4 Application of Methodology

In the following section the stochastic analysis process is applied to three case studies. This will serve to illustrate the power of the technique, demonstrate the mechanics of the evaluation and highlight some performance trends which will be relevant to a broad range of practical examples.

The first case will compare the statistical distributions of the two wall current orientations induced by a perpendicular magnetic dipole at low frequencies. The second will look at the effect of phase variations for low, medium and high frequency applications. The third will examine the effects of restricting the placement area of the devices within the enclosure at different frequencies.

The information derived from the statistical analysis will be compared with that which is obtained from the deterministic analysis of the previous chapter.

All of the calculations performed in this section use the mapping matrix values derived from equation (5-51), repeated here as equation (7-2) for clarity:

(7-2)

$$\bar{J}^{m_x}\lambda = \frac{-m_x}{\alpha\beta}\sum_m\sum_n e_m e_n \left[\left(\frac{\kappa_g}{\kappa_c^2\kappa^2}\right)\frac{\cos(k_g z')}{\sin(k_g c)}\right]\times$$
$$\{[\kappa_x\kappa_y\cos(k_x x)\sin(k_y y)\sin(k_x x')]\,\hat{x}$$
$$-[\kappa_x^2\sin(k_x x)\cos(k_y y)\sin(k_x x')]\,\hat{y}\}$$

In these examples the normalized forms of the equations are used. The enclosure under study is one for which the depth and width are of equal size and the height is one third of this dimension. The source grid is four by four and the points of interest on the wall are on a three by five grid as shown in Figure 7.1 and in more detail in Figure 6.4.

The three frequency ranges used in these examples are the same as those used in the examples of Chapter 6 and are defined as:

- Low Frequency: Wavelength is significantly longer than the linear dimensions of the enclosure. In this example $\lambda = 10$ L.
- Medium Frequency: Wavelength is shorter than long dimension but longer than height. In this example $\lambda = 0.71$ L.
- High Frequency: Wavelength is shorter than all linear dimensions of the enclosure. In this example $\lambda = 0.24$ L

Equation (7-2) yields the current-wavelength product from the normalized Green's function relationship. In order to compare the relative magnitudes of induced currents for a unit magnetic dipole at different frequencies it is necessary to eliminate the wavelength factor in the equation. In the following examples this is done by multiplying the low, medium and high frequency answers by 1, 14 and 42 respectively. To calculate an actual current value a specific frequency and enclosure dimension would have to be selected.

7.4.1 Comparison of the Low Frequency 'x' and 'y' Current Components From a Perpendicular Magnetic Dipole Source.

In this example the mean and ninth decile values of the 'x' and 'y' components of the induced wall current due to a random set of perpendicular, unit magnitude magnetic dipoles are calculated. The mapping coefficients of Matrix 3 and Matrix 4 of Section 6.4 are used as the basis of the mapping. The distribution of the sources is determined in terms of a 50% probability of the source existing at each grid point. Figure 7.3 shows the ideal distribution of numbers of sources for 1000 random iterations. The distributions for the actual examples are given in Figure 7.4 and Figure 7.5.

Figure 7.4: Distribution of Source Points; Horizontal Current; Perpendicular Magnetic Moment

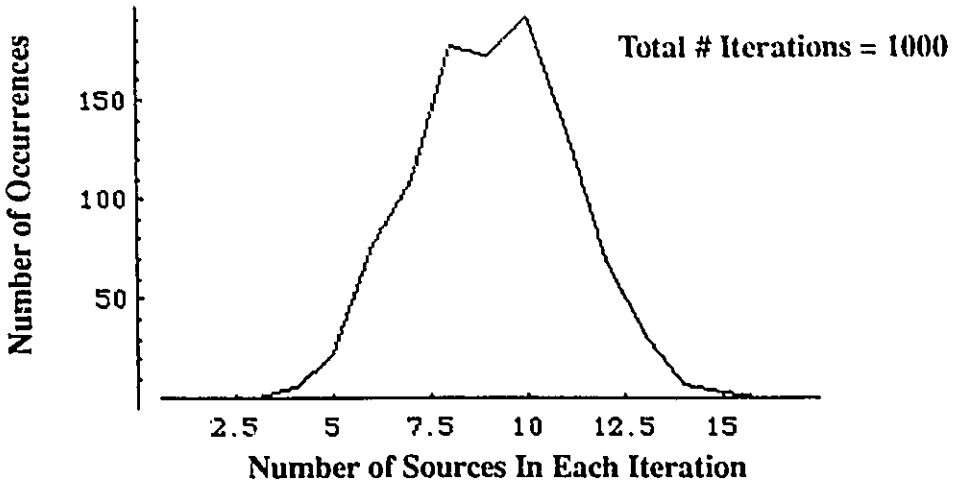

Figure 7.5: Distribution of Source Points; Vertical Current; Perpendicular Magnetic Moment

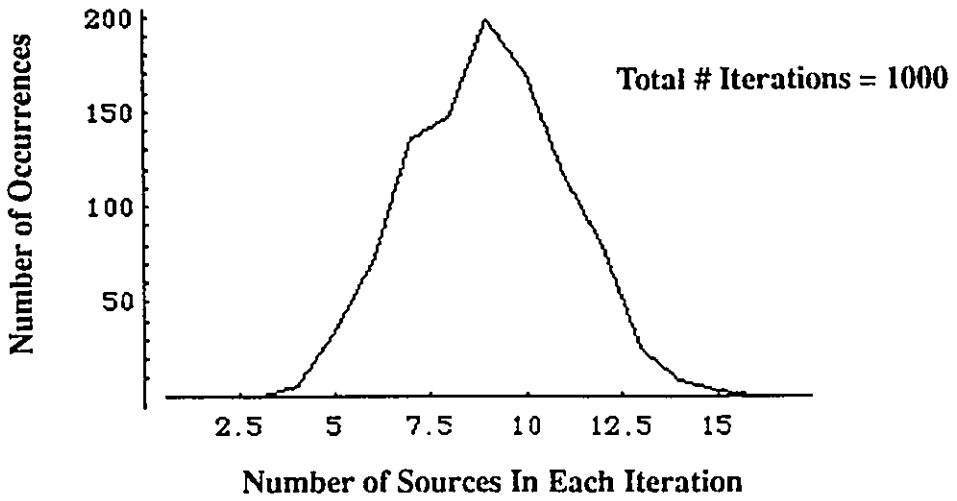

The distribution of wall current was calculated using the program listed in Appendix IV. The results are graphically displayed in Figure 7.6 and Figure 7.7. In Figure 7.6 the mean current values in the 'x' and the 'y' directions are superimposed on the largest single coupling coefficient from each of the mapping matrices.

Figure 7.6: Mean Value of 'x' and 'y' Current Components

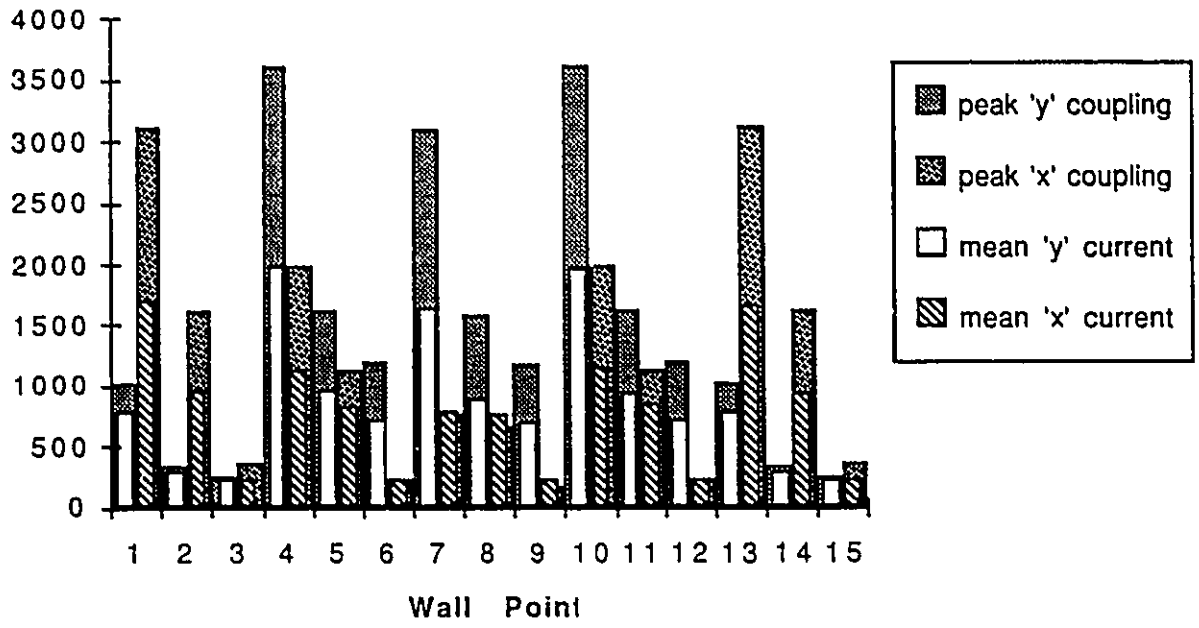

The following observations can be made from Figure 7.6:

- **The mean value for the dominant components is seen to be about half of the value of the peak coupling.** This despite the fact that the average number of contributing sources to the mean current value is eight while the peak coupling value is based on a single source. This reflects the dominance of the single closest source which has a fifty percent probability of existence;
- **At low frequencies the closest coupling point dominates the sum of currents.** In the previous chapter it was noted that, as expected, the closest source had the largest coupling coefficient. Using the statistical approach it is shown that this one source is not only dominant relative to any other single source but also with respect to all the other sources in the enclosure taken together;

- **Symmetry and anti-symmetry of the mapping matrix does not play a dominant role in determining the average current.** It was observed in the previous chapter that the mapping matrix for the 'y' component was anti-symmetric while the one for the 'x' component was symmetric, as determined by the trigonometric terms in the Green's function equation. This could potentially have caused a significant difference in the overall summing trend in terms of cancellation or accumulation of coupling components. It is evident from this analysis that, in general, this effect does not play an important role in determining the total current; and
- **The trigonometric terms do make a significant difference to the location on the wall at which different current polarities are induced.** This will have a significant effect on the design decisions that are made regarding the construction of the enclosure.

In Figure 7.7 the peak coupling coefficients for each point are superimposed on the 9th decile value of the current magnitude. In this case it can be observed that the highest 10% of cases (100 out of 1000) result in wall field values that are around 10% higher than the peak coupling value of the mapping matrix. This would indicate that, when designing at low frequencies, designing to the peak coupling values plus a small margin would be a successful strategy with a 90% confidence. It also shows that keeping a source exclusion zone around susceptible points in the enclosure will yield significantly lower emissions in almost all cases. This could be confirmed by re-running the analysis for a single wall point with the probability of a source being in close proximity set to zero.

Figure 7.7: 9th Decile of 'x' and 'y' Current Component

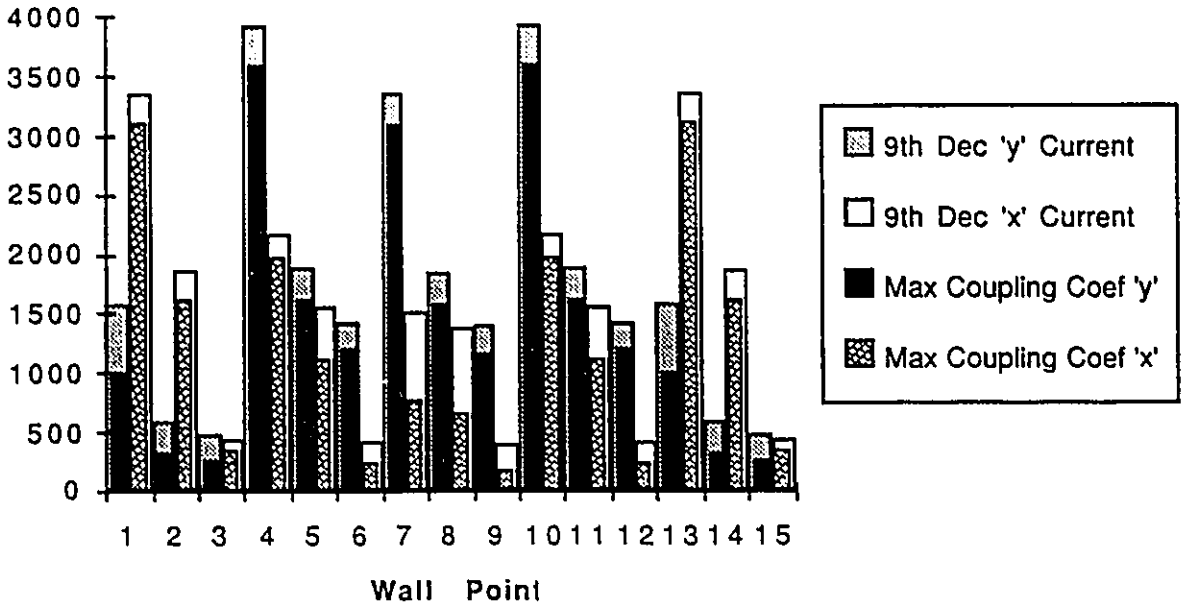

7.4.2 Effects of Phase Variation on Wall Current

In this set of examples the mean, standard deviation and magnitude of the 9th decile for the 'y' component of the current induced by perpendicular magnetic dipoles are calculated for 1000 random iterations with 5 different phase relationships. Each of the sixteen sources is randomly chosen to exist with a probability of 0.5. It is then assigned a random phase angle over a predefined range. These sources are then summed as vectors. The ranges used in the following example are 0°, ±15°, ±30°, ±45° and ±180°.

7.4.2.a Low Frequency

Figure 7.8 shows the mean value of current induced at each wall location. Several observations may be made

- **Greater phase variation results in higher mean current at the points of maximum current:** This is because the maximum current values are found near the centre of the wall. As can be seen from the mapping matrix, these contributions tend to cancel. This is most clearly observed from the highlighted mapping coefficients for the current value at point #7 from sources # 8 and # 12 which are 3092 and -3092 respectively. In the perfectly symmetric case any deviation from 0° phase angle will result in a higher mean amplitude.

Figure 7.8: Mean Magnitude For Different Phase Variations; Low Frequency

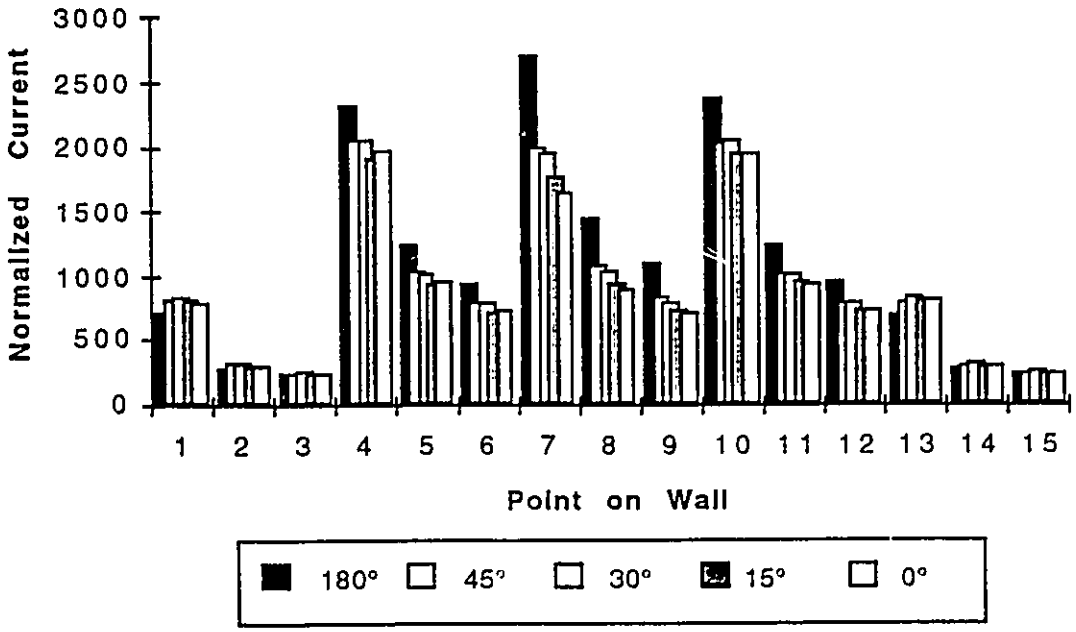

- The highest mean current values are found at the bottom centre of the enclosure: The mean current values are at least 50% higher around the lower mid section of the wall (Figure 7.9) than elsewhere regardless of the phase scheme. This translates into a 6dB emissions potential penalty;
- **Phase relationships are not a significant variable other than at the high current points:** From Figure 7.8 it can be observed that at the ends of the wall and across the top there is almost no change in the mean value with phase;
- **At low frequencies the 9th decile value of maximum current amplitude is independent of phase for phase variations up to at least ± 45°.** It is only the higher number of instance of constructive interference that occur with the ±180° phase variation that significantly raises the 9th decile value; and
- **The peak value of the 9th decile is 100% higher than the peak mean.**

Figure 7.9: High Emission Potential Zone; Low Frequency

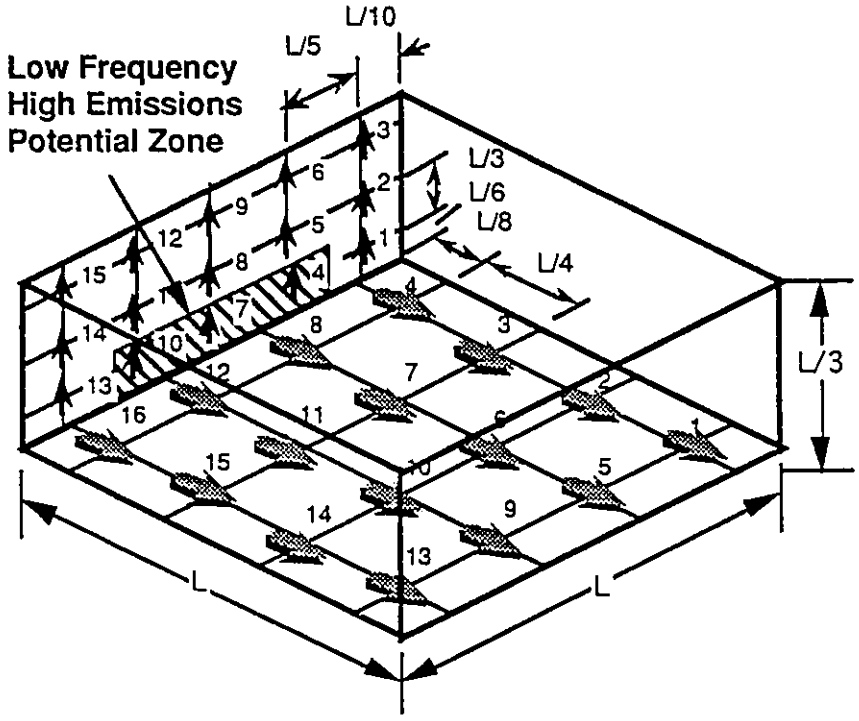

The high sensitivity of the maximum current to the balancing action of the principle contributing sources is seen in the high value of the standard deviation (Figure 7.10) and the value of the emissions at the 9th decile (Figure 7.11) which are twice as high as the mean.

Figure 7.10: Standard Deviation For Different Phase Variations; Low Frequency

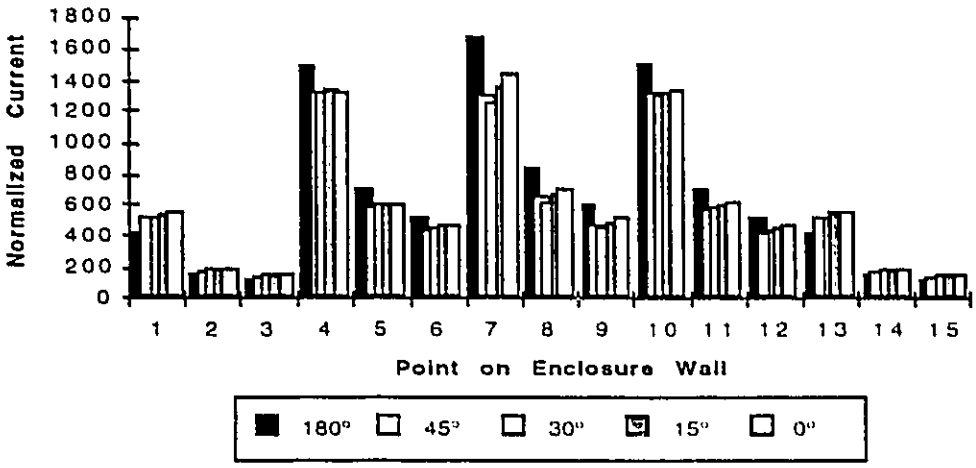

Figure 7.11: 9th Decile Magnitude For Different Phase Variations; Low Frequency

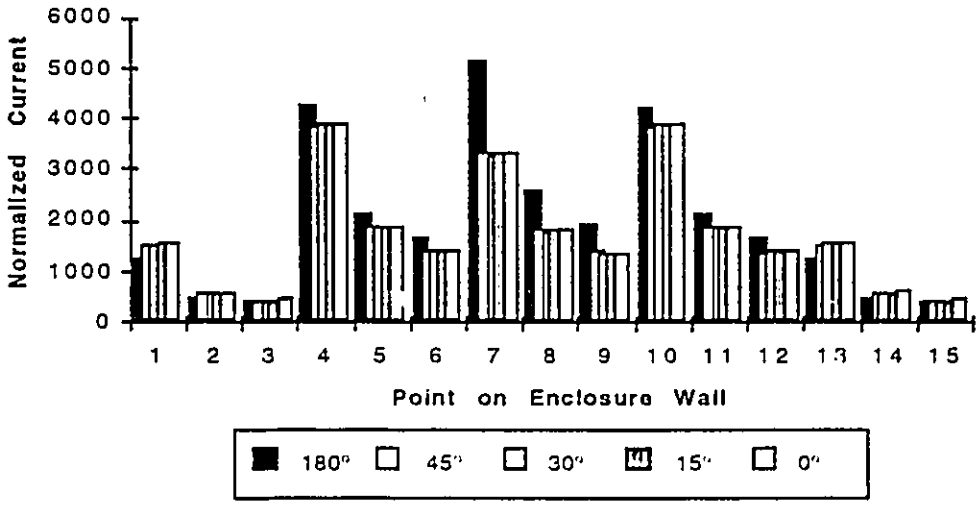

7.4.2.b Medium Frequency

Figure 7.12 shows the mean amplitude variation with respect to position and phase relationship. Some significant observations can be made:

- **The point that had a maximum emissions potential for low frequencies is one of the lowest at medium frequencies:** The effect of passing the first resonance of the enclosure can be seen from the relative null in the plot. From the mapping matrix values it is seen that only relatively low values of current may be induced on the centre of the wall regardless of the source point;

Figure 7.12: Mean Magnitude For Different Phase Variations; Medium Frequency

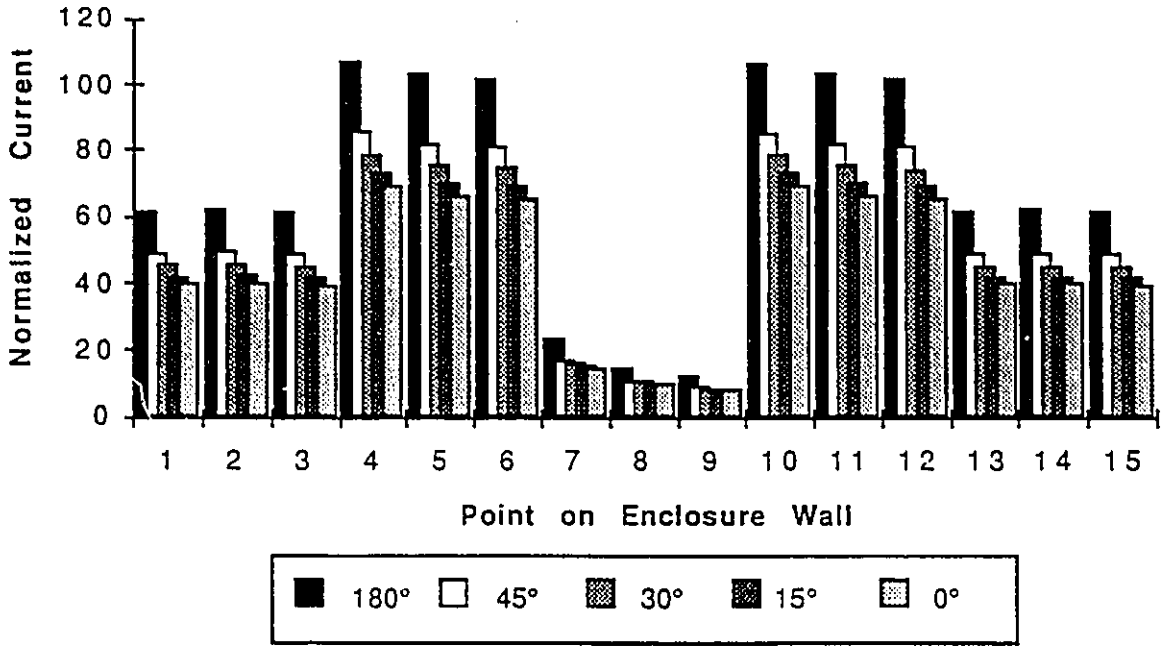

- **The relative amplitude of the current induced by the medium frequency source is significantly lower than that of the low frequency source:** Peak current values are more than 20 times lower than for the low frequency case. The distance of the first row of sources from the wall in terms of wave length is 14 times further away. This reflects the non-linear rate of fall-off of the induced fields in the near field zone. This implies that the emissions potential drops off with frequency. In terms of total radiation from the non-ideal enclosure this is somewhat off-set by the increase in emissions efficiency with frequency for many of the leakage paths that may be driven by the wall currents;
- **Current distribution is quite uniform from top to bottom of the wall:** Unlike the low frequency case, the zone of maximum emissions potential can not be constrained to the bottom of the wall;
- **All source points contribute significantly to the peak current values:** From the mapping matrix (Chapter 6; Matrix 5) it is seen that there is, in general, only about a factor of two difference between source points relative to any points. Unlike the low frequency case, the peak value of the 9th decile is more than three times greater than any one source;
- **Much less sensitive to phase scheme than the low frequency case:** The mean varies less than 20% from the ±180° scenario to the 0° scenario compared to almost 50% for the low frequency case. The same basic trends are observed; and
- **The peak value of the 9th decile is 80% higher than the mean:** Although slightly lower than the 100% of the low frequency case this is quite similar in trend despite the very different relationship to the individual contributions.

Figure 7.13: Standard Deviation For Different Phase Variations; Medium Frequency

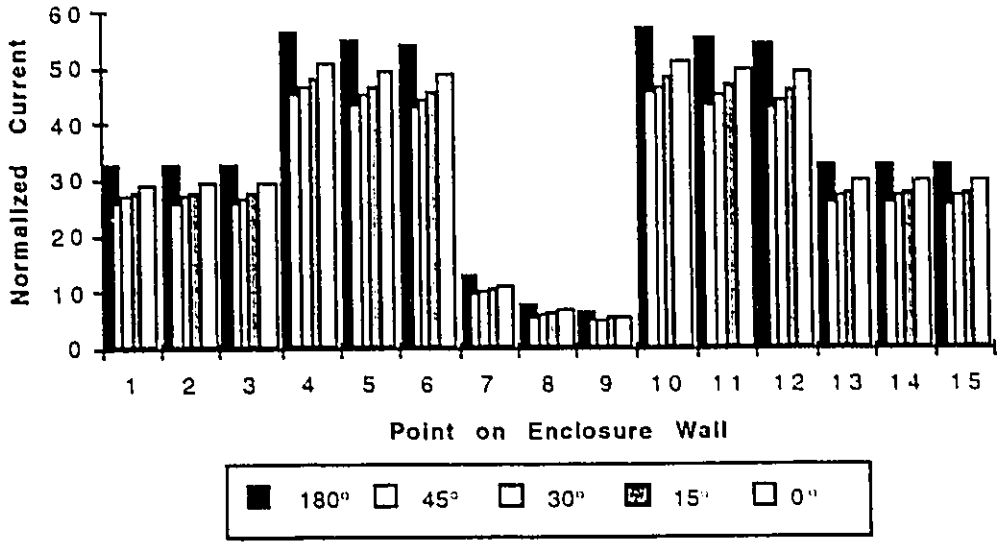

Figure 7.14: 9th Decile Magnitude For Different Phase Variations; Medium Frequency

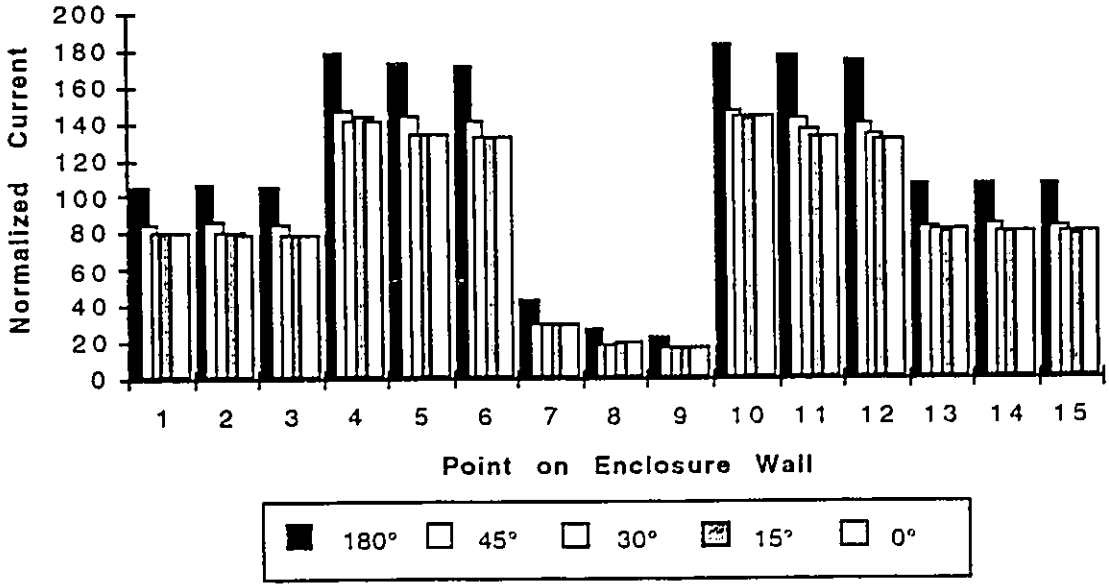

7.4.2.c High Frequency

Figure 7.15 shows the mean values for the high frequency case. The following observations may be made:

- **The peak mean current values are found along the mid height of the wall:** The mid-height values, particularly of the ±180° phase scenario, are significantly higher than the top and bottom row on the wall but not particularly sensitive to position across the width of the enclosure. This translates into a 3dB to 6dB increase in emissions potential at the mid-height;

Figure 7.15: Mean Magnitude For Different Phase Variations; High Frequency

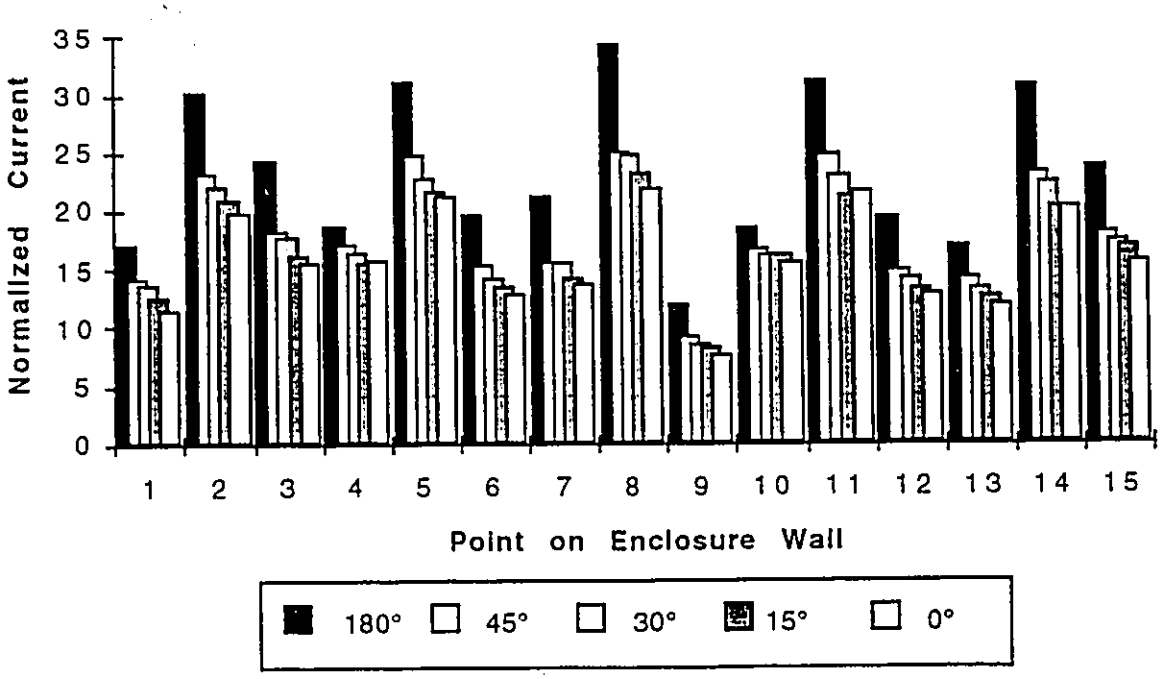

- **Significant variation in individual source to wall point coupling pairs without clear pattern:** Although generally lower in value than the medium frequency case, the coupling terms from the mapping matrix show greater variance due to having passed the first resonance frequencies in all directions;
- **Lower current for a unit magnetic dipole than found for either low or medium case:** The peak mean current value is 1/100th of the low frequency case although the frequency is only 42 times higher. Similarly the peak mean value is 1/5th of the medium frequency case while the frequency is only three times as high;
- **9th decile values are relatively consistent across the board:** This indicates that there are no truly advantageous areas to place enclosure features in terms of reduced emissions potential for frequencies which are above the resonant frequency of all of the principle dimensions; and
- **The highest coupling coefficients do not correspond to the closest points to the wall:** In a significant departure from the previous cases, the significance of any particular source point does not correlate to its proximity to a wall.

Figure 7.16: Standard Deviation For Different Phase Variations; High Frequency

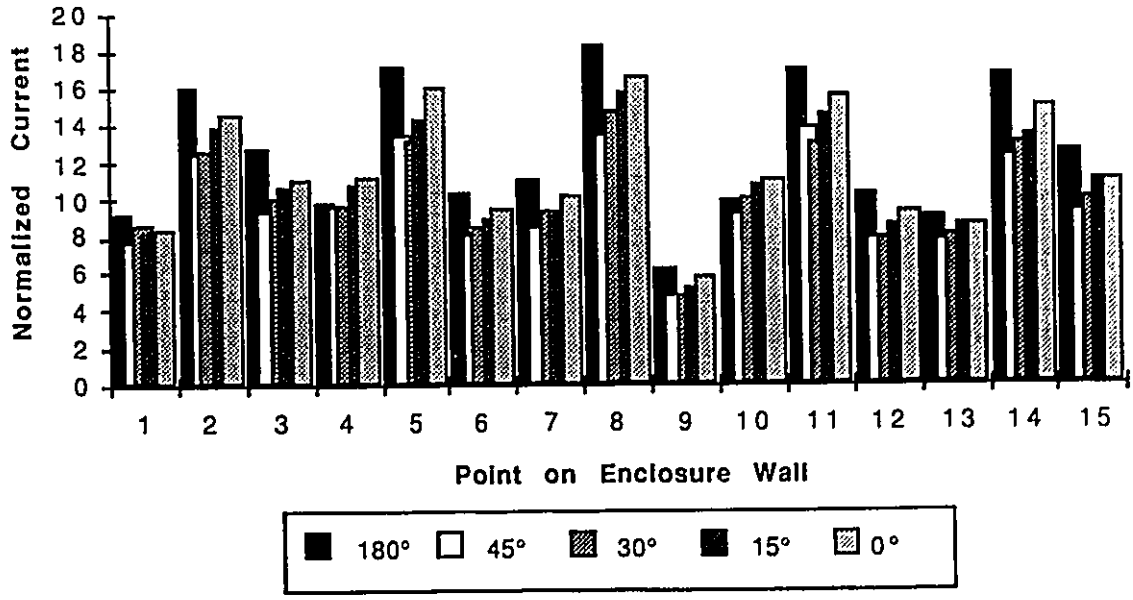

Figure 7.17: 9th Decile of Magnitude for Different Phase Variations; High Frequency

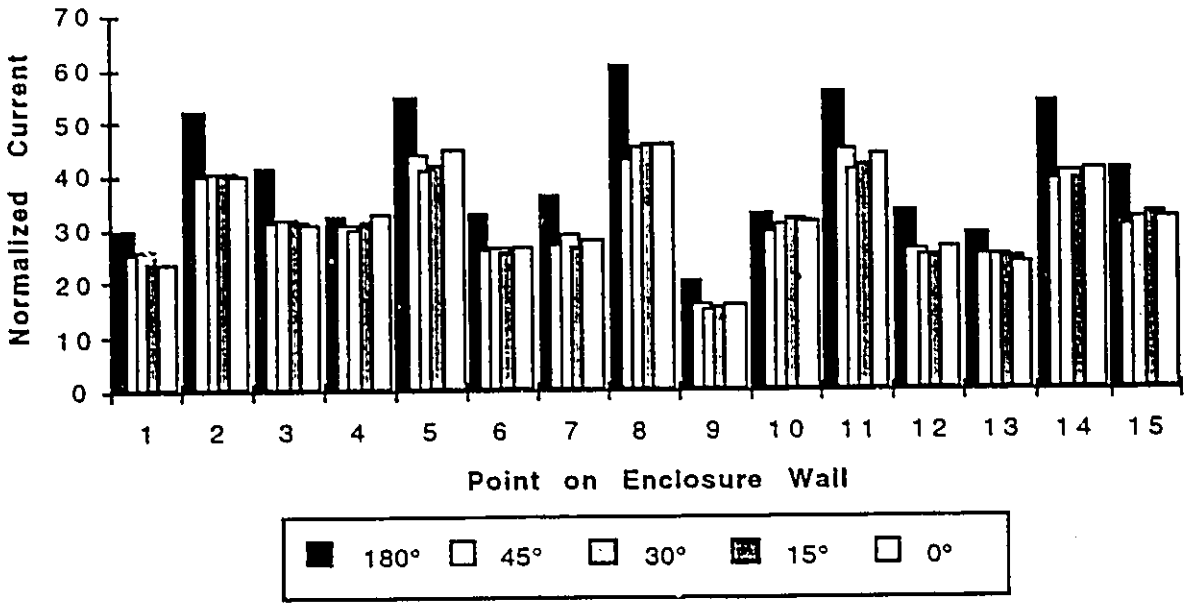

7.4.3 The Effect of Placement Restriction on Wall Current

In this example the 4X4 grid of source points is restricted in terms of the placement within the cavity (Figure 6.7). This restriction serves to keep the sources further away from the wall. In this particular implementation the source area is reduced symmetrically around the bottom of the enclosure

7.4.3.a Low Frequencies

Figure 7.18: Mean Magnitude For Restricted Layout; Low Frequencies

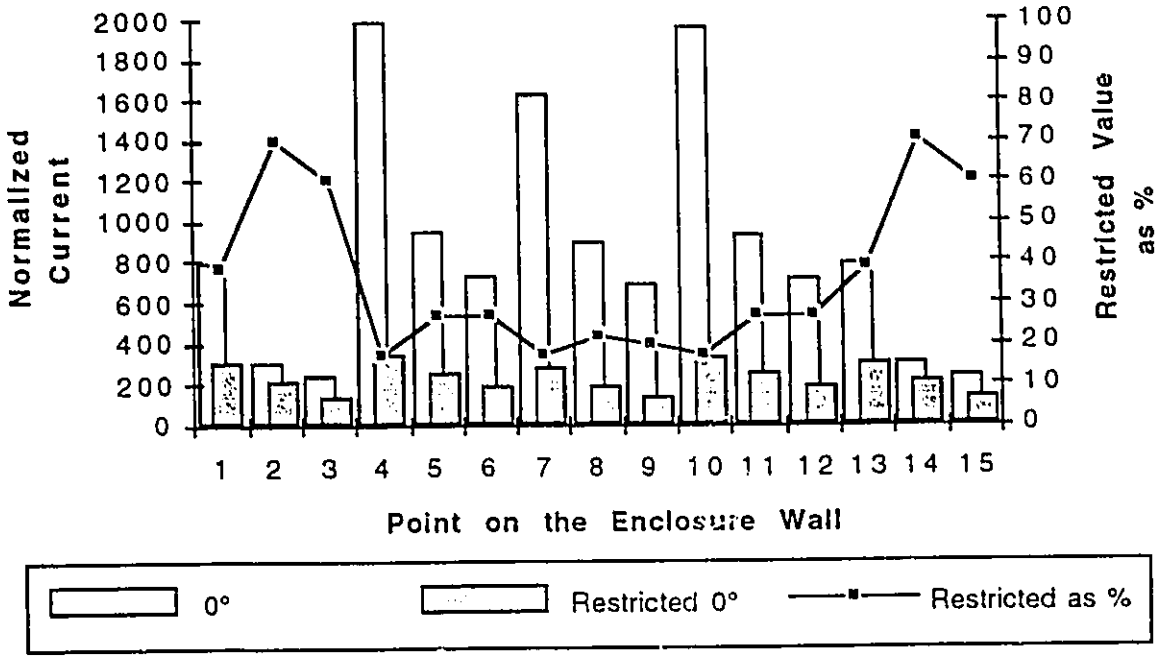

Figure 7.18 shows the difference in mean current amplitudes achieved by confining the lay-out of sources to an area in the middle of the board. The following observations can be made:

- **The peak mean current is reduced by an order of magnitude:** Although the shortest distance from a source to the wall has only been increased by a factor of 2, the peak emissions potential has reduced by a factor of 10;

- The peak mean current is slightly higher than the highest single contributor: As with the unrestricted case, the highest values still occur at the base of the wall but the effect is much less pronounced; and
- **Peak value of 9th decile is 20% of unrestricted counterpart.**

Figure 7.19: Standard Deviation For Restricted Layout; Low Frequency

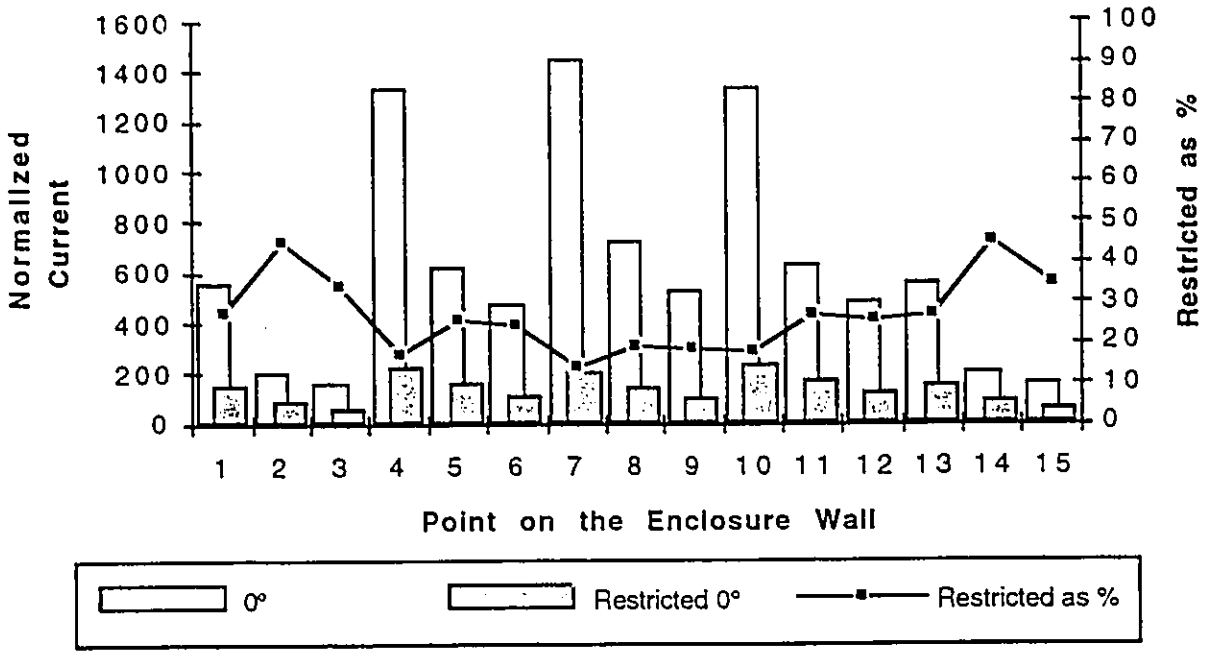

Figure 7.20: 9th Decile For Restricted Source; Low Frequency

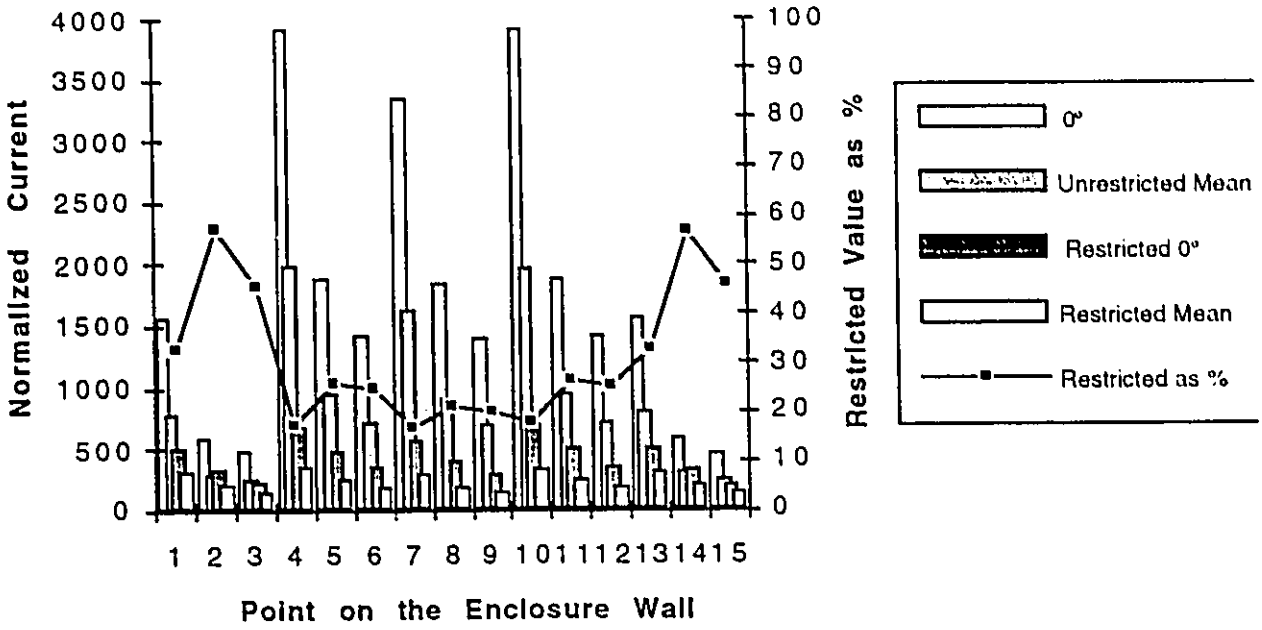

7.4.3.b Medium Frequencies

Figure 7.21: Mean Magnitude ForRestricted Source; Medium Frequencies

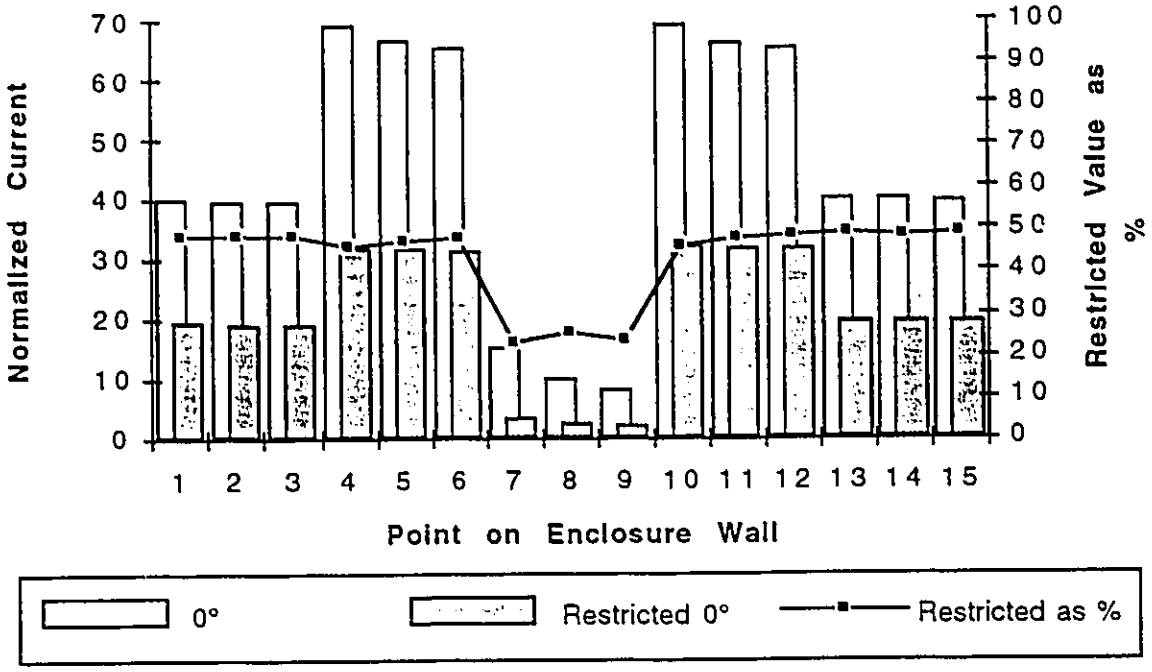

Figure 7.21 shows the mean current values for the medium frequency case. The following observations may be made:

- The same trends in terms of areas of null current distribution occur as they did for the unrestricted case; and
- The reduction in peak values are much less pronounced than they were for the low frequency case.

Figure 7.22: Standard Deviation For Restricted Source; Medium Frequency.

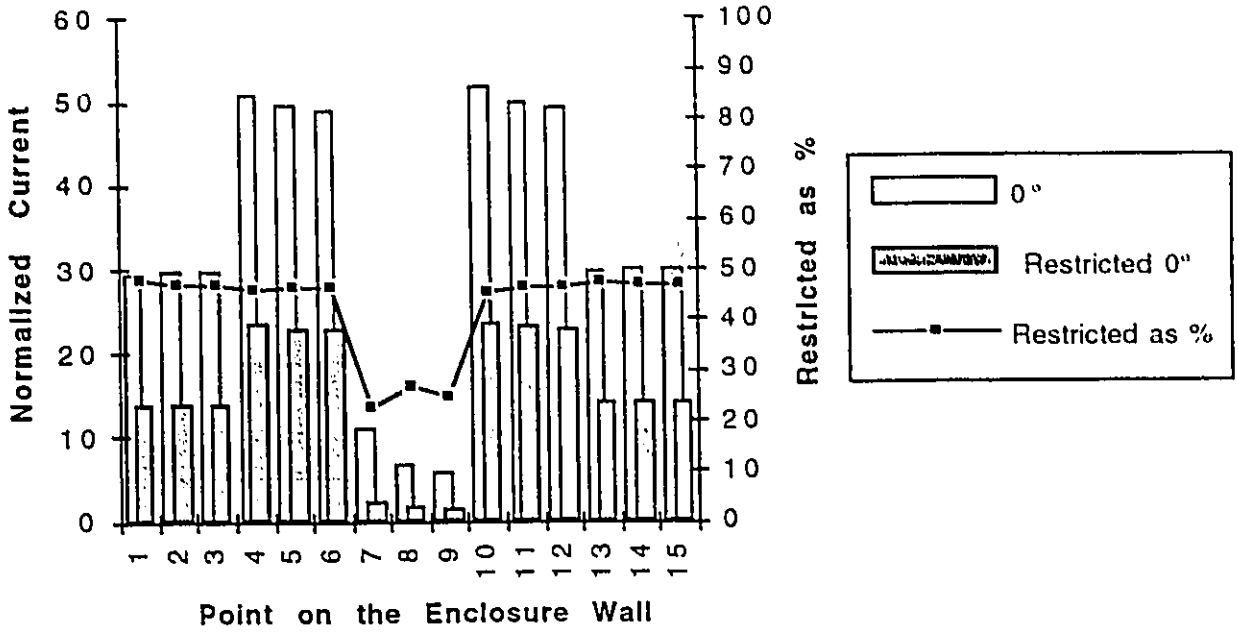

- The 9th decile of the restricted case is of about the same value as the mean of the unrestricted case and 50% lower than its unrestricted counterpart;

Figure 7.23: 9th Decile For RestrictedSource: Medium Frequencies

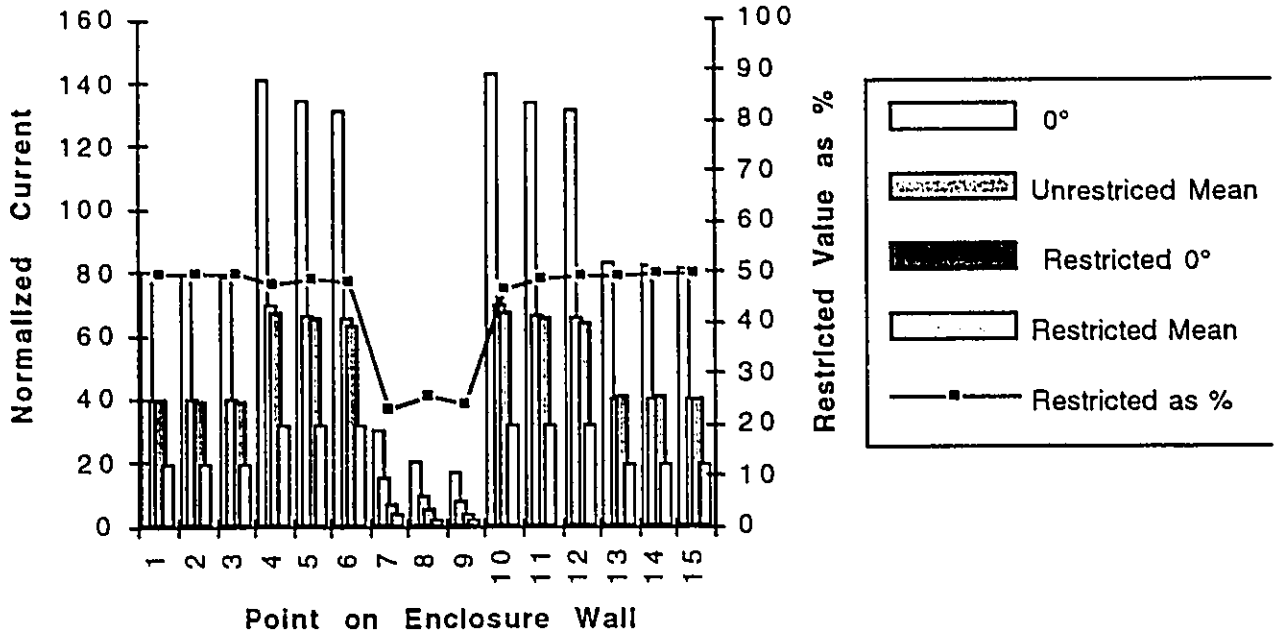

7.4.3.c High Frequencies

Figure 7.24: Mean Magnitude For Restricted Sources: High Frequency

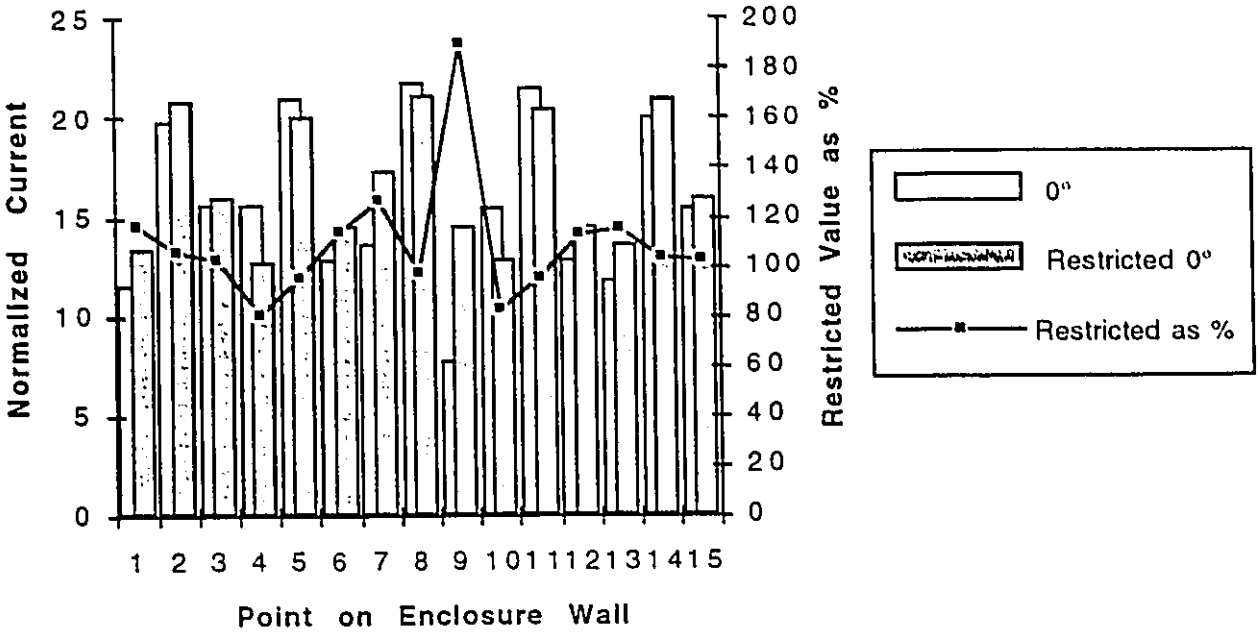

From Figure 7.24 it can be seen that restriction of the source placement influenced the current at specific locations but resulted in no significant net reduction in peak current values. As such the major observation that can be made is:

- At high frequencies restriction of placement area does not appreciably effect the peak current value; and
- There is not a significant difference between the restricted high frequency values and the restricted medium frequency current values.

Figure 7.25: Standard Deviation For Restricted Source; High Frequency

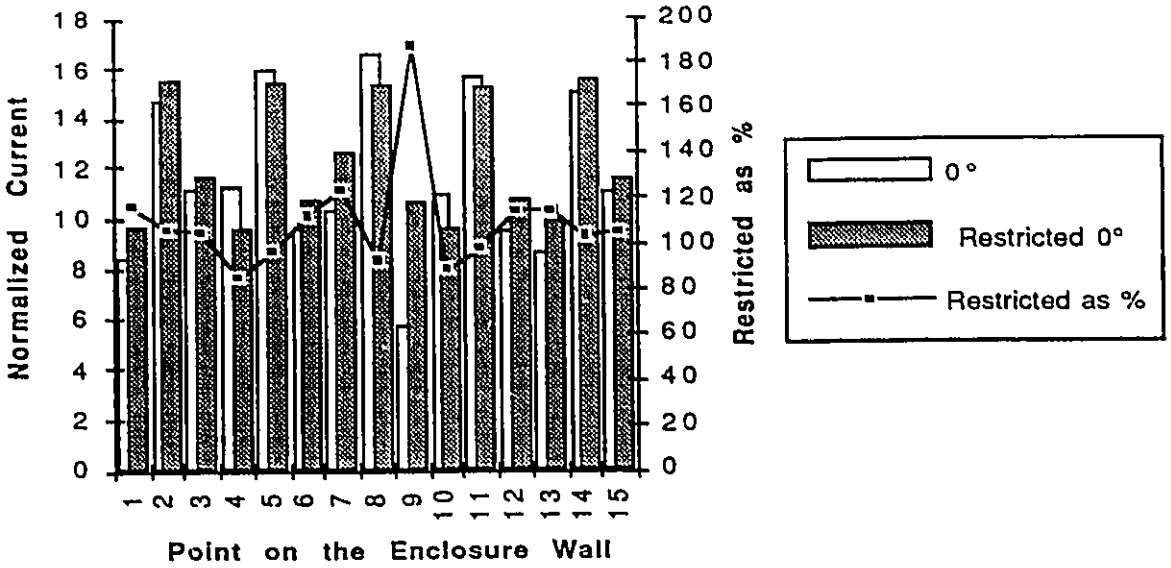

Figure 7.26: 9th Decile For Restricted Source Placement; High Frequency

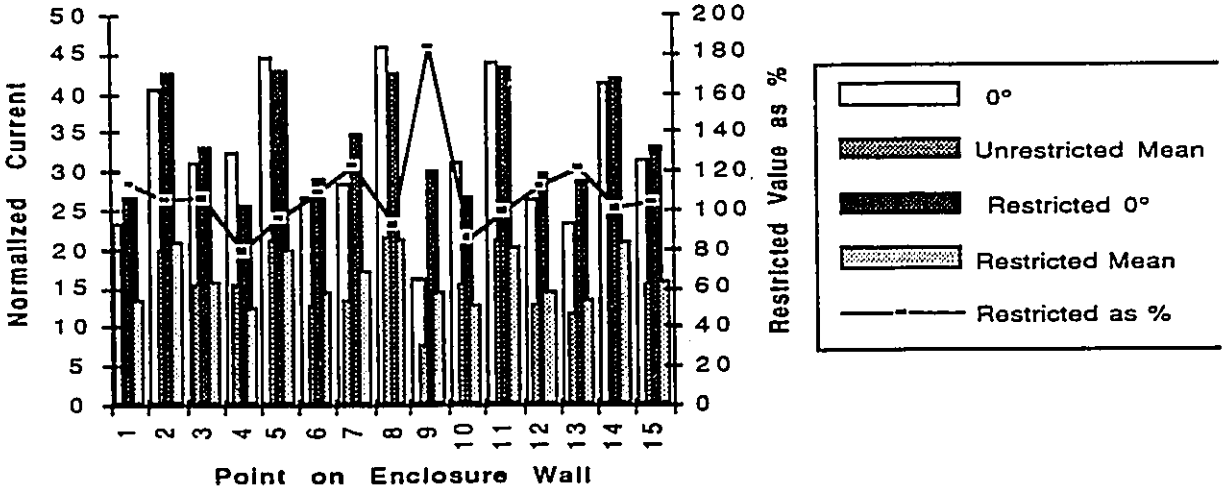

7.5 Conclusion

Stochastic techniques can be applied effectively to the characterization of shielded enclosures with multiple sources inside. This has been achieved using the mapping matrices of Chapter 6 in conjunction with Monte Carlo simulation.

The variable parameters are introduced through the addition of random variable multipliers in the mapping matrix. In the examples presented in this thesis these multipliers provide the probability distributions for existence, amplitude and phase.

Simulations were done at low, medium and high frequencies. This illustrated distinctly different trends in the multiple source problem in these frequency ranges. None of the trends justified the '10 log N' power sum approach to the multiple source problem.

At low frequencies the emissions distribution is dominated by sources close to the wall point of interest. In the example given, there is only a 10% likelihood that the peak total induced current due to multiple sources would exceed the level of the single closest source. The peak current level is always found at the bottom of the wall. A strategy of not placing apertures or connectors at the bottom of the enclosure would be quite effective for low frequency signals.

The influence of phase variation at low frequencies for the source component studied was contrary to expectations. Broader phase variation resulted in higher average currents on the wall. On the other hand the 9th decile amplitude was not effected by phase variations up to ±45°. The 9th decile amplitude was found to be twice that of the mean.

The disturbance levels and distribution due to medium frequency sources was quite different from that of the lower frequencies. The location of the maximum currents in the low fre-

quency case became a null in the medium case. The 9th decile amplitude was 80% higher than the mean.

The actual induced current value for the medium frequency case was a lot lower than for the lower frequency. Since higher frequencies are generally associated with higher EMI efficiencies this is contrary to expectations.

The wall currents due to high frequency sources induced a maximum along the horizontal axis of the wall. This contrasts to the medium frequency case wherein a null existed along the vertical axis.

Restrictions in the component layout to the central 75% of the pcb area was found to produce an 80% drop in mean emissions levels for low frequencies but had no noticeable effects in the high frequency range.

Division of the sources into cartesian components of electric and magnetic dipoles permits clear trends in the enclosure behavior to be distinguished in the multiple source problem. Use of mean and 9th decile magnitudes provides a view of the range of currents that are likely to be produced. Although the simulation modelled up to 16 devices, the total increase in current at any given point seldom went up by a factor of more than two.

Stochastic analysis has proven to be a powerful tool in the understanding of EMI problems in shielded enclosures.

Chapter 8

Apertures and Seams; Inhomogeneity in the Ideal Boundary Condition

8.1 Emissions from Small Apertures in Cavities

An ideal cavity will not have any radiated emissions since the electromagnetic fields are completely contained. Radiated emissions will be determined by the detailed make-up of the physical structure of the box. From the maximum current and electric field strength on the inner surface of the cavity it is possible to predict some of the more common emissions mechanisms from the enclosure. There are 3 major sources of leakage:

- Small apertures;
- Conductors penetrating the cavity; and
- Seams such as gaskets which have a finite impedance.

If the apertures are small, radiation may be calculated using perturbation techniques. This was a basic assumption for the use of the dyadic Green's function formulation of the problem. For larger apertures numerical techniques are generally required as explained in Chapter 5.

The dyadic Green's function is used to determine the field, current or charge distribution over a localized area on the boundary of the cavity. This information can then be used to obtain an estimate of the radiation that would occur if an aperture existed at that point. This may be either a deterministic quantity such as was calculated in Chapter 6, or a statistical one as calculated in Chapter 7.

Two approaches may be used for the small aperture approximations. The first relies on the equivalence principle [Lee 86] in which the aperture is represented by equivalent magnetic and electric dipoles. The second approach assumes that the field distribution over the aperture can be calculated from the values of surface current determined from ideal cavity solution. In this thesis the first approach will be used to calculate the field strength at 3m normal to the aperture in the enclosure.

8.2 Modelling Small Apertures

Following the method of [Mendez 76], the emissions from a small aperture may be given in terms of an equivalent electric or magnetic dipole on the wall of the enclosure. These can be calculated from the electric and magnetic field distributions (or currents) at the cavity boundary. This is a very simple model in which the aperture in the enclosure is represented as an aperture in an infinite plane. If this model is not adequate in a real world application, the source currents and fields driving the aperture which were calculated using the methods of the previous sections may be applied to a more representative numerical model of the radiator.

Figure 8.1: Rectangular Enclosure with Aperture

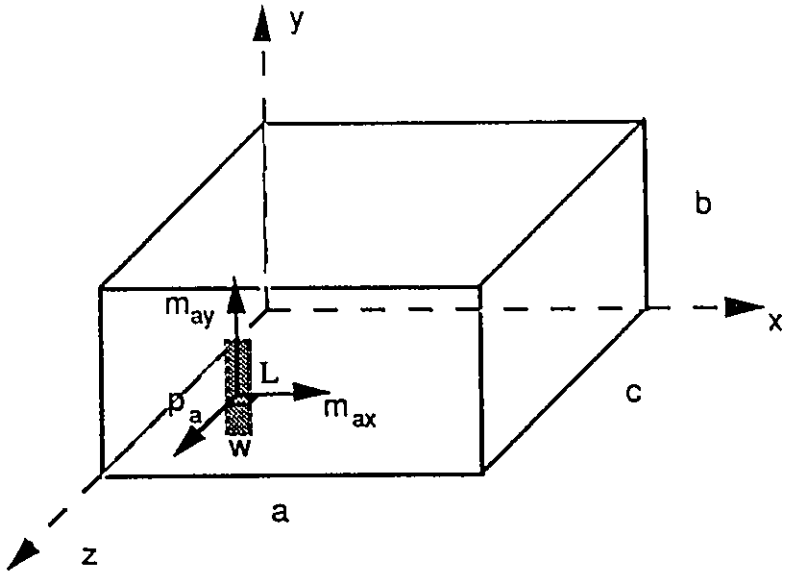

The aperture equivalent dipoles are derived from the electric and magnetic fields on the wall using the equations [Cooray 91-1]:

$$\bar{p}_a = \varepsilon\, \alpha_{e,zz} E_z(\bar{r})\,\hat{z} \tag{8-1}$$

$$\bar{m}_a = -\,\bar{\bar{\alpha}}_m \cdot \left(H_x(\bar{r})\hat{x} + H_y(\bar{r})\hat{y}\right) \tag{8-2}$$

Applying the boundary condition relating magnetic field to current yields

$$\bar{J}_s = \hat{n} \times \bar{H} \tag{8-3}$$

so that equation (8-2)becomes:

$$\bar{m}_a = -\,\bar{\bar{\alpha}}_m \cdot \left(J_y(\bar{r})\,\hat{x} - J_x(\bar{r})\,\hat{y}\right) \tag{8-4}$$

where:

(8-5)

$$\overline{\overline{\alpha}}_m = \alpha_{m,xx}\,\hat{x}\hat{x} + \alpha_{m,yy}\,\hat{y}\hat{y}$$

For a single slot aperture in which l and w are the length and width of the aperture respectively, with L >> w, the α terms are given by:

(8-6)

$$\alpha_{m,xx} = \frac{\pi L^3}{24\,\ln(4L/w) - 1},\ \alpha_{m,yy} = \frac{\pi}{16}\,w^2L,\ \ \alpha_{e,zz} = \frac{\pi}{16}\,w^2L,$$

If the aperture is loaded with sheet impedance Z_s, the value of $\alpha_{e,zz}$ remains the same but the value of α_m is modified to give:

(8-7)

$$\overline{\overline{\alpha}}'_m = \left(1 + \frac{2}{3\pi}\frac{j\omega L_a}{Z_s}\right)^{-1}\overline{\overline{\alpha}}_m$$

where the effective length L_a is given in terms of the aperture area (A), perimeter (p) and the dielectric constant of the loading material:

(8-8)

$$L_a = \mu_0\frac{A}{P}$$

8.3 Radiated Field From a Small Aperture

Following the method of [Lee 86], the electric field (E^d) and magnetic field (H^d) at distance (r) from their origin are given by equations (8-9) and (8-10) respectively.

(8-9)

$$\overline{E}^d = -\frac{1}{\varepsilon}\nabla\times\left[\overline{p}_a\times\nabla G(\overline{r})\right] + j\omega\mu\overline{m}_a\times\nabla G(\overline{r})$$

(8-10)

$$\overline{H}^{d}(\bar{r}) = -j\omega\overline{p}_a \times \nabla G(\bar{r}) - \nabla \times \left[\overline{m}_a \times \nabla G(\bar{r})\right]$$

Where the function G(r) is the freespace Green's function given by:

(8-11)

$$G(\bar{r}) = \frac{\varepsilon^{-jkr}}{4\pi r}$$

Since the equations for electric field and current are given in terms of closed form equations in Chapter 5, the curl operation in equations (8-9) and (8-10) may be evaluated explicitly.

Figure 8.2: **Emissions at 100 MHz, Unloaded Aperture**

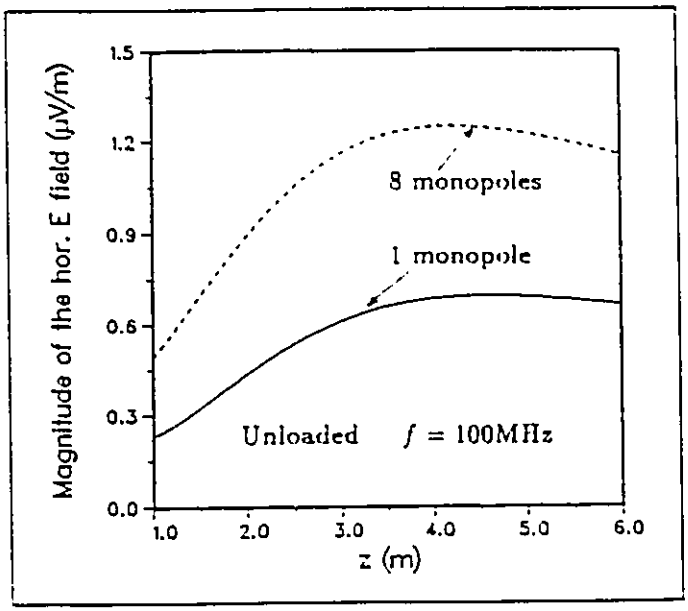

Figure 8.3: Emissions at 100 MHz, Conductively Loaded Aperture

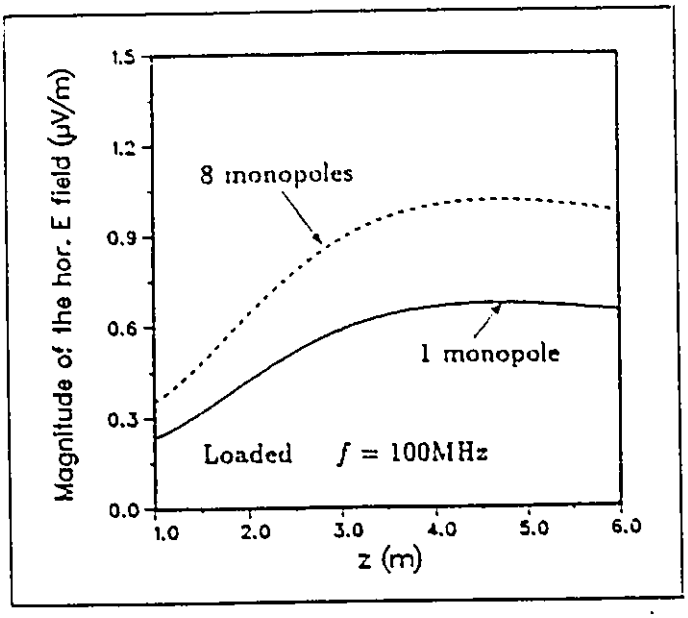

Figure 8.4: Emissions at 1 GHz, Unloaded Aperture

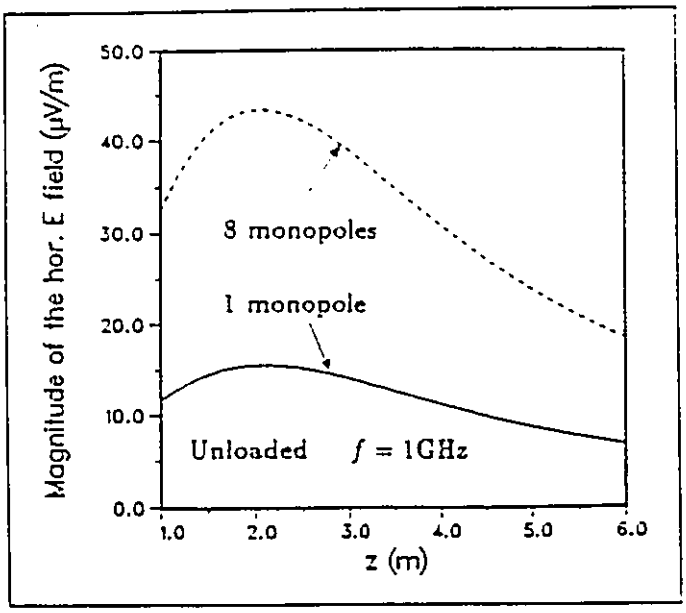

Figure 8.5: Emissions at 1 GHz, Conductively Loaded Aperture

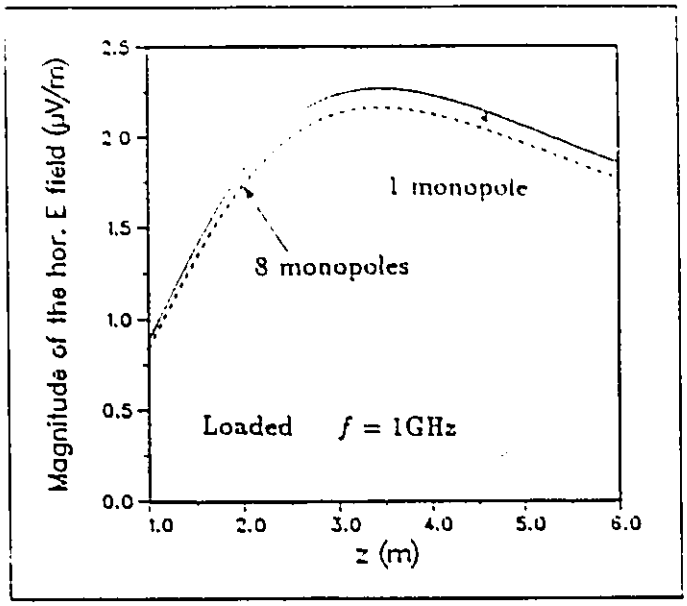

Figure 8.3 through Figure 8.5 show the radiation from a rectangular enclosure with an aperture on one of its walls as shown in Figure 8.1. In this case the source is located slightly above the floor of the cavity. This permits the use of electric dipole moments in all three directions. The continuous curve is for an enclosure with a single source with x,y and z components of electric moment, each of 0.01 A-m. This source is located at (0.05, 0.12, 0.14).

The dashed curve represents the radiated fields due to 8 monopole sources. The first being as above, the rest spaced every 20 mm in the x direction and having a 40° phase shift relative to the preceding one.

The radiated electric field polarization is parallel to the length (L) of the aperture. The rectangular enclosure has dimensions a = b = c = 0.2 m, and the aperture has dimensions L = 0.1 m w = 0.01 m. The location of the aperture is given by (0.0, 0.1, 0.1). The plots in Figure 8.2 and Figure 8.4 are for enclosures with unloaded apertures at 100 MHz and 1GHz respec-

tively. The plots in Figure 8.3 and Figure 8.5 are for enclosures with loaded apertures with a conductivity of 1000 mho/m.

Figure 8.5 shows that at high frequencies the emissions from eight sources gives a lower emissions level than the emissions from a single source. This is consistent with the deterministic and statistical analysis of the previous chapters.

8.4 Conclusion

The magnitudes and directions of the electromagnetic disturbances on the inner boundary of an enclosure may be used as the excitation parameters for perturbation models such as the dipole equivalent small aperture model presented in this chapter. A similar approach may be used for wires penetrating the cavity or for seams and arrays of holes.

Shielding effectiveness of a cavity may be calculated using parameters that are important in the engineering of a shielded enclosure and in a manner that truly reflects the overall EMI performance of the equipment.

The enclosure leakage models may either be used with deterministic field and current values calculated for a specific source distribution or with probabilistic data such as that shown in the previous chapter.

There are many other factors that must be taken into account to create a full representation of the emissions from a complex system. Some of these have been touched on in the introductory chapters, however, a solid representation of the emissions from the shielded enclosures that surround the active components in an electronic design is a major step in engineering electromagnetic compatibility into equipment.

Appendix I

List of Abreviations

Abbreviation	Meaning
AMI	Alternate-mark-inversion or bipolar code
ANSI	American National Standards Institute
APD	Amplitude probability distribution
ASIC	Application specific integrated circuit
CDF	Cumulative distribution function
CISPR	Committee International Speciale de Perturbations Radioelectrique
EM	Electromagnetic
EMC	Electromagnetic compatibility
EMI	Electromagnetic interference
ETSI	European Telecommunications Standards Institute
EUA	Equipment under analysis
EUT	Equipment under test
IC	Integrated circuit
I/O	Input/ Output
PCB	Printed circuit board
PCP	Printed circuit pack
PDF	Probability density function
RF	Radio frequency

Appendix II

Review of Random Processes

A random process is termed "stationary" if an observation of the process in the time interval (t_o, t_1) exhibits the same type of random behavior as an observation in some other time interval $(t_o + \tau, t_1 + \tau)$. Formally this means that the random process X(t) is stationary if the joint Cumulative Distribution Function (CDF) of $X(t_1), X(t_2), \ldots, X(t_k)$ is the same as that of $X(t_1 + \tau), X(t_2 + \tau), \ldots, X(t_k + \tau)$ for all time shifts τ, all k and all choices of sample times $t_1, t_2, \ldots, t_k$. This condition can be considered to hold for the period of time over which a given interference measurement is made.

The CDF of a random variable X is defined as the probability of the event $\{X < x\}$:

(AII-1)

$$F_x(x) = P[X \leq x] \quad \text{for } -\infty < x < +\infty$$

It is frequently difficult to prove true stationarity, however the mean value of the process, mx(t), can often be determined to be constant. That is:

(AII-2)

$$m_x(t) = m \quad \text{for all t,}$$

and the autocovariance, $C_x(t_1, t_2)$ can be shown to be a function of the difference in sampling time rather than the specific values. That is:

(AII-3)

$$C_x(t_1, t_2) = C_x(t_1 - t_2) \text{ for all } t_1, t_2$$

In this case the process is referred to as Wide-Sense Stationary (WSS).

If a random process X(t) is WSS with mean m_x and autocorrelation function $R_x(t)$, then the power spectral density, $S_x(f)$, of X(t) is given by the Fourier transform of the autocorrelation function:

(AII-4)

$$S_x(f) = F\{R_x(\tau)\} = \int_{-\infty}^{\infty} R_x(\tau) e^{-j2\pi f\tau} d\tau$$

Where the autocorrelation function, $R_x(t_1, t_2)$ is defined as the joint moment of the random process X(t) at $t = t_1, t_2$ which is given by:

(AII-5)

$$R_x(t_1, t_2) = E[X(t_1)X(t_2)] = \int_{-\infty}^{\infty} \int_{-\infty}^{\infty} xy f_{X(t_1),X(t_2)}(x,y) dx dy$$

where $f_{X(t1),X(t2)}(x,y)$ is the second order probability density function (pdf) of X(t). The pdf is defined as the derivative of the CDF:

(AII-6)

$$f_x(x) = \frac{dF_x(x)}{dx}$$

As is evident from this brief review the autocorrelation function can be found from the power spectral density through the use of the inverse Fourier transform.

The second moment of the random process X(t) is given by:

(AII-7)

$$E[X^2(t)] = R_x(0) = \int_{-\infty}^{\infty} S_x(f)\, df$$

which is the sum of the power spectral density over all frequencies or the average power of X(t).

The autocorrelation and autocovariance functions are related by:

(AII-8)

$$R_x(\tau) = C_x(\tau) + m_x^2$$

and hence the power spectral density can be expressed in terms of autocovariance as:

(AII-9)

$$\begin{aligned} S_x(\tau) &= F\ \{C_x(\tau) + m_x^2\} \\ &= F\ \{C_x(\tau)\} + m_x^2\delta(f) \end{aligned}$$

where m_x is the "dc" component of the random variable given by X(t).

In stochastic processes the probability density functions assume that an infinite number of the process are occurring simultaneously. This is referred to as the ensemble of the process.

An ergodic process is one in which the time average of a single instance of the process converges to the ensemble average as time goes to infinity

Appendix III

Characteristics of Common

Telecommunications Protocols

AIII.1 Introduction

This appendix contains data that is useful in the modelling of different data signals.

AIII.2 Basic Rate ISDN

Table AIII.1 ISDN S/T Interface Specification

Line Rate	
Line Code	Bipolar with Alternate Mark Inversion (BAMI)
Pulse Amplitude:	5V (+/- 10%)
Pulse Width:	
Rise and Fall Times:	4.5 (+/-1.5 ns)
Max. Undershoot	Less than 10% of pulse amplitude
Transmitted Signal:	
Power Level:	

Figure AIII.1: ISDN S/T Loop Waveform

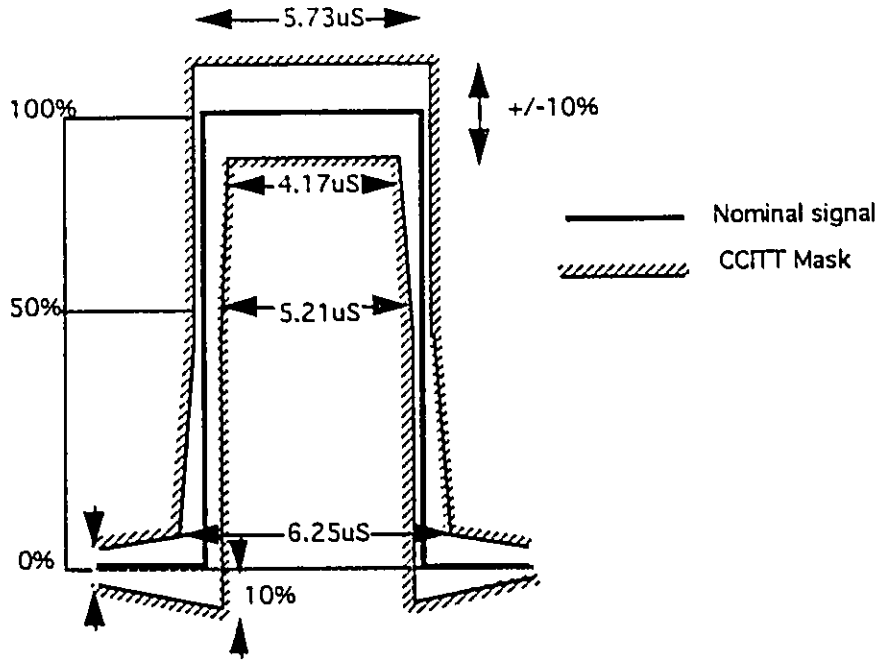

Theoretical and measured spectra for the ISDN U and T interfaces are given. Emission potential relative to CISPR receiver are provided.

AIII.3 DS1

4 types of interfaces based on services offered over the link. This analysis will concentrate on Type I for which a 1.544 Mb/s digital transmission Interface network facility connects customer location to customer location. Types II to IV consist of digital subrate carriers multiplexed onto the DS-1 channel. For more information refer to [ComCan 90]

Table AIII.2 **DS-1 Interface Specification**

Line Rate	1.544 Mb/s (Nominal)
Line Code	Bipolar with Alternate Mark Inversion (BAMI)
Pulse Amplitude:	3.0 (+/-0.7V)
Pulse Width:	
Rise and Fall Times:	4.5 (+/-1.5 ns)
Max. Undershoot	Less than 40% of pulse amplitude
Transmitted Signal:	No more than 15 spaces between successive marks and average mark density shall be at least 1 in 8 for Type I signals
Power Level:	For a transmitted pattern of all "ones": a) the power at 772 kHz shall not reach +19 dBm , b) power at 154-kHz shall be 25 dB less. Both measurements are made with a 3 kHz pass band averaged over 3 seconds

Figure AIII.2: **DS-1 Waveform Mask**

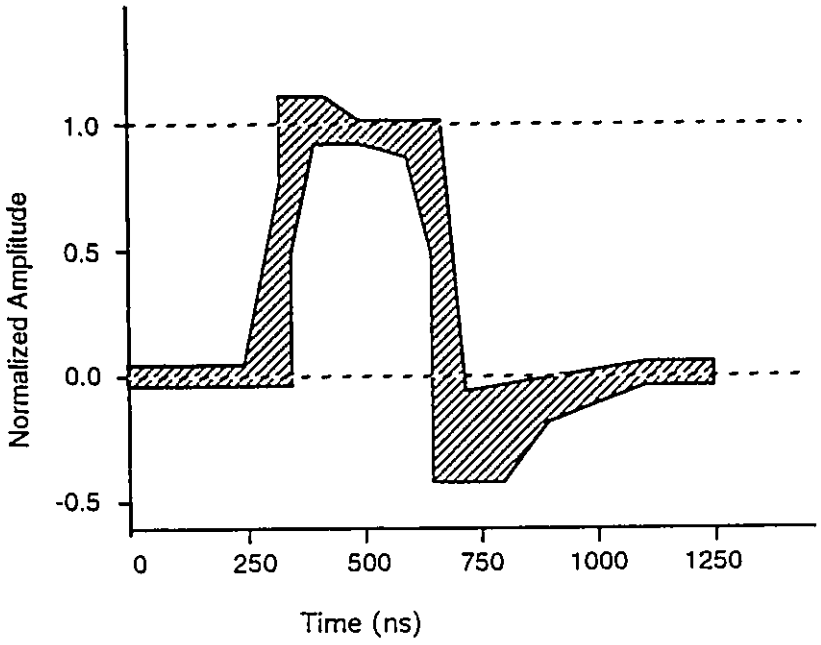

AIII.4 DS3

The DS-3 protocol is the first of the transmission protocols under analysis for which the basic rate of the transmission (44.7 MHz) falls within the emissions range under investiga-

tion. This is a very common signal and, unlike SONET, tends to occur in large quantities within a single piece of equipment.

Table AIII.3 DS-3 Interface Specification

Line Rate	44.7 36 Mb/s (+/- 2 ppm)
Line Code	Bipolar with 3 Zero Substitution (B3ZS)
Pulse Amplitude:	between 0.36 V and 0.85 V peak
Pulse Width:	see template
Rise and Fall Times:	see template
Max. Undershoot Transmitted Signal:	
Power Level:	For an all-ones transmitted pattern, the power in a band no wider than 3 kHz centred at 22.368 MHz shall be -1.8 to + 5.7 ppm.

Figure AIII.3: DS-3 Waveform Mask

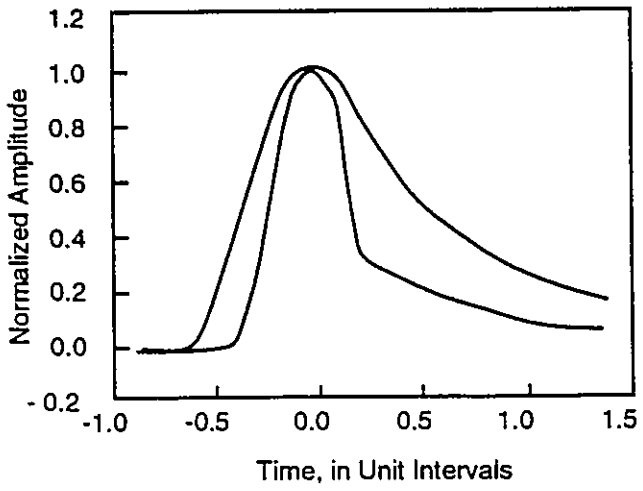

AIII.5 Synchronous Optical Network Transport Systems (SONET)

The SONET is the latest and fastest standard for telecommunications transmission. It is described in detail in [Bellcore 90]. Although predominantly an optical protocol, there are two sources of electrical energy associated with it:

- There are copper implementations of the same protocol at STS-1 and STS-3 rates of 51.840 Mb/s and 622 MBit/s respectively; and
- Driver circuitry inside the EUA that feeds the optical and electrical interfaces functions at these same speeds.

The power level at the interface is specified in terms of a wideband power measurement of a quasi-random signal with nominal 50% mark probability.

Table AIII.4 STS-1 Interface Specification

Line Rate	51.840 Mb/s (Nominal
Line Code	Bipolar with 3 Zero Substitution (B3ZS)
Pulse Amplitude:	+/- 1.75V (+/- 10%)
Pulse Width:	9.64 (+/- 0.96 ns)
Rise and Fall Times:	4.5 (+/-1.5 ns)
Max. Undershoot	Less than 10% of pulse amplitude
Flat Loss	4.6 dB
Transmitted Signal:	Nominal 50% duty cycle Return to Zero (RZ) pulse. The electrical signal is scrambled before encoding
Power Level:	A wide-band power level, as measured at the STS-1 interface using a low-pass filter with a 3 dB cutoff frequency of at least 200 MHz shall be between -2.7 dBm and 4.7 dBm

Appendix IV

Computer Programs

IV.1 Introduction

This appendix contains the source code used to generate the mapping matrix data in Section 6.4. and the Monte Carlo simulations for Chapter 7.

IV.2 Code Used To Generate Mapping Matrices

These programs were written in Think C and run on an Apple Powerbook computer. The code is intended to be completely ANSI C compatible and should run on any platform that runs C in accordance with the ANSI standard.

IV.2.1 Horizontal Current Due to Parallel Magnetic Dipole

```
/*************************************************************************
```

* This program calculates the mapping coefficients for an x-directed current on the wall for due to a magnetic dipole source parallel to the wall. This is an implementation of the x-component of equation (5-48)

```
*/


#include <math.h>
#include <stdio.h>

#define HEIGHT          0.03  /*height of module normalized to lambda*/
#define WIDTH           0.10  /*width of module normalized to lambda*/
#define DEPTH           0.10  /*depth of module normalized to lambda*/
#define DIVH            3     /*number of divisions in height*/
#define DIVW            4     /*number of divisions in width*/
#define DIVDB           4     /*number of divisions in depth of bottom*/
#define DIVDW           5     /*number of divisions in depth of wall*/
#define FILESIZ         240         /*size of final data file*/
#define MMODES          10          /*number of modes in m */
#define NMODES          10          /*number of modes in n */
#define APPROX          35          /*number of n+m modes before approximation of sinh*/
#define MAP       "JxHx1"/*mapping of current in x direction due to H source in z direction */
/*Magic Numbers*/
#define pi              3.141593
#define Zo              376.7       /*impedance of free space (ohms)*/
#define c               2.998e8     /*speed of light (metres/sec)*/
#define uo              12.566e-7/*permeability of free-space (henry/metre)*/
#define eo              8.854e-12/*permitivity of free-space (farad/metre)*/

main ()
{
FILE *map;
/* integer variables */
int i,yi,xi,r,s;        /* counter variables */
int m,n;                        /* mode counters */
int aps,scs;            /* final array dimensions*/
/* float variables */
float k2,kc2,kk;                /* free space propagation coeficient squared */
float kxp;                      /* coefficients for source terms */
float dy,dxx,dx,dz,y,xx,x,spd,spw;/* increment of movement along boundary */
float kyy,kxx;          /* propagation constant times aperture position y */
float kg,kg2,ky,kx;  /* waveguide propagation constant */
float em;                       /* multiplier coefficient */
/* double variables */
double con;                     /* convergence terms */
double denom;           /* hyperbolic denominator */
/* array variables */
```

```
float JxHpp[FILESIZ];/*mapping matrix*/
        for (i = 0; i < FILESIZ; ++i) JxHpp[i] = 0.0; /* initialize arrays
                                                to zero */
        k2 = 4*pi*pi;           /*propagation constant normalized to lambda*/
        dy = HEIGHT/DIVH;
        dx = DEPTH/DIVDB;
        dxx = DEPTH/DIVDW;
        dz = WIDTH/DIVW;
/* calculate terms with modal variance */
        for (m = 0; m < MMODES; m++)
                for (n = 1; n < NMODES; n++)
                        ky = n*pi/HEIGHT;
                        kx = m*pi/DEPTH;
                        kc2 = ky*ky + kx*kx;
                        kg2 = kc2 - k2;

/* rotate through source points */

                        for (r = 0; r < DIVDB; r++)
                        {
                                spd = dx/2 + r*dx;
                                kxp = kx*spd;
                                for (s = 0; s < DIVW; s++)
                                {
                                        spw = dz/2 + s*dz;
                                        if (kg2 >= 0.0)
                                        {
                                                kg = sqrt(kg2);
                                                kk = kg*kx*ky/(kc2*k2);
                                                if (kg <= APPROX)
                                                {
                                                denom = sinh(kg*WIDTH);
                                                con = kk*cosh(kg*spw)*sin(kx*spd)/denom;
                                                }
                                                else con = kk*(exp(kg*(spw - WIDTH)) + exp(-kg*(spw
                                                + WIDTH)))*sin(kx*spd);
                                        }
                                        else
                                        {
                                                kg = sqrt(-kg2);
                                                kk = kg*kg*kx*ky/(kc2*k2);
                                                if (kg <= APPROX)
                                                {
```

```
                                denom = sin(kg*WIDTH);
                                con = kk*cos(kg*spw)*sin(kx*spd)/denom;
                                }
                                else  printf("m+n too low");
                        }

/* rotate through aperture points */

                        for (xi = 0; xi < DIVDW; xi++)
                        {
                                xx = dxx/2 + xi*dxx;
                                kxx = xx*kx;
                                for (yi = 0; yi < DIVH; yi++)
                                {
                                i = yi + xi*DIVH + s*DIVH*DIVDW + r*DIVH*DIVDW*DIVW;
                                y = dy/2 + yi*dy;
                                kyy = y*ky;
                                if (n == 0) em = 2.0;
                                else em = 4.0;
                                JxHpp[i] += em*con*cos(kxx)*sin(kyy);
                                }/*xi*/
                        }       /*yi*/
                }       /*s*/
        }       /*r*/
    }       /*n*/
}       /*m*/

    for (i = 0; i < FILESIZ; i++) JxHpp[i] = -JxHpp[i]/(DEPTH*HEIGHT);

    map = fopen(MAP, "a");
    i = 0;
    aps = DIVH*DIVDW;
    scs = DIVW*DIVDB;

    for (yi = 0; yi < scs; yi++)
    {
        for (xi = 0; xi < aps; xi++)
        {
            if ( yi == 0)
            {
                if ( xi == 0) fprintf(map,"{{%.4f,",JxHpp[i]);
                else if ( xi == (aps -1))
                    fprintf(map,"%.0f},\n",JxHpp[i]);
```

```
                else fprintf(map,"%.0f,",JxHpp[i]);
            }
            else if (yi == (scs -1))
            {
                if ( xi == 0) fprintf(map,"{%.0f,",JxHpp[i]);
                else if ( xi == (aps -1))
                    fprintf(map,"%.0f}",JxHpp[i]);
                else fprintf(map,"%.0f,",JxHpp[i]);
            }
            else
            {
                if ( xi == 0) fprintf(map,"{%.0f,",JxHpp[i]);
                else if ( xi == (aps -1))
                    fprintf(map,"%.0f},\n",JxHpp[i]);
                else fprintf(map,"%.0f,",JxHpp[i]);
            }   /* end filling in middle rows */
            i++;
        }   /* end rotating through sources */
    }   /* end rotating through apertures */
    fclose(map);
}                                   /*close main*/
```

IV.2.2 Vertical Current Due to Parallel Magnetic Dipole

This program implements the y-directed portion of equation (5-48).

```
*
 * This program calculates the vertical current  on the wall for a
 * Magnetic Dipole source parallel to the wall.
 */

#include <math.h>
#include <stdio.h>

#define HEIGHT      0.03  /*height of module normalized to lambda*/
#define WIDTH       0.1       /*width of module normalized to lambda*/
#define DEPTH       0.1       /*depth of module normalized to lambda*/
#define DIVH        3         /*number of divisions in height*/
#define DIVW        4         /*number of divisions in width*/
```

```
#define DIVDB       4           /*number of divisions in depth of bottom*/
#define DIVDW       5           /*number of divisions in depth of wall*/

#define FILESIZ     240         /*size of final data file*/

#define MMODES      10          /*number of modes in m */
#define NMODES      10          /*number of modes in n */
#define APPROX      35          /*number of n+m modes before approximation of sinh*/


#define MAP                 "JyHx1c"/*mapping of current in x direction due to
                                H source in z direction */

/*Magic Numbers*/

#define pi          3.141593
#define Zo          376.7       /*impedance of free space (ohms)*/
#define c           2.998e8     /*speed of light (metres/sec)*/
#define uo          12.566e-7/*permeability of free-space (henry/metre)*/
#define eo          8.854e-12/*permitivity of free-space (farad/metre)*/

main ()
{

FILE *map;

/* integer variables */

int i,yi,xi,r,s;        /* counter variables */
int m,n;                    /* mode counters */
int aps,scs;            /* final array dimensions*/

/* float variables */

float k2,kc2,kk;            /* free space propagation coeficient squared */
float kxp;                  /* coefficients for source terms */
float dy,dxx,dx,dz,y,xx,x,spd,spw;/* increment of movement along boundary */
float kyy,kxx;          /* propagation constant times aperture position y */
float kg,kg2,ky,kx;  /* waveguide propagation constant */
float en;                   /* multiplier coefficient */

/* double variables */
```

```
double con;                    /* convergence terms */
double denom;                  /* hyperbolic denominator */

/* array variables */

float JyHpp[FILESIZ];/*mapping matrix*/

        for (i = 0; i < FILESIZ; ++i) JyHpp[i] = 0.0; /* initialize arrays to zero */
        k2 = 4*pi*pi;          /* free space propagation constant normalized to lambda*/

        dy = HEIGHT/DIVH;
        dx = DEPTH/DIVDB;
        dxx = DEPTH/DIVDW;
        dz = WIDTH/DIVW;

/* calculate terms with modal variance */

        for (m = 1; m < MMODES; m++)
        {
                for (n = 0; n < NMODES; n++)
                {
                        ky = n*pi/HEIGHT;
                        kx = m*pi/DEPTH;
                        kc2 = ky*ky + kx*kx;
                        kg2 = kc2 - k2;

/* rotate through source points */

                        for (r = 0; r < DIVDB; r++)
                        {
                                spd = dx/2 + r*dx;
                                kxp = kx*spd;
                                for (s = 0; s < DIVW; s++)
                                {
                                        spw = dz/2 + s*dz;
                                        if (kg2 >= 0.0)
                                        {
                                                kg = sqrt(kg2);
                                                kk = kg*kx*kx/(kc2*k2);
                                                if (kg <= APPROX)
                                                {
                                                denom = sinh(kg*WIDTH);
                                                con = kk*cosh(kg*spw)*sin(kx*spd)/denom;
```

```
                                        }
                                        else con = kk*(exp(kg*(spw - WIDTH)) + exp(-kg*(spw + WIDTH)))*-
sin(kx*spd);
                                }
                                else
                                {
                                        kg = sqrt(-kg2);
                                        kk = kg*kg*kx*kx/(kc2*k2);
                                        if (kg <= APPROX)
                                        {
                                        denom = sin(kg*WIDTH);
                                        con = kk*cos(kg*spw)*sin(kx*spd)/denom;
                                        }
                                        else  printf("m+n too low");
                                }

/* rotate through aperture points */

                                for (xi = 0; xi < DIVDW; xi++)
                                {
                                        xx = dxx/2 + xi*dxx;
                                        kxx = xx*kx;
                                        for (yi = 0; yi < DIVH; yi++)
                                        {
                                        i = yi + xi*DIVH + s*DIVH*DIVDW + r*DIVH*DIVDW*DIVW;
                                        y = dy/2 + yi*dy;
                                        kyy = y*ky;
                                        if (m == 0) en = 2.0;
                                        else en = 4.0;
                                        JyHpp[i] += en*con*sin(kxx)*cos(kyy);
                                        }/*xi*/
                                }       /*yi*/
                        }       /*s*/
                }       /*r*/
        }       /*n*/
}       /*m*/

for (i = 0; i < FILESIZ; i++) JyHpp[i] = JyHpp[i]/(DEPTH*HEIGHT);

map = fopen(MAP, "a");
i = 0;
aps = DIVH*DIVDW;
scs = DIVW*DIVDB;
```

```
        for (yi = 0; yi < scs; yi++)
        {
                for (xi = 0; xi < aps; xi++)
                {
                        if ( yi == 0)
                        {
                                if ( xi == 0) fprintf(map,"{{%.f,",JyHpp[i]);
                                else if ( xi == (aps -1)) fprintf(map,"%.f},\n",JyHpp[i]);
                                else fprintf(map,"%.f,",JyHpp[i]);
                        }
                        else if (yi == (scs -1))
                        {
                                if ( xi == 0) fprintf(map,"{%.f,",JyHpp[i]);
                                else if ( xi == (aps -1)) fprintf(map,"%.f}}",JyHpp[i]);
                                else fprintf(map,"%.f,",JyHpp[i]);
                        }
                        else
                        {
                                if ( xi == 0) fprintf(map,"{%.f,",JyHpp[i]);
                                else if ( xi == (aps -1)) fprintf(map,"%.f},\n",JyHpp[i]);
                                else fprintf(map,"%.f,",JyHpp[i]);
                        }       /* end filling in middle rows */
                        i++;
                }       /* end rotating through sources */
        }       /* end rotating through apertures */
        fclose(map);
}                                       /*close main*/
```

IV.2.3 Vertical Current Due to Perpendicular Magnetic Dipole

This program implements the y-component of equation (5-50).

```
*
 * This program calculates the verticalcurrent mapping on the wall for a
 *  H field source perpendicular to the wall.
 */

#include <math.h>
#include <stdio.h>
```

```
#define HEIGHT      1.26  /*height of module normalized to lambda*/
#define WIDTH       4.20  /*width of module normalized to lambda*/
#define DEPTH       4.20  /*depth of module normalized to lambda*/
#define DIVH        3           /*number of divisions in height*/
#define DIVW        4           /*number of divisions in width*/
#define DIVDB       4           /*number of divisions in depth of bottom*/
#define DIVDW       5           /*number of divisions in depth of wall*/

#define FILESIZ     240         /*size of final data file*/

#define MMODES      10          /*number of modes in m */
#define NMODES      10          /*number of modes in n */
#define APPROX      35          /*number of n+m modes before approximation of sinh*/


#define MAP                 "JyHzRest42"/*mapping of current in x direction due to
                                H source in z direction */

/*Magic Numbers*/

#define pi          3.141593
#define Zo          376.7       /*impedance of free space (ohms)*/
#define c           2.998e8     /*speed of light (metres/sec)*/
#define uo          12.566e-7/*permeability of free-space (henry/metre)*/
#define eo          8.854e-12/*permitivity of free-space (farad/metre)*/

main ()
{

FILE *map;

/* integer variables */

int i,yi,xi,r,s;        /* counter variables */
int m,n;                    /* mode counters */
int aps,scs;            /* final array dimensions*/

/* float variables */

float k2,kc2,kk;            /* free space propagation coeficient squared */
float kxp;                  /* coefficients for source terms */
float dy,dxx,dx,dz,y,xx,x,spd,spw;/* increment of movement along boundary */
```

```
float kyy,kxx;              /* propagation constant times aperture position y */
float kg,kg2,ky,kx;  /* waveguide propagation constant */
float em;                   /* multiplier coefficient */

/* double variables */

double con;                 /* convergence terms */
double denom;          /* hyperbolic denominator */

/* array variables */

float JyHzRes[FILESIZ];/*mapping matrix*/

      for (i = 0; i < FILESIZ; ++i) JyHzRes[i] = 0.0; /* initialize arrays to zero */
      k2 = 4*pi*pi;        /* free space propagation constant normalized to lambda*/

      dy = HEIGHT/DIVH;
      dx = DEPTH/(2*(DIVDB-1));
      dxx = DEPTH/DIVDW;
      dz = WIDTH/(2*(DIVW-1));

/* calculate terms with modal variance */

      for (m = 1; m < MMODES; m++)
      {
            for (n = 0; n < NMODES; n++)
            {
                  ky = n*pi/HEIGHT;
                  kx = m*pi/DEPTH;
                  kc2 = ky*ky + kx*kx;
                  kg2 = kc2 - k2;

/* rotate through source points */

                  for (r = 0; r < DIVDB; r++)
                  {
                        spd = DEPTH/DIVDB + r*dx;
                        kxp = kx*spd;
                        for (s = 0; s < DIVW; s++)
                        {
                              spw = WIDTH/DIVW + s*dz;
                              if (kg2 >= 0.0)
                              {
```

```
                                        kg = sqrt(kg2);
                                        kk = kx/k2;
                                        if (kg <= APPROX)
                                        {
                                        denom = sinh(kg*WIDTH);
                                        con = kk*sinh(kg*spw)*cos(kx*spd)/denom;
                                        }
                                        else con = kk*(exp(kg*(spw - WIDTH)) - exp(-kg*(spw + WIDTH)))*-
cos(kx*spd);
                                }
                                else
                                {
                                        kg = sqrt(-kg2);
                                        kk = kx/k2;
                                        if (kg <= APPROX)
                                        {
                                        denom = sin(kg*WIDTH);
                                        con = kk*sin(kg*spw)*cos(kx*spd)/denom;
                                        }
                                        else  printf("m+n too low");
                                }

/* rotate through aperture points */

                                for (xi = 0; xi < DIVDW; xi++)
                                {
                                        xx = dxx/2 + xi*dxx;
                                        kxx = xx*kx;
                                        for (yi = 0; yi < DIVH; yi++)
                                        {
                                        i = yi + xi*DIVH + s*DIVH*DIVDW + r*DIVH*DIVDW*DIVW;
                                        y = dy/2 + yi*dy;
                                        kyy = y*ky;
                                        if (n == 0) em = 2.0;
                                        else em = 4.0;
                                        JyHzRes[i] += em*con*sin(kxx)*cos(kyy);
                                        }/*xi*/
                                }       /*yi*/
                        }       /*s*/
                }       /*r*/
        }       /*n*/
}       /*m*/
```

```
    for (i = 0; i < FILESIZ; i++) JyHzRes[i] = JyHzRes[i]/(DEPTH*HEIGHT);

    map = fopen(MAP, "a");
    i = 0;
    aps = DIVH*DIVDW;
    scs = DIVW*DIVDB;

    for (yi = 0; yi < scs; yi++)
    {
        for (xi = 0; xi < aps; xi++)
        {
            if ( yi == 0)
            {
                if ( xi == 0) fprintf(map,"{{%.4f,",JyHzRes[i]);
                else if ( xi == (aps -1)) fprintf(map,"%.4f},\n",JyHzRes[i]);
                else fprintf(map,"%.4f,",JyHzRes[i]);
            }
            else if (yi == (scs -1))
            {
                if ( xi == 0) fprintf(map,"{%.4f,",JyHzRes[i]);
                else if ( xi == (aps -1)) fprintf(map,"%.4f}}",JyHzRes[i]);
                else fprintf(map,"%.4f,",JyHzRes[i]);
            }
            else
            {
                if ( xi == 0) fprintf(map,"{%.4f,",JyHzRes[i]);
                else if ( xi == (aps -1)) fprintf(map,"%.4f},\n",JyHzRes[i]);
                else fprintf(map,"%.4f,",JyHzRes[i]);
            }       /* end filling in middle rows */
            i++;
        }       /* end rotating through sources */
    }       /* end rotating through apertures */
    fclose(map);
}                                       /*close main*/
```

IV.2.4 Horizontal Current Due to Perpendicular Magnetic Moment

This program implements the x-component of equation (5-50).

```
*
 * This program calculates the current mapping on the wall for a
 *  H field source perpendicular to the wall.
 */

#include <math.h>
#include <stdio.h>

#define HEIGHT      0.03        /*height of module normalized to lambda*/
#define WIDTH       0.10        /*width of module normalized to lambda*/
#define DEPTH       0.10        /*depth of module normalized to lambda*/
#define DIVH                    3/*number of divisions in height*/
#define DIVW                    4/*number of divisions in width*/
#define DIVDB                   4/*number of divisions in depth of bottom*/
#define DIVDW                   5/*number of divisions in depth of wall*/

#define FILESIZ                 240/*size of final data file*/

#define MMODES      10          /*number of modes in m */
#define NMODES      10          /*number of modes in n */
#define APPROX      35          /*number of n+m modes before approximation of sinh*/


#define MAP             "JxHz1a"/*mapping of current in x direction due to
                                  H source in z direction */

/*Magic Numbers*/

#define pi          3.141593
#define Zo          376.7       /*impedance of free space (ohms)*/
#define c           2.998e8     /*speed of light (metres/sec)*/
#define uo          12.566e-7/*permeability of free-space (henry/metre)*/
#define eo          8.854e-12/*permitivity of free-space (farad/metre)*/

main ()
{

FILE *map;
```

```
/* integer variables */

int i,yi,xi,r,s;        /* counter variables */
int m,n;                        /* mode counters */
int aps,scs;            /* final array dimensions*/

/* float variables */

float k2,kc2,kk;                /* free space propagation coeficient squared */
float kxp;                      /* coefficients for source terms */
float dy,dxx,dx,dz,y,xx,x,spd,spw;/* increment of movement along boundary */
float kyy,kxx;          /* propagation constant times aperture position y */
float kg,kg2,ky,kx;  /* waveguide propagation constant */
float en;                       /* multiplier coefficient */

/* double variables */

double con;                     /* convergence terms */
double denom;           /* hyperbolic denominator */

/* array variables */

float JyHpp[FILESIZ];/*mapping matrix*/

        for (i = 0; i < FILESIZ; ++i) JyHpp[i] = 0.0; /* initialize arrays to zero */
        k2 = 4*pi*pi;           /* free space propagation constant normalized to lambda*/

        dy = HEIGHT/DIVH;
        dx = DEPTH/DIVDB;
        dxx = DEPTH/DIVDW;
        dz = WIDTH/DIVW;

/* calculate terms with modal variance */

        for (m = 0; m < MMODES; m++)
        {
                for (n = 1; n < NMODES; n++)
                {
                        ky = n*pi/HEIGHT;
                        kx = m*pi/DEPTH;
                        kc2 = ky*ky + kx*kx;
                        kg2 = kc2 - k2;
```

```
/* rotate through source points */

                for (r = 0; r < DIVDB; r++)
                {
                        spd = dx/2 + r*dx;
                        kxp = kx*spd;
                        for (s = 0; s < DIVW; s++)
                        {
                                spw = dz/2 + s*dz;
                                if (kg2 >= 0.0)
                                {
                                        kg = sqrt(kg2);
                                        kk = ky/k2;
                                        if (kg <= APPROX)
                                        {
                                        denom = sinh(kg*WIDTH);
                                        con = kk*sinh(kg*spw)*cos(kx*spd)/denom;
                                        }
                                        else con = kk*(exp(kg*(spw - WIDTH)) - exp(-kg*(spw + WIDTH)))*-
cos(kx*spd);
                                }
                                else
                                {
                                        kg = sqrt(-kg2);
                                        kk = ky/k2;
                                        if (kg <= APPROX)
                                        {
                                        denom = sin(kg*WIDTH);
                                        con = kk*sin(kg*spw)*cos(kx*spd)/denom;
                                        }
                                        else  printf("m+n too low");
                                }

/* rotate through aperture points */

                                for (xi = 0; xi < DIVDW; xi++)
                                {
                                        xx = dxx/2 + xi*dxx;
                                        kxx = xx*kx;
                                        for (yi = 0; yi < DIVH; yi++)
                                        {
                                        i = yi + xi*DIVH + s*DIVH*DIVDW + r*DIVH*DIVDW*DIVW;
```

```
                                y = dy/2 + yi*dy;
                                kyy = y*ky;
                                if (m == 0) en = 2.0;
                                else en = 4.0;
                                JyHpp[i] += en*con*cos(kxx)*sin(kyy);
                                }/*xi*/
                        }       /*yi*/
                }       /*s*/
        }       /*r*/
}       /*n*/
}       /*m*/

for (i = 0; i < FILESIZ; i++) JyHpp[i] = -JyHpp[i]/(DEPTH*HEIGHT);

map = fopen(MAP, "a");
i = 0;
aps = DIVH*DIVDW;
scs = DIVW*DIVDB;

for (yi = 0; yi < scs; yi++)
{
        for (xi = 0; xi < aps; xi++)
        {
                if ( yi == 0)
                {
                        if ( xi == 0) fprintf(map,"{{%.4f,",JyHpp[i]);
                        else if ( xi == (aps -1)) fprintf(map,"%.4f},\n",JyHpp[i]);
                        else fprintf(map,"%.4f,",JyHpp[i]);
                }
                else if (yi == (scs -1))
                {
                        if ( xi == 0) fprintf(map,"{%.4f,",JyHpp[i]);
                        else if ( xi == (aps -1)) fprintf(map,"%.4f}}",JyHpp[i]);
                        else fprintf(map,"%.4f,",JyHpp[i]);
                }
                else
                {
                        if ( xi == 0) fprintf(map,"{%.4f,",JyHpp[i]);
                        else if ( xi == (aps -1)) fprintf(map,"%.4f},\n",JyHpp[i]);
                        else fprintf(map,"%.4f,",JyHpp[i]);
                }       /* end filling in middle rows */
                i++;
        }       /* end rotating through sources */
```

```
        }       /* end rotating through apertures */
        fclose(map);
}                                       /*close main*/
```

IV.3 Code For Mathematica Simulation

This code was written on a Mac II Ci using Mathematica. This is a platform independent program that can be run on DOS or UNIX systems. The application listed here is for the calculation of the vertical current due to the perpendicular magnetic dipole moment. The application is changed by changing the mapping matrix data derived from the code in the previous section. Italic text indicates output.

```
<<DescriptiveStatistics.m
<<DataManipulation.m


m = 15;      (*number of aperture points*)
n = 16;    (*number of source zones*)
q = 1000;     (*number of iterations*)
lim = m*n*q+20; (*set recursion limit based on matrix size*)
$RecursionLimit = $IterationLimit = lim;
greendata =
{{14.2325,14.1946,14.1567,33.7777,33.7031,33.6286,35.4288,35.3770,35.3253,24.2236,24.2038,24.1839,8.
3287,8.3245,8.3203},
{60.8650,60.0936,59.3278,135.5463,134.1232,132.7106,126.4476,125.6928,124.9408,77.4654,77.2626,77.0
600,25.0747,25.0426,25.0106},
{209.3539,195.7515,182.8029,427.5815,398.7672,372.4986,271.1129,263.1499,255.4213,123.9075,122.775
2,121.6472,35.1054,34.9885,34.8709},
{-1011.5494,-156.6772,-
107.9150,1545.4066,1089.5585,821.2570,151.6541,212.0965,196.3877,11.2677,54.7381,56.7227,-
2.0477,11.9766,12.9983},
{1.0433,1.0616,1.0799,6.9678,6.9799,6.9920,15.5267,15.4919,15.4572,16.5219,16.4793,16.4368,6.9472,6.9
318,6.9164},
{-7.9147,-7.3819,-
6.8542,11.5990,12.0516,12.4981,62.8277,62.0225,61.2258,69.6859,68.9171,68.1525,27.8793,27.6721,27.46
53},
```

```
{-111.8740,-99.1785,-87.3996,-95.9115,-77.9721,-
62.5253,249.4821,225.3411,204.1219,211.4835,200.4819,189.9837,64.6743,63.1059,61.5569},
{-464.0951,-335.5596,-260.4547,-3593.1670,-1623.1370,-
1195.5420,3092.3955,1580.0950,1162.9324,474.8100,332.9890,283.7147,92.3987,65.1837,60.3535},
{-6.9472,-6.9318,-6.9164,-16.5219,-16.4793,-16.4368,-15.5267,-15.4920,-15.4572,-6.9678,-6.9800,-6.9921,-
1.0433,-1.0616,-1.0799},
{-27.8793,-27.6721,-27.4653,-69.6860,-68.9171,-68.1525,-62.8277,-62.0225,-61.2259,-11.5990,-12.0517,-
12.4981,7.9147,7.3818,6.8542},
{-64.6744,-63.1060,-61.5569,-211.4835,-200.4819,-189.9837,-249.4821,-225.3412,-
204.1219,95.9114,77.9720,62.5252,111.8740,99.1784,87.3995},
{-92.3992,-65.1840,-60.3537,-474.8089,-332.9887,-283.7145,-3092.3901,-1580.0938,-
1162.9312,3593.1677,1623.1372,1195.5419,464.0962,335.5599,260.4551},
{-8.3287,-8.3245,-8.3203,-24.2237,-24.2038,-24.1839,-35.4288,-35.3770,-35.3253,-33.7777,-33.7031,-
33.6286,-14.2325,-14.1946,-14.1567},
{-25.0748,-25.0427,-25.0106,-77.4654,-77.2626,-77.0600,-126.4476,-125.6928,-124.9408,-135.5464,-
134.1232,-132.7106,-60.8650,-60.0936,-59.3277},
{-35.1054,-34.9885,-34.8710,-123.9075,-122.7752,-121.6473,-271.1130,-263.1500,-255.4213,-427.5817,-
398.7674,-372.4988,-209.3540,-195.7516,-182.8029},
{2.0460,-11.9772,-12.9988,-11.2668,-54.7377,-56.7225,-151.6542,-212.0967,-196.3878,-1545.4070,-
1089.5586,-821.2577,1011.5479,156.6763,107.9144}};
Tgreen = Transpose[greendata];
dis = Table[0,{(n+1)}];  (*table that records incidences of N sources*)
contrib = Table[0.0,{m},{n}]; (*table of each source contribution*)
subtot = Table[0.0,{q},{m}]; (*table of total at each aperture*);
Do[      (*loop that generates random data*)
weight = Table[Random[Integer],{n}];
num = Apply[Plus,weight]+1;(*number of points +1*)
dis[[num]]++;
      Do[          (*loop that iterates through aperture points*)
      contrib[[j]] = weight*Tgreen[[j]];(*mapping matrix *random*)
      subtot[[i,j]] = Apply[Plus,contrib[[j]]], (*sum for in phase*)
      {j,m}],
{i,q}]
ListPlot[dis,PlotJoined -> True,PlotRange -> All, AxesOrigin -> {0,0}]

-Graphics-

moyen = Table[0.0,{m}];
sd = Table[0.0,{m}];
iq = Table[0.0,{m}];
Tsubtot = Transpose[Abs[subtot]];
Do[
avg = Mean[Tsubtot[[k]]];
moyen[[k]] = avg,{k,m}]
```

```
Print[moyen]
```

General::spell1:
787.114 301.02238.119 1985.81 952.51723.601 1635.06 901.306691.34 1961.33 938.454 711.394 794.887301.292238.223

```
Do[
sigma = StandardDeviation[Tsubtot[[l]]];
sd[[l]] = sigma,{l,m}]
Print[sd]
```

552.476202.379161.6841333.42619.618475.5891449.2717.798526.1451336.11626.043481.552 551.069200.844159.87

```
Do[
atsubtot = Abs[Tsubtot[[a]]];
tsubsort = Sort[atsubtot];
ts = InterpolatedQuantile[tsubsort,0.9];
iq[[a]] = ts,{a,m}]
Print[iq]
```

1570.71589.143474.4533927.861875.111418.473345.411840.811402.383926.221872.531417. 1570.08593.103470.054

References

[Aho 74] Aho, A.V., Hopcropft, J.E., Ullman, J.D., **The Design and Analysis of Computer Algorithms**, Addison-Wesley Publishing Company, Don Mills, Ont. 1974.

[ANSI 87-1] **ANSI T1.101-1987, Synchronization Interface Standards for Digital Networks**, American National Standards Institute, New York,N.Y..

[ANSI 87-2] **ANSI T1.102-1987, American National Standard for Telecommunications - Digital Hierarchy - Electrical Interfaces**, American National Standards Institute, New York, N.Y..

[ANSI 89] **ANSI T1X1/89-003R1, A Technical Report on Mathematical Modelling of DS1, DS1A, DS1C, DS3, and DS4NA Waveshapes**, American National Standards Institute, New York, N.Y..

[ANSI 91] **ANSI C63.4, Methods of Measurement of Radio Noise Emissions from Low-Voltage Electrical and Electronic Equipment in the Range of 9 kHz to 40 GHz**, American National Standards Institute, New York, N.Y..

[Bellcore 89] **Bellcore TR-TSY-000499,, Transport Systems Generic Requirements (TSGR): Common Requirements, Issue 3**, Morristown, New Jersey, December 1989.

[Bellcore 90] **Bellcore TA-NWT-000253, Synchronous Optical Network (SONET) Transport Systems: Common Generic Criteria,** Issue 6, Bellcore, Morristown, New Jersey, September 1990.

[Bennett 58] Bennett, W.R., *Statistics of Regenerative Digital Transmission* , The Bell System Technical Journal, November 1958, 37, pp. 1501-1542.

[Bronaugh 91] Bronaugh, T., *Radiated Emissions Test Performance of the GHz TEM Cell* , 1991 IEEE EMC Symposium, Cherry Hill, New Jersey.

[Bylanski 80] Bylanski, P., Ingram, D.G.W., **Digital Transmission Systems, 2nd Ed., IEE Telecommunications Series 4,** Peter Peregrinus Ltd., Stevenage, England, 1980.

[CISPR 87] C.I.S.P.R. Publication 16, C.I.S.P.R. **Specification for Radio Interference Measuring Apparatus and Measurement Methods,** International Electrotechnical Commission, Geneva, 1987.

[CISPR 84] **C.I.S.P.R. Publication 22, Limits and methods of measurement of radio interference characteristics of information technology equipment,** First Edition, International Electrotechnical Commission, Geneva, 1984.

[ComCan 90] **CS-03, Issue 7, Part II; Requirements and Test Methods for TE Interfaces for Attachment to 1.544 Mb/s (DS-1) Digital Facilities,** Communications Canada, Ottawa, Ontario

[Cook 79] Cook, J.H., *Quasi-Peak-to-RMS Voltage Conversion* , IEEE Trans. Electromag. Compat., vol. EMC-21, no. 1, pp. 9-12, Feb. 1979.

[Cooray 91-1] Cooray, F.R., Crawhall, R., Costache,G.I.,*Radiated Fields from Circuit Components Inside Rectangular Enclosures with Apertures* , Can. J. Electrical and Comput. Eng., vol. 16, no. 4, pp.143-147, 1991.

[Cooray 91-2] Cooray, F.R., Crawhall, R., Costache,G.I., *Simplified Models for EM Coupling Inside Rectangular Enclosures*, Proc. 2nd Int. Conf. Electromagnetics in Aerospace Applications, pp. 107-109, Politechnico di Torino, Italy, Sept. 17-20, 1991.

[Cover 91] Cover, T.M., Thomas, J.A., **Elements of Information Theory**, John Wiley & Sons, Toronto, 1991.

[Crawhall 91] Crawhall, R., *EMI Potential of Non-Periodic Signals* , IEEE Int. EMC Symp., pp.334-339, Anaheim, Calif. Aug 17-21, 1992.

[Diaz-Olavarrieta 91] Diaz-Olavarrieta, L., *Groundbounce in ASICs : Modelling and Test Results* , 2nd European Test Conference, Munich, April 10-12, 1991.

[Duc 75] Duc, N.Q., *Line Coding Techniques for Baseband Digital Transmission* , A.T.R., vol. 9, no. 1, 1975.

[Duc 77] Duc, N.Q., Smith, B.M., *Line Coding for Digital Data Transmission* , A.T.R., vol. 11, no. 2, 1977.

[FCC 89] **FCC 89-103 (Gen. Docket No. 87-389), Revision of Part 15 of the Rules Regarding the Operation of Radio Frequency Devices Without an Individual License**, Federal Communications Commission, Washington D.C., 1989.

[Goulette 92-1] Goulette,R.R., Crawhall, R.J. ,Xavier, S.K., *The Determination of Radiated Emissions Limits For Integrated Circuits Within Telecommunications Equipment* , IEICE Trans. Commun., vol E75 B, no. 3, March 1992.

[Goulette 92-2] Goulette, R.R., *The Measurement of Radiated Emissions from Integrated Circuits*, IEEE Int. EMC Symp., Anaheim, Calif., pp.340-345, Aug. 17-21, 1992.

[Hoefer 86] Hoefer, W.J.R.,*The Transmission Line Matrix Method - Theory and Applications* , IEEE Trans. Microwave Theory Tech. vol. MPT-33, no. 10 pp 882-893, Oct. 1985.,

[Kama 86] Kama, Y., Sato, R., *Radiation model of finite-length transmission lines* , IEEE Int. EMC Symp., San Diego, Calif., Sept. 16-18, 1986.

[Khan 89] Khan, R.L., Costache, G.I., *Finite element method applied to modelling crosstalk on printed circuit boards*, IEEE Trans. Electromagn. Compat., vol. EMC-31, pp.5-15, Feb. 1989.

[Laurin 91] Laurin, J-J., **EMI-Induced Failures In Digital Systems**, Doctoral Thesis, University of Toronto, Department of Electrical Engineering, Toronto, Ontario, August 1991.

[Lee 86] Lee, K.S.H., **EMP Interaction: Principles, Techniques, and Reference Data**, Hemisphere Publishing, New York, 1986.

[Leon-Garcia 89] Leon-Garcia, A., **Probability and Random Processes for Electrical Engineering**, Addison-Wesley, Don Mills, Ontario, 1989.

[LoVetri 90] LoVetri, J., **Computer Techniques for Electromagnetic Interaction Modelling**, Doctoral Thesis, University of Ottawa, Ottawa, Ontario, Aug. 1990.

[Méndez 78] Méndez, H.A., *Shielding Theory of Enclosures with Apertures* , IEEE Trans. Electromagn. Compat., vol. EMC-20, no. 2, pp. 296-305, May 1978.

[Mitchell 80] Mitchell, A.R., Griffiths, D.F., **The Finite Difference Method in Partial Differential Equations**, John Wiley & Sons, New York, 1980.

[Nano 91] Nano, E., Correlation Factors for Quasi-Peak Measurements with Spectrum Analyser , .

[Ott 88] Ott, H.W., **Noise Reduction Techniques in Electronic Systems, 2nd ed.**, Wiley-Interscience, Toronto, 1988.

[Papoulis 84] Papoulis, A., **Probability, Random Variables, and Stochastic Processes, Second Edition,** McGraw-Hill Series in Electrical Engineering, McGraw-Hill Book Company, New York, 1984.

[Pathak 83] Pathak, P.H., *On the Eigenfunction Expansion of Electromagnetic Dyadic Green's Functions*, IEEE Trans. Antennas Propagat., vol. AP-31, no. 6, Nov., 1983.

[Paul 85] Paul, C.R., Everett, W.W., *Modelling crosstalk on printed circuit boards*, Phase Rep., RADC-TR-85-107, Rome Air Development Center, Griffiss AFB, NY, July 1985.

[Paul 92] Paul, C.R., **Introduction to Electromagnetic Compatibility**, John Wiley & Sons, New York, 1980.

[Ramo 84] Ramo, S., Whinnery, J.R., Van Duzer, T.,**Fields and Waves in Communications Electronics, Second Edition**, John Wiley & Sons, New York, 1984.

[Radojicic 91] Radojicic, M., Costache, G., *A model to predict radiated emissions from electronic circuits* , IEEE Int.EMC Symp., Cherry Hill, New Jersey, 1991.

[Rahmat-Samii 75] Rahmat-Samii, Y., *On the question of computation of the dyadic Green's function at the source region in waveguides and cavities* , IEEE Trans. Microwave Theory Tech., vol. MTT-23, pp.908-914, Sept. 1975.

[Rumsey 54] Rumsey, V.H., *Reaction Concept in Electromagnetic Theory* , Physical Review, vol. 94, no. 6, pp. 1483 - 1491, June 15, 1954.

[Seidel 78] Seidel, D.B. *Aperture excitation of a wire in a rectangular cavity*, IEEE Trans. Microwave Theory & Tech., vol. MTT-24, pp. 597-601, Sept. 1976.

[Shankar 89] Shankar, V., Hall, W.F, Mohammadian, A.H.., *A Time-Domain Differential Solver for Electromagnetic Scattering Problems* , Proc. IEEE, vol.77, no. 5, pp. 709-721, May 1989.

[Silvester 83] Silvester, P., Ferrari, R.L., **Finite Elements for Electrical Engineers**, Cambridge University Press, 1983.

[Simpson 88] Simpson, J.P., Goulette, R.R., *Radiation from microstrip transmission lines* , IEEE Int. EMC Symp., Seattle, Washington, August 2-4, 1988.

[Stutzman 81] Stutzman,W.L.,Theile,G.A., **Antenna Theory and Design, John Wiley & Sons**, Toronto, 1981.

[Tai 76] Tai, C.T., Rozenfeld, P., *Different representations of Dyadic Green's Functions for a Rectangular Cavity,* IEEE Trans. Microwave Theory Tech., vol. MTT 24, pp 597-601, Sept. 1976.

[Taflove 89] Taflove, A., Umashankar, K.R., *Review of FD-TD Numerical Modelling of Electromagnetic Wave Scattering and Radar Cross Section*, Proceedings of the IEEE, vol. 77, no. 5, pp. 682-699, May 1989.

[Tilston 90] Tilston, M.A., Balmain, K.G., *A multiradius, reciprocal implementation of the thin-wire moment method* , IEEE Trans. Antennas Propagat., vol. AP-38, no. 2, pp. 281-285, Feb. 1990.

[Violette 87] Violette, J.L.N., White, D.R.J., Violette, M.F., **Electromagnetic Compatibility Handbook**, Van Nostrand Reinhold Company Inc., New York, 1987.

[Wallace 92] (enter reference to bell report)

[Wolff 88] Wolff, E.A., **Antenna Analysis**, Artech House Inc., pp. 166-169, 1988.

[Wood 91] Wood, D.V., *The Prediction of the EMC Performance of `Electronic Systems Prior to Fabrication* , IEEE Int. EMC Symp., New Jersey, pp. 145-148, Aug. 1991.

[Yee 66] Yee, K.S. *Numerical Solution of Initial Boundary Value Problems Involving Maxwell's Equations in Isotropic Media* , IEEE Trans. Antennas Propagat., vol. AP-14, no. 3, pp. 302-307, May 1966.